THERMOELECTRIC STUDIES OF THE TIN TELLURIDE

THERMOELECTRIC STUDIES OF THE TIN TELLURIDE

By

SHAOCHANG SONG, B.Sc.

A Thesis submitted to the School of Graduate Studies in Partial Fulfillment of the Requirements for the Degree Doctor of Philosophy

McMaster University

DOCTOR OF PHILOSOPHY (2023) McMaster University

Hamilton, Ontario (chemistry)

TITLE: Thermoelectric Studies of the Tin Telluride

AUTHOR: Shaochang Song, B.Sc. (McMaster University)

SUPERVISOR: Yurij Mozharivskyj

NUMBER OF PAGES: xxix, 230.

Lay Abstract

In recent decades, renewable energy has attracted a lot of attention due to an increase in the global energy use and depletion of fossil fuel reserves. Thermoelectric materials are expected to play a vital role as green energy generators to overcome the upcoming energy crisis as they can directly convert waste heat into electricity through the Seebeck effect.

In this dissertation, the main goal is optimizing the thermoelectric performance of SnTe for the above room temperature applications. Different doping/ substituting/alloying strategies were applied to improve the performance. The obtained thermoelectric properties of the SnTe-based materials were rationalized in terms of the charge carrier behavior, changes in the electronic structure, and phonon propagation.

Abstract

The lead-free tin telluride (SnTe) is considered as a potential candidate to substitute lead telluride (PbTe) for thermoelectric power generation based on their similar crystal and electronic structures. However, the relatively high lattice thermal conductivity and low Seebeck coefficient of pristine SnTe are detrimental for real-life applications. This dissertation explored elements-doping/substituting of SnTe to overcome those shortcomings and improve SnTe thermoelectric performance.

A series of the $Sn_{1-x}Ge_xTe$ phases were synthesized and studied. When the Ge amount reaches 50% or higher, $Sn_{1-x}Ge_xTe$ undergoes a phase transition from the rock-salt structure ($Fm\overline{3}m$) to the rhombohedral one ($R3m$). The $Sn_{0.5}Ge_{0.5}Te$ phase was explored in more details because it delivers the best thermoelectric performance with the $Sn_{1-x}Ge_xTe$ series. The electron-richer Sb and Bi were substituted on the Sn/Ge site to optimize the charge transport properties, and Cu_2Te was added into the matrix to improve the thermoelectric performance further.

The In/Sb and In/Bi co-doping on the Sn/Ge sites was employed for Seebeck coefficient optimization. A comparative study of the electronic structure of the $Sn_{0.5}Ge_{0.5}Te$-based samples was performed. The calculations indicated a band convergence and changes in the valence band, thus providing insight into the co-doping effects.

Suppression of the lattice thermal conductivity of SnTe was performed via alloying with $AgSnSe_2$ and PbTe, which introduced strong atomic disorder. Additionally, $AgSnSe_2$ showed a hole donor behavior in SnTe, and the increased carrier concentration

compensated for the reduction in the carrier mobility, thus rendering a decent electrical conductivity in alloyed samples. As a result, the alloying effectively improved the samples' thermoelectric performance.

Acknowledgements

Not only this work but also the completion of my graduate studies will never have been achieved without the guidance of my supervisor, Dr. Yurij Mozharivskyj, who has been more than generous with help from the topic selection to the research efforts. Also, I would like to express my sincere appreciation to the supervisory committee members, Dr. John Greedan and Dr. Peter Kruse, for their guidance in the committee meetings. Their knowledgeable insights always pinpoint the exact problems in my study, which save me much time and lead me in the right direction.

The experimental part of my study's success is inseparable from the strong support from one of the collaborators, Dr. Yu-Chih Tseng, for years. I am very thankful for the training, advising, and companionship of the senior student Chun-Wan Timothy Lo in my studies. Also, I want to acknowledge Dr. Jan-Hendrik Pöhls, who has a rigorous research attitude, critical thinking, and inquiring mind; his guidance always inspired me, and a light bulb went on in my head during the discussion between us. I am thankful to have worked with my current and former group members for their help in my studies and beyond. Besides, the debate on solid-state NMR with Mengyang Cui is valuable for broadening my knowledge in the solid-state NMR area and completing my study efficiently.

I am also very grateful for the continued support from my family. The positive impacts they brought me are indispensable and invaluable to completing my study.

Table of contents

List of Figures

List of Tables

List of all Abbreviations and Symbols

Symbol	Description
a	Lattice constant
A	The effective cross area
A_n	The cross area of the *n*-type branch
A_p	The cross area of the *p*-type branch
A_s	The cross-sectional area
B	Magnetic field
c	Specific heat capacity
C_p	The heat capacity under constant pressure
C_p	The heat capacity obtained from the Neumann-Kopp rule
c_v	The specific heat capacity per unit volume
C_v	The heat capacity under constant volumes
$C_{v,ele}$	The heat capacity under constant volumes contributed by electrons
d	The thickness of the sample
d_{grain}	The grain sizes
d_{hkl}	The interplanar distance between adjacent Miller planes
D	The thermal diffusivity
e	Electron charge
$E_{electronic}$	The total electronic energy
E_{estat}	Electrostatic interactions energy
E_{exc}	The exchange-correlation energy
E_F	Fermi energy
E_g	Energy gap
E_g	Band gap
E_J	Where the current flow happened
E_k	The possible energy state of the electron
$f(E)$	The Fermi-Dirac function
f_i	The fraction of doping/alloying elements
f_j	The atomic scattering factor for the j^{th} atom
F_{hkl}	Structure amplitude

$\|F_{hkl}\|^2$	The structure factor
$\|F_{hkl}^{obs}\|$	The absolute value of the structure amplitude
g_j	The occupation factor for the j^{th} atom
h	The Planck's constant
ħ	The reduced the Planck's constant
I	Electrical current
I_{hkl}	Imaginary component of structure amplitude
I_{max}	The maximum current of the Peltier cooling
j	Electric current density
k	The wavevector
k_B	The Boltzmann constant
k_e	Electronic thermal conductivity
k_l	Lattice thermal conductivity
k_n	The thermal conductivity of the *n*-type branch
k_p	The thermal conductivity of the *p*-type branch
K_{tot}	The total thermal conductance
k_{vector}	The wave vector
L	Lorenz number
L_{eff}	Effective Lorenz number
L_n	The length of the *n*-type branch
l_0	The effective distance between the two thermal couples.
L_p	The length of the *p*-type branch
l_p	The mean free path of phonons
l_s	The length of the specimen
m	The ratio of the load resistance to the total resistance of the thermoelectric generator
$\overline{m}$	The average mass in the site
$\overline{M}$	The average atomic mass
m_b^*	The band effective mass
m_{DOS}	The density of states effective mass
$M(E)$	The number of channels for conduction
m_e	The mass of an electron
m_i	The mass of fraction of doping/alloying elements

n	The carrier concentration
n_H	Hall concentration
n_H	Hall carrier concentration
N_{band}	The number of valleys that are converged at the energy level
$N_{symmetry}$	The number of the degeneracy of the high symmetry point in the Brillouin zone
N_V	The number of conducting valleys
Q	Heat energy
q	The elementary charge
Q_c	Heat energy at the cold junction
Q_h	Heat energy at the hot junction
τ	The relaxation time of charge carriers
$\bar{r}$	The average radius in the site
r_i	The radius of fraction of doping/alloying elements
R	The universal gas constant
R_H	Hall coefficients
R_{hkl}	Real component of structure amplitude
R_L	Load resistance
R_o	The electrical resistance determined by Ohm’s law
R_{tot}	The total electrical resistance of the thermoelectric generator
t	Thickness of the sample
$t_{\frac{1}{2}}$	The time required for the recording surface to reach half of the maximum temperature rise
t_j	The atomic displacement parameter for the j^{th} atom
T	The temperature of the specimen
T_c	The temperature at the cold junction
T_h	The temperature at the hot junction
$T_{kinetic}$	The kinetic energy
u_H	Hall mobility
V_a	The volume per atom
v_D	The Debye frequency
v_g	The phonon group velocity
v_p	The phonon phase velocity
v_s	The speed of sound

v_T	The frequency of atomic vibration with temperature
V_{direct}	The volume of the unit cell of the direct lattice
V_H	Hall voltage
V_U	The unit cell volume
V_{unit}	The volume of the unit cell in the real space
W_{in}	The network in
W_{out}	The network output
z	The temperature dependent figure of merit of thermoelectricity
zT	The figure of merit for a thermoelectric generator
Z	Atomic number
α	Seebeck coefficient
α_e	The Seebeck coefficient contributed by electrons
α_h	The Seebeck coefficient contributed by holes
α_n	The Seebeck coefficient of the *n*-type branch
α_p	The Seebeck coefficient of the *p*-type branch
α_{tot}	The total Seebeck coefficient
ΔT	Temperature difference
ΔT	The temperature difference between hot and cold junction
ΔT_{max}	The maximum temperature differences
ΔV	Potential difference
ΔV_I	resistive voltage difference
ΔV_s	Seebeck coefficient voltage
γ	The Grüneisen parameter
γ_{ele}	The Sommerfeld constant
θ	The angle between the incident beam with the Miller planes
θ_D	The Debye temperature
λ	The wavelength of the radiation X-ray
$\lambda(E)$	The mean-free-path for backscattering
μ	The carrier mobility
μ_H	Hall carrier mobility
Π	Peltier coefficient
ρ	The electrical resistivity
ρ_n	The electrical resistivity of the *n*-type branch

ρ_p	The electrical resistivity of the *p*-type branch
σ	The electrical conductivity
σ_e	The electrical conductivity contributed by electrons
σ_h	The electrical conductivity contributed by holes
τ	The relaxation time of charge carriers
τ_{grain}	The relaxation time due to phonon-grain boundary scattering
τ_i	The relaxation time due to different phonon scattering modes
τ_p	The relaxation time of phonons
τ_{PD}	The relaxation time due to phonon point defect scattering
τ_{tot}	The totally relaxation time
τ_U	The relaxation time due to Umklapp scattering
$\psi_k(\boldsymbol{r})$	The wavefunction of the electron
ω_p	The phonon vibration frequency
ASA	Atomic sphere approximation
C	heat capacity
CB	Conduction band
CBM	Conduction band minimum
DFT	Density functional theory
DOS	Density of state
EDS	Energy Dispersive X-ray Spectroscopy
LA	Longitudinal acoustic mode
LMTO	linear-muffin tin orbital method
LO	Longitudinal optical mode
MSI	Low-dimensional metal-semiconductor interfaces
NFE	Nearly-Free Electron
PAW	Projector-augmented wave
PBE	Perdew-Burke-Ernzerhof
PF	Power factor
PXRD	Powder X-ray diffraction
SEM	Scanning electron microscopy
SPB	Single parabolic band
SPS	Spark Plasm Sintering
TA	Transverse acoustic mode
TB	Tight-binding

TE	Thermoelectric
TO	Transverse optical mode
VB	Valence band
VBM	Valence band maximum
XRD	X-ray diffraction

Declaration of Academic Achievement

Published Manuscript

1. **Song, S**.; Tseng, Y.-C.; Mozharivskyj, Y. Optimizing Thermoelectric Performance of SnTe via Alloying with $AgSnSe_2$ and PbTe. *Journal of Alloys and Compounds* **2023**, *947*, 169415.

2. **Song, S**.; Huang, Y.; Tseng, Y.-C.; Valiyaveettil, S. M.; Chen, K.-H.; Mozharivskyj, Y. Converting N-Type $Co_4Ge_6Te_6$ Skutterudite into p-Type and Enhancing Its Thermoelectric Properties through Fe Substitution. *Journal of Alloys and Compounds* **2022**, *913*, 165314.
3. **Song, S**.; Yang, Z.; Huang, Y.; Tseng, Y.-C.; Valiyaveettil, S. M.; Chen, K.-H.; Mozharivskyj, Y. Enhancing Thermoelectric Performance of $Sn_{0.5}Ge_{0.5}Te$ via Doping with In/Zn, In/Sb and In/Bi. *Journal of Solid State Chemistry* **2021**, *302*, 122444.
4. Bakhshi, H.; Sarraf-Mamoory, R.; Yourdkhani, A.; **Song, S**.; Tseng, Y.-C.; Mozharivskyj, Y. Improvements in the Thermoelectric Efficiency of SrTiO3 through Donor Doping. *Ceramics International* **2022**, *48* (4), 5831–5839.
5. **Song, S**.; Lo, C.-W. T.; Aminzare, M.; Tseng, Y.-C.; Valiyaveettil, S. M.; Mozharivskyj, Y. Enhancing the Thermoelectric Performance of $Sn_{0.5}Ge_{0.5}$ Te *via* Doping with Sb/Bi and Alloying with Cu_2Te: Optimization of Transport Properties and Thermal Conductivities. *Dalton Trans.* **2020**, *49* (18), 6135–6144.
6. Lo, C.-W. T.; Kolodiazhnyi, T.; **Song, S**.; Tseng, Y.-C.; Mozharivskyj, Y. Experimental Survey of Dopants in $Zn_{13}Sb_{10}$ Thermoelectric Material. *Intermetallics* **2020**, *123*, 106831.

Chapter 1. Introduction

Today, fossil fuels are still a significant energy source; however, only around 40% of their energy is used, and the rest is rejected into the environment as waste heat.[1] If this waste heat could be captured and converted into electricity, this would significantly increase the overall efficiency of energy consumption processes and, thereby, reduce our carbon footprint. Thermoelectric materials can directly convert heat into electricity through the Seebeck effect, and they are expected to play a vital role as green energy generators in the future.[2]

1.1 Thermoelectric effects

In the thermoelectric field, the Seebeck, Peltier, and Thomson effects are the fundamental principles that explain the relationship between temperature gradient, electric voltage and current.[3]

1.1.1 Seebeck effect

In 1822, the German physicist Thomas Johann Seebeck observed that a magnetic field was produced when a closed circuit was made of two dissimilar metals with a temperature gradient at the junction. As a result, the needle of a nearby magnetic compass was deflected. Upon further experimentation, Seebeck concluded the phenomenon was due to changes in a magnetic field, and the degree of deflection of the magnetic compass needle is proportional to the temperature gradient applied on the junction of two dissimilar metals.[4] Seebeck named this phenomenon is a Seebeck effect. Unfortunately, he didn’t realize the electrical nature of the effect, so the Seebeck effect was classified as a thermomagnetic effect until 1823.

The Danish physicist Hans Christian Ørsted reported the current generated in a closed circuit made of two dissimilar metals when a temperature gradient is applied at the junctions of the circuit.[5] Today, the Seebeck effect is described as the potential difference induced by a temperature gradient in a closed circuit made of two dissimilar metals, and the Seebeck coefficient α (referenced as thermopower) is expressed by the potential difference (ΔV) against the temperature gradient (ΔT) at the linked junctions of two dissimilar metal, as given by equation (1-1).[6]

$$\alpha = -\frac{\Delta V}{\Delta T} \quad (1\text{-}1)$$

The sign of the Seebeck coefficient is dependent on the dominant charge carriers in a material; this coefficient is negative for an *n*-type material and positive for a *p*-type material.[7]

1.1.2 Peltier effect

In 1834, the French scientist Jean Charles Athanase Peltier discovered the Peltier effect, which can be understood as the reverse phenomenon of the Seebeck effect. Peltier observed a temperature difference between two junctions when an electrical current was applied in a closed circuit made of two dissimilar metals.[6,7] The definition of Pletier effects was completed by Russian scientist Heinrich Friedrich Emil Lenz in 1839; he reported that the absorption/dissipation of heat at junctions is related to the direction of the electrical current in the closed circuit.[8] The mathematical expression of the Peltier effect is shown by the equation (1-2),[7] where Π is the Peltier coefficient, Q is the heat flow, and I is the electrical current.

$$\Pi = \frac{Q}{I} \text{ (1-2)}$$

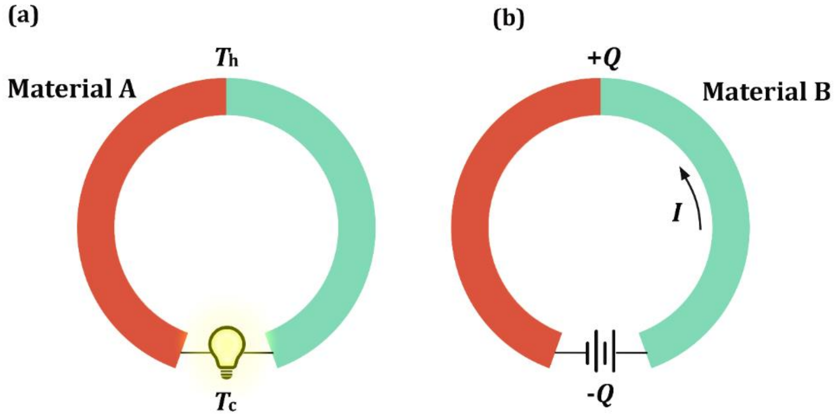

Figure 1.1. A schematic diagram of (a) Seebeck effect and (b) Peltier effect.

1.1.3 Thomson Effect

The British mathematical physicist William Thomson discovered the Thomson effect and published this effect in 1854.[9] Unlike the Seebeck and Peltier effects which are observed in a closed circuit made of two dissimilar metals, the Thomson effect is defined by absorption/dissipation of heat along a homogeneous conductor when an electrical current is applied with a temperature gradient.[6–8] Heat energy Q that is produced for a current density j across a non-isothermal homogeneous conductor is given by the equation (1-3).[8,10]

$$Q = -Tj \cdot \nabla\alpha \text{ (1-3)}$$

Where T is the absolute temperature, j is current density, and $\nabla\alpha$ is the change of Seebeck coefficient with the temperature, multiplied by the temperature gradient ∇T in a homogeneous conductor (1-4).

$$\nabla\alpha = (\frac{d\alpha}{dT})\nabla T \text{ (1-4)}$$

By combing equations (1-3) and (1-4):

$$Q = -Tj \cdot (\frac{d\alpha}{dT})\nabla T \text{ (1-5)}$$

Based on equation (1-5), the Thomson coefficient τ_T is defined as:

$$\tau_T = T(\frac{d\alpha}{dT}) \text{ (1-6)}$$

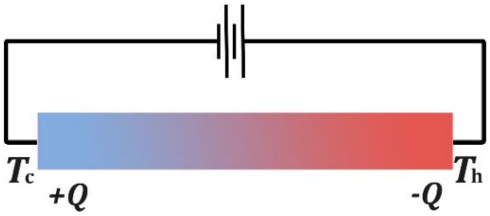

Figure 1.2. A schematic diagram of Thomson effect.

Thomson also established mathematical relationship between the Seebeck and Peliter coefficients:[8]

$$\Pi = \alpha T \text{ (1-7)}$$

1.2 Thermoelectric Materials

The thermoelectric (TE) devices are made from both an *n*- and a *p*-type semiconductors, and they can directly convert electricity into thermal energy via the Peltier effect or thermal energy into electrical current via the Seebeck effet.[11] Figure 1.4 (a) shows the refrigeration mode; holes follow the direction of the current and electrons follow the inverse direction of the current applied in the loop, and the heat is absorbed or released at each end of the junction. Figure 1.4 (b) shows the power generation mode; charge carriers follow the temperature gradient from the hot side to the cold side, and an electrical current is generated in the loop.

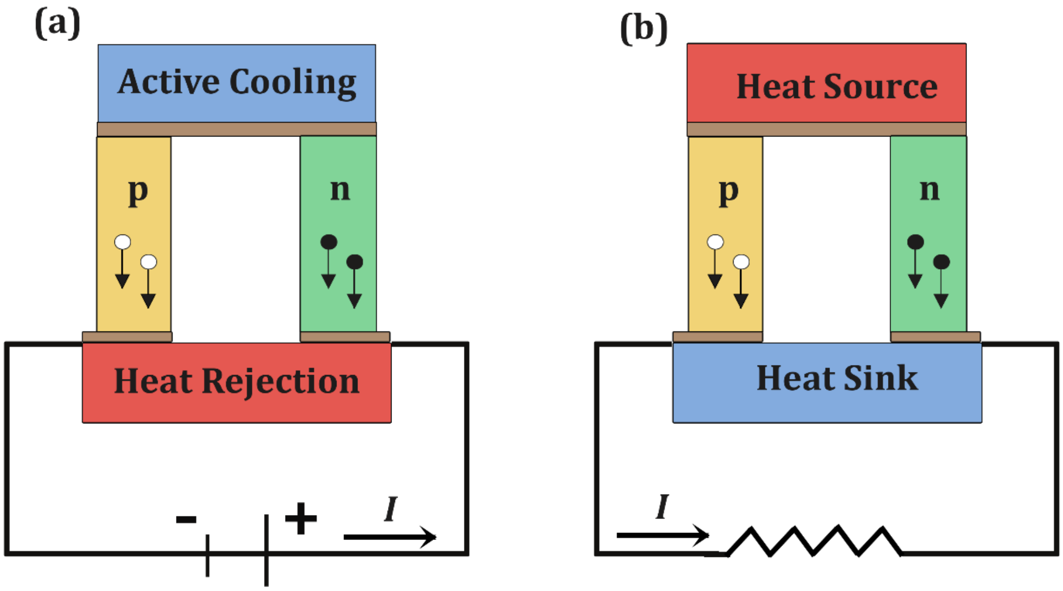

Figure 1.3. (a) The refrigeration mode and (b) the power generation mode for a thermoelectric generator.

1.2.1 Thermoelectric Figure of Merit

In 1949, the Russian physicist Abram Fedorovich Ioffe defined the figure of merit of thermoelectricity by using the dimensional parameter *ZT*.[8,12] In Figure 1.3 (a), the total heat energy Q_c absorbed at the cold junction of a thermoelectric cooler is given by the equation:[13]

$$Q_c = (\alpha_p - \alpha_n)IT_c - K_{tot}\Delta T - \frac{1}{2}I^2R_{tot} \quad (1\text{-}8)$$

Where $\alpha_p\ and\ \alpha_n$ is the Seebeck coefficient of the *p*- and *n*-type branches (note: the *n*-type semiconductor presents a negative Seebeck coefficient, which leads to a negative Peltier heat flow), I is the current applied in the loop, T_c is the temperature at the cold junction, K_{tot} is the total thermal conductance, ΔT is the temperature difference between hot and cold junction, and R_{tot} is the total electrical resistance of the thermoelectric generator. And the K_{tot} and R_{tot} can be described by equations (1-9) and (1-10).[13]

$$K_{tot} = k_p\frac{A_p}{L_p} + k_n\frac{A_n}{L_n} \quad (1\text{-}9)$$

$$R_{tot} = \rho_p\frac{L_p}{A_p} + \rho_n\frac{L_n}{A_n} \quad (1\text{-}10)$$

Where $k_p\ and\ k_n$, $A_p\ and\ A_n$, $L_p\ and\ L_n$ and $\rho_p\ and\ \rho_n$ are the thermal conductivity, the cross area, the thermoelement length, and the electrical resistivity of the *p*- and *n*-type branches.

The maximum current I_{max} of the cooling mode can be calculated by taking the 1st derivative of Q_c with respect to I and setting it to zero:[13]

$$I_{max} = \frac{(\alpha_p - \alpha_n)T_c}{R_{tot}} \quad (1\text{-}11)$$

Based the equation (1-8) and (1-11), the maximum temperature differences ΔT_{max} can be written as:[13]

$$\Delta T_{max} = \frac{(\alpha_p - \alpha_n)^2 {T_c}^2}{2K_{tot}R_{tot}} \quad (1\text{-}12)$$

Then the temperature-dependent figure of merit, *z*, is defined by the equation (1-13).[13]

$$z = \frac{(\alpha_p - \alpha_n)^2}{K_{tot}R_{tot}} \quad (1\text{-}13)$$

Based on the equation (1-13), *z* is only depended on the properties of *n*- and *p*-type legs. Due to R_{tot} and K_{tot} are both dependent on the dimensions of the legs, the equation (1-13) can be expanded by plugging equations (1-9) and (1-10) into equation (1-13).

$$z = \frac{(\alpha_p - \alpha_n)^2}{k_p\rho_p + k_p\rho_n(\frac{L_nA_p}{L_pA_n})^{\frac{1}{2}} + k_n\rho_p(\frac{L_pA_n}{L_nA_p})^{\frac{1}{2}} + k_n\rho_n} \quad (1\text{-}14)$$

When

$$\frac{L_nA_p}{L_pA_n} = \frac{k_p\rho_p}{k_n\rho_n} \quad (1\text{-}15)$$

the equation (1-14) can be optimized to

$$z = \frac{(\alpha_p - \alpha_n)^2}{[(k_p\rho_p)^{\frac{1}{2}} + (k_n\rho_n)^{\frac{1}{2}}]^2}\,. \quad (1\text{-}16)$$

For a single *n*- and *p*-type semiconductor, the thermoelectric figure of merit is defined by the equation (1-17).[13]

$$zT = \frac{\alpha^2 T}{\rho k} \text{ (1-17)}$$

And the power factor for a single *n*- and *p*-type semiconductor is defined as the equation (1-18).[13]

$$PF = \frac{\alpha^2}{\rho} = \alpha^2 \sigma \text{ (1-18)}$$

Where σ is the electrical conductivity.

1.2.2 Thermoelectric Efficiency

In 1909, the German scientist Edmund Altenkirch satisfactorily formulated the efficiency η of a thermoelectric generator via equation (1-19).[14]

$$\eta = \frac{W_{out}}{W_{in}} = \frac{W_{out}}{Q_h} = \frac{I^2 R_L}{Q_h} \text{ (1-19)}$$

Where W_{out} and W_{in} are the work output and input. In Figure 1.4 (b), W_{in} equals to the total heat energy drawn from the heat source, Q_h ,of the thermoelectric generator (equation (1-20)), and the W_{out} can be calculated by the load resistance, R_L.[15]

$$Q_h = (\alpha_p - \alpha_n) I T_h + K_{tot} \Delta T \text{(1-20)}$$

Assuming $\Delta T = T_h - T_c$, then the equation can be expanded to

$$\eta = \frac{I^2 R_L}{Q_h} = \frac{I^2 R_L}{(\alpha_p - \alpha_n) I T_h + K_{tot}(T_h - T_c)} \text{ (1-21).}$$

In the thermoelectric system, the generated electrical current can be described by

$$I = \frac{(\alpha_p - \alpha_n)(T_h - T_c)}{R_{tot} + R_L} \text{ . (1-22)}^{14}$$

Let's define parameter, m, as the ratio of the load resistance to the total resistance of the thermoelectric generator.[14]

$$m = \frac{R_L}{R_{tot}} \quad (1\text{-}23)$$

Then equations (1-22) and (1-23) can be substituted in equation (1-21) leading to

$$\eta = \frac{T_h - T_c}{T_h} \frac{\frac{m}{m+1}}{1 + \frac{K_{tot} R_{tot}(m+1)}{T_h (\alpha_p - \alpha_n)^2}} . \quad (1\text{-}24)$$

And the maximum efficiency η_{max} of the thermoelectric generator can be derived by calculating the 1st derivative of the equation (1-24) with respect to m, through $\frac{d\eta}{dm} = 0$[14]

$$\eta_{max} = \frac{T_h - T_c}{T_h} \frac{\sqrt{1 + Z\bar{T}} - 1}{\sqrt{1 + Z\bar{T}} + \frac{T_c}{T_h}} \quad (1\text{-}25)$$

with $\bar{T} = \frac{T_h + T_c}{2}$. The thermoelectric efficiency would approach the Carnot efficiency when $Z\bar{T}$ approaches infinity.[14]

1.3 Theory

1.3.1 Electron Transport in Crystals

The "Free-Electron Gas" approximation is a good model for electron transport in metals. In this model, all electrons are delocalized and there are no interactions between electrons the ion cores. The electrons move freely in a three-dimensional cube of an edge L_{cube} with an infinite barrier at the surfaces.[16,17] With these boundary conditions, the behavior of electrons can be described by the time-independent Schrödinger equation:[16,17]

$$-\frac{\hbar^2}{2m_e}\nabla^2\psi_k(\boldsymbol{r}) = E_k\psi_k(\boldsymbol{r}) \text{ (1-26)}$$

Where $\psi_k(\boldsymbol{r})$ is the wavefunction of the electron, m_e is the mass of an electron, and E_k is energy of the electron. Solution of the time-independent Schrödinger equation provides possible energy states of the electron:[16,17]

$$E_k = \frac{\hbar^2\boldsymbol{k}^2}{2m_e} = \frac{\hbar^2}{2m_e}(k_x^2 + k_y^2 + k_z^2) \text{ (1-27)}$$

Where $\boldsymbol{k}$ is the wavevector that is quantized by the principal quantum number n_p:[16,17]

$$k = \frac{\pi}{L_{cube}}n_p \text{ (1-28)}$$

While the “Free-Electron” model can give us insights into the electrical properties of metals, it is inadequate to explain some transport phenomena in semiconductors (e.g., energy gap). The “Nearly-Free Electron” (NFE) model was derived based on the “Free-Electron” model, and it describes the carrier’s transport in semiconductors more appropriately. In the NFE model, the interactions between delocalized electron waves with the ion cores are modeled by a periodic potential, and the potential has the same periodicity as the crystal lattice.[18,19] In the NFE model, the periodic boundary conditions over a cube of side L_{cube} is defined as $k_x = k_y = k_z = 0, \pm\frac{2\pi}{L_{cube}} \ldots, \pm\frac{2\pi}{L_{cube}}n \ (n = 1,2,3 \ldots)$.[18,19] And the possible energy state of an electron move in a three-dimensional cube of an edge L_{cube} can be described by the equation (1-27) with the periodic boundary conditions. The wavefunction for an electron with a periodic potential in a crystal lattice is given by the Bloch’s theorem:[18,19]

$$\psi_k(\boldsymbol{r}) = u_k(\boldsymbol{r})e^{ik\cdot\boldsymbol{r}} \text{ (1-29)}$$

Where $u_k(r)$ is a function that has the same periodicity as the crystal lattice. According to equation (1-29), the wave of electron oscillates periodically from one unit cell to the next.[18,19]

1.3.1.1 Energy gap in a Physicist's View

Energy gaps in electron band structure is an essential characteristic of semiconductor. However, the "Free-Electron" model cannot describe the energy gap formation. In the NFE model, the energy gap formation can be clearly explained by Bragg's reflection of electron waves in crystals.[18,19] The Bragg reflection is an essential character of a wave propagating in crystals,[20] and the equation (1-30) describes the condition for the Bragg reflection in a linear monatomic lattice with the lattice constant a within the NFE model.[18,19]

$$k = \pm\frac{\pi}{a}n\ (n = 1,2,3\ldots)\ (1\text{-}30)$$

Based on the equation (1-30), the 1st Brillouin zone is defined at the region between $+\frac{\pi}{a}$ and $-\frac{\pi}{a}$ in the E_k versus $\boldsymbol{k}$ plot, and the 1st energy gap occur at $\pm\frac{\pi}{a}$. The wavefunctions at the edges of 1st Brillouin zone ($k = \pm\frac{\pi}{a}$) contribute equally to the wave traveling to the left and to the right. The condition of Bragg reflection is also satisfied by a traveling wave at $k = \pm\frac{\pi}{a}$, so the counter-propagating "Bragg-reflected" waves can be formed. Two standing waves $\psi_+$and $\psi_-$are formed at $= \pm\frac{\pi}{a}$, these two sanding waves can be represented as the superposition of an incoming and a reflected wave. Two standing waves are formed and shown by equation (1-31) and (1-32).[18,19]

$$\psi_+ = u_k(\boldsymbol{r})2\cos\left(\frac{\pi r}{a}\right) \quad (1\text{-}31)$$

$$\psi_- = u_k(\boldsymbol{r})2i\sin\left(\frac{\pi r}{a}\right) \quad (1\text{-}32)$$

The delocalized electrons in the state ψ_+ have the maximum charge density at the ion cores, and in the state ψ_- between the ion cores. As these two standing waves pile up electrons at different regions, the potential energies of electrons in ψ_+ and ψ_- are different. The difference in the potential energy is represented as a deviation from the free-electron energy parabola in the E_k versus $\boldsymbol{k}$ plot, and this energy difference is called "Energy Gap".[18,19] The Figure 1.4 schematically describes the energy gap E_g associated with the splitting of the free-electron energy parabolas at $k = \pm\frac{\pi}{a}$.

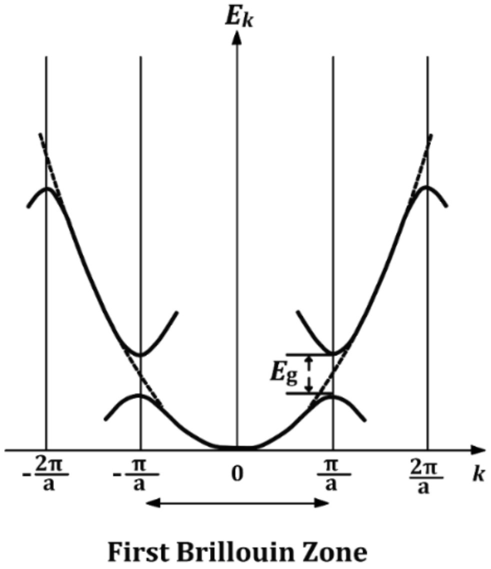

Figure 1.4. Illustration of the energy gap E_g associated with the 1st Bragg reflection at $\pm\frac{\pi}{a}$ in the E_k versus $\boldsymbol{k}$ polt.[18]

1.3.1.2 Energy gap in a Chemist's View

Hydrogen atoms or hydrogen molecules in a one-dimensional linear chain will be employed as a model to explain the energy gap formation. For the hydrogen atoms model, equally-spaced atoms are aligned periodically in a one-dimensional linear chain, and two hydrogen atoms are assumed within one unit cell of edge $2a$. Figure 1.5 (a) shows that the unit cell contributes two bands: the upper and lower bands stems from the anti-bonding and bonding combinations. The most bonding combination and anti-bonding combination are both observed at $k = 0$, and the non-bonding combinations are observed at $k = \frac{\pi}{a}$.[21]

For the hydrogen molecule, instead of having a linear chain of equal-spaced hydrogen atoms, there is a linear chain of dimerized hydrogen atoms in the unit cell of edge $2a$. Now the atoms within the unit cell are closer than the atom between the unit cells, therefore the bonding interactions in the unit cell will be stronger than the anti-bonding between the unit cells at $k = \frac{\pi}{a}$. As a result, the energy of the bonding combinations is reduced at $k = \frac{\pi}{a}$ on the E_k versus $\boldsymbol{k}$ plot. A similar argument can be used to explain the increasing energy of the anti-bonding combination at $k = \frac{\pi}{a}$. The energy separation of bands is called a Peierls distortion, and it leads to the energy gap.

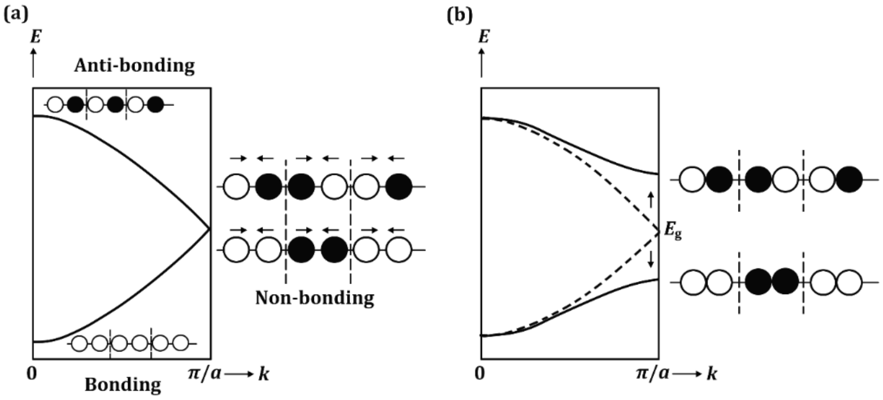

Figure 1.5. (a) Electronic structure of hydrogen atoms in a one-dimensional linear chain, and (b) the resulting Peierls distortion.[21]

1.3.2 Effective Mass of Carriers

Electrons in a crystal are not free, instead they interact with the periodic potential of the lattice. Thus, an electron in a crystal can behave as if it had a mass different from the free electron mass. Generally, the electron effective mass (m_b^*) of a single parabolic band is defined by the inverse of the curvature of the band in the k space. The mathematic expression of the m_b^* can be derived by the nearly free electrons (NFE) model:[22,23]

$$\frac{1}{m_b^*} = \frac{1}{\hbar^2}\frac{d^2E(k)}{d^2k} \text{ (1-33)}$$

Where ħ is the reduced the Planck's constant ($\frac{h}{2\pi}$), $E(k)$ is the energy of the charge carrier at the wavevector k, and m_b^* is a band effective mass. Based on the equation (1-33), the band with a high curvature (light band) has a small effective mass, and the band with a low curvature (heavy band) has a larger effective mass. Also, the m_b^* can be a negative value when the electron sits near the top of a valence band (concave shape). To avoid using an electron with negative mass, the concept of holes is involved: a particle with a positive charge and a positive mass.

In a degenerate semiconductor, the charge carrier transport is generally dominated by degenerate bands. The density of state (DOS) effective mass (m_{DOS}) is introduced, it is proportional to the m_b^*:[24,25]

$$m_{DOS} = N_V^{\frac{2}{3}} m_b^* \quad (1\text{-}34)$$

Where N_V is the number of conducting valleys, and it can be separated into two parts: $N_V = N_{band} \cdot N_{symmetry}$.[24,25] Where N_{band} is the number of valleys that are converged at the energy level and $N_{symmetry}$ is the number of the degeneracy of the high symmetry point in the Brillouin zone. Figure 1.6 shows the Fermi surface of SnTe with a rock-salt structure ($Fm\overline{3}m$) in the 1st Brillouin zone.[26] The conducting valley exists at L with $N_{band} = 1$ and $N_{symmetry} = 4$, and at Σ with $N_{band} = 1$ and $N_{symmetry} = 12$.

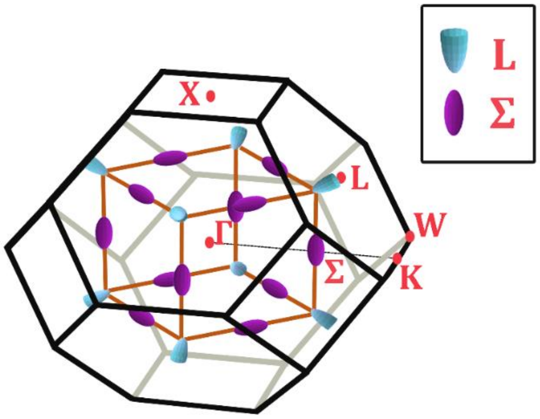

Figure 1.6. The Fermi surface of the L and Σ bands in the pristine SnTe ($Fm\overline{3}m$) in the 1st Brillouin zone.[26]

1.3.3 Electrical Conductivity

The electrical conductivity (σ) is ability to conduct electrical current, and it has an inverse relationship with the electrical resistivity (ρ):

$$\sigma = \frac{1}{\rho} = \frac{l_s}{R_o \cdot A_s}\ . \text{ (1-35)}$$

Where R_o is the electrical resistance, l_s is the length and A_s is the cross area of the specimen.[27]

Based on the electrical conductivity, materials can be classified as metals ($\sigma > 10^4$ S m^{-1}), semiconductors (10^{-3} S m^{-1} < σ < 10^4 S m^{-1}) and insulators ($\sigma < 10^{-3}$ S m^{-1}).[27]

1.3.3.1 Electrical Conductivity Estimated by Drude Model

In highly electrically conductive materials, the Drude model assumes electrons behave like an ideal gas, and an individual electron will be scattered every τ second.[17] According to the Drude model,[17] the electrical conductivity can be expressed by

$$\sigma = \frac{ne^2\tau}{m_b^*}. \text{ (1-36)}$$

Where n is the carrier concentration, e is the electron charge, τ is the relaxation time of charge carriers, and m_b^* is the band effective mass. The carrier mobility, μ, is defined as

$$\mu = \frac{e\tau}{m_b^*}. \text{ (1-37)}$$

Then the expression of electrical conductivity can be simplified as.

$$\sigma = ne\mu \text{ (1-38)}$$

For metal-like conductors and intrinsic semiconductors, the temperature dependence of electrical conductivity is generally different.

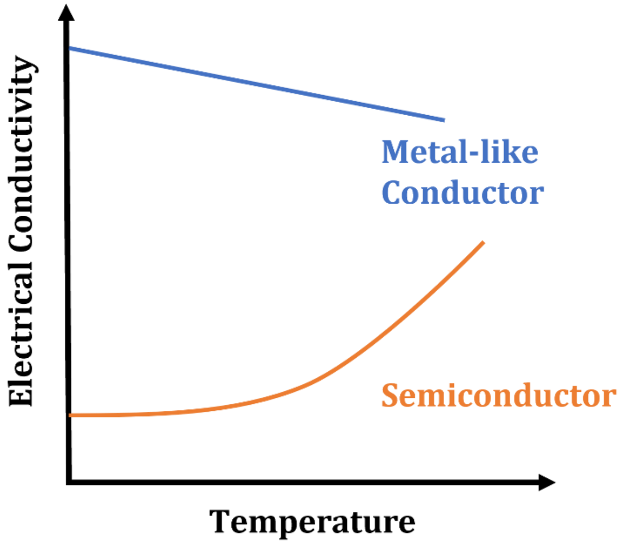

Figure 1.7. The temperature dependence of electrical conductivity in a metal-like conductor and an intrinsic semiconductor.[28]

The electrical conductivity of metal-like conductors decreases with temperature; such behavior is related to the temperature-dependent phonon-electron interactions, i.e. to the electron scattering induced by atomic vibrations.[29] In the intrinsic semiconductor, the electrical conductivity increases as more electrons are excited from the valence band into the conduction band at higher temperatures.[17]

1.3.4 Seebeck coefficient

Within the nearly free electrons (NFE) model, the Seebeck coefficient for metals and degenerate semiconductors can be represented by the Mott formula:[30,31]

$$\alpha = \frac{8\pi^2 {k_B}^2}{3eh^2} m_{DOS} T (\frac{\pi}{3n})^{\frac{2}{3}} \text{ (1-39)}$$

Where k_B is the Boltzmann constant, h is the Planck's constant, m_{DOS} is the density of states (DOS) effective mass, T is the temperature, and n is the carrier concentration. This equation shows the α is linearly dependent on T and m_{DOS}, however, α has an inverse relationship with n.

Generally, both electrons and holes are present in a material, the total Seebeck coefficient (α_{tot}) is given by:[32,33]

$$\alpha_{tot} = \frac{\sigma_h \alpha_h + \sigma_e \alpha_e}{\sigma_h + \sigma_e} \text{ (1-40)}$$

Where σ_h and σ_e is the electrical conductivity of holes and electrons, and α_h and α_e is the Seebeck coefficient contributed by holes and electrons. The α_{tot} can be negatively affected by the minority charge carriers and temperature. The concentration of minority charge carriers potentially increases with temperature, which increases their contribution to the Seebeck coefficient and electrical conductivity. As a result, larger temperatures decrease the nominator (α_h and α_e are positive and negative, respectively) and increase the denominator in equation (1-40).

Increased contribution of the minor carriers is known as bipolar effect. Bipolar effect is easily observed during thermopower and electrical conductivity measurement: $|\alpha_{tot}|$ reaches a peak value and $\sigma_h + \sigma_e$ reaches a bottom value at certain temperature.[34] The bipolar effect is widely observed in SnTe, GeTe and PbTe based thermoelectric (TE) materials with a small band gap.[35–38]

1.3.5 Thermal Conductivity

The total thermal conductivity (k_{tot}) is the sum of two components: electronic thermal conductivity (k_e) and lattice thermal conductivity (k_l).[39]

$$k_{tot} = k_e + k_l \text{ (1-41)}$$

1.3.5.1 Electronic Thermal Conductivity

In metals, the k_e is the amount of heat carried by conducting electrons at a given temperature (*T*), and the mathematical expression for such process is:[40]

$$k_e = \frac{\pi^2 n k_B^2 \tau}{3m_b^*} T \text{ (1-42)}$$

Where n is the carrier concentration, τ_e is the relaxation time of carriers, and m_b^* is the band effective mass. By dividing equation (1-42) divided by (1-38), the following relationship between k_e and σ is obtained (also known as the Wiedmann-Franz Law[41]).

$$\frac{k_e}{\sigma} = \frac{\pi^2 k_B^2}{3e^2} T \text{ (1-43)}$$

The constant ($\frac{\pi^2 k_B^2}{3e^2}$) is called the Lorenz number (L). Thus, the electronic conductivity is proportional to the electrical conductivity, and the equation (1-43) can be re-written as:

$$k_e = L\sigma T \text{ (1-44)}$$

For semiconductors, the electronic structure can be affected by temperature, thus the L will be temperature dependent. As the result, the effective Lorenz number (L_{eff}) is widely used to estimate the thermal conductivity in semiconductors, and its value is calculated by:[42]

$$L_{eff} = 1.5 + \exp\left[-\frac{|\alpha|}{116}\right] \quad (1\text{-}45)$$

Where L_{eff} is in 10^{-8} $W\Omega K^{-2}$, and α is in μV/K. α is the only variable in this estimation, and the error of predicted results is lower than 26%.[42]

1.3.5.2 Lattice Thermal Conductivity and Heat Capacity

The lattice thermal conductivity is the phononic contribution to the thermal conductivity, and it can be described by:[43]

$$k_l = \frac{1}{3} c_v v_s l_p = \frac{1}{3} c_v v_s^2 \tau_p \quad (1\text{-}46)$$

Where c_v is the specific heat capacity under constant volume, v_s is the speed of sound, l_p is the mean free path of phonons, and is τ_p the relaxation time of phonons. Normally, the heat capacity at the constant pressure, C_p, and is measured experimentally. Since the volume of a solid material does not really change with pressure (under the pressures experimentally used), the heat capacity at the constant volume C_v is similar to C_p, which is generally used for the analysis.[44] C_v is temperature dependent, and the Debye model is used to describe its temperature dependence:[45]

$$C_v = 9R\left(\frac{T}{\theta_D}\right)^3 \int_0^{\frac{\theta_D}{T}} \frac{x^4 e^x}{(e^x-1)^2} dx \quad (1\text{-}47)$$

$$\theta_D = \frac{h v_D}{k_B} \quad (1\text{-}48)$$

$$x = \frac{hv_T}{k_B T} \text{ (1-49)}$$

Where R is the universal gas constant, θ_D is the Debye temperature, v_D is the Debye frequency, i.e. the maximum atomic vibration frequency in a crystal, and v_T is the frequency of an atomic vibration at a given temperature.

If the temperature is much higher than θ_D ($T \gg \theta_D$), the integral part becomes $\frac{1}{3}(\frac{\theta_D}{T})^3$ $(\int_0^{\frac{\theta_D}{T}} \frac{x^4 e^x}{(e^x-1)^2} dx \approx \frac{1}{3}(\frac{\theta_D}{T})^3)$. Therefore, the equation (1-47) can be simplified to the equation (1-50). This result is in agreement with Dulong-Petit law for $T \gg \theta_D$.[46]

$$C_v = 9R(\frac{T}{\theta_D})^3 \frac{1}{3}(\frac{\theta_D}{T})^3 = 3R \text{ (1-50)}$$

For temperatures much smaller than θ_D ($T \ll \theta_D$), the lattice/phononic contribution has a linear relationship with T^3. At such temperatures, contribution from conduction electrons becomes noticable, and this contribution is linearly dependent on T:[47,48]

$$C_{v,ele} = \gamma_{ele} T \text{ (1-51)}$$

Where γ_{ele} is the Sommerfeld constant that depends on the material.[41] Then the C_v can be written as the sum of electronic and phononic contributions:[47,48]

$$C_v = \gamma_{ele} T + AT^3 \text{ (1-52)}$$

A is constant characteristic of the material.

1.3.5.3 Phonons

Lattice thermal conductivity is tightly related to the presence of phonons. A phonon is a quantized vibration mode in a crystal lattice, and phonons can be divided into acoustic and optical phonons.[49] Figure 1.8 schematically describes an acoustic phonon, which is an in-phase movement of atoms, and an optical phonon, which is an out-of-phase movement of atoms in a crystal lattice.[50] For a unit cell consisting of n_{cell} atoms, there are total 3 acoustic phonon modes and $3n_{cell} - 3$ optical phonon modes. Moreover, the acoustic and optical phonon modes can be further divided into the longitudinal acoustic (LA), transverse acoustic (TA), longitudinal optical (LO) and transverse optical (TO) modes, respectivelly.[49]

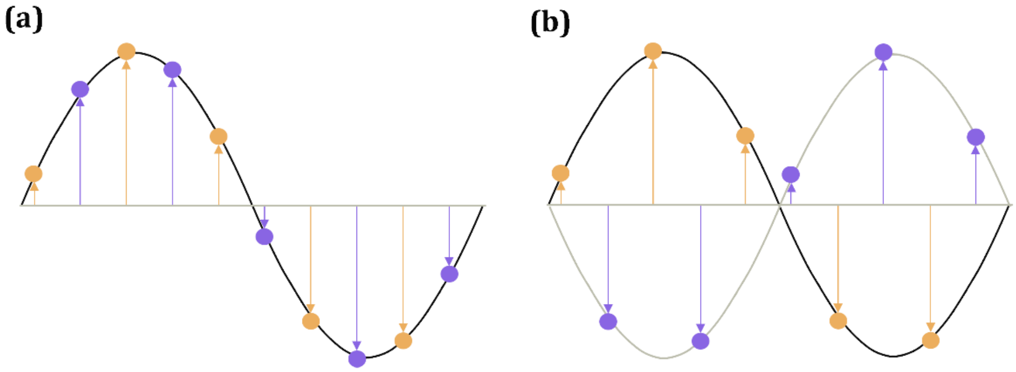

Figure 1.8. (a) Acoustic and optical phonon modes a crystal lattice.[51]

1.3.5.4 Phonon Scattering

As the lattice thermal conductivity depends on the relaxation time of phonons, τ_p, it is important to understand how τ_p is affected by different phonon scattering mechanisms. Generally, phonons are scattered by grain boundaries and lattice imperfections, which would be temperature independent.[52,53] The lattice thermal conductivity contributed by the phonon scattering can be estimated by Callaway model:[54,55]

$$k_l = \int_0^{\omega_{p\,max}} C_s\,(\omega_p\,)v_g\big(\omega_p\,\big)^2 \tau_{rel}(\omega_p\,)d\omega_p \text{ (1-53)}$$

Where ω_p is the phonon vibration frequency, $C_s(\omega)$ is the heat capacity under constant pressure per unit volume, $v_g(\omega)$ is the phonon group velocity which can be estimated by $\frac{d\omega_p}{dk_{vector}}$ (k_{vector} is the wave vector), $\tau_{rel}(\omega)$ is the relaxation time. In the current thermoelectric research, only acoustic phonons are considered in boundary scattering and point defects scattering. The optical phonons are ignored since their group velocity is too low.[50,56] However, optical phonons can interacted with acoustic phonons which is typically known as the Umklapp scattering.[53,57] Such contribution from optical phonons is important since such interactions can reduce the phonon mean free path.

The relationship between the total relaxation time of phonons τ_{tot} and the relaxation time due to different phonon scattering mechanism, τ_i, can be estimated as:[53]

$$\frac{1}{\tau_{tot}} = \sum \frac{1}{\tau_i} \text{ (1-54)}$$

Since the grain boundary scattering occurs at the interface between two grains (crystallites) in a polycrystalline material, and the relaxation time due to phonon-grain boundary scattering, τ_{grain}, is given by:[53]

$$\tau_{grain} = \frac{d_{grain}}{v_g} \text{ (1-55)}$$

Where d_{grain} is the grain sizes, and v_g is the phonon group velocity. Based on this equation, the phonon-grain boundary scattering is independent of the phonon frequency. The phonon-grain boundary scattering can be effectively enhanced by decreasing the grain size of polycrystalline materials.

Phonon point defect scattering is due to the presence of foreign atoms in doped or alloyed compounds. Such foreign atoms lead to the mass contrast and strain field fluctuations in a host lattice and thus significantly affect the phonon point defect scattering. The relaxation time due to the phonon point defect scattering τ_{PD} is given by:[53]

$$\frac{1}{\tau_{PD}} = \frac{V_a {\omega_p}^4}{4\pi v_p^2 v_g} \sum f_i (\left[1 - \frac{m_i}{\bar{m}}\right]^2 + \left[1 - \frac{r_i}{\bar{r}}\right]^2) \text{ (1-56)}$$

Where ω_p is the phonon vibration frequency, v_p is the phonon phase velocity, V_a is the volume per atom, f_i is the fraction of the doping/alloying atoms with mass m_i and radius r_i, and $\bar{m}$ and $\bar{r}$ are the average mass and radius of the site. Based on this equation, the phonon point defect scattering depends strongly on ω_p ($\tau_{PD} \propto {\omega_p}^{-4}$), thus the phonon point defect scattering is pronounced at a high ω_p.

For phonon-phonon scattering, a new wavevector $\overrightarrow{k_3}$ can be formed by the interaction between the wavevectors $\overrightarrow{k_1}$ and $\overrightarrow{k_2}$ at low temperature, which is named a Normal process: $\overrightarrow{k_1} + \overrightarrow{k_2} = \overrightarrow{k_3}$ as shown in Figure 1.9 (a).[58] The amplitude of wavevector $\overrightarrow{k_1}$ and $\overrightarrow{k_2}$ can be increased with increasing temperature, therefore the wavevector sum $\overrightarrow{k_3}$ can exceeds the 1st Brillouin zone above a certain temperature. A wavevector outside the 1st Brillouin zone is brought back by a reciprocal wavevector $\vec{G}$, as a result a new wavevector $\overrightarrow{k_3'}$ with the opposite direction to the original wavevectors is formed: $\overrightarrow{k_1} + \overrightarrow{k_2} = \overrightarrow{k_3'} + \vec{G}$ as shown in Figure 1.9 (b).[58] This process is named an Umklapp process and is temperature-dependent.[59,60] The relaxation time, τ_U, due to the Umklapp scattering is given by:[53]

$$\tau_U \propto \frac{\bar{M} v_g v_p^2}{V_U^{\frac{1}{3}} \gamma^2 {\omega_p}^2 T} \text{ (1-57)}$$

Where $\bar{M}$ is the average atomic mass, γ is the Grüneisen parameter that is used to describe the strength of anharmonicity, and V_U is the unit cell volume. As shown by this equation, the relaxation time of Umklapp scattering is inversely proportional to the square of the phonon vibration frequency ($\tau_U \propto {\omega_p}^{-2}$). Figure 1.9 (c)[53] schematically describes the frequency dependance of the relaxation time for the different phonon scattering mechanisms. As shown, boundary scattering is dominant at low frequencies, while point defect and Umklapp scatterings at high frequencies.

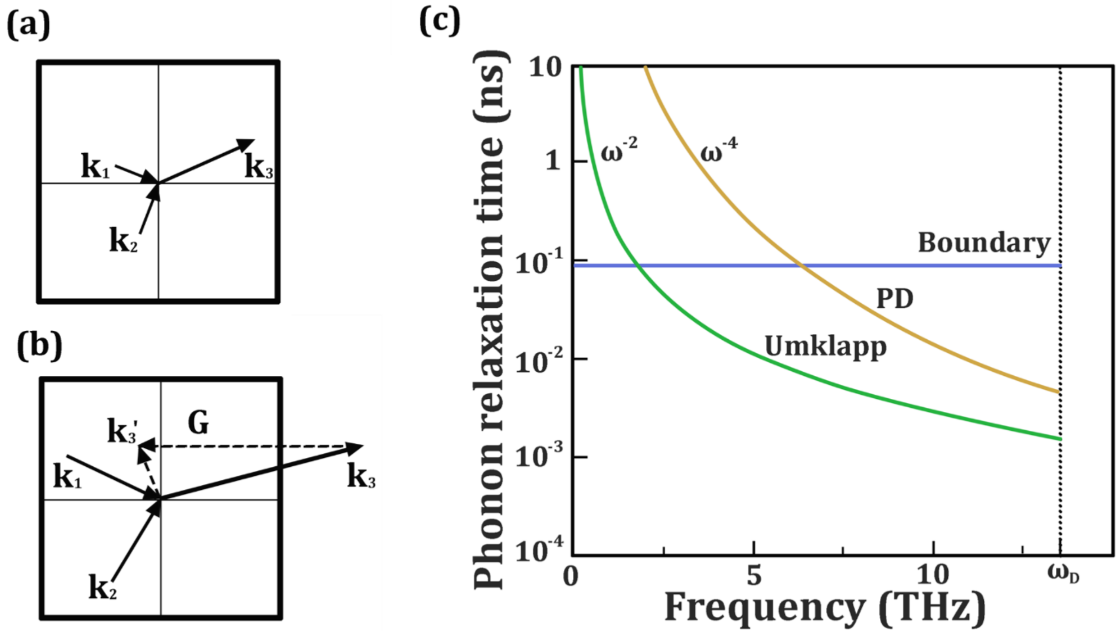

Figure 1.9. (a) Normal and (b) Umklapp processes in the 1st Brillouin zone. (c) The relationship between the relaxation time and phonon vibration frequencies for the different scattering mechanisms.[53]

1.3.6 Landauer Perspective on Carrier Transport

The Landauer approach is a method to study the performance of a thermoelectric material affected by its electronic structure.[61–65] In the Landauer approach, electrons in materials are assumed in thermodynamic equilibrium. The probability that an electronic state with energy E near the Fermi energy E_F is occupied at temperature, T, is given by the Fermi-Dirac distribution:[64]

$$f(E) = \frac{1}{e^{\frac{(E-E_F)}{k_B T}}+1} \quad (1\text{-}58)$$

Within the Landauer approach, the electrical conductivity at energy, *σ(E)* can be described by the number of conduction channels *M(E)*, the mean-free-path for backscattering *λ(E)*, and the derivative of the Fermi-Dirac function with respect to the energy ($\frac{df(E)}{dE}$), as shown by equation (1-59).[62]

$$\sigma(E) = \frac{2q^2}{h}\int \lambda(E)\frac{M(E)}{A_s}(-\frac{df(E)}{dE})dE \text{ (1-59)}$$

Where q is the elementary charge, *h* is the Planck constant, and A_s is the cross-sectional area. Here, the number of channels for conduction, *M(E)*, is proportional to the carrier velocity *v(E)* times the density of state *D(E)*:[61]

$$M(E) \propto v(E)D(E) \text{ (1-60)}$$

In the Landauer approach, the transport distribution function, *ΣE*, is proportional to the product of *M(E)* and *λ(E)*:[62]

$$\Sigma E = \frac{2}{h}\lambda(E)\frac{M(E)}{A_s} \text{ (1-61)}$$

The expression for the electrical conductivity can be simplified by plugging equation (1-61) into equation (1-59), and the result is given by equation (1-62).[62]

$$\sigma(E) = q^2\int \Sigma E(-\frac{df(E)}{dE})dE \text{ (1-62)}$$

Here, electrical conductivity involves the derivative of the Fermi-Dirac function. According to this equation, energies for which the derivative is nonzero are those where the current is flowing.[63] Therefore, $-\frac{df(E)}{dE}$ is defined as the "Fermi window" and mathematically describes why the carrier transport properties depend on the carriers near the Fermi energy. Figure 1.10 shows the “Fermi window” and Fermi-Dirac distribution.[64]

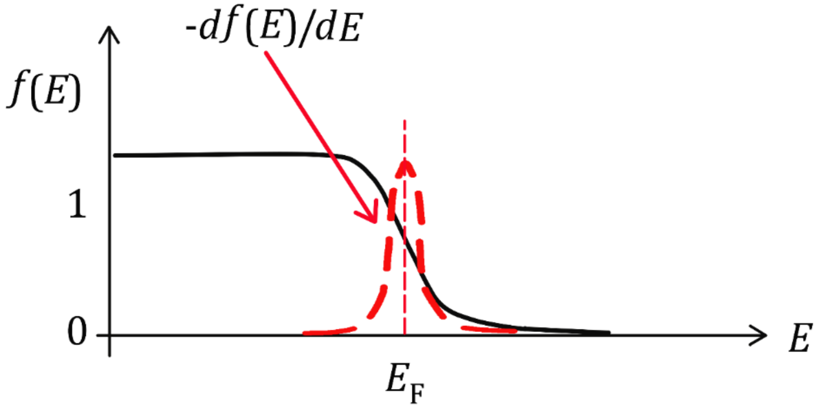

Figure 1.10. Illustration of Fermi window” and Fermi-Dirac distribution at T>0.

In the Landauer approach, if all the conduction channels are assumed at energy E, the Seebeck coefficient can be described as the energy at which the current flows with respect to the Fermi energy E_F at temperature T:[62]

$$S = -\frac{(E-E_F)}{qT} \text{ (1-63).}$$

Figure 1.11 schematically shows the Fermi level for metals, *n*-type and *p*-type semiconductors.[66] For metals, the E_F is deep inside the band, and the current flows at the “Fermi window” that is very close to E_F. There is little difference between the energy of the current flow E_J and E_F; as the result, S is approaching zero. For *n*-type semiconductors, the current will flow at E_J near the bottom of the conduction band (CB), and since E_F is lower, the S will be negative. For *p*-type semiconductors, E_F is above the valence band (VB) and the states that carry the current are below E_F, thus S is positive.

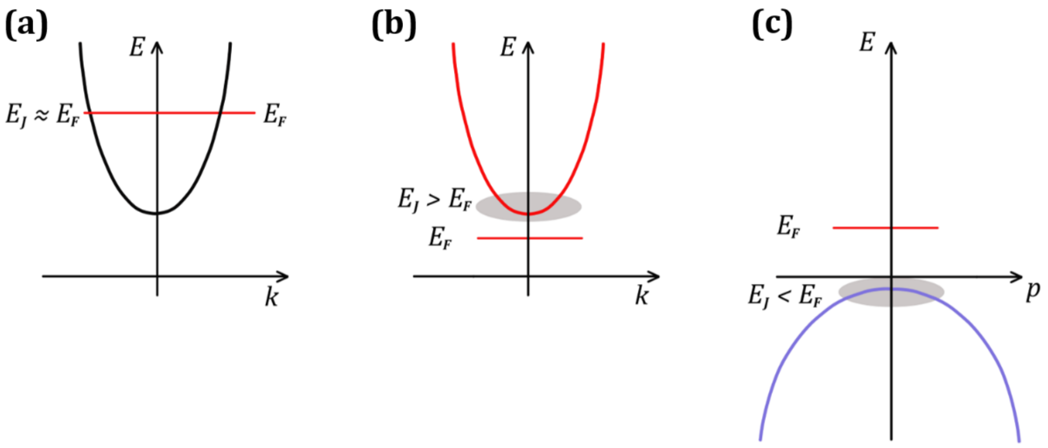

Figure 1.11. Illustration of the Fermi level and energy E_J of the current flow for a) metals, b) *n*-type and c) *p*-type semiconductors.[66]

Figure 1.12 schematically describes the electrical conductivity and Seebeck coefficient versus the Fermi energy, E_F.[66] If the current flow is assumed at the energy E_J, the electrical conductivity increases when E_F approaches E_J. However, the magnitude of the Seebeck coefficient is larger when E_F is far away from the E_J.

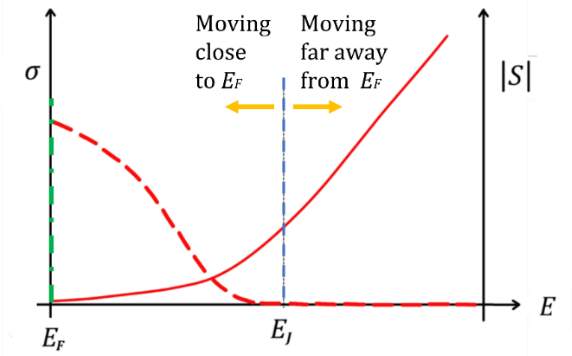

Figure 1.12. Illustration of the electrical conductivity (dash line) and Seebeck coefficient (solid line) as a function of E_J. The values of E_J are with respect to the Fermi energy E_F.[66]

1.3.7 Single Parabolic Band Model

The single parabolic band (SPB) model is a well-known model for thermoelectric materials that provides insights into the understanding of charge carrier transport properties. This model assumes a single parabolic band for energy states in the *k* space and a constant carrier effective mass, and the influence of the minority carriers on the charge carrier transport is negligible.[67,68] Since the SPB model disregards the optical scattering of the charge carriers, acoustic scattering is assumed to be the limiting factor for the electron mobility during the phonon-electron scattering. Using the SPB model, optimum carrier concentration can be estimated based on the experimental Hall mobility u_H, Hall concentration n_H and Seebeck coefficient α.

As n_H and u_H are different from the carrier concentration n and carrier mobility u_c, the SPB model ways to relate these parameters by numerically solving equation (1-64) to (1-67).[67,68]

$$F_n(\eta) = \int_0^\infty \frac{x^n}{1+e^{x-\eta}}\,dx \text{ (1-64)}$$

$$r_H = \frac{3}{2}F_{1/2}\frac{F_{-1/2}}{2{F_0}^2} \text{ (1-65)}$$

$$n = \frac{n_H}{r_H} \text{ (1-66)}$$

$$u_c = u_H\frac{2F_0}{F_{-1/2}} \text{ (1-67)}$$

Where η, $F_n(\eta)$ and e represent reduced chemical potential, n^{th} order Fermi integral, and electron charge, respectively.

In the SPB model, the density of state effective mass m_{DOS} can be determined by numerically solving equation (1-68) to (1-69).[67,68]

$$\alpha = \pm \frac{k_B}{e}\left[\frac{(r+{}^{3}/_{2})F_{r+{}^{3}/_{2}}(\eta)}{(r+{}^{3}/_{2})F_{r+{}^{1}/_{2}}(\eta)} - \eta\right] \text{ (1-68)}$$

$$m_{DOS} = \frac{h^2}{2k_BT}\left[\frac{n}{4\pi F_{\frac{1}{2}}(\eta)}\right]^{\frac{2}{3}} \text{ (1-69)}$$

Here, r is a scattering factor and is -½, if only the acoustic phonon scattering is considered within a SPB model.[67] The effective Lorenz number (L_{SPB}) can be also obtained using the SPB model with acoustic phonon scattering. This approach is widely used in semiconductors, and the Lorenz number is given by equation (1-70).

$$L_{SPB} = \left(\frac{k_B}{q}\right)^2 \frac{3F_0F_2 - 4{F_1}^2}{{F_0}^2} \text{ (1-70)}$$

Due to its simplicity, the SPB model is widely applied in thermoelectric materials for charge carrier transport properties estimation.[68–73] However, multiple bands and band degeneracy is usually observed in thermoelectric materials.[74–79] Therefore, inaccuracies arise when the SPB model is applied to materials that have a complex band structure.

1.4 State-of-the-art Chalcogenide Thermoelectric Materials

Over the past few decades, chalcogenide (group VI) materials consisting of group IV and V elements have been widely utilized for thermoelectric applications.[39,80–84] Most chalcogenide-based materials can be doped into *n*- or *p*-type ones, allowing the thermoelectric devices to be assembled from similar materials.[36,85–89] Moreover, chalcogenide-based materials consisting of heavy elements possess low thermal conductivity, which is essential for thermoelectric performance.[38,90–92] Furthermore, chalcogenide-based materials adopt various structures: cubic rock-salt, or lower symmetry rhombohedral, orthorhombic ones, which provide a good platform for doping and substitution. Some of the known chalcogenide materials are discussed in the following section.

1.4.1 Bismuth Telluride

Bi_2Te_3-based compounds are the most promising room-temperature *n*- and *p*-type thermoelectric materials. Pristine Bi_2Te_3 has a rhombohedral structure ($R\bar{3}m$) with lattice parameters a = 4.383 Å, c = 30.545 Å, α = 90°, γ = 120° at room temperature and atmospheric pressure.[93] The Bi_2Te_3 structure consists of quintuple layers stacked in order Te-Bi-Te-Bi-Te along the *c* axis, and the adjacent quintuple layers are mainly connected via van der Walls forces.[94]

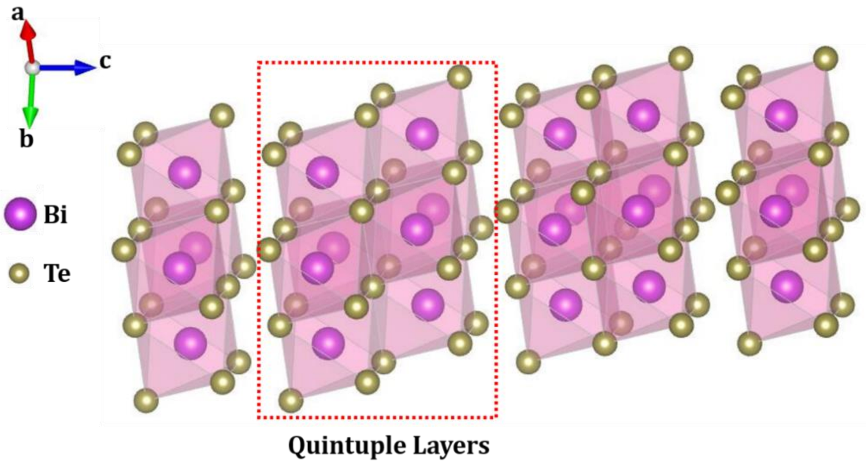

Fig 1.13. Crystal structure of Bi_2Te_3.[93] The quintuple layer is highlighted in the dashed square.

The Bi_2Te_3-based materials show a strong anisotropy in electrical and lattice thermal conductivities; the electrical conductivity along the basal plane (*a* and *b* directions) is around six times higher in *n*-type and three times in *p*-type Bi_2Te_3 than along the *c* direction, and the lattice thermal conductivity along the *c* direction is around half of that along the basal plane.[94–96] Bi_2Te_3 is usually alloyed with isostructural Sb_2Te_3 and Bi_2Se_3 for *p*- and *n*-type materials, respectively. A *p*-type $Bi_{0.52}Sb_{1.48}Te_3$ with a peak *ZT* of ~ 1.56 at 300 K was prepared via a melt spinning followed by a spark plasma sintering (by Xie *et al*.).[97] The authors mentioned that the high thermoelectrical performance benefits from the extremely low lattice thermal conductivity of ~ 0.26 $Wm^{-1}K^{-1}$ at 300 K, which consists of nanocrystalline domains embedded in the sample matrix.[97] Unlike *p*-type Bi_2Te_3-based materials, less progress has been achieved for the *n*-type Bi_2Te_3.[94,98–100] The textured *n*-type $Bi_2Te_{2.2}Se_{0.8}$ with a peak *ZT* of ~ 1.1 at 474 K and an average *ZT* of ~ 0.97 from 325 to 575 K was fabricated using spark plasma sintering (by Pan *et al*.).[85] The thermoelectrical performance improved mainly due to the enhanced carrier mobility, which is brought about by a weaker electron scattering at the grain boundaries along the textured direction.[85]

1.4.2 Tin Selenide

Pristine SnSe adopts two stable phases: *α*-SnSe and *β*-SnSe. α-SnSe is stable below 800 K, and has a layered orthorhombic structure (*Pnma*) with the lattice parameters a = 11.500 Å, b = 4.152 Å and c = 4.445 Å.[101] Above 800 K, the *α*-SnSe (*Pnma*) converts to *β*-SnSe (*Cmcm*) with the lattice parameters a = 4.293 Å, b = 11.620 Å and c = 4.282 Å according to neutron diffraction experiments.[102]

The *α*-SnSe is a *p*-type semiconductor and has a layered structure consisting of two atom-thick SnSe slabs with a zigzag accordion-like geometry in the *bc* plane. The adjacent SnSe slabs are connected to each other by van der Waals forces along the *a* axis.[103] The distorted $SnSe_7$ coordination polyhedron with three short and four long Sn-Se bonds can be observed in the structure, which reflects a large anharmonicity in SnSe. Benefiting from this anharmonicity, the single crystal SnSe shows an ultralow thermal conductivity: 0.46, 0.70 and 0.68 $Wm^{-1}K^{-1}$ along the *a*, *b* and c axis at room temperature, respectively.[104] And the thermal conductivity of single crystal SnSe even further decreases with temperature, resulting in an exciting *ZT* = 2.6 at 923K along the *b* axis, as reported by Zhao *et al*.[104]

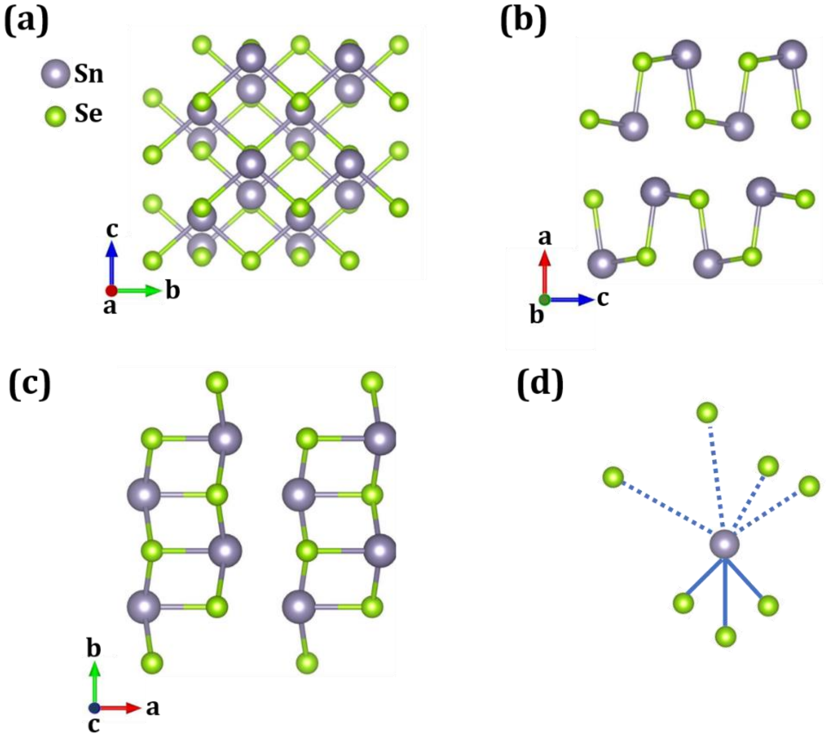

Fig 1.14. Crystal structure of SnSe (*Pnma*) at room temperature (a) along the *a*-axis, (b) *b*-axis, and (c) *c*-axis.[101] (d) The $SnSe_7$ coordination polyhedron.[105]

Both the poor mechanical properties and cost of crystal growth restrict industrial applications of SnSe single crystals. To avoid these issues, researchers focused on polycrystalline SnSe. Unlike the single crystal, the polycrystalline SnSe always shows a relatively high thermal conductivity ~ 0.9-1.35 $Wm^{-1}K^{-1}$ at room temperature.[106,107] The higher thermal conductivity is attributed to surface oxidation in polycrystalline SnSe; SnO_2 has an extremely high thermal conductivity of ~ 98 $Wm^{-1}K^{-1}$ at room temperature.[105] Zhou *et al.*[108] showed that removal of tin oxide from the *p*-type Na-doped SnSe polycrystalline sample yielded a *ZT* of 3.1 at 783K.

1.4.3 Skutterudites

Binary skutterudites have a general formula MX_3 (M = Co, Rh or Ir; X = P, As, or Sb) and adopt the $CoAs_3$ structure with the space group $Im\overline{3}$. The structure contains X_4^{4-} rectangular anionic rings formed by tilting the MX_6 octahedra.[109–111] Large voids present in the structure can be filled by electropositive atoms, and filled skutterudites with the general formula, $A_yM_4X_{12}$ are obtained.[112]

The most studied binary skutterudite is $CoSb_3$ because of its excellent electrical transport properties.[113–116] However, the thermoelectric performance of pristine $CoSb_3$ is low due to its high thermal conductivity (~ 2.3 $Wm^{-1}K^{-1}$ at room temperature).[113,116] The pristine $CoSb_3$ shows an *n*-type behavior and a peak *ZT* of ~ 0.1 at ~ 700 K.[113,116]To optimize its lattice thermal conductivity, guest atoms are introduced into the voids, and this leads to significant phonon scattering.[116–120] A *n*-type $Ba_{0.08}La_{0.05}Yb_{0.04}Co_4Sb_3$ with a peak *ZT* of ~ 1.7 at 850 K was reported by (Shi *et al.*).[119] The fillers, e.g. Ba, La, and Yb, not only introduce extra phonon scattering but also provide additional electrons; as a result, the thermoelectric performance is improved.

Mixed ternary skutterudites with the formula $AX_{1.5}Y_{1.5}$ result from the isoelectronic substitution on the anion site of binary skutterudites. $CoGe_{1.5}Y_{1.5}$ (Y = S, Se) is the first member of this family reported by Korenstein *et al.*[121], and its structure was studied by Vaqueiro *et al*. using powder neutron diffraction.[122] in 2006. The study of the ternary skutterudites $CoGe_{1.5}Te_{1.5}$ was stimulated by its large Seebeck coefficient of ~ -380 μV K^{-1} at 423 K.[123] However, it also displays low electrical conductivity (σ_{max} of ~ 52 S cm^{-1}) that limits its thermoelectric performance.[124,125]

In contrast to the binary skutterudites $CoSb_3$, which has only one crystallographicly distinct rectangular ring ($[Sb_4]^{4-}$),[126] the ternary skutterudites $CoGe_{1.5}Te_{1.5}$ has two crystallographicly distinct four-membered rings ($[Ge_2Te_2]^{4-}$), in which the Ge and Te atoms are trans to each other.[122] In $CoGe_{1.5}Te_{1.5}$, the four-membered rings($[Ge_2Te_2]^{4-}$) are diamond-like rather than rectangular.[122] Also, as indicated in the powder neutron diffraction study of $CoGe_{1.5}Te_{1.5}$, the anions are ordered in the layers perpendicular to the [111] direction of the unit cell. This arrangement, along with the distortion of the anion ring, leads to the symmetry reduction from the cubic *Im-3* to rhombohedral *R-3* one.[122] At 610°C, $CoGe_{1.5}Te_{1.5}$ undergoes a phase transition from rhombohedral *R-3* to *Im-3*, as shown by Kaltzoglou et al.[123] An *n*-type $CoGe_{1.45}Te_{1.45}Sb_{0.1}$ with a peak *ZT* of ~ 0.65 at 723 K was reported by (Valiyaveettil *et al*.).[127] They mentioned that the Sb-doping not only increases the electron concentration but also promotes the valence band convergence that improves the carrier effective mass and as a result the thermoelectric performance.

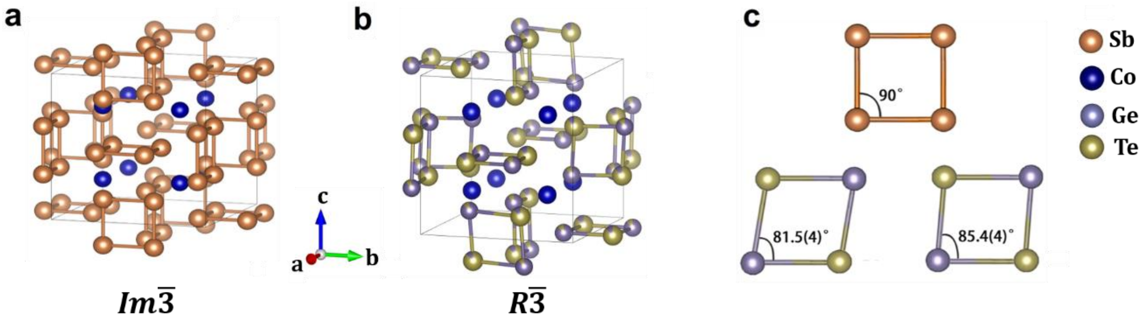

Figure 1.15. Crystal structure of (a) $CoSb_3$[126] and (b) $CoGe_{1.5}Te_{1.5}$[128]. In $CoGe_{1.5}Te_{1.5}$, the Ge sites have some Te atoms and vice versa. (c) A four-membered rectangular ring ($[Sb_4]^{4-}$) in $CoSb_3$ and two crystallographically distinct diamond-like rings ($[Ge_2Te_2]^{4-}$) in $CoGe_{1.5}Te_{1.5}$. Reproduced with permission from reference [110].[125]

1.4.4 Lead Telluride and Germanium Telluride

Pristine PbTe adopts a rock salt structure ($Fm\bar{3}m$) with a lattice parameter a = 6.462 Å[129] and is a *p*-type semiconductor with a direct band gap E_g ~ 0.32 eV.[130] Benefiting from the strong anharmonic coupling between the longitudinal acoustic and transverse optical phonons, pristine PbTe shows a relatively low bulk lattice thermal conductivity of ~ 2 $Wm^{-1}K^{-1}$ at room temperature.[131] In the past few decades, *p*-type PbTe was investigated as a high-performance thermoelectric material in the mid-temperature range. One of the famous PbTe-based materials is Lead Antimony Silver Tellurium, named LAST-*m*: $AgPb_mSbTe_{2+m}$ (*m* = 0 to 18). LAST-*18* shows an outstanding *ZT* ~ 2.2 at 800K; this is mainly contributed by the nanocrystals of the Ag-Sb-rich phase embedded in the PbTe matrix, significantly lowering the lattice thermal conductivity.[132,133] Up to date, the highest *ZT* value of a *p*-type PbTe-based material is reported by Tan *et al.*;[134] the Na-doped

PbTe/SrTe with a peak *ZT* of ~ 2.5 at 923 K. *n-type* PbTe-based materials also show high thermoelectric performance; Lee *et al.*[135] reported that Bi-doped PbTe/Ag_2Te achieves peak *ZT* of ~ 2 at 800K.

Pristine GeTe has a rhombohedral structure (*R3m*) with lattice parameters a = 4.164 Å, c = 10.690 Å, α = 90˚, γ = 120˚ (rhombohedral angle is 58.35°) at room temperature. It undergoes a phase transition at ~ 673 K to a higher-symmetry rock salt structure ($Fm\overline{3}m$) with lattice parameters a = 6.009 Å, as confirmed by neutron powder diffraction experiments.[136] The rhombohedral GeTe (*R3m*) structure can be understood as a distortion of the cubic GeTe structure ($Fm\overline{3}m$) along the [111] direction. The directional distortion results in off-center shifts of Ge atoms in the octahedra formed by six Te atoms, which splits six Ge-Te bonds into three shorter (2.844 Å) and three larger bonds (3.156 Å).[136] The bond angles between the Ge-Te bonds deviate from 180° or 90° due to the different bond lengths.

Pristine GeTe is a *p*-type semiconductor with a high hole concentration of ~ 10^{21} cm^{-3} (due to the intrinsic Ge vacancies) and an indirect band gap E_g ~ 0.21eV.[84,137,138] The $(GeTe)_x(AgSbTe_2)_{100-x}$ (TAGS-x) based materials are well known and used as the *p*-type leg radio-isotope thermoelectric generators in the NASA space mission,[39] and a peak *ZT* of ~ 1.9 is achieved in the TAGS-80 at 800 K.[139] In 2018, Li *et al*. reported a record high device figure of merit *ZT* of ~ 2.4 at 600 K in the Bi/Pb co-doped GeTe.[137] They attributed such good performance to synergistic optimization: valence band convergence significantly improves the carrier effective mass, and lattice thermal conductivity is effectively suppressed by acoustic-optical phonon interactions due to the Bi/Pb co-doping.

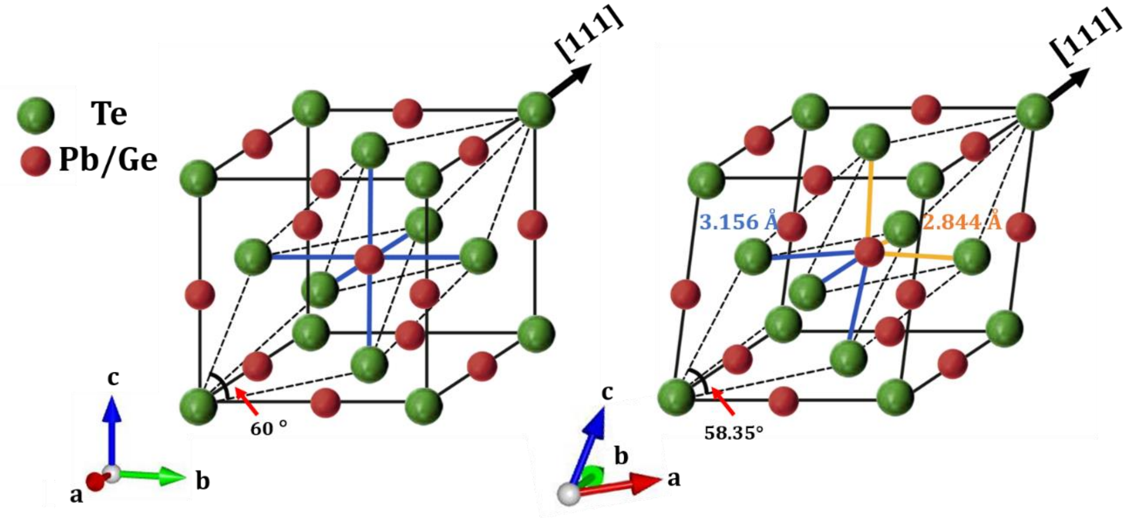

Figure 1.16. (a) Crystal structure of cubic PbTe and high temperature GeTe. (b) Crystal structure of rhombohedral GeTe.[37]

1.5 Materials in Focus

Pristine SnTe addopts a rock-salt structure ($Fm\bar{3}m$) with lattice parameter a = 6.318 Å at $T > 100\ K$.[90] Intrinsic Sn deficiencies result in a p-type semiconducting behavior with a high hole concentration of 10^{20} to 10^{21} cm^{-3},[140] which negatively affects the Seebeck coefficient and produces a high carrier thermal conductivity in pristine SnTe.[141,142] Moreover, the pristine SnTe has a higher lattice thermal conductivity due to the lighter atomic mass of Sn when compared to Pb.

Both the valence band maximum (VBM) and conduction band minimum (CBM) are located at the L point, giving a direct band gap E_g (~0.18 eV).[143] Below the VBM, there is a heavy Σ band with the highest point along the Γ→K direction, and the energy separation, $E_{L-\Sigma}$, between the VBM and Σ band is ~ 0.36 eV.[143] Since the $E_{L-\Sigma}$ is larger than the band gap in pristine SnTe, carriers from the heavy Σ band do not contribute much to the transport properties in the pristine SnTe, which causes a low Seebeck coefficient. In combination, all these factors render an inferior figure, *ZT*, of 0.4 at 850 K for pristine SnTe.

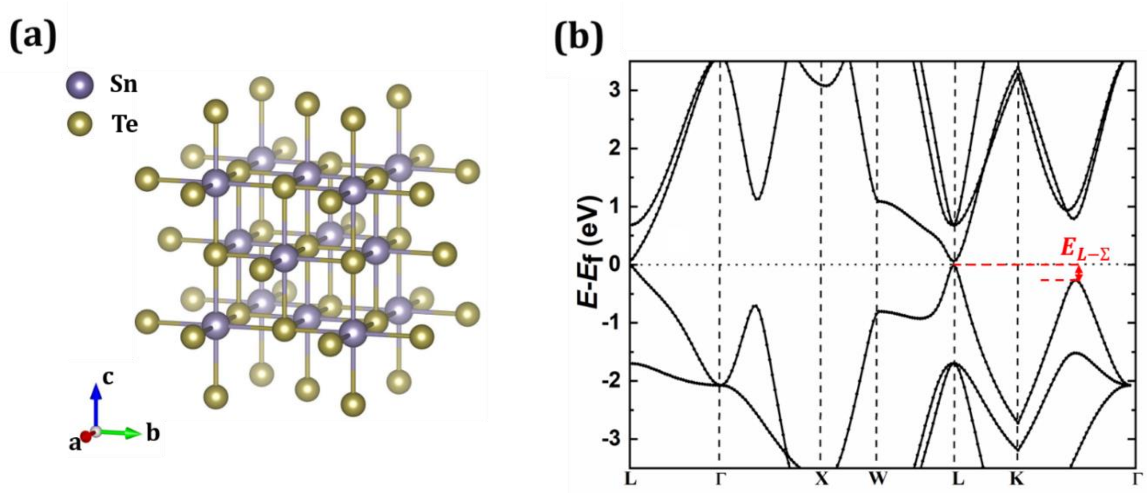

Figure 1.17. (a) Crystal structure of SnTe.[90] (b) Calculated electronic band structure of the cubic Sn_4Te_4.

In this dissertation, doping/substituting/alloying was employed for band engineering and thus to optimize the Seebeck coefficient for SnTe. The resulting valence band convergence, band inversion and resonance states at the Fermi level improved the Seebeck coefficient in SnTe. The electronic structures of pristine and doping/substituting/alloying samples were calculated by the tight-binding-linear-muffin tin orbital method (TB-LMTO) with the atomic sphere approximation (ASA) or density functional theory (DFT). The carrier effective mass was calculated using the single parabolic band model (SPB). To enhance the phonon scattering and optimize the lattice thermal conductivity, the extra atomic disorder was introduced by point defects, precipitates, and lattice distortion in SnTe.

Chapter 2. Methodology and Experimentation

2.1 *Synthetic Approach*

In this dissertation, solid-state synthetic approaches were used to prepare samples. Since starting reagents and products are easily oxidized in air at elevated temperatures, inert atmosphere is required for the reactions. The stoichiometric mixtures of elements were weighted and loaded into silica tubes with a diameter of 10 mm. The tubes were evacuated below 0.002 Toor and flamed sealed. The air-sensitive elements were handled in an argon-filled glove box, and the tubes were closed with a valve, transferred to a vacuum line and flamed sealed. The SnTe samples were heated to 1000 °C at 100 °C/h and annealed for 12 h. They were then quenched in an ice-water bath to avoid the formation of SnTe with varying elemental compositions in the homogeneity region.[144]

Densification of samples was done using spark plasm sintering (SPS). SPS is performed by applying uniaxial pressure while heating the sample with a pulsed direct electrical current of few hundreds amps and of low voltage.

The SPS process proceeds through three stages: plasma heating, joule heating, and plastic deformation.[145,146] For plasma heating, the electrical discharge between powder particles generates localized and momentary heating of powder particle surfaces. At the joule heating stage, the sample powder particles are heated through resistive heating. The heated sample undergoes plastic deformation under uniaxial pressure.

Unlike the hot press, where the sample is heated by an external source; the SPS allows heat to be generated internally by a pulsed direct electrical current. Therefore, the SPS can achieve a rapid heating rate (up to 1000 K/min), which significantly decreases the sintering time and diminishes grain growth.

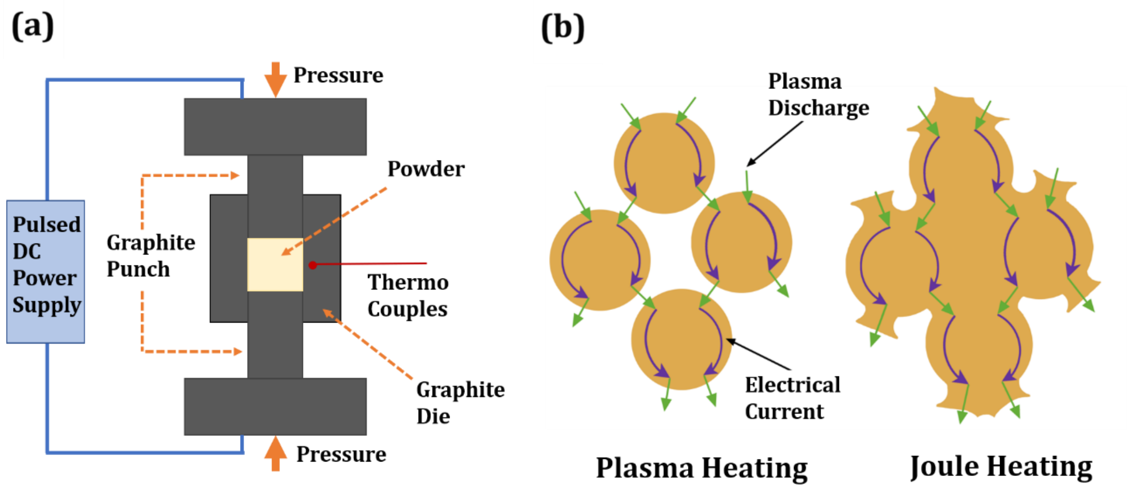

Figure 2.1. (a) Schematic representation of spark plasma sintering (SPS). (b) The SPS heating mechanism: plasma heating and Joule heating.[145,146]

2.2 *X-ray Diffraction*

During powder or single crystal X-ray diffraction (XRD), a material is irradiated with a monochromatic X-ray beam, and a detector is used to collect information about the interference pattern generated by diffracted beams. Due to the rapid data collection, low-cost, and non-destructive properties, XRD is widely used for phase identification of polycrystalline samples and structural studies on single crystals.

2.2.1 Basic Theory

2.2.1.1 Bragg's Law and Ewald's sphere

X-rays are scattered by electrons of atoms in lattice planes, and constructive interference occurs when Braggs' law is obeyed. The Braggs' law is given by equation (2-1) and schematically described in Figure 2.2.[147]

$$n\lambda = 2d_{hkl}sin\theta \text{ (2-1)}$$

Where n is an integer, λ is the wavelength of the radiation X-ray, d_{hkl} is the interplanar distance between adjacent planes with the (*hkl*) Miller indeces, and θ is the angle between the incident beam with the Miller planes.

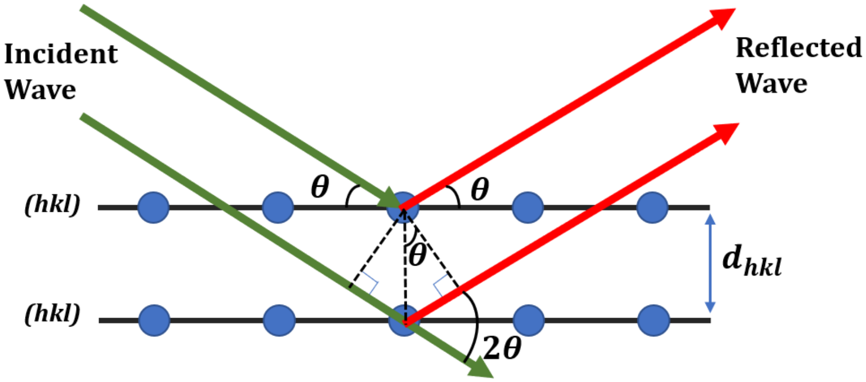

Figure 2.2 Derivation of Bragg's Law. The constructive interference occurs when the path difference (red line) is equal to an integral multiple of the wavelength λ.[148]

Crystalline materials have a periodic arrangement of atoms in real space. The basic building block is defined as a unit cell with three lattice vectors, $\boldsymbol{a}$, $\boldsymbol{b}$ and $\boldsymbol{c}$, and three angles, α, β and γ. However, the XRD data are usually analyzed in the reciprocal space rather than real space. The German crystallographer and physicist Paul Peter Ewald connected the real and reciprocal lattices through the following relationships:[149]

$$\boldsymbol{a}^{*} = \frac{\boldsymbol{b}\times\boldsymbol{c}}{V_{unit}}, \boldsymbol{b}^{*} = \frac{\boldsymbol{a}\times\boldsymbol{c}}{V_{unit}}, \boldsymbol{c}^{*} = \frac{\boldsymbol{a}\times\boldsymbol{b}}{V_{unit}} \text{ (2-2)}$$

Here, $\boldsymbol{a}^{*}, \boldsymbol{b}^{*}$ and $\boldsymbol{c}^{*}$ are the reciprocal lattice vectors, and V_{unit} is the unit cell volume in the real space.

The reciprocal vector $\boldsymbol{d}_{\boldsymbol{hkl}}^{*}$ which represents the corresponding Miller plane is related to the reciprocal lattice vectors:[149]

$$\boldsymbol{d}_{\boldsymbol{hkl}}^{*} = h\boldsymbol{a}^{*} + k\boldsymbol{b}^{*} + l\boldsymbol{c}^{*}, |\boldsymbol{d}_{\boldsymbol{hkl}}^{*}| = \frac{1}{|\boldsymbol{d}_{\boldsymbol{hkl}}|} \text{ (2-3)}$$

Diffraction from a lattice can be presented using the reciprocal lattice and Ewalds' sphere. Ewald's sphere has the radius of $\frac{1}{\lambda}$ and is placed at the origin of the diffraction (Figure 2.3). The incident, $\boldsymbol{k_0}$, and diffracted, $\boldsymbol{k_1}$, beam wavevectors are of the same length $\frac{1}{\lambda}$ and are 2θ apart. When the diffracted beam $\boldsymbol{k_1}$, terminates at a lattice point on the Ewalds sphere, the diffraction even occurs. This can be also rephrases as when the reciprocal lattice point touches the Ewald's sphere, the diffraction occurs. One can show that such geometric conditions lead to the satisfaction of Bragg's law.

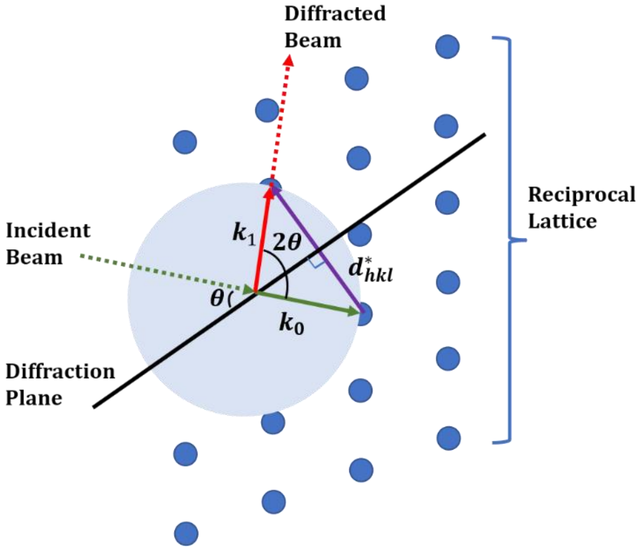

Figure 2.3 Schematic diagram of diffraction event. Diffraction only occurs whenever the Braggs' law is satisfied if the reciprocal lattice points exist on the surface of the Ewald's.

In case of a single crystal in a given orientation, there will be only some reciprocal lattice points represented by $\boldsymbol{d}^*_{hkl}$ that satisfies Braggs' law. In polycrystalline or powder samples, there are many crystallites in random orientations, and there will be many crystallites that satisfy Braggs' law for any given d^*_{hkl}. In such case, the diffraction events for a given d^*_{hkl} will be collected as one Debye ring.

2.2.1.2 The Structure Amplitude

The structure amplitude F_{hkl} play an essential role in the crystal structure determination as it carries information about the relative occupation of atomic sites, atomic displacements and most importantly about atomic positions. The mathematical expression of F_{hkl} is given by:[150,151]

$$F_{hkl} = \sum_{j=1}^{n} g_j t_j\, f_j e^{[2\pi i(hx_j + ky_j + lz_j)]}. \text{ (2-5)}$$

Where *h*, *k*, *l* are the Miller indices and x_j, y_j, z_j are the fractional coordinates in real space for the *j*th atom. g_j is the occupancy factor for the *j*th atom; the site is fully occupied when $g_j = 1$. t_j is the atomic displacement parameter, which describes vibrations of the *j*th atom. The atomic scattering factor, f_j, for the *j*th atom is proportional to the number of electrons.

The exponential part in the equation (2-5) can be expanded into the sin and cosine terms by the Euler's formula (equation (2-6)). The F_{hkl} can be plotted as a vector with phase angle $\alpha_{hkl} = 2\pi(hx_j + ky_j + lz_j)$ in a 2D space with real and imaginary axes.

$$F_{hkl} = \sum_{j=1}^{n} g_j t_j\, f_j cos[2\pi(hx_j + ky_j + lz_j)] + i \sum_{j=1}^{n} g_j t_j\, f_j sin[2\pi(hx_j + ky_j + lz_j)]$$

(2-6)

2.2.1.3 Phase Problem

The intensity of the diffracted beam is proportional to $|F_{hkl}|^2$. Thus, it is $|F_{hkl}|^2$ that is experimentally measured, but the information on phase angle α_{hkl} is absent. The diffraction data by themselves are not sufficient to determine the atomic structure, as the α_{hkl} is also needed to derive the electron density distribution:

$$\rho_{xyz} = \frac{1}{V_{unit}} \sum_{h=-\infty}^{h=+\infty} \sum_{k=-\infty}^{k=+\infty} \sum_{l=-\infty}^{l=+\infty} |F_{hkl}^{obs}| \cos\,[2\pi(hx + ky + lz) - \alpha_{hkl}]. \text{ (2-7)}$$

Here, ρ_{xyz} is the electron density at the (*x*, *y*, *z*) point in the unit cell, and $|F_{hkl}^{obs}|$ is the absolute value of the structure amplitude and is obtained from the intensity of the diffracted beam.[151]

The solution of the phase problem can be divided into approaches: one for a centrosymmetric structure and another for a non-centrosymmetric one. In a centrosymmetric crystal structure, an (*x, y, z*) atom has a symmetrically equivalent atom with coordinates (-*x*, -*y*, -*z*). Based on the properties of sin and cos functions, the imaginary part of $\boldsymbol{F}_{hkl}$ will be zero in the equation (2-6). Thus, the structure amplitude is only dependent on the real component R_{hkl} for a centrosymmetric crystal structure:

$$F_{hkl} = \sum_{j=1}^{n} g_j t_j f_j cos\left[2\pi\left(hx_j + ky_j + lz_j\right)\right] \text{ (2-8)}$$

α_{hkl} is either 0 or π for a centrosymmetric structure while it can adopt any value between 0 and 2π in a non-centrosymmetric structure (Figure 2.4). In case of a centrosymmetric structure, the electron density equation (2-7) can be simplified to

$$\rho_{xyz} = \frac{1}{V_{unit}} \sum_{h=-\infty}^{h=+\infty} \sum_{k=-\infty}^{k=+\infty} \sum_{l=-\infty}^{l=+\infty} s_{hkl} |F_{hkl}^{obs}| \cos\left[2\pi(hx + ky + lz)\right]. \text{ (2-9)}$$

Where s_{hkl} is 1 for $\alpha_{hkl} = 0$ or -1 for $\alpha_{hkl} = \pi$.

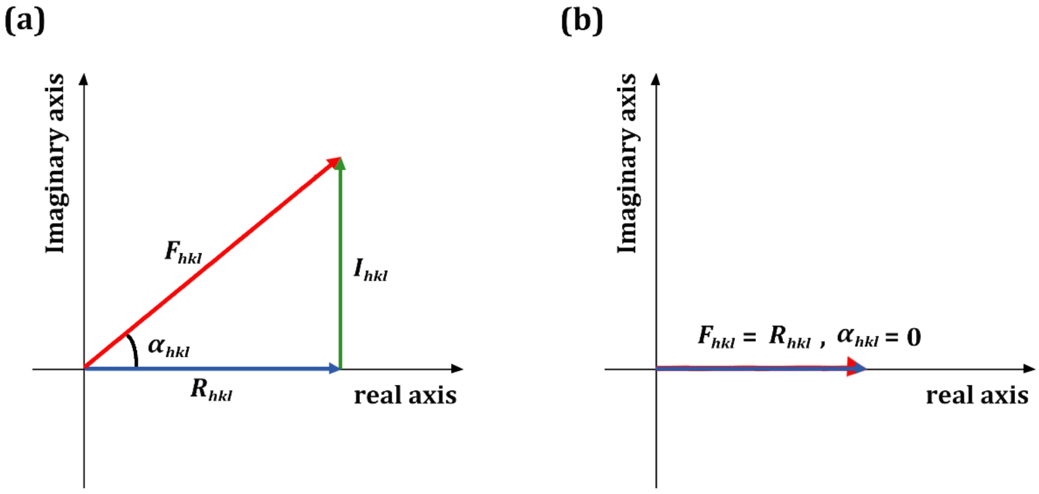

Figure 2.4 Schematic diagram of structure amplitude F_{hkl} in the two dimensional space with a real and an imaginary axis for (a) non-centrosymmetric and (b) centrosymmetric structures.[151]

2.2.1.4 Patterson Method and Direct Method

Patterson and direct methods are used to crystal structures. Phase angles are not required for the Patterson function calculations, and the Fourier transformation is applied directly to $|F_{hkl}|^2$.[152] The Patterson function reveals the distribution of interatomic vectors rather than the distribution of atoms in a unit cell. Although the Patterson method can avoid the difficultly of phase angle determination, the associated structural solution has some drawbacks. The first difficulty is that the number of Patterson peaks is $n(n-1)$ for a unit cell with n atoms, which makes it difficult to solve structures with complicated unit cells. Secondly, Patterson peaks are commonly broader than electron density peaks. These two drawbacks can cause peak overlap for different interatomic vectors. Moreover, the Patterson function is always centrosymmetric; as a result, non-centrosymmetric structures cannot be solved correctly.

In the direct method, the phase angle of a reflection can be derived from other two reflections using the triplet relationship. The three reflections are defined as (*h*, *k*, *l*), (*h'*, *k'*, *l'*) and (*h*-*h'*, *k*-*k'*, *l*-*l'*).[152] In case of a centrosymmetric structure, the phase angle α_{hkl} is either 0 or π, and the corresponding signs are + and -. The signs of two reflections can provide the sign of the third reflection through the Sayre equation:

$$s_{hkl} \approx s_{h'k'l'} s_{(h-h')(k-k')(l-l')}.^{152} \quad (2\text{-}10)$$

In case of a non-centrosymmetric structure, the relationship between phase angles of a triplet can be described by Sayre equation:

$$\alpha_{hkl} \approx \alpha_{h'k'l'} + \alpha_{(h-h')(k-k')(l-l')}.^{152} \quad (2\text{-}11)$$

In both cases, the phases of the two reflections must be known in order to obtain the phase of the third reflection. In centrosymmetric structures, the phase angles of some reflections are set at 0 or π to fix the origin. The phase angle determination is much more complicated in non-centrosymmetric structures because the phase angles of two reflections of a triplet may have values between 0 and 2π.[152] As the result, a few possible arrays of phases are generated for a non-centrosymmetric structure, and they are tested until the correct solution is obtained.

2.2.2 Powder X-ray Diffraction

Powder X-Ray Diffraction (PXRD) analysis was performed at temperature on a PANalytical X'Pert Pro diffractometer equipped with a CuKα_1 source and an X'Celerator linear detector. The samples were finely grinded into powders using a mortar and pestle and evenly deposited on a zero-background silicon sample holder.

A ceramic vacuum sealed X-ray tube is employed for X-ray generation. Inside a tube, a tungsten heated filament works as the cathode, and it emits electrons. Electrons are accelerated by the electric potential (in tens of kV) applied to a tube. When high-speed electrons strike the anode, the inner-shell electrons of metal atoms can be knocked. As the outer-shell electrons fill the inner shell vacant, X-ray photons of characteristic energy/wavelength are emitted. For this study, copper was employed for the anode, and a germanium single crystal monochromator was used to filter the CuKα_2 and white radiation.

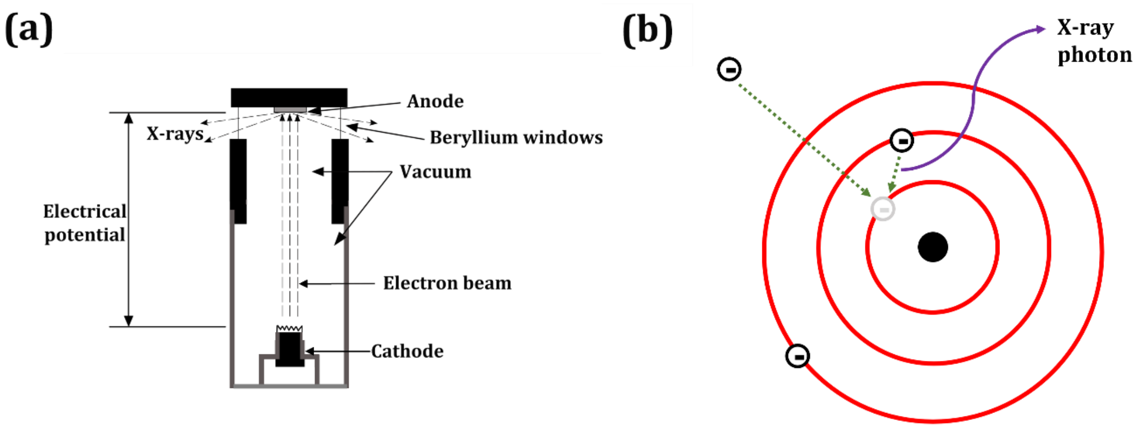

Figure 2.5. Schematic diagram of (a) a X-ray tube and (b) generation of characteristic X-ray.[153]

The PXRD data were analyzed and refined using the Rietveld technique (Rietica program[154]). For the lattice parameter and sample purity determination, the profile parameters (background and peak shape), lattice parameters, and sample displacement were refined. The literature data were used for the atomic parameters and occupancies. The least-squares method was employed to estimate the quality of refinement, and the mathematical expression of the profile R_p, weighted profile R_{wp}, and goodness χ^2 parameters are:[154]

$$R_p = \frac{\sum |y_o - y_c|}{\sum y_o} \quad (2\text{-}12)$$

$$R_{wp} = \sqrt{\frac{\sum w_i (y_o - y_c)^2}{\sum w_i {y_o}^2}} \quad (2\text{-}13)$$

$$\chi^2 = \frac{\sum w_i (y_o - y_c)^2}{N - P} \quad (2\text{-}14)$$

Where y_o and y_c are the observed and calculated intensities, and w_i is the weighting parameter,[155] N is the total number of data points, and P is the number of adjusted parameters.

2.3 Scanning Electron Microscopy (SEM) and Energy Dispersive X-ray Spectroscopy (EDS)

SEM and EDS are non-destructive analytical techniques widely used for materials characterization. SEM is a type of electron microscope in which a specimen's image is directly produced by scanning the surface with a beam of focused electrons. An EDS analyzer is an attachment to the SEM and is used for elemental analysis.

2.3.1 Principles

Generally, there are two modes of electrons in SEM: secondary and backscattered electrons. Secondary electrons are generated from inelastic scattering events, and they are electrons knocked out from the atom's inner shell by the primary electrons.[156] The intensity of the secondary electron signal is directly related to the number of secondary electrons detected; the secondary electrons mode is generally used for the topography analysis.

Backscattered electrons are the primary electrons reflected from the specimen by elastic scattering.[156] The trajectories of primary electrons are deviated by the atomic nuclei; the heavier nuclei, the more significant deviation of the primary electrons, and the more backscattered electrons are observed. Thus, the intensity of the backscattered electron signals is proportional to the atomic number *Z*, and backscattered electron mode is generally used to analyze the spatial elemental/phase distribution in samples.

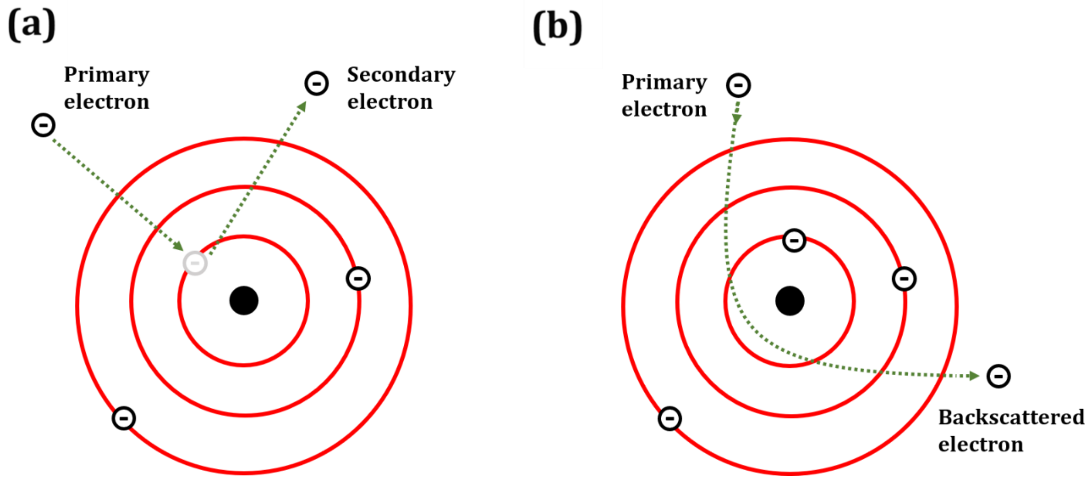

Figure 2.6 Schematically describes the (a) secondary electrons and (b) backscattered electrons.

The EDS analytical technique uses characteristic X-ray emitted from the specimen for elemental analysis. Generation of characteristic X-ray is described in Figure 2.5 (b), in the previous chapter, 2.2.2. The position of X-ray peaks (i.e. energy of the peaks) indicates the element, and the intensity of the peaks gives the element's concentration.[157] Due to the low energy resolution, the characteristic peaks from the elements with close atomic numbers can overlap; as a result, the quantitative analysis becomes difficult and the EDS is considered a semi-quantitative technique.

2.3.2 Instrumentation

The SEM-EDS analysis was performed on a TESCAN VEGA II LSU scanning electron microscope (20 kV accelerating voltage) equipped with an X-MAX (80mm^2) X-ray EDS spectrometer (Oxford Instruments), located at the Canadian Center for Electron Microscopy, McMaster University, Hamilton, ON. A pure nickel metal was used for signal calibration. Samples were finely polished with 800 and 1200 grit sandpapers, and a layer of double-sided carbon tape was used to mount samples on the SEM sample holders.

2.4 Thermoelectric Property Measurements

To calculate the figure of merit, ZT, Seebeck coefficient, electrical resistivity/conductivity, and thermal conductivity must be determined. The Hall coefficient and mobility are also measured to gain better understanding of the Seebeck coefficient and electrical resistivity/conductivity.

2.4.1 Seebeck Coefficient and Electrical Conductivity Measurements

A ULVAC-RIKO ZEM-3 instrument was used for Seebeck coefficient and electrical resistivity measurement. The instrument is located at CanmetMATERIALS, Natural Resources of Canada, Hamilton, ON. All samples were cut into bars (3mm × 3mm × 10mm) using a revolving diamond blade and kerosene as a lubricant. Measurements were under a helium atmosphere; a sample was heated and held at a specified temperature. The temperature difference heating is used to provide a temperature difference ($\Delta T = T_1 - T_2$) to the sample bar, and the temperature difference obeys the limitation: ΔT ($\frac{\Delta T}{\frac{T_1+T_2}{2}} \ll 1$).[158]

Seebeck coefficient was derived from the temperature difference at the two thermocouples without application of current and voltage difference ΔV_s between the two thermocouples[159] according to equation (1-1). The electrical resistivity ρ was measured using a dc 4-probe method, in which a constant current I was applied to the sample while maintaining the temperature difference and a voltage difference ΔV between the two thermocouples was measured. To eliminate the Seebeck coefficient contribution ΔV_S to the measured voltage, ΔV, between the two thermocouples, a resistive voltage difference ΔV_I is calculated by:

$$\Delta V_I = \Delta V - \Delta V_S \text{ (2-15).}$$

And the electrical resistivity ρ is then calculated:

$$\rho = \frac{\Delta V_I A}{I l_0} \text{ (2-16).}$$

A is the effective cross area, I is a constant current is applied to both ends of the sample and l_0 is the effective distance between the two thermocouples.

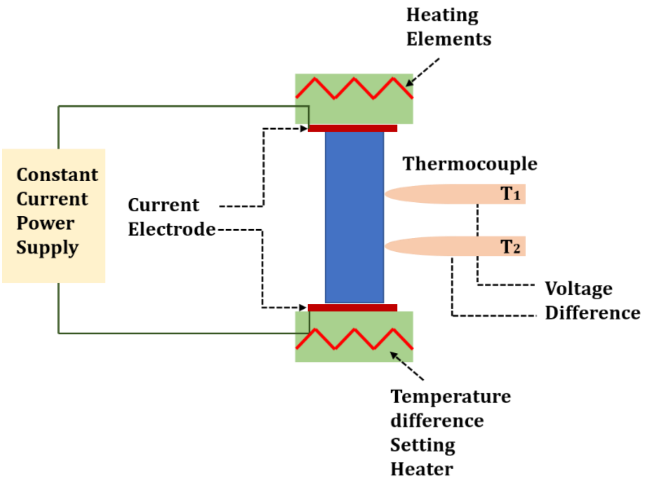

Figure 2.7 Schematically describes the ULVAC-RIKO ZEM-3 instrument.[160]

2.4.2 Thermal Conductivity Determinations

The thermal conductivity of samples was calculated by:

$$k = c_p \rho_k D \text{ (2-17).}$$

c_p is the specific heat capacity obtained from the Neumann-Kopp rule[161], which states that a compound's molar specific heat capacity equals the sum of its constituent molar heat capacities. The sample density ρ_k was measured using a home-built Archimedes setup at room temperature. And D is the thermal diffusivity measured by the laser flash method, in which a laser pulse irradiates one side of the sample, and an infrared detector records the thermal response on the other side. The thermal diffusivity of samples can be determined by

$$D = \frac{\ln(4) d}{\pi^2 t_{\frac{1}{2}}} \text{ (2-18).}$$

Where $t_{\frac{1}{2}}$ is the time required for the recording surface to reach half of the maximum temperature rise, and d is the thickness of the sample.[162]

Laser flash experiments were performed on 10 mm × 10 mm × 1 mm plate samples under a nitrogen atmosphere using a Netzsch LFA 457 instrument in the laboratory of Dr. Kuei-Hsien Chen, Department of Physics, National Central University, Taoyuan City 32001, Taiwan, by Dr. Suneesh Meledath Valiyaveettil. Some laser flash experiments were also performed on round samples (Diameter = 12.75 mm and thickness = 1 mm) under a nitrogen atmosphere using a Netzsch LFA 467 instrument located at Automotive Resource Center, McMaster University, Hamilton, ON.

2.4.3 Hall Effect Measurements

The Hall effect is generation of a voltage difference across a conductor when an electrical current is passed through it and a magnetic field perpendicular to the current is applied. Hall effect measurements were performed on square plate samples (1 mm × 10 mm × 10 mm) using a home-built instrument with the Van der Pauw geometry, at room temperature and in air. The instrument is equipped with a GMW 5403 electromagnet and with AC excitation and detection from a Stanford Research SR830 lock-in amplifier. The instrument is located at the CanmetMATERIALS, Natural Resources of Canada, Hamilton, ON. During the measuremens, a magnetic field (*B*) swapped from -1.3 *T* to 1.3 *T*, and a AC current (*I*) was fixed at 5 mA. The measured Hall voltage V_H, the thickness of the sample, *d*, were used to determine the Hall coefficients R_H :

$$R_H = \frac{d \times V_H}{I \times B} \text{ (2-19).}^{163}$$

The Hall coefficient is positive if holes dominate carrier transport, and it is negative when electrons dominate the carrier transport. To eliminate the experimental errors, a linear fit was applied to a scatter graph with V_H as the *y*-axis and *B* as the *x*-axis. The slope obtained was used to derive the Hall coefficient. The derived R_H was employed to calculate the Hall carrier concentration, n_H, and Hall carrier mobility, μ_H,:

$$n_H = \frac{1}{eR_H} \text{ (2-20).}^{163}$$

$$\mu_H = \frac{R_H}{\rho} \quad (2\text{-}21),^{163}$$

where e is an electron charge, and ρ is the electrical resistivity.

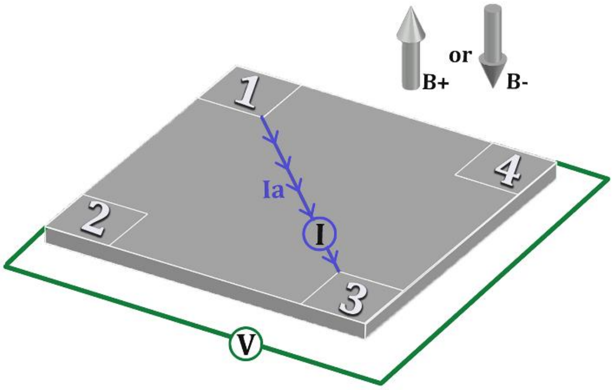

Figure 2.8. Schematic representation of the Hall effect measurements. Magnetic field is applied perpendicular to the current; the current is applied between contacts 1 and 3, and the voltage is measured between 2 and 4.

2.5. Electronic structure calculations

Knowledge of the electronic structure is necessary to understand and manipulate material's transport properties. For example, the Seebeck coefficient is sensitive to the changes in the electronic band structure, and the researchers have used band convergence, band degeneracy, band inversion, and resonant states to tune the thermopower. In this dissertation, the tight-binding, linear-muffin tin orbital method with the atomic sphere approximation (TB-LMTO-ASA) was used for the SnTe and $Co_4Ge_4Te_6$ phases, and density functional theory (DFT) was employed for $Sn_{0.5}Ge_{0.5}Te$.

2.5.1 Tight-Binding-Linear-Muffin Tin Orbital Method with the Atomic Sphere Approximation

TB-LMTO-ASA is an efficient method for electronic structure calculations. For the tight-binding (TB) model, electrons are assumed to be tightly bound to the atom to which they belong, and the influence of the neighbor atoms on these electrons are ignored.[164–166] The linear-muffin tin orbital (LMTO) approximation is a standard method for the orbital basis set determination. To determine the basis set, each ion core is located at the center of a "muffin tin" sphere with a radius R_l. The muffin tin geometry has two distinct spatial regions: inside and outside the muffin tins; the outside regions is also called the interstitial region. The potential is assumed to be spherically symmetric inside the muffin tins and flat (constant) in the interstitial region.[166] Atomic sphere approximation (ASA) assumes all atoms to be spherical, and empty spheres are placed into the interstitial region, allowing spherical potentials to describe all spatial regions.[167]

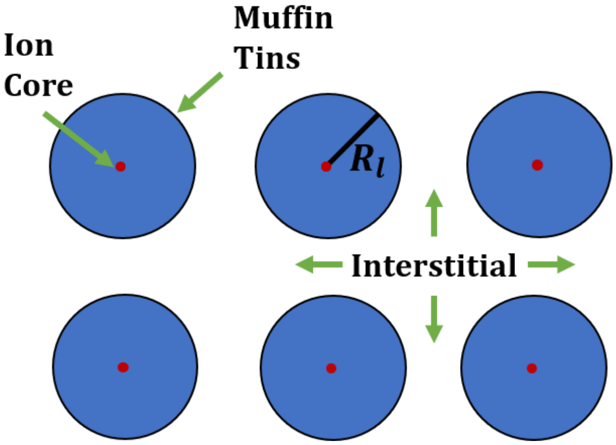

Figure 2.9. Schematics of the muffin tin geometry: the space is divided into muffin tin spheres, and the region between these spheres is the interstitial region.

The TB-LMTO-ASA[168] calculations were performed on the room-temperature structures of SnTe,[90] GeTe[90] and $Co_8Ge_{12}Te_{12}$.[128] Space-filling empty spheres were included into the unit cell by the automatic sphere generation to satisfy the overlap criteria of the TB-LMTO-ASA model. For SnTe and GeTe, 4*d*, 5*s*, and 5*p* ones of Sn, 3*d*, 4*s*, and 4*p* ones of Ge, and 4*d*, 5*s*, and 5*p* ones of Te were employed during the calculations. For $Co_8Ge_{12}Te_{12}$, the 3*d*, 4*s* orbitals of Co, 3*d*, 4*s*, and 4*p* ones of Ge and 4*d*, 5*s*, and 5*p* ones of Te were employed.

2.5.2 Density Functional Theory Calculations

Density functional theory (DFT) plays a vital role in studying the electronic structure of solid-state materials. Unlike the LMTO approach, the potential around the atoms is complex in the DFT, which produces more accurate results for the electronic structure calculations for materials with complex structures. Generally, the kinetic energy $T_{kinetic}$ and electrostatic interactions E_{estat} of the electrons with their charge density and with the nuclei are counted as the significant contribution to the total electronic energy $E_{electronic}$ in the DFT.[169] Also, the remaining electronic energy not included in $T_{kinetic}$ and E_{estat} is described by the exchange-correlation energy, E_{exc}.[170] The mathematical expression for $E_{electronic}$ is given by:

$$E_{electronic} = T_{kinetic} + E_{estat} + E_{exc}. \text{ (2-22)}$$

The DFT calculations of $Sn_{14}Ge_{13}Te_{27}$, $Sn_{13}Ge_{13}InTe_{27}$, $Sn_{16}Ge_{14}SbInTe_{32}$, and $Sn_{16}Ge_{14}BiInTe_{32}$ were performed with the Quantum Espresso software[171,172] in collaborator with Yang Zan. The electron-ion interaction for the Ge, In, Sb, Bi, and Te atoms were modeled by the projector-augmented wave (PAW) technique.[173] Perdew-

Burke-Ernzerhof (PBE) approximation was chosen to describe the exchange-correlation energy, and the cutoff energy for the wave functions was set to 50 Ry.[174] Calculations were performed on the 3 × 3 ×3 rhombohedral supercells containing 27 Ge sites and 27 Te sites and the 2 × 2 ×2 cubic phase supercell containing 16 Ge sites, 16 Sn sites, and 32 Te sites. Only the Ge substitution was considered since the dominant defect in the phases studied is Ge vacancy. Two Ge sites were randomly chosen to be replaced by Bi, In, or Sb. Both cell parameters and atomic positions were fully relaxed until the force on each atom was less than 0.001eV/Å.

Chapter 3. Enhancing Thermoelectric Performance of $Sn_{0.5}Ge_{0.5}Te$ via Doping with Sb/Bi and Alloying with Cu_2Te. Optimization of Transport Properties and Thermal Conductivity

This chapter encompasses the manuscript “Enhancing Thermoelectric Performance of $Sn_{0.5}Ge_{0.5}Te$ via Doping with Sb/Bi and Alloying with Cu_2Te. Optimization of Transport Properties and Thermal Conductivity”, which was published in *Dalton Transactions* (*Dalton Trans.* **2020**, *49* (18), 6135–6144). Partial electrical properties measurements were collected by Dr. Chun-Wan Timothy Lo and Mr. Masoud Aminzare at CanmetMATERIALS, Natural Resources of Canada, Hamilton, ON. Mr. Suneesh Meledath Valiyaveettil collected the thermal diffusivities, specific heat capacity, and density of materials at the Department of Physics, National Central University, Taoyuan City 32001, Taiwan. The candidate completed the experimental procedures, sample characterization, electronic structure calculations, data interpretation, and manuscript preparation.

Reproduced with permission from Song, S.; Lo, C.-W. T.; Aminzare, M.; Tseng, Y.-C.; Valiyaveettil, S. M.; Mozharivskyj, *Dalton Trans.* **2020**, *49* (18), 6135–6144. Copyright by 2020 Royal Society of Chemistry

This work provides a comparative study of the thermoelectric properties for the $Sn_{0.5}Ge_{0.5}Te$ phases doped with Sb and Bi and alloyed with Cu_2Te. The $Sn_{0.5}Ge_{0.5}Te$ composition was chosen because it delivers the highest ZT value within the $Sn_{1-x}Ge_xTe$ series ($x \leq 0.5$). Doping $Sn_{0.5}Ge_{0.5}Te$ with electron-richer Sb and Bi improves both the charge transport properties and thermal conductivity. Further alloying with Cu_2Te optimizes the thermoelectric performance of the samples even further, yielding the ZT value of 0.99 for $(Sn_{0.5}Ge_{0.5})_{0.91}Bi_{0.06}Te(Cu_2Te)_{0.05}$ at 500 °C. Hall measurements were performed to understand the effects of doping and alloying.

3.1 Introduction

Nowadays, fossil fuels still retain a dominant position in the energy production. However, 60% of the energy generated is expelled into environment as waste heat.[1] If some of this waste heat were converted into electricity, it would greatly reduce green-house emissions and improve efficiency of many energy-intense processes at the same time.[175] High-temperature thermoelectric power generation can successfully tackle this issue and the research in the field has attracted significant attention.[7] Thermoelectric materials can directly convert heat into electricity and they are expected to play a vital role as green energy generator, thereby mitigating future energy challenges.[2,176]

The efficiency of thermoelectric materials at a given temperature T is represented by the figure of merit, $ZT = \frac{\alpha^2\sigma}{\kappa_{total}}T$, where α is the Seebeck coefficient and σ is the electrical conductivity. κ_{total} is the total thermal conductivity and consists of the electronic (κ_e) and lattice (κ_l) thermal conductivities. An ideal thermoelectric material should have a low, glass-like thermal conductivity and a high-power factor ($\alpha^2\sigma$) to achieve suitable ZT values. However, parameters α, σ and κ_e are interrelated with each other. For example, Seebeck coefficient is inversely proportional to the charge carrier concentration (n) via $\alpha = \frac{8\pi^2 {k_B}^2}{3eh^2} m^* T (\frac{\pi}{3n})^{\frac{2}{3}}$, while electrical conductivity, $\sigma = ne\mu$, is directly proportional to n.[39] Additionally, the electronic thermal conductivity, $\kappa_e = L\sigma$T,[39] is related to the electrical conductivity via Wiedemann-Franz law, and thus has the same linear dependence on n.

The current thermoelectric research focuses on optimization of the power factor and lattice thermal conductivity. Strategies for the power factor improvement include introduction of resonant levels at the Fermi level,[177–179] convergence of electronic bands and presence of degenerate valleys,[75,180–182] and adjustment of the carrier concentration.[183] The lattice thermal conductivity could be optimized via nano-precipitation in the matrix,[184–186] introduction of point defects and nanoscale grain boundaries to enhance phonon scattering.[187–190]

p-Type lead telluride (PbTe) based phases are excellent thermoelectric materials within the 500 to 800 K range.[178,187,191,192] However, their industrial applications are becoming more restricted because of the lead toxicity. Instead, tin telluride (SnTe) is being explored as a potential substitute for PbTe for thermoelectric power generation. While the two materials have similar crystal and electronic structures,[193,194] there are some differences, which negatively affect the transport properties of SnTe. One of them is the energy separation between the higher energy, light hole L band and the lower energy, heavy hole Σ band, both of which are located at the top of the valence band. In the pristine SnTe, this separation is larger (≈0.35 eV)[143] than in PbTe (≈0.17 eV),[130] which leads to the dominance of light holes (with a low effective mass) in the transport properties, and to a low Seebeck coefficient as the result.[195] In addition, intrinsic Sn deficiency creates a high hole concentration of 10^{20} to 10^{21} cm^{-3} and subsequently a low Seebeck coefficient.[196] Moreover, SnTe possesses a much higher lattice thermal conductivity stemming from the lighter atomic mass of Sn, which leads to a faster sound velocity.[197,198]

Another potential substitute for PbTe is GeTe. Similar to SnTe, GeTe possesses significant Ge vacancies, and as a result, a very high hole concentration (~10^{21} cm^{-3}) and a high electronic thermal conductivity.[199,200] It is worth mentioning that a theoretical band gap of GeTe is small (E_g ~0.24 eV)[199] and the energy separation ($\Delta E_{L-\Sigma}$ ~0.27-0.38 eV) is large. In summary, GeTe displays the charge transport problems similar to those in SnTe, and thus the same optimization approaches can be applied to both systems.[201,202]

3.2 Materials and Methods

3.2.1 Synthesis

Pieces of tin, germanium, antimony, bismuth and tellurium (purity 99.9 wt.% or better) were used for the solid state synthesis of $Sn_{1-x}Ge_xTe$ (x=0.10-0.50), $(Sn_{0.5}Ge_{0.5})_{1-1.5x}Sb_xTe$ (x=0.02, 0.06 and 0.10), $(Sn_{0.5}Ge_{0.5})_{1-1.5x}Bi_xTe$ (x=0.02 and 0.06), $Sn_{0.5}Ge_{0.5}Te(Cu_2Te)_x$ (x=0.03, 0.05), $(Sn_{0.5}Ge_{0.5})_{0.91}Sb_{0.06}Te(Cu_2Te)_x$ (x=0.03, 0.05), $(Sn_{0.5}Ge_{0.5})_{0.91}Bi_{0.06}Te(Cu_2Te)_x$ (x=0.03, 0.05) Starting materials with appropriate ratios were loaded into silica tubes, which were evacuated to 0.02 torr and flamed sealed. To eliminate temperature variances, all samples were placed in the same furnace. The samples were slowly heated to 1000 °C to ensure elemental mixing, and kept at this temperature for 12 hours. The samples were quenched in an ice bath.

3.2.2 Spark Plasma Sintering (SPS)

To obtain high-density samples suitable for property measurements, the alloys were hand grinded in an agate mortar and loaded into a 15 mm diameter graphite die. A layer of graphite paper was placed between the sample powders and graphite plungers. During the SPS, the samples were heated under a pressure of 45 MPa. The heating profile was as follows:

$$R.T. \xrightarrow{100°\mathrm{C/mins}} 600\ °\mathrm{C} \xrightarrow{5mins} 600°\mathrm{C} \xrightarrow{No\ pressure\ and\ current\ applied} R.T.$$

3.2.3 Density

The geometrical and Archimedean density of each sample are measured by a $\mathbf{10mm \times 3mm \times 3mm}$ bar sample. These samples have been soaked overnight in distilled water before Archimedean measurement.

Table 3.1 Geometrical and Archimedean density of samples

	Geometrical Density (g/cm^3)	Archimedean Density (g/cm^3)	Compactness (%)
$Sn_{0.9}Ge_{0.1}Te$	6.32	6.47	97.66
$Sn_{0.7}Ge_{0.3}Te$	6.21	6.34	98.05
$Sn_{0.5}Ge_{0.5}Te$	6.28	6.38	98.48
$(Sn_{0.5}Ge_{0.5})_{0.97}Sb_{0.02}Te$	6.17	6.28	98.23
$(Sn_{0.5}Ge_{0.5})_{0.91}Sb_{0.06}Te$	6.17	6.29	98.13
$(Sn_{0.5}Ge_{0.5})_{0.85}Sb_{0.1}Te$	6.21	6.34	97.82
$(Sn_{0.5}Ge_{0.5})_{0.97}Bi_{0.02}Te$	6.20	6.32	98.06

$(Sn_{0.5}Ge_{0.5})_{0.91}Bi_{0.06}Te$	6.23	6.38	97.66
$Sn_{0.5}Ge_{0.5}Te(Cu_2Te)_{0.03}$	6.41	6.49	98.73
$Sn_{0.5}Ge_{0.5}Te(Cu_2Te)_{0.05}$	6.39	6.46	98.90
$(Sn_{0.5}Ge_{0.5})_{0.91}Sb_{0.06}Te(Cu_2Te)_{0.05}$	6.21	6.29	98.70
$(Sn_{0.5}Ge_{0.5})_{0.91}Bi_{0.06}Te(Cu_2Te)_{0.05}$	6.32	6.44	98.08

3.2.4 X-ray Powder Diffraction

All samples were analyzed by X-ray powder diffraction (PXRD) on a PANalytical X’Pert Pro diffractometer with $CuK\alpha_1$ and an X’Celerator detector at room temperature. For data collection, the samples were finely grinded using a mortar and pestle and deposited on the zero background silicon discs. The diffraction data were collected between 20° to 140°. Rietveld refinement (Rietica program)[154] was used to determine the lattice parameters and amounts of impurities.

3.2.5 Thermoelectric Measurements

For Seebeck coefficient and electric conductivity measurements, the SPS samples were cut into 3mm x 3mm x 10mm rectangular bars using a diamond saw. Kerosene was used as a lubricant to prevent sample oxidation. Electrical conductivity and Seebeck coefficient were simultaneously measured under He atmosphere from room temperature to 500 ˚C on an ULVAC-RIKO ZEM-3 instrument system.

The 10mm x 10mm x 1mm plates were cut for the measurements of thermal conductivity and Hall effect. The total thermal conductivity is calculated by $\kappa_{total}=D\times C_p\times\rho$. Thermal diffusivity D was measured in the range 25-500 ˚C by using the laser flash diffusivity method on a Netzsch LFA 457 instrument. The temperature dependent heat capacity, C_p, was derived using a standard pyroceram on the same LFA 457 instrument, and the density, ρ, of these samples was measured by the Archimedes method.

The hole concentration, n_p, was calculated from $n_p = \frac{1}{eR_H}$, where e is an electron charge and R_H is Hall coefficient. Concerning R_H, the $R_H = \frac{t*V_H}{I*B}$ formula was used, with t being the thickness of the sample, I the fixed AC current (5mA), B magnetic field swapped from -12800 G to 12800 G, and V_H Hall voltage measured at room temperature. A scatter graph was plotted based on the Hall voltage (y axis) and magnetic field (x axis) with a linear fit applied to minimize the measurement errors. The slope of the linear fit was taken as $\frac{V_H}{B}$ in the R_H formula. The carrier mobility, μ_h, was calculated from $\mu_h = {}^{R_H}/_{\rho}$, where ρ is the sheet resistance measured by the Van der Pauw method.

3.2.6 Computational Details

In order to understand the relationship between the composition and physical properties, tight-binding linear-muffin-tin-orbital calculations using the atomic sphere approximation (TB-LMTO-ASA)[168] were performed on the room-temperature structures of SnTe and GeTe.[90] Space-filling empty spheres were included into the unit cell by the automatic sphere generation in order to satisfy the overlap criteria of the TB-LMTO-ASA model. Valence and semicore electronic states were $4d^{10}$ $5s^2$ $5p^2$ for Sn, $3d^{10}$ $4s^2$ $4p^2$ for Ge and $4d^{10}$ $5s^2$ $5p^4$ for Sn.

3.3 Results and discussion

3.3.1 Ge-substituted SnTe

According to the powder X-ray diffraction (PXRD) results in Figure 3.1 (a), $Sn_{1-x}Ge_xTe$ undergoes a phase transition from the cubic ($Fm\overline{3}m$) to rhombohedral ($R3m$) structure at room temperature when the Ge amount is 50% and above. Additionally, the unit cell volume decreases with an increasing Ge amount, which is manifested by the shift of the diffraction peaks to higher angles (Figure 3.1 (a)). This tendency can be mainly attributed to a smaller Pauling radius of Ge^{2+} (1.223 Å) compared with Sn^{2+}(1.399 Å).[203] The cubic structures of SnTe, $Sn_{0.9}Ge_{0.1}Te$ and $Sn_{0.7}Ge_{0.3}Te$ are the cubic close packing of the Te^{2-} anions with Sn^{2+} and Ge^{2+} in octahedral voids. In the $Sn_{0.5}Ge_{0.5}Te$ and GeTe structures, Sn and Ge atoms shift from (½, ½, ½) to (½-*x*, ½-*x*, ½-*x*).[211] This dislocation reduces the symmetry from $Fm\overline{3}m$ to $R3m$ and distorts the 90˚ angles of the unit cell to 88.35˚.[90,200,204]

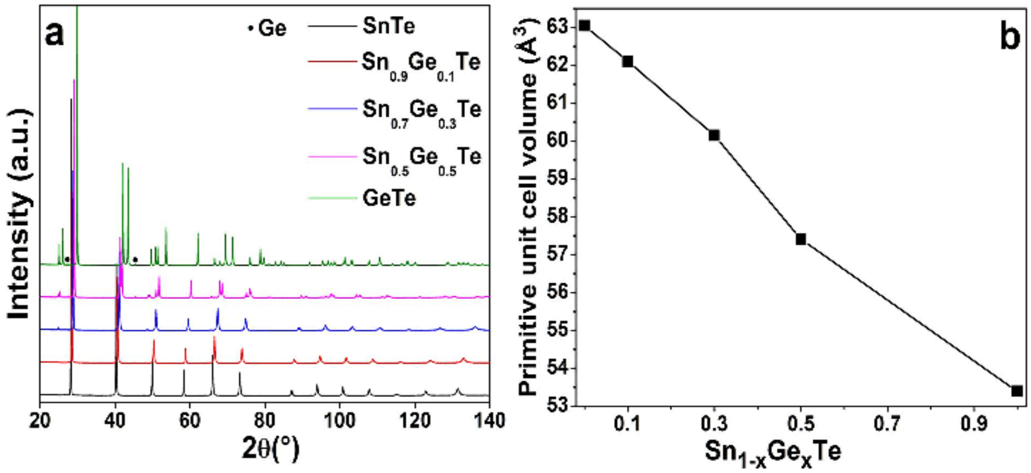

Figure 3.1 (a) Powder X-ray diffraction patterns at room temperature. (b) Primitive unit cell volume of $Sn_{1-x}Ge_xTe$ (x = 0.1 to 0.5).

In order to understand how the Ge substitution affects the carrier concentration, mobility and effective mass, we measured Hall and Seebeck coefficients for SnTe, $Sn_{0.5}Ge_{0.5}Te$ and GeTe. The experimental values of the Seebeck coefficient and carrier concentration (from Hall measurements) at room temperature were used to derive the Fermi integral,[205] which was employed to calculate the carrier effective mass (Equation (3.3)):

$$\alpha = \pm \frac{k_B}{e}\left[\frac{(r+{}^{3}/_{2})F_{r+{}^{3}/_{2}}(\eta)}{(r+{}^{3}/_{2})F_{r+{}^{1}/_{2}}(\eta)} - \eta \right. \quad (3.1)$$

$$F_n(\eta) = \int_0^\infty \frac{x^n}{1+e^{x-\eta}}\,dx \quad (3.2)$$

$$m^* = \frac{h^2}{2k_BT}\left[\frac{n}{4\pi F_{\frac{1}{2}}(\eta)}\right]^{\frac{2}{3}} \quad (3.3)$$

h, k_B, η, $F_n(\eta)$, r and e represent Planck constant, Boltzmann constant, reduced Fermi energy, n^{th} order Fermi integral, scattering factor and electron charge, respectively. In our case, the scattering factor is -½ because only the acoustic phonon scattering is considered within a single parabolic band model.[206]

Table 3.2 Carrier concentration, carrier mobility and effective mass of SnTe, $Sn_{0.5}Ge_{0.5}Te$ and GeTe at room temperature.

Composition	Concentration (10^{21}*cm^{-3})	Mobility ($cm^2V^{-1}s^{-1}$)	m^*/m_0
SnTe	0.40(6)	100(2)	0.44
$Sn_{0.5}Ge_{0.5}Te$	1.75(4)	11.2(3)	3.00
GeTe	1.38(3)	25.4(5)	2.25

As shown in Table 3.2, the $Sn_{0.5}Ge_{0.5}Te$ sample has the largest carrier concentration, followed by GeTe. According to powder X-ray results, Ge precipitates are present both in the $Sn_{0.5}Ge_{0.5}Te$ (0.94(9) mol. %) and GeTe (0.40(6)%) samples. The higher carrier density in $Sn_{0.5}Ge_{0.5}Te$ stems from larger Ge vacancies. In terms of the carrier mobility, the trend is different: SnTe has the highest carrier mobility, followed by GeTe. A lower mobility in $Sn_{0.5}Ge_{0.5}Te$ can be attributed to a more disordered structure; a Sn/Ge disorder will scatter electrons more efficiently, thus shortening their relaxation time.[207,208] Moreover, the charge carriers are heavier in $Sn_{0.5}Ge_{0.5}Te$, which further reduces the carrier mobility. The presented data suggest that the Ge substitution has a significant impact on the charge transport properties and that the carrier mobility is affected the most.

Figure 3.2 (a) displays the electrical conductivity of $Sn_{1-x}Ge_xTe$ within the 100 – 500 ˚C temperature range. Generally, the electrical conductivity of the substituted samples decreases with an increase in the Ge amount. Interestingly, all the Sn/Ge mixed samples show lower electrical conductivity below 200 ^{o}C, which can be attributed to a reduced carrier mobility stemming from the Sn/Ge disorder and associated charge carrier scattering, which is temperature independent.[188] In contrast, carrier scattering (and mobility) in SnTe and GeTe is dominated by phonon-electron interactions, which are temperature dependent.[29] As a result, the conductivity of SnTe and GeTe decrease more rapidly with temperature and drops below that of the mixed Sn/Ge samples above 200 ˚C.

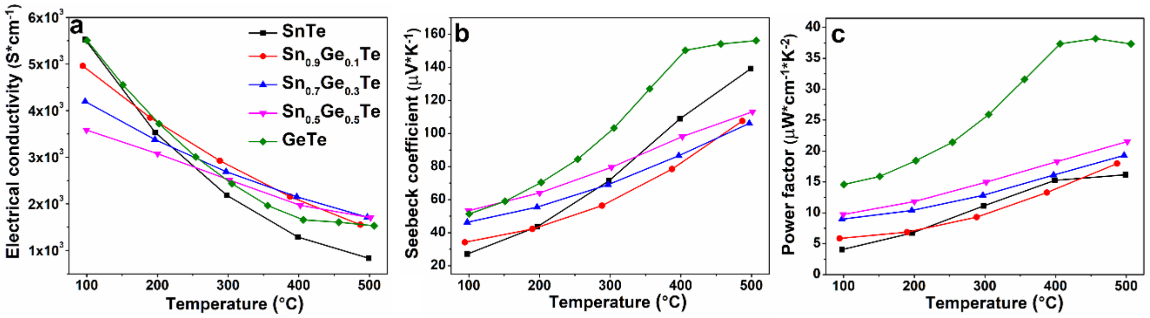

Figure 3.2 (a) Electrical conductivity; (b) Seebeck coefficient and (c) power factor of SnTe, $Sn_{0.9}Ge_{0.1}Te$, $Sn_{0.7}Ge_{0.3}Te$, $Sn_{0.5}Ge_{0.5}Te$ and GeTe.

Seebeck coefficients (Figure 3.2 (b)) are positive for all samples, suggesting that holes are the dominant charge carriers, in agreement with the literature data.[137,195] An increase in the thermopower for larger Ge amounts at lower temperatures can be attributed primarily to the changes in the carrier effective mass. As shown in Table 3.2, the carrier effective mass in SnTe is 0.44 m_0, in $Sn_{0.5}Ge_{0.5}Te$ is 3.00 m_0 and in GeTe is 2.25 m_0. The trends in the effective mass were verified through the band structure calculations (Figure 3.3). Compared to SnTe, the valence band maximum (VBM) in GeTe moved from the L point to the Γ point and the band around the Fermi level became flatter. This suggests an increased effective mass for the Ge-substituted SnTe, which is in agreement with the experimental values.

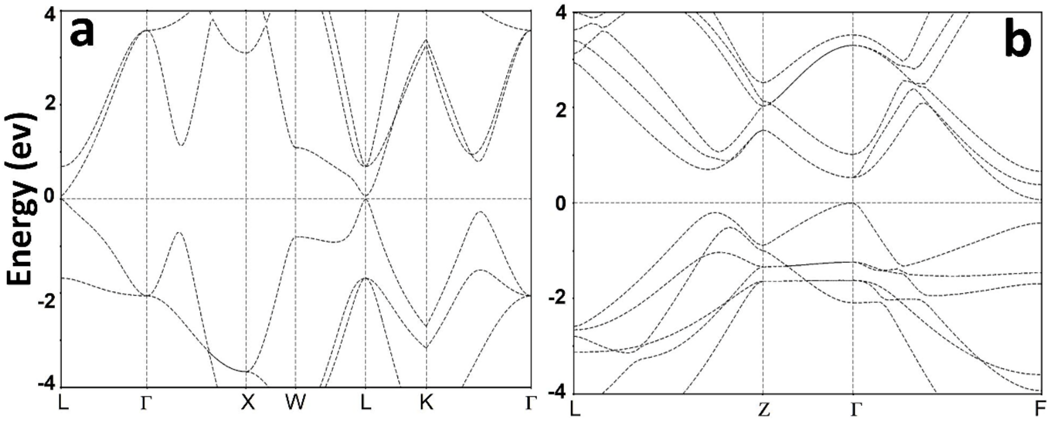

Figure 3.3 The calculated band structure of (a) SnTe and (b) GeTe.

Figure 3.2 (c) shows the temperature dependent power factors of $Sn_{1-x}Ge_xTe$. GeTe displays the highest power factor due to its high Seebeck coefficient and high electrical conductivity. The temperature dependence of the total (k_{total}), charge carrier (k_c), and lattice (k_L) conductivities is presented in Figure 3.4. The carrier contribution is estimated from the Wiedemann-Franz law ($k_c=L\sigma T$), where L is the Lorenz factor defined from:

$L= 1.5 + \exp\left(-{}^{|S|}/_{116}\right)$.[42] (3-4)

Within 100-200 ˚C, $Sn_{0.5}Ge_{0.5}Te$ has the lowest k_c due to the strong point defect scattering of the charge carriers.[207,208] However above 250 ˚C, pristine SnTe and GeTe have a lower k_c due to the dominance of the phonon-electron scattering. The lattice contribution, k_L, is estimated by

$$k_L= k_{\mathrm{total}} - k_c \quad (3\text{-}5).$$

The temperature dependence of k_L is shown in Figure 3.4 (b). All Ge-containing samples have a lower lattice thermal conductivity than SnTe due to the point defect scattering, stemming from the Sn/Ge mixture. The lattice thermal conductivities of $Sn_{0.9}Ge_{0.1}Te$ and $Sn_{0.5}Ge_{0.5}Te$ have a negative slope with temperature, which is driven by the Umklapp scattering.[60] The lattice conductivity of the cubic $Sn_{0.7}Ge_{0.3}Te$ phase is almost temperature independent and is lower than those of other samples below 350 ^{o}C. Such reduction in k_L can be attributed to significant scattering of acoustic phonons by ferroelectric lattice instability.[131,209,210] Total thermal conductivity is illustrated in Figure 3.4 (c). $Sn_{0.7}Ge_{0.3}Te$ has the lowest thermal conductivity within 100 ˚C to 350 ˚C due to its lowest lattice contribution. In the 350 to 425 ˚C range, $Sn_{0.5}Ge_{0.5}Te$ offers the lowest thermal conductivity and, above 425 ˚C, $Sn_{0.9}Ge_{0.1}Te$ takes over due to its optimized carrier thermal conductivity.

Figure 3.4 (d) summarizes the *ZT* values. All Ge-containing samples have higher figure-of-merit values than SnTe, with the pristine GeTe displaying the best performance and $Sn_{0.5}Ge_{0.5}Te$ being second. Considering a high market price for germanium (two times more than that for tin), we focused on optimizing the thermoelectric properties of $Sn_{0.5}Ge_{0.5}Te$ via targeted doping.

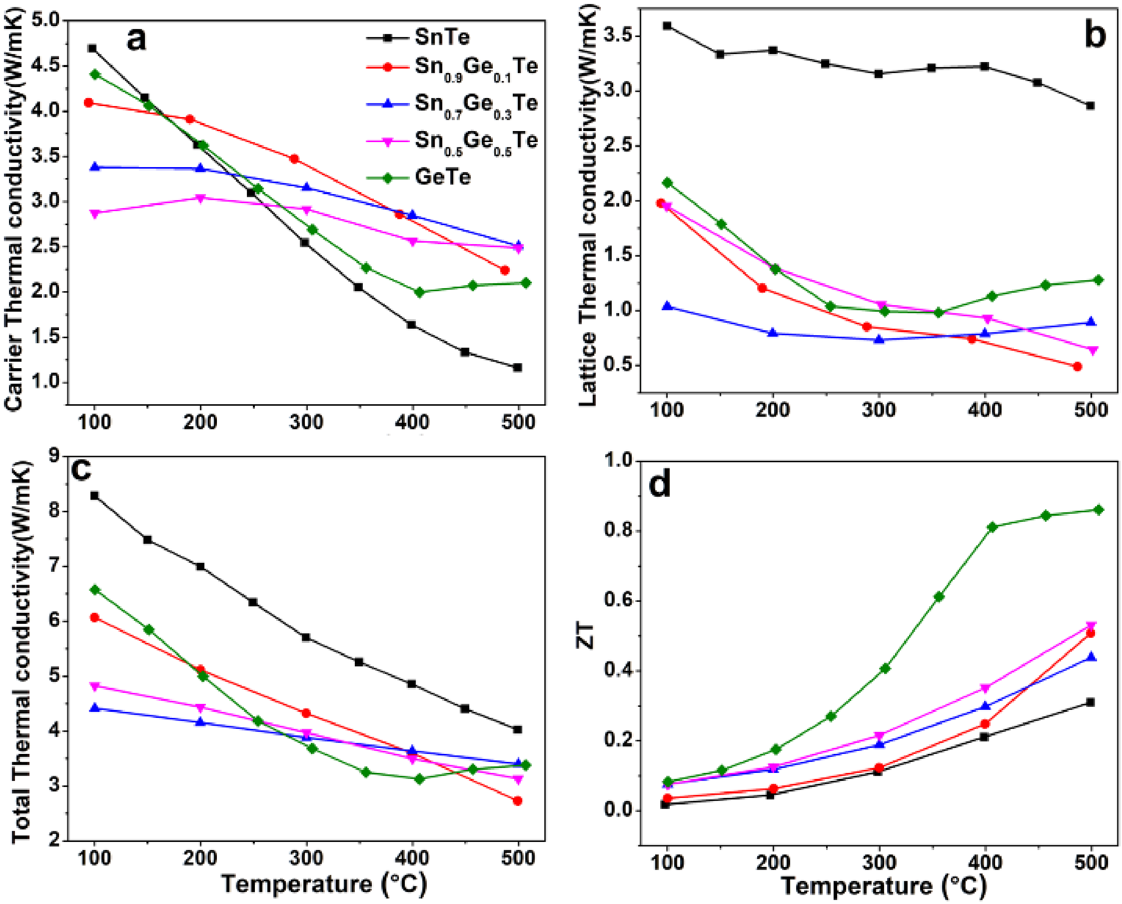

Figure 3.4 Temperature dependent (a) carrier thermal conductivity, (b) lattice thermal conductivity, (c) total thermal conductivity and (d) *ZT* values for SnTe, $Sn_{0.9}Ge_{0.1}Te$, $Sn_{0.7}Ge_{0.3}Te$, $Sn_{0.5}Ge_{0.5}Te$ and GeTe.

3.3.2 Sb- and Bi-doped on $Sn_{0.5}Ge_{0.5}Te$

The doping of $Sn_{0.5}Ge_{0.5}Te$ with Sb and Bi was performed according to the $(Sn_{0.5}Ge_{0.5})_{1-1.5x}Sb_xTe$ and $(Sn_{0.5}Ge_{0.5})_{1-1.5x}Bi_xTe$ formulas, i.e. for one fraction of Sb or Bi, 50% more of Sn/Ge were removed. This was done in accordance with the dominant oxidation states of cations in tellurides, which are Sn^{2+}, Ge^{2+}, Sb^{3+} and Bi^{3+}. Based on the X-ray diffraction data (Figure 3.5 (a) and (b)), Sb and Bi doping increases the symmetry from $R3m$ to $Fm\bar{3}m$.

$(Sn_{0.5}Ge_{0.5})_{0.97}Sb_{0.02}Te$ and $(Sn_{0.5}Ge_{0.5})_{0.97}Bi_{0.02}Te$ exhibit clear splitting of the diffraction peaks characteristic of the rhombohedral symmetry. In $(Sn_{0.5}Ge_{0.5})_{0.91}Sb_{0.06}Te$ and $(Sn_{0.5}Ge_{0.5})_{0.91}Bi_{0.06}Te$, the peaks started to coalesce, and in $(Sn_{0.5}Ge_{0.5})_{0.85}Sb_{0.1}Te$ they are fully merged (*Fm-3m*).

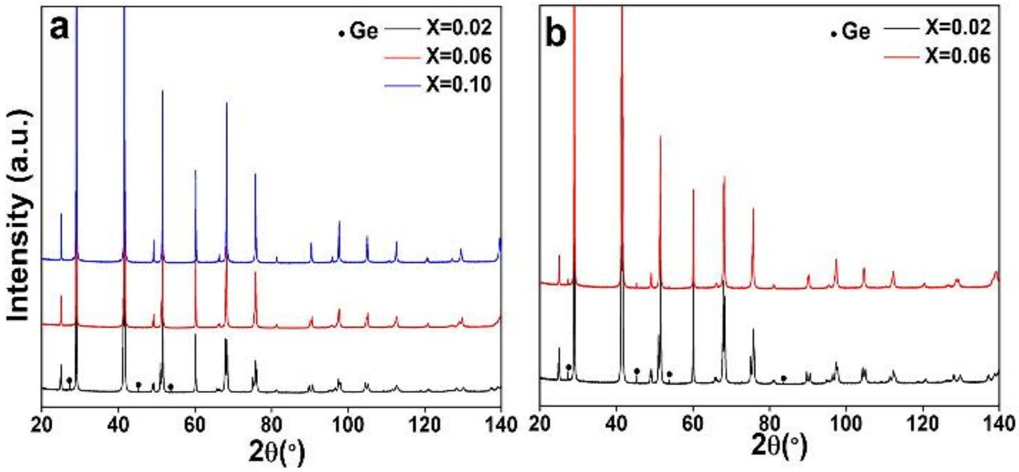

Figure 3.5 Powder X-ray diffraction patterns of $(Sn_{0.5}Ge_{0.5})_{1-1.5x}Sb_xTe$ (a) and $(Sn_{0.5}Ge_{0.5})_{1-1.5x}Bi_xTe$ (b) at room temperature.

Figure 3.6 (a) and (b) display electrical conductivities of the $(Sn_{0.5}Ge_{0.5})_{1-1.5x}Sb_xTe$ and $(Sn_{0.5}Ge_{0.5})_{1-1.5x}Bi_xTe$ samples in the 100 - 500 ˚C range. Both Sb- and Bi-doping reduces the electrical conductivity. In the case of the Sb-series, the doping level of x=0.1 yields the electrical conductivity (and thermopower) similar to those of x=0.06. For that reason, we did not pursue higher doping levels. To understand the changes in charge transport properties, the carrier concentration, mobility and effective mass of $Sn_{0.5}Ge_{0.5}Te$, $(Sn_{0.5}Ge_{0.5})_{0.91}Sb_{0.06}Te$ and $(Sn_{0.5}Ge_{0.5})_{0.91}Bi_{0.06}Te$ were analyzed. As shown in Table 3.3, both $(Sn_{0.5}Ge_{0.5})_{0.91}Sb_{0.06}Te$ and $(Sn_{0.5}Ge_{0.5})_{0.91}Bi_{0.06}Te$ possess a much lower carrier mobility than $Sn_{0.5}Ge_{0.5}Te$. The two main reasons are heavier charge carriers (Table 3.3) and increased atomic disorder on the Sn/Ge site due to the doping.[207,211] Moreover, $(Sn_{0.5}Ge_{0.5})_{0.91}Bi_{0.06}Te$ has a lower carrier mobility than $(Sn_{0.5}Ge_{0.5})_{0.91}Sb_{0.06}Te$ likely due to the bigger size and heavier mass of Bi.[207,211] These two factors will enlarge the strain field and mass fluctuation scattering parameters, and as a result, the carrier relaxation time and mobility will be lower.[188]

To explain the decrease in the carrier concentration, we performed the X-ray phase analysis of the polycrystalline samples. The powder X-ray patterns of $(Sn_{0.5}Ge_{0.5})_{1-1.5x}Sb_xTe$ and $(Sn_{0.5}Ge_{0.5})_{1-1.5x}Bi_xTe$ (Figure 3.5 (a) and (b)) indicate a decrease in the Ge precipitates, with the Ge amounts being lower for smaller Sb or Bi doping. As such, Ge vacancies and carrier concentration are slightly suppressed upon the Sb and Bi doping.

Table 3.3 Carrier concentration, carrier mobility and effective mass of $Sn_{0.5}Ge_{0.5}Te$, $(Sn_{0.5}Ge_{0.5})_{0.91}Sb_{0.06}Te$ and $(Sn_{0.5}Ge_{0.5})_{0.91}Bi_{0.06}Te$ at room temperature.

Composition	Concentration (10^{21}*cm^{-3})	Mobility ($cm^2V^{-1}s^{-1}$)	m^*/m_0
$Sn_{0.5}Ge_{0.5}Te$	1.75(4)	11.2(3)	3.00
$(Sn_{0.5}Ge_{0.5})_{0.91}Sb_{0.06}Te$	1.53(3)	7.8(2)	3.81
$(Sn_{0.5}Ge_{0.5})_{0.91}Bi_{0.06}Te$	1.42(3)	6.7(1)	3.73

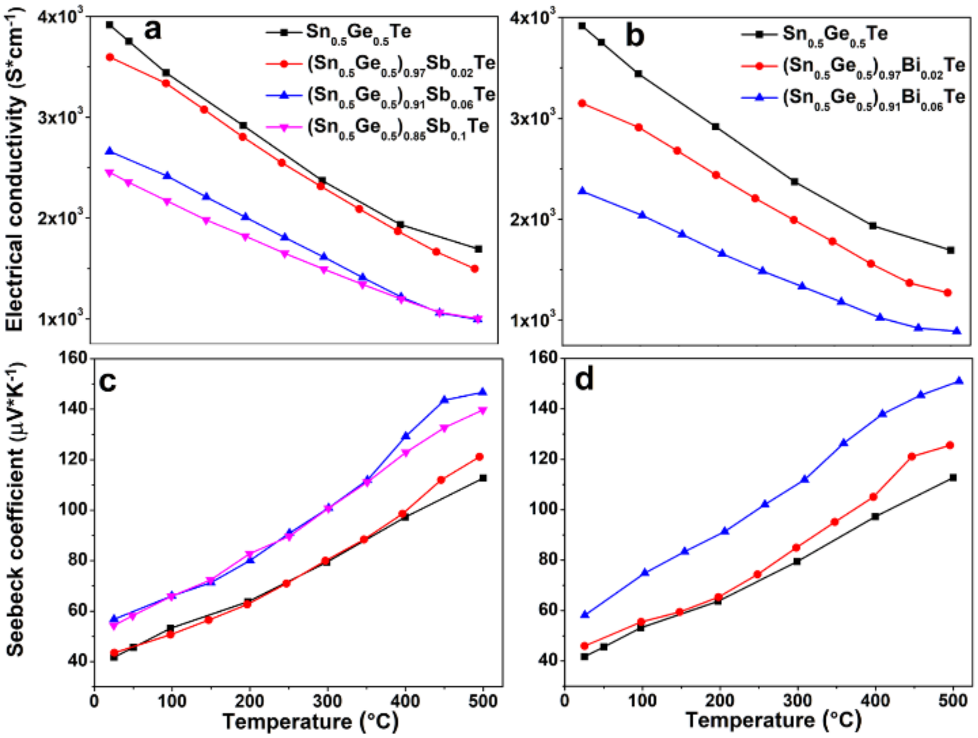

Figure 3.6 (a) and (b) Electrical conductivity, (c) and (d) Seebeck coefficient of $(Sn_{0.5}Ge_{0.5})_{1-1.5x}Sb_xTe$ and $(Sn_{0.5}Ge_{0.5})_{1-1.5x}Bi_xTe$.

Seebeck coefficients of $(Sn_{0.5}Ge_{0.5})_{1-1.5x}Sb_xTe$ and $(Sn_{0.5}Ge_{0.5})_{1-1.5x}Bi_xTe$ are shown in Figure 3.6 (c) and (d), respectively. *p*-Type behavior (positive thermopower) is observed for all samples. An increase in the Seebeck coefficient in the doped samples may be attributed to a larger effective mass and lower carrier concentration, with the former potentially being more consequential as judged from the data in Table 3.3. It is worth mentioning that the Sb- and Bi- doping tends to reduce rhombohedral distortion of the structure (Figure 3.5 (a) and (b)), thus leading to the valence band convergence,[212] an increase in the valence band degeneracy,[194] and a subsequent increase in the thermopower.

Figure 3.7 (a) and (b) display the power factors, *PF*. The highest *PF*s are observed for *x*=0.06 and they stem from the optimized Seebeck coefficient.

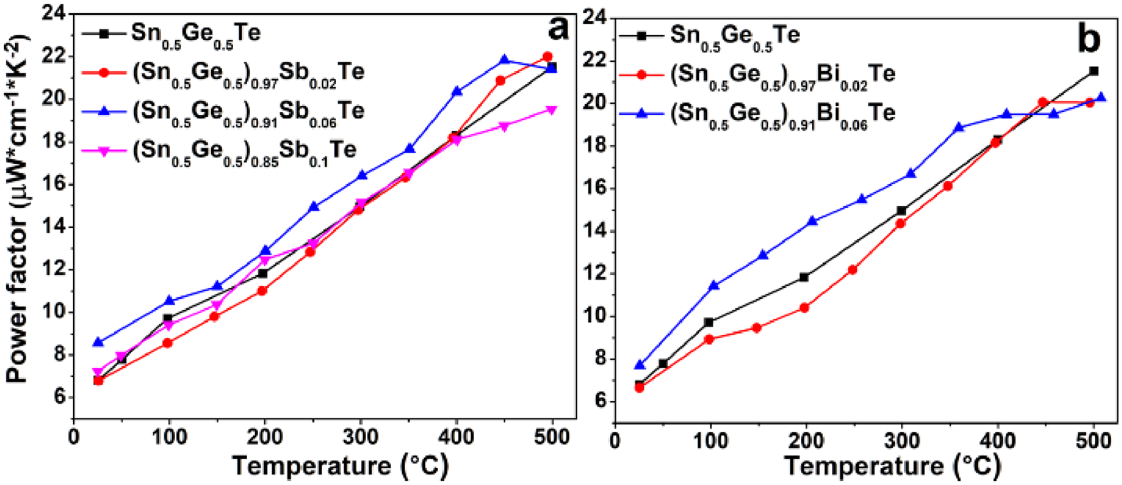

Figure 3.7 Power factor of $(Sn_{0.5}Ge_{0.5})_{1-1.5x}Sb_xTe$ (a) and $(Sn_{0.5}Ge_{0.5})_{1-1.5x}Bi_xTe$ (b).

The total thermal conductivity (Figure 3.8 (a)) of $(Sn_{0.5}Ge_{0.5})_{0.91}Sb_{0.06}Te$ and $(Sn_{0.5}Ge_{0.5})_{0.91}Bi_{0.06}Te$ is much lower than that of undoped $Sn_{0.5}Ge_{0.5}Te$. An increase above 450 ˚C is likely related to the rhombohedral-to-cubic structural transformation, but this will have to be confirmed via HT structural studies. The carrier thermal conductivity in Figure 3.8 (b) was calculated using the Wiedemann-Franz law ($k_e = L\sigma T$); and it is lower for $(Sn_{0.5}Ge_{0.5})_{0.91}Sb_{0.06}Te$ and $(Sn_{0.5}Ge_{0.5})_{0.91}Bi_{0.06}Te$. The lattice thermal conductivity of $Sn_{0.5}Ge_{0.5}Te$ decreases with temperature, which is characteristic of the Umklapp scattering. On the other hand, the lattice conductivity of $(Sn_{0.5}Ge_{0.5})_{0.91}Sb_{0.06}Te$ and $(Sn_{0.5}Ge_{0.5})_{0.91}Bi_{0.06}Te$ is almost temperature independent, which suggests that point defect scattering of phonons is likely a dominant scattering mechanism.[104,213] Moreover, this type of scattering should be more pronounced in the Bi-doped samples, and this is consistent with data in Figure 3.8 (c). Figure 3.8 (d) shows the temperature dependent thermal conductivities and *ZT* values of $(Sn_{0.5}Ge_{0.5})_{0.91}Sb_{0.06}Te$, $(Sn_{0.5}Ge_{0.5})_{0.91}Bi_{0.06}Te$ and $Sn_{0.5}Ge_{0.5}Te$.

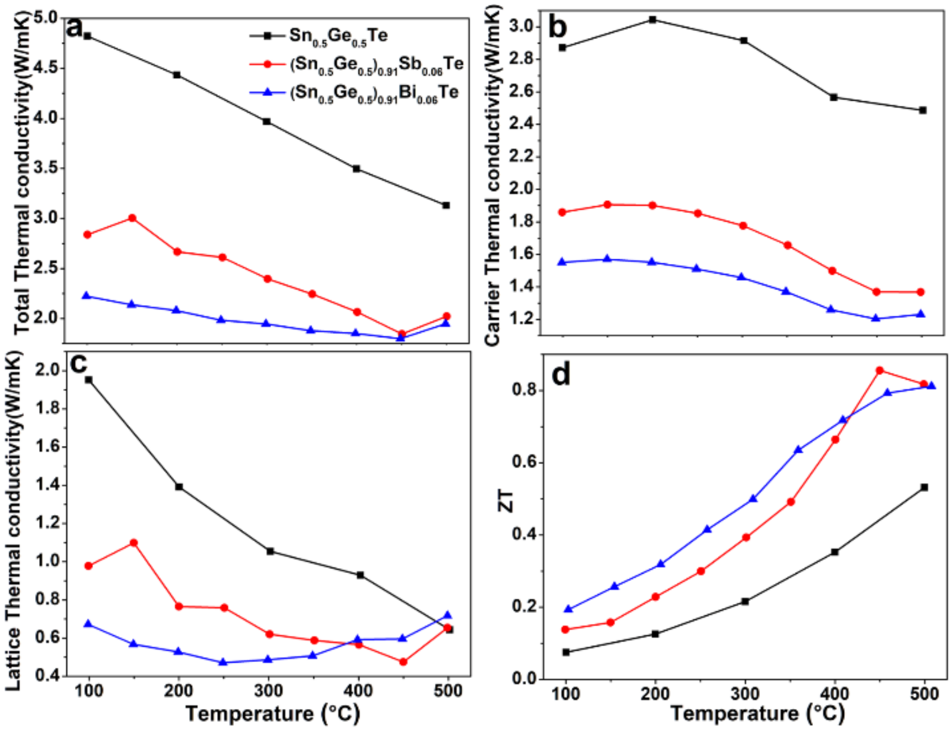

Figure 3.8 (a) Total, (b) carrier, and (c) lattice thermal conductivity and (d) *ZT* values of $Sn_{0.5}Ge_{0.5}Te$, $(Sn_{0.5}Ge_{0.5})_{0.91}Sb_{0.06}Te$ and $(Sn_{0.5}Ge_{0.5})_{0.91}Bi_{0.06}Te$.

3.3.3 Cu_2Te-containing $(SnGe)_{0.5}Te$, $(Sn_{0.5}Ge_{0.5})_{0.91}Sb_{0.06}Te$ and $(Sn_{0.5}Ge_{0.5})_{0.91}Bi_{0.06}Te$

Cu_2Te can be introduced into the PbTe[214] and SnTe phases[36,215,216] to optimize their thermal conductivity. In this study, Cu_2Te is incorporated into $Sn_{0.5}Ge_{0.5}Te$ to reduce its lattice thermal conductivity. $Sn_{0.5}Ge_{0.5}Te(Cu_2Te)_{0.03}$ and $Sn_{0.5}Ge_{0.5}Te(Cu_2Te)_{0.05}$ samples have a rhombohedral structure (*R*3*m*) and they contain Ge and $Cu_{1.79}Te$ precipitates as seen in their X-ray diffraction patterns (Figure 3.9 (d)).

The electrical conductivity of the $Sn_{0.5}Ge_{0.5}Te(Cu_2Te)_{0.03}$ and $Sn_{0.5}Ge_{0.5}Te(Cu_2Te)_{0.05}$ samples is lower than that of $Sn_{0.5}Ge_{0.5}Te$ (Figure 3.9 (a)) and decreases with temperature. Seebeck coefficients of the pristine and Cu_2Te-containing samples are identical and increase with temperature (Figure 3.9 (b)). Since both electrical conductivity and thermopower depend on the carrier concentration and effective mass (although in the opposite ways), we have measured Hall effect of $Sn_{0.5}Ge_{0.5}Te(Cu_2Te)_{0.05}$ and $Sn_{0.5}Ge_{0.5}Te$ to gain insights into different behaviors of the transport properties.

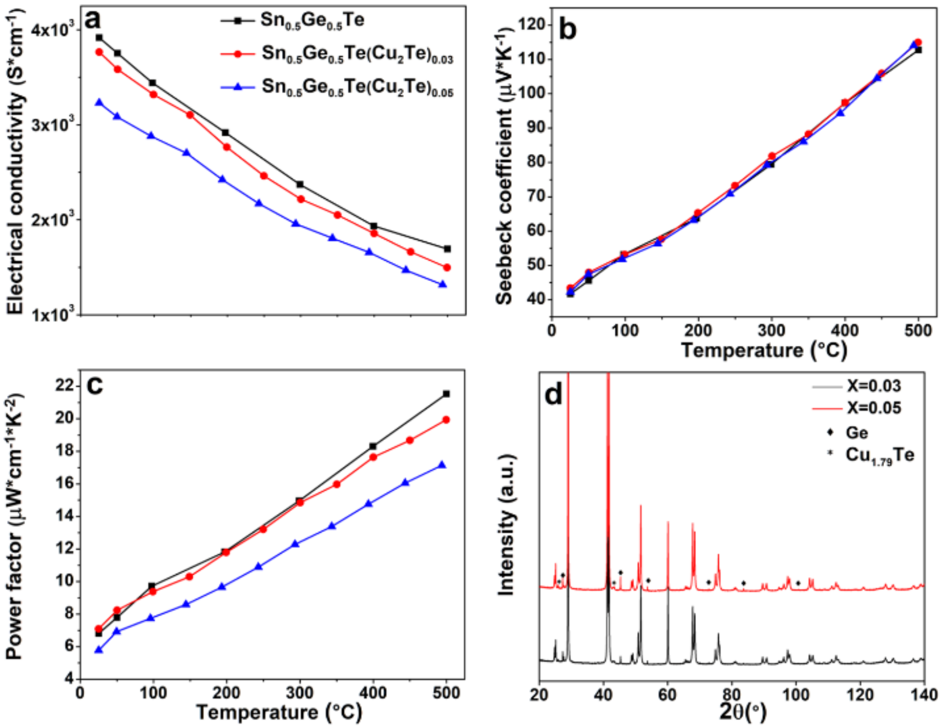

Figure 3.9 (a) Electrical conductivity, (b) Seebeck coefficient and (c) power factor of $Sn_{0.5}Ge_{0.5}Te$, $Sn_{0.5}Ge_{0.5}Te(Cu_2Te)_{0.03}$ and $Sn_{0.5}Ge_{0.5}Te(Cu_2Te)_{0.05}$. (d) Powder X-ray diffraction patterns of $Sn_{0.5}Ge_{0.5}Te(Cu_2Te)_x$ at room temperature.

Table 3.4 Carrier concentration, carrier mobility and effective mass of $Sn_{0.5}Ge_{0.5}Te$ and $Sn_{0.5}Ge_{0.5}Te(Cu_2Te)_{0.05}$ at room temperature.

Composition	Concentration (10^{21}*cm^{-3})	Mobility ($cm^2V^{-1}s^{-1}$)	m^*/m_0
$Sn_{0.5}Ge_{0.5}Te$	1.75(4)	11.2(3)	3.00
$Sn_{0.5}Ge_{0.5}Te(Cu_2Te)_{0.05}$	1.64(3)	8.6(2)	2.95

$Sn_{0.5}Ge_{0.5}Te(Cu_2Te)_{0.05}$ has only a slightly lower carrier concentration and effective mass than $Sn_{0.5}Ge_{0.5}Te$ (Table 3.4). According to the Mott equation,[30] $\alpha = \frac{8\pi^2 {k_B}^2}{3eh^2} m^* T (\frac{\pi}{3n})^{\frac{2}{3}}$, their thermopower will be similar, which is observed experimentally. A slightly lower carrier concentration in $Sn_{0.5}Ge_{0.5}Te(Cu_2Te)_{0.05}$ may be related to a lower deficiency of the Sn/Ge site upon Cu_2Te doping,[232] although it has to be stated that both Ge and $Cu_{1.79}Te$ precipitates were detected in the X-ray power diffraction patter of $Sn_{0.5}Ge_{0.5}Te(Cu_2Te)_{0.05}$ (Figure 3.9 (d)), and thus the deficiency level is not clear. The lower electrical conductivity of $Sn_{0.5}Ge_{0.5}Te(Cu_2Te)_{0.05}$ stems primarily from the lower carrier mobility (Table 3.4), which in turn results from the increased carrier scattering by additional atomic disorder and presence of the impurities. The power factor, *PF*, (Figure 3.9 (c)) is the lowest for $Sn_{0.5}Ge_{0.5}Te(Cu_2Te)_{0.05}$ due to its low electrical conductivity. Since the *PF* of $Sn_{0.5}Ge_{0.5}Te$ alloyed with Cu_2Te was inferior to that of the Sb- and Bi-doped $Sn_{0.5}Ge_{0.5}Te$, we did not measure its thermal conductivity. Instead, we have proceeded to explore the Cu_2Te alloying of the $(Sn_{0.5}Ge_{0.5})_{0.91}Bi_{0.06}Te$ and $(Sn_{0.5}Ge_{0.5})_{0.91}Sb_{0.06}$ phases, which showed improvements in the *PF* and *ZT* values over $Sn_{0.5}Ge_{0.5}Te$ (see above). $(Sn_{0.5}Ge_{0.5})_{0.91}Sb_{0.06}Te(Cu_2Te)_{0.05}$ and $(Sn_{0.5}Ge_{0.5})_{0.91}Bi_{0.06}Te(Cu_2Te)_{0.05}$ still have a rhombohedral structure (*R*3*m*), however, the peaks started to coalesce in their X-ray diffraction patterns (Figure 3.10 (d)). And they also contain Ge and $Cu_{1.79}Te$ precipitates.

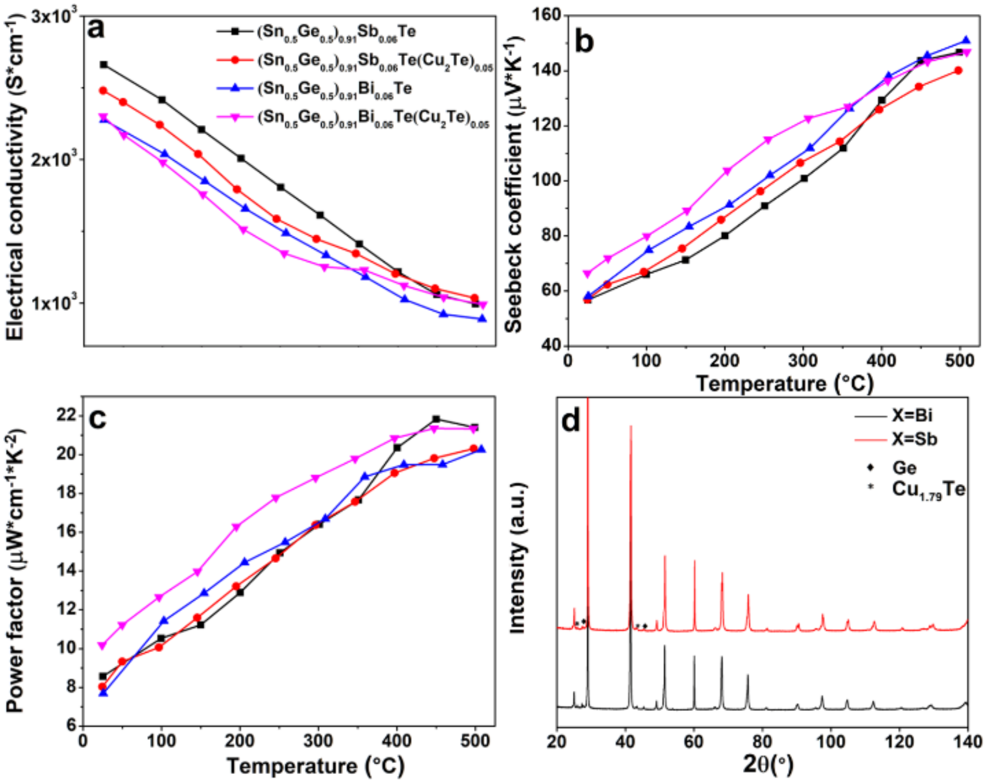

Figure 3.10 (a) Electrical conductivity, (b) Seebeck coefficient, (c) power factor of $(Sn_{0.5}Ge_{0.5})_{0.91}Bi_{0.06}Te$, $(Sn_{0.5}Ge_{0.5})_{0.91}Bi_{0.06}Te(Cu_2Te)_{0.05}$, $(Sn_{0.5}Ge_{0.5})_{0.91}Sb_{0.06}Te$ and $(Sn_{0.5}Ge_{0.5})_{0.91}Sb_{0.06}Te(Cu_2Te)_{0.05}$, respectively. (d) Powder X-ray diffraction patterns of $(Sn_{0.5}Ge_{0.5})_{0.91}X_{0.06}Te(Cu_2Te)_{0.05}$ at room temperature.

The temperature dependent electrical conductivity, Seebeck coefficients and power factors are shown in Figure 3.10 (a), (b) and (c), respectively. The Cu_2Te-containing samples have a lower electrical conductivity and a higher Seebeck coefficient compared to those without Cu_2Te. For $(Sn_{0.5}Ge_{0.5})_{0.91}Sb_{0.06}Te(Cu_2Te)_{0.05}$ and $(Sn_{0.5}Ge_{0.5})_{0.91}Bi_{0.06}Te(Cu_2Te)_{0.05}$, the slope in the electrical conductivity changes after 350 ˚C, which could be related to the rhombohedral-to-cubic phase transition.[209,217,218]

The Hall effect of $(Sn_{0.5}Ge_{0.5})_{0.91}Sb_{0.06}Te(Cu_2Te)_{0.05}$ and $(Sn_{0.5}Ge_{0.5})_{0.91}Bi_{0.06}Te(Cu_2Te)_{0.05}$ were measured at room temperature and the parameters derived are given in Table 3.5. Most likely, the electrical conductivity is reduced due to the increased scattering of charge carriers by extra disorder. The changes in the Seebeck coefficient can be explained by a larger effective mass. The increased carrier concentrations can be related to higher amounts of the impurity precipitates (Figure 3.10 (d)), and subsequently more deficient Sn/Ge site.

Table 3.5 Carrier concentration, carrier mobility and effective mass of $(Sn_{0.5}Ge_{0.5})_{0.91}Sb_{0.06}Te(Cu_2Te)_{0.05}$ and $(Sn_{0.5}Ge_{0.5})_{0.91}Bi_{0.06}Te(Cu_2Te)_{0.05}$ at room temperature.

Composition	Concentration (10^{21}*cm^{-3})	Mobility (cm^{2}V^{-1}s^{-1})	m^*/m_0
$(Sn_{0.5}Ge_{0.5})_{0.91}Sb_{0.06}Te$	1.53(3)	7.8(2)	3.81
$(Sn_{0.5}Ge_{0.5})_{0.91}Bi_{0.06}Te$	1.42(3)	6.7(1)	3.73
$(Sn_{0.5}Ge_{0.5})_{0.91}Sb_{0.06}Te(Cu_2Te)_{0.05}$	1.75(8)	7.0(1)	4.17
$(Sn_{0.5}Ge_{0.5})_{0.91}Bi_{0.06}Te(Cu_2Te)_{0.05}$	1.67(5)	6.4(2)	4.74

Figure 3.11 (a) and (b) show total thermal conductivity, carrier and lattice contributions for the $(Sn_{0.5}Ge_{0.5})_{0.91}Sb_{0.06}Te$, $(Sn_{0.5}Ge_{0.5})_{0.91}Sb_{0.06}Te(Cu_2Te)_{0.05}$, $(Sn_{0.5}Ge_{0.5})_{0.91}Bi_{0.06}Te$ and $(Sn_{0.5}Ge_{0.5})_{0.91}Bi_{0.06}Te(Cu_2Te)_{0.05}$ samples over the 100 - 500 ˚C range. Presence of Cu_2Te in the $(Sn_{0.5}Ge_{0.5})_{0.91}Sb_{0.06}Te$ and $(Sn_{0.5}Ge_{0.5})_{0.91}Bi_{0.06}Te$ matrixes reduces their carrier and

lattice thermal conductivities below 350-400 °C; but only $(Sn_{0.5}Ge_{0.5})_{0.91}Bi_{0.06}Te(Cu_2Te)_{0.05}$ maintains a lower lattice thermal conductivity in the entire temperature range.

Figure 3.11 (c) compares the *ZT* values of the Sb-containing samples and $Sn_{0.5}Ge_{0.5}Te$. The *ZT* value of $(Sn_{0.5}Ge_{0.5})_{0.91}Sb_{0.06}Te(Cu_2Te)_{0.05}$ reaches 0.92 at 500 ˚C and it is approximately 7% larger than the highest *ZT* of $(Sn_{0.5}Ge_{0.5})_{0.91}Sb_{0.06}Te$, observed at 450 ˚C. The average *ZT* of $(Sn_{0.5}Ge_{0.5})_{0.91}Sb_{0.06}Te$ is improved from 0.45 to 0.47 within the 100-500 ˚C range upon alloying with Cu_2Te. The *ZT* value of $(Sn_{0.5}Ge_{0.5})_{0.91}Bi_{0.06}Te(Cu_2Te)_{0.05}$ reaches 0.99 at 500 ˚C (Figure 3.11(d)), which is 22% higher than that of $(Sn_{0.5}Ge_{0.5})_{0.91}Bi_{0.06}Te$ at the same temperature. From 100 ˚C to 500 ˚C, the average *ZT* of $(Sn_{0.5}Ge_{0.5})_{0.91}Bi_{0.06}Te$ is improved from 0.52 to 0.63 upon incorporation of Cu_2Te.

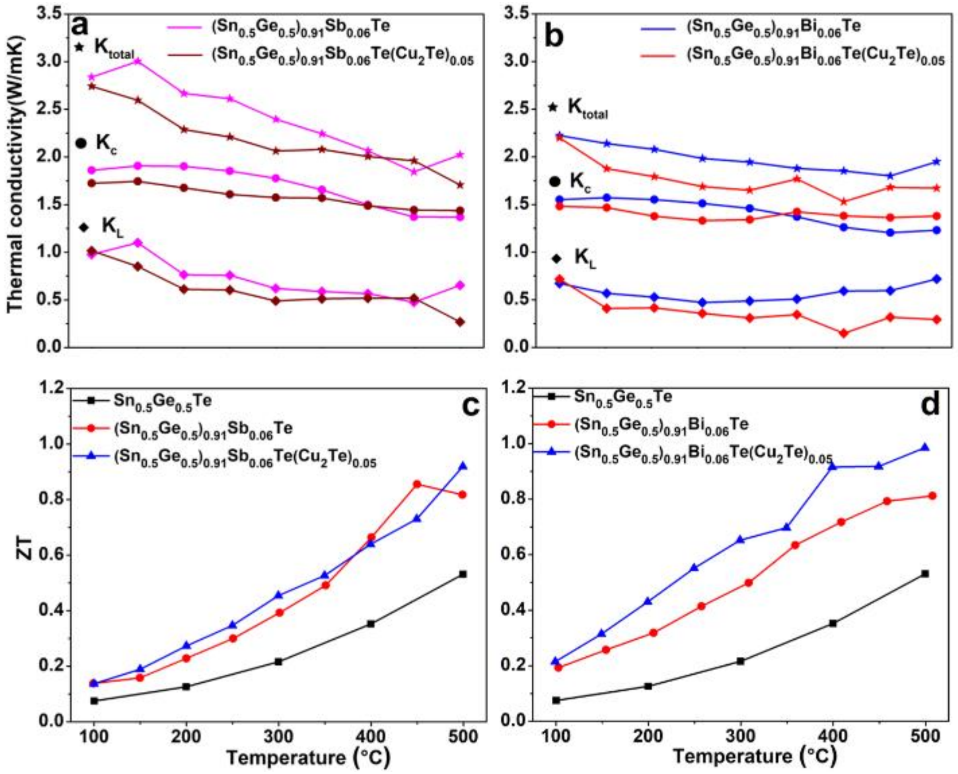

Figure 3.11. (a-b) Thermal conductivity, charge carrier and lattice contributions; (c-d) *ZT* of $(Sn_{0.5}Ge_{0.5})_{0.91}X_{0.06}Te$ and $(Sn_{0.5}Ge_{0.5})_{0.91}X_{0.06}Te(Cu_2Te)_{0.05}$ (X=Sb or Bi) in comparison to $Sn_{0.5}Ge_{0.5}Te$.

3.4 Conclusions

Thermoelectric performance of the explored phases is summarized in Figure 3.12 in terms of the highest *ZT* values achieved and the average *ZT* values over the 100-500 ˚C range. The current data suggests that the thermoelectric performance of the SnTe-based materials can be greatly increased; e.g., the average *ZT* value of $Sn_{0.5}Ge_{0.5}Te$ is more than doubled. It is also obvious that the property optimization may require combination of substitution, doping and alloying, which targets different aspects of the transport properties. In our study, we found the Sb and Bi doping can optimize both the charge transport and thermal conductivity, and the subsequent alloying with Cu_2Te disrupts the phonon propagation even further, thus yielding a superior material. Such approach can be applied to other phases in the $Sn_{1-x}Ge_xTe$ series.

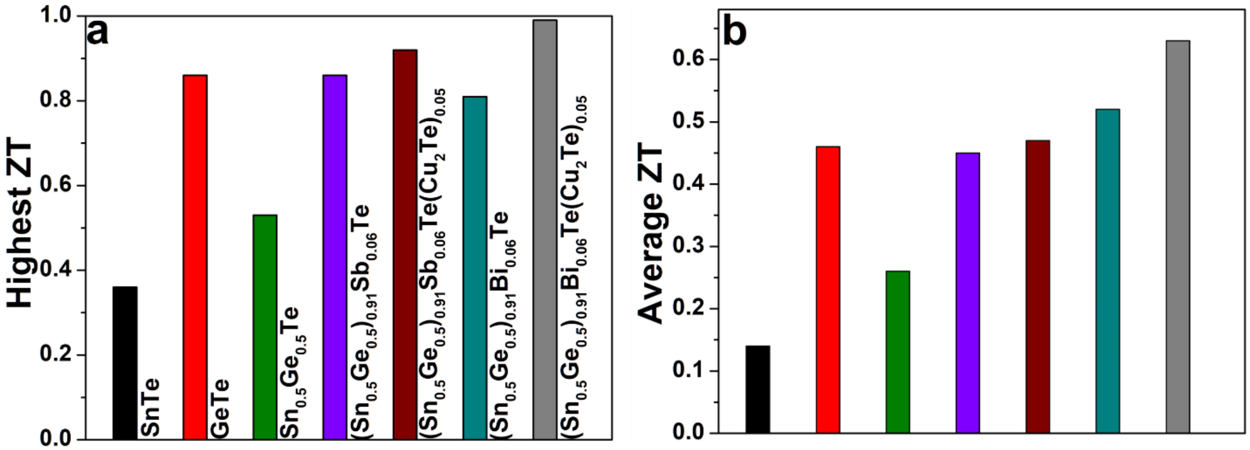

Figure 3.12 (a) The highest and (b) average *ZT* at 100 to 500 ˚C of SnTe, GeTe, $Sn_{0.5}Ge_{0.5}Te$, $(Sn_{0.5}Ge_{0.5})_{0.91}Sb_{0.06}Te$, $(Sn_{0.5}Ge_{0.5})_{0.91}Sb_{0.06}Te(Cu_2Te)_{0.05}$, $(Sn_{0.5}Ge_{0.5})_{0.91}Bi_{0.06}Te$ and $(Sn_{0.5}Ge_{0.5})_{0.91}Bi_{0.06}Te(Cu_2Te)_{0.05}$.

3.5 Supporting Information

Expanded view of the X-ray powder diffraction patterns.

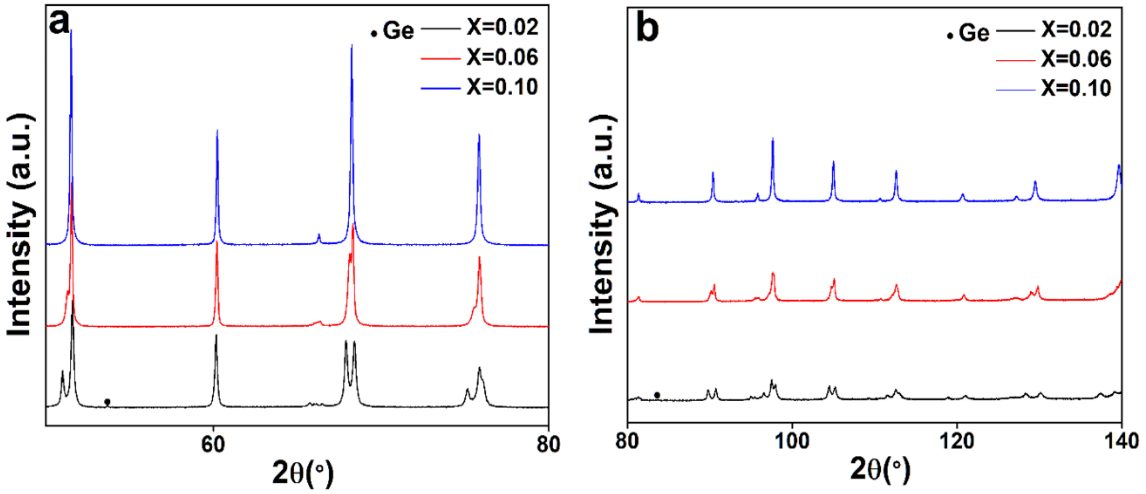

Fig 3.S1: Powder X-ray diffraction patterns of $(Sn_{0.5}Ge_{0.5})_{1-1.5x}Sb_xTe$ in the (a) 40-80˚, (b) 80-140˚ 2θ range at room temperature. The peak splitting is representative of the rhombohedral symmetry.

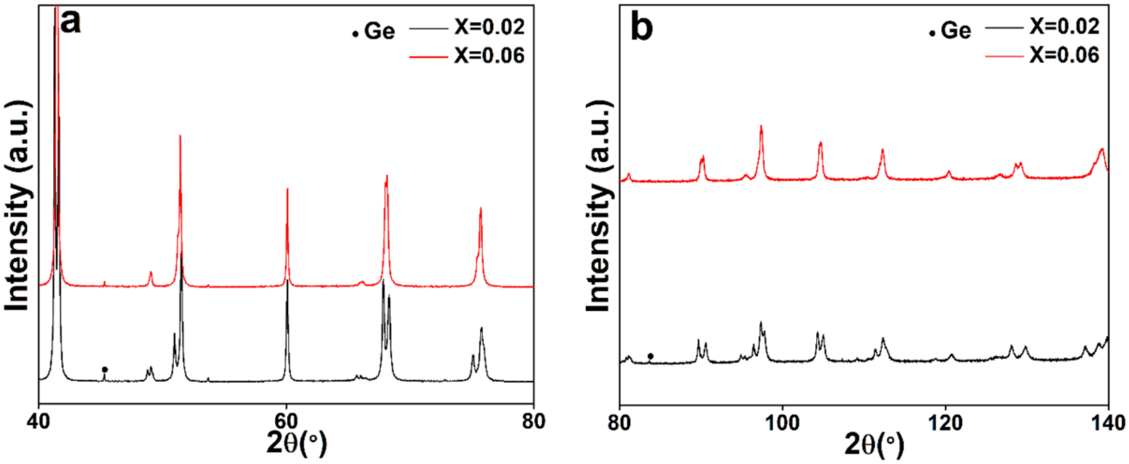

Fig3.S2: Powder X-ray diffraction patterns of $(Sn_{0.5}Ge_{0.5})_{1-1.5x}Bi_xTe$ in the (a) 40-80˚, (b) 80-140˚ 2θ range at room temperature. The peak splitting is representative of the rhombohedral symmetry.

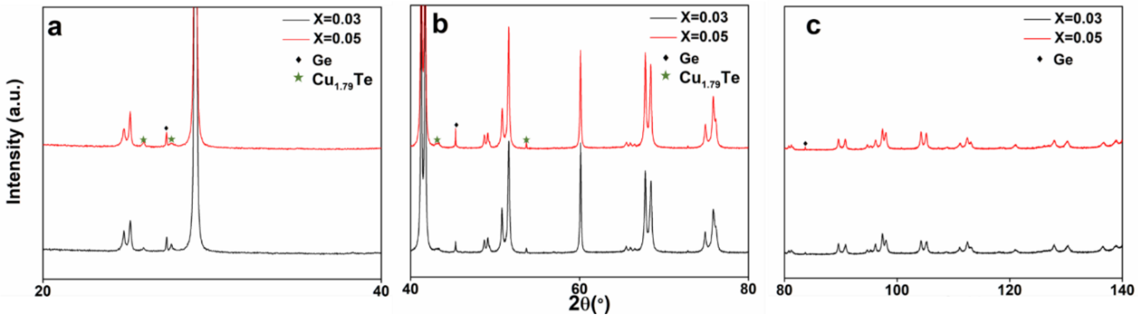

Fig 3.S3: Powder X-ray diffraction patterns of $Sn_{0.5}Ge_{0.5}Te(Cu_2Te)_x$ in the (a) 20-40˚, (b) 40-80˚, (c) 80-140˚ 2θ range at room temperature. The peak splitting is representative of the rhombohedral symmetry.

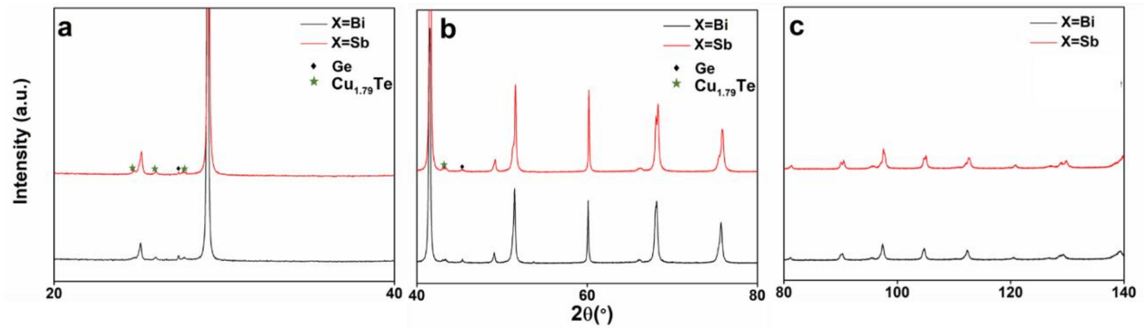

Fig 3.S4: Powder X-ray diffraction patterns of $((Sn_{0.5}Ge_{0.5})_{0.91}X_{0.06}Te\ (Cu_2Te)_{0.05}$ in the (a) 20-40˚, (b) 40-80˚, (c) 80-140˚ 2θ range at room temperature. The peak splitting is representative of the rhombohedral symmetry. The peak splitting in the $(Sn_{0.5}Ge_{0.5})_{0.91}Bi_{0.06}Te(Cu_2Te)_{0.05}$ sample is small but still present.

Scanning Electron Microscopy-Energy Dispersive X-ray Spectroscopy (SEM-EDS).

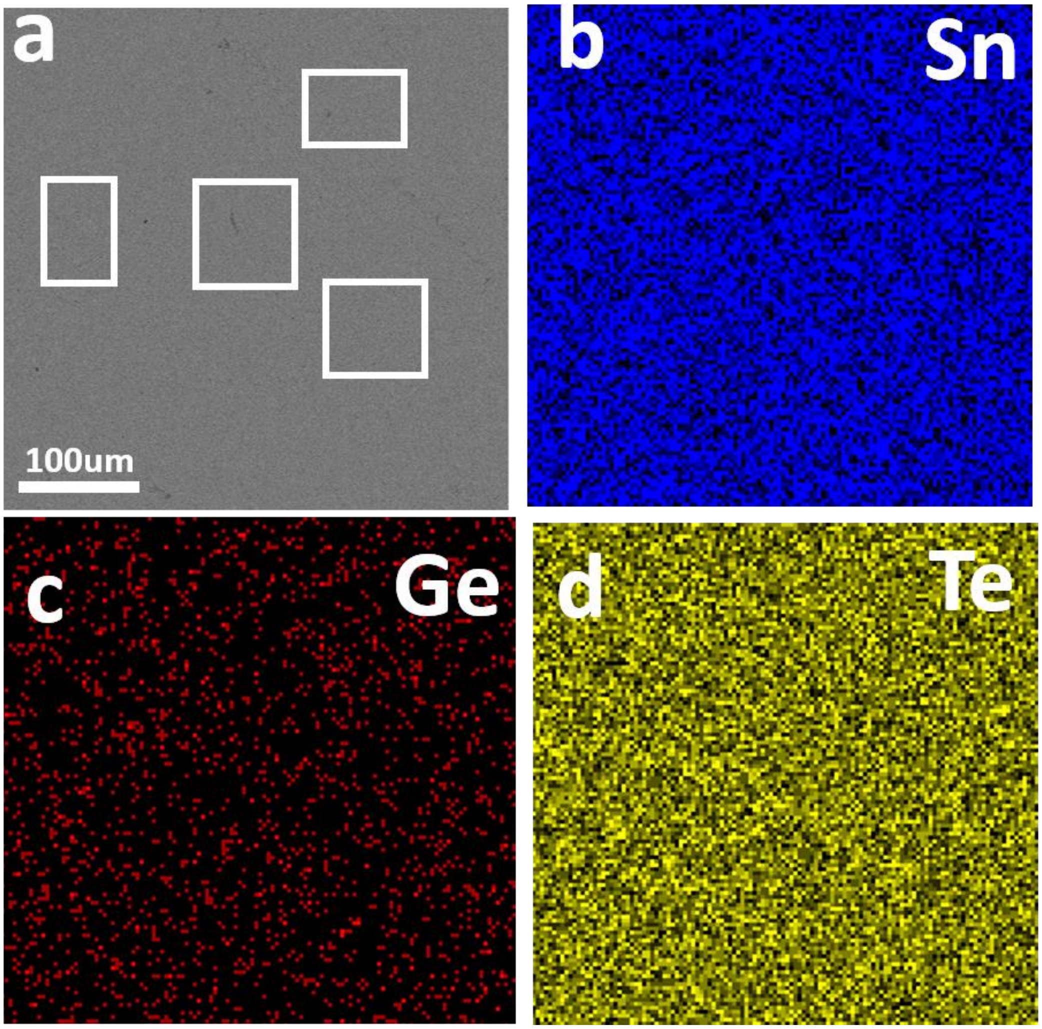

Fig 3.S5: (a) Back-scattered electron image; and (b-d) elemental mappings of Te, Sn and Ge of $Sn_{0.9}Ge_{0.1}Te$. Composition of the selected areas in (a) 46.3(3) of Sn, 5.0(6) of Ge, and 48.7(5) at.% of Te.

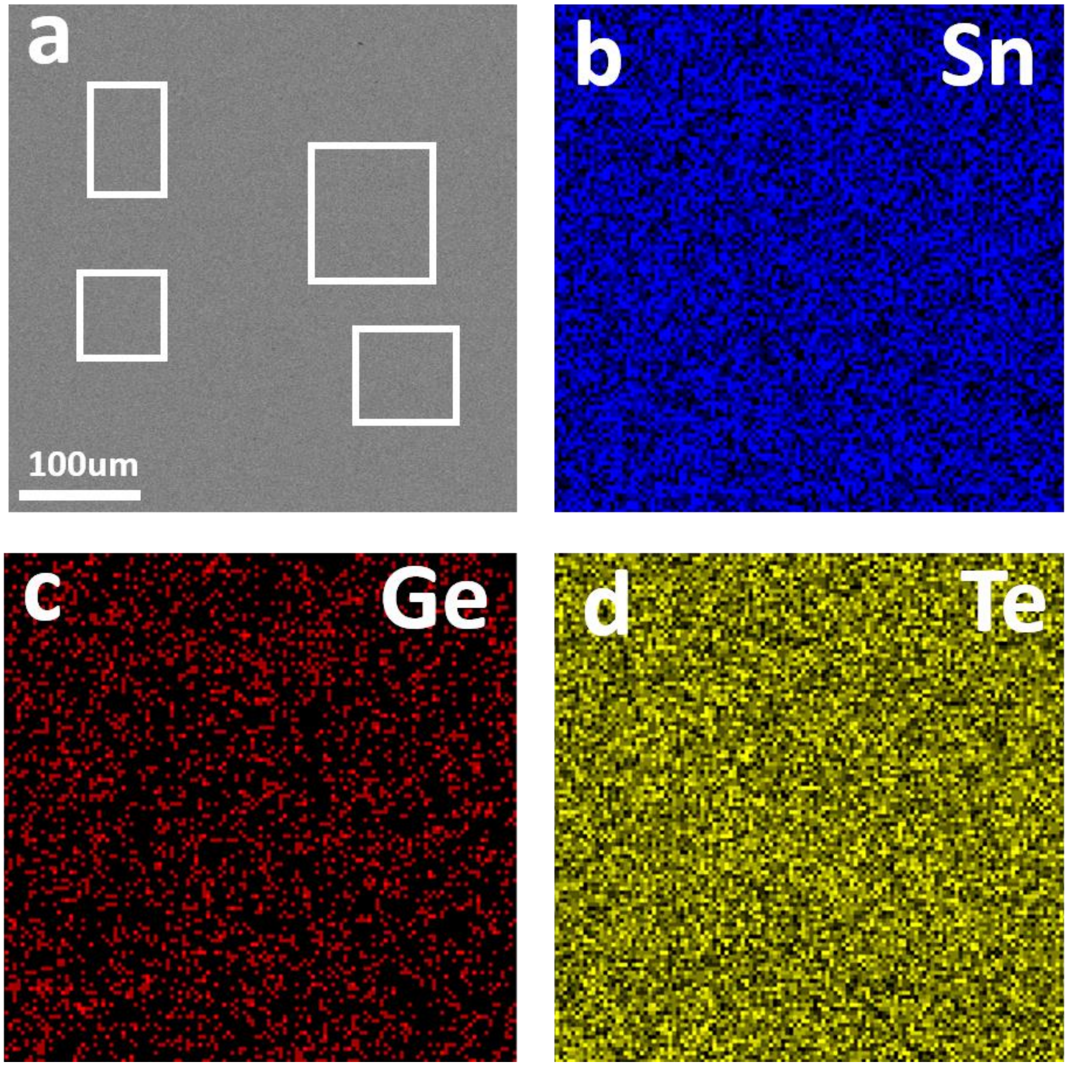

Fig 3.S6: (a) Back-scattered electron image; and (b-d) elemental mappings of Te, Sn and Ge of $Sn_{0.7}Ge_{0.3}Te$. Composition of the selected areas in (a) 37.2(1) of Sn, 14.2(4) of Ge, and 48.6(2) at.% of Te.

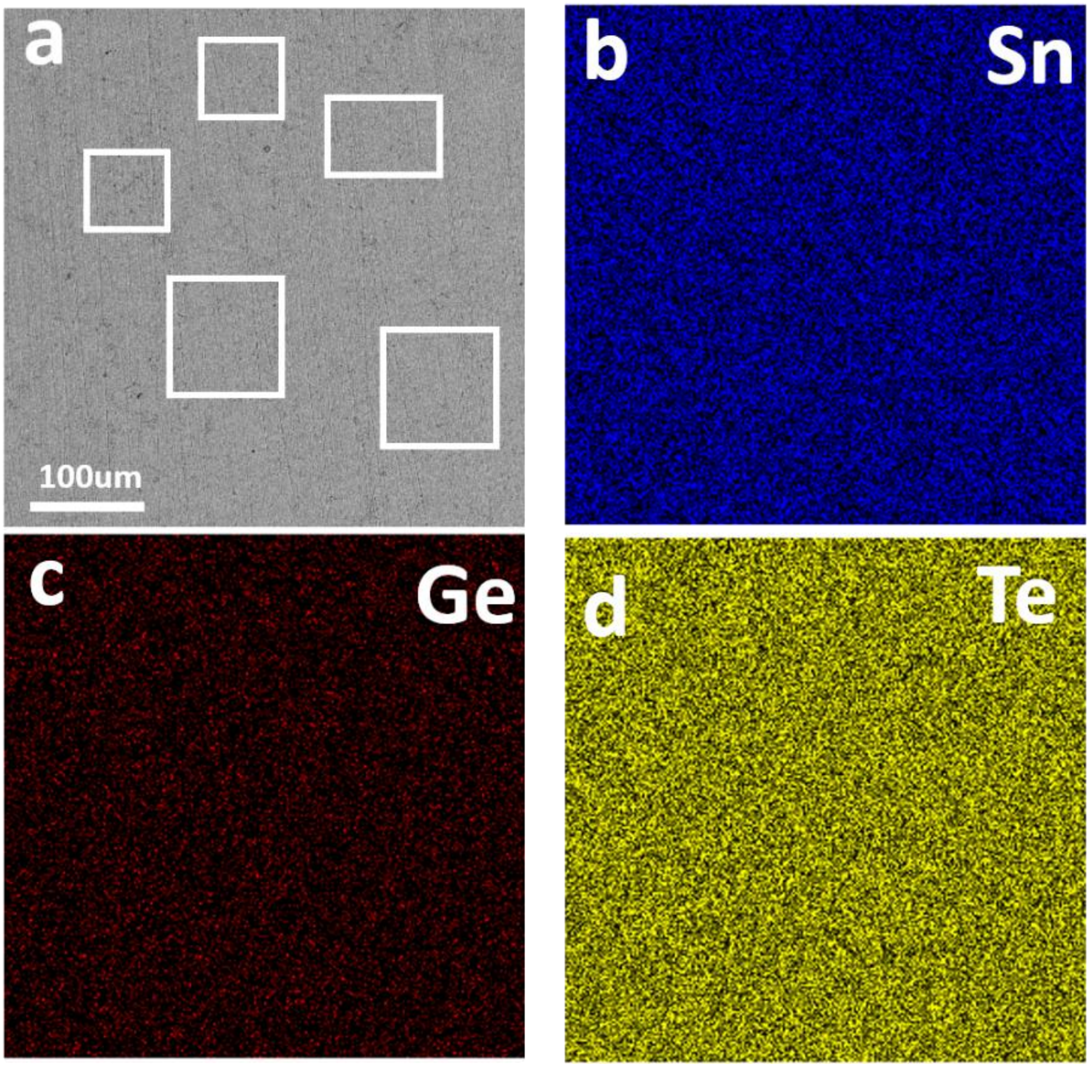

Fig 3.S7: (a) Back-scattered electron image; and (b-d) elemental mappings of Te, Sn and Ge of $Sn_{0.9}Ge_{0.1}Te$. Composition of the selected areas in (a) 25.9(1) of Sn, 25.1(2) of Ge, and 49.0(2) at.% of Te.

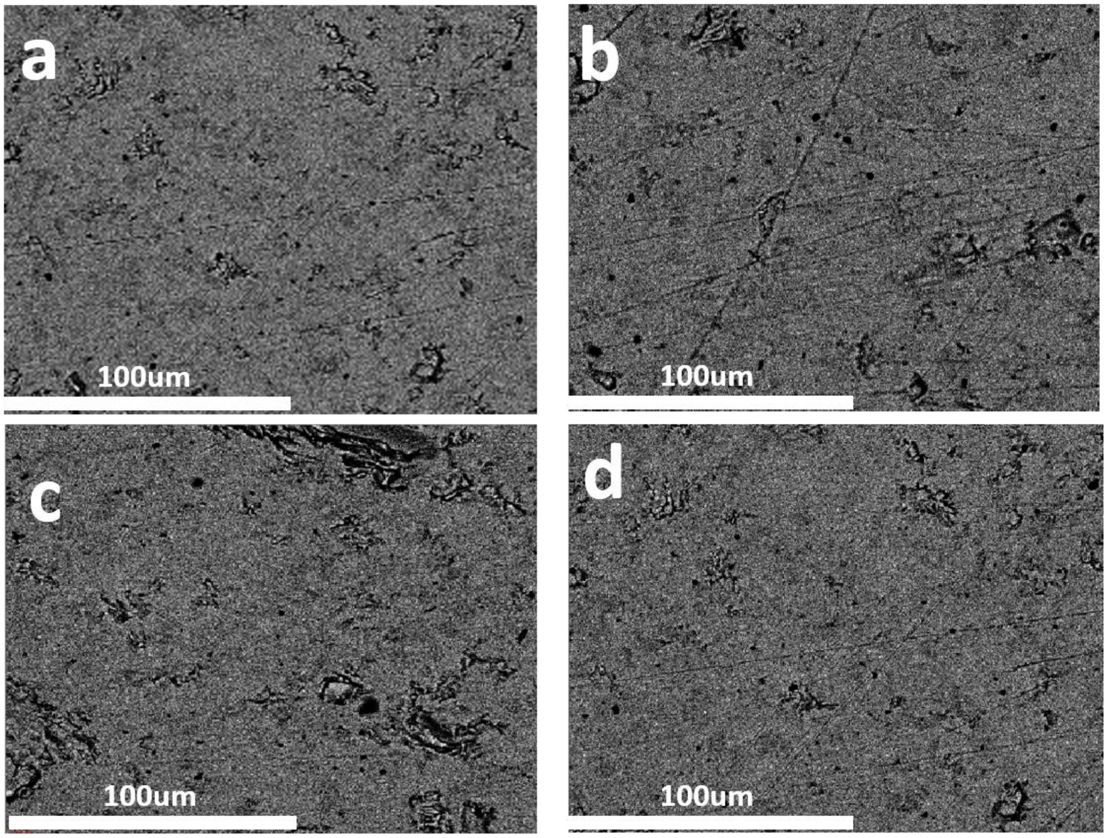

Fig 3.S8: Schematic diagram of $(Sn_{0.5}Ge_{0.5})_{0.97}Sb_{0.02}Te$ SEM-EDS result. (a-d) Composition analysis of these area, gave Sn, Ge, Te and Sb with 24.7(5), 23.7(9), 50.2(1) and 1.4(3) Atomic% respectively.

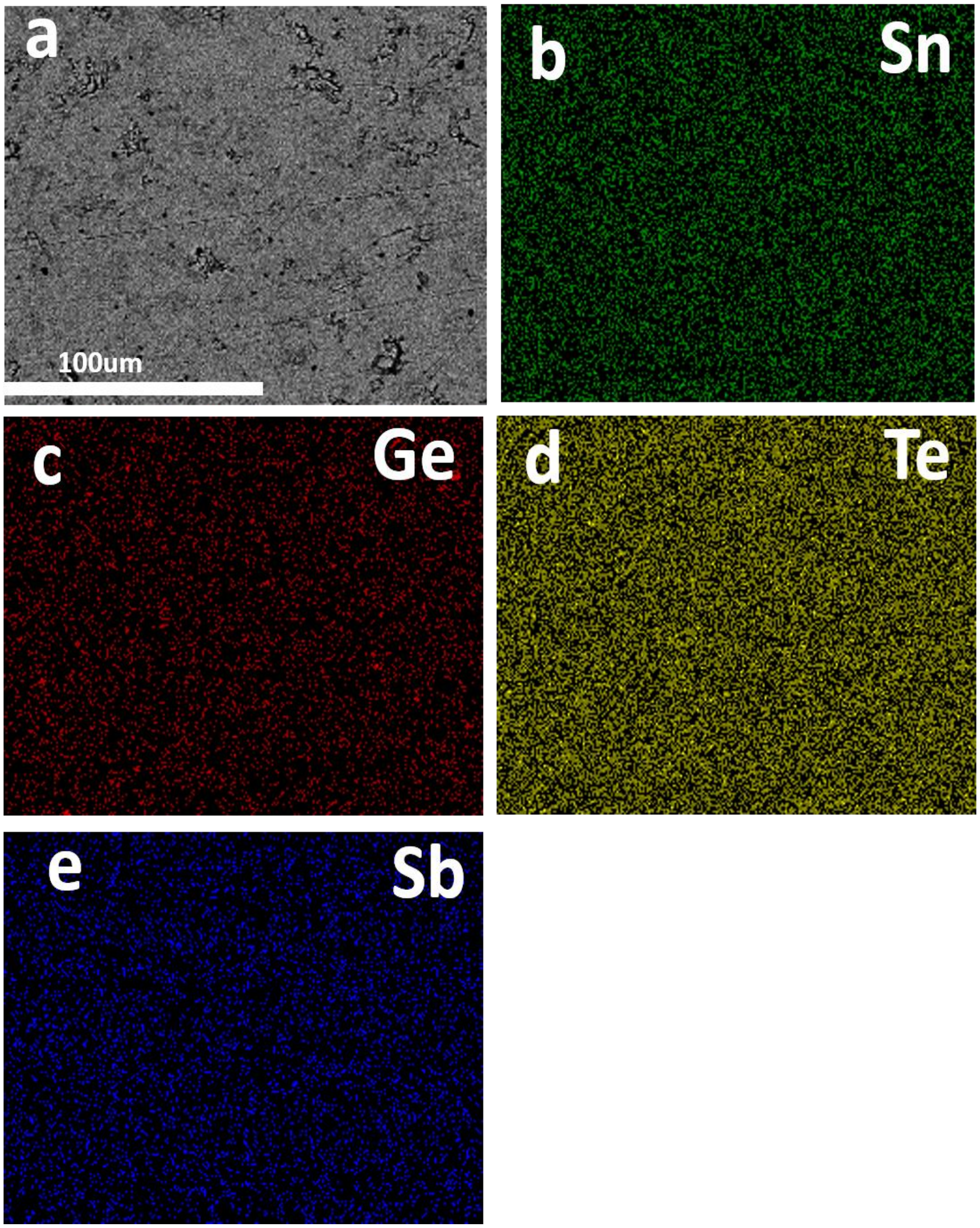

Fig 3.S9: (a)Back-scattered electron image; and (b-e) elemental mappings of Sn, Ge, Te and Sb of $(Sn_{0.5}Ge_{0.5})_{0.97}Sb_{0.02}Te$.

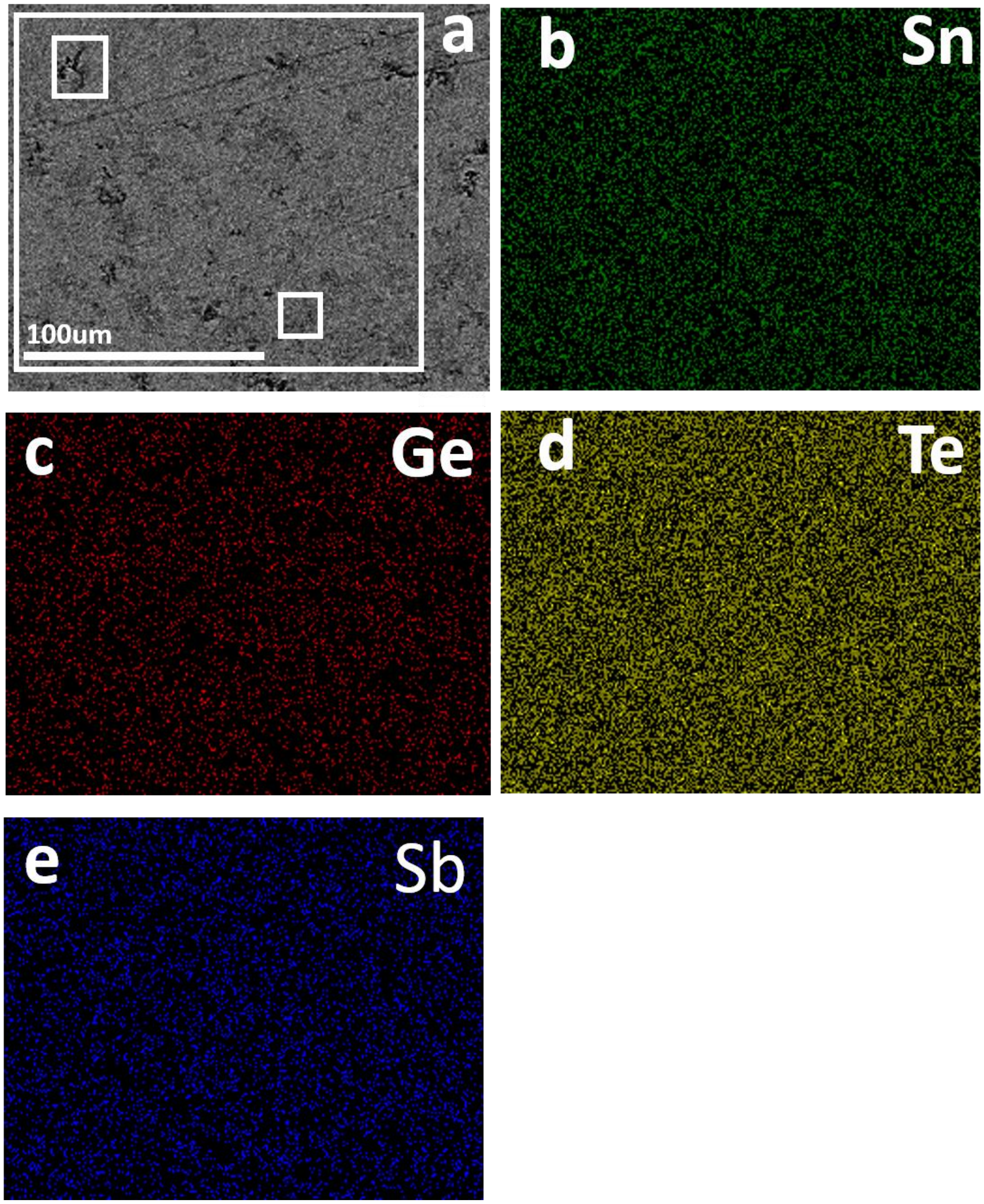

Fig 3.S10: (a) Back-scattered electron image; and (b-e) elemental mappings of Sn, Ge, Te and Sb of $(Sn_{0.5}Ge_{0.5})_{0.91}Sb_{0.06}Te$. EDS analysis of the selected areas in (a) yielded Sn, Ge, Te and Sb with 23.2(9), 22.9(6), 50.7(7) and 3.2(3) at. %, respectively.

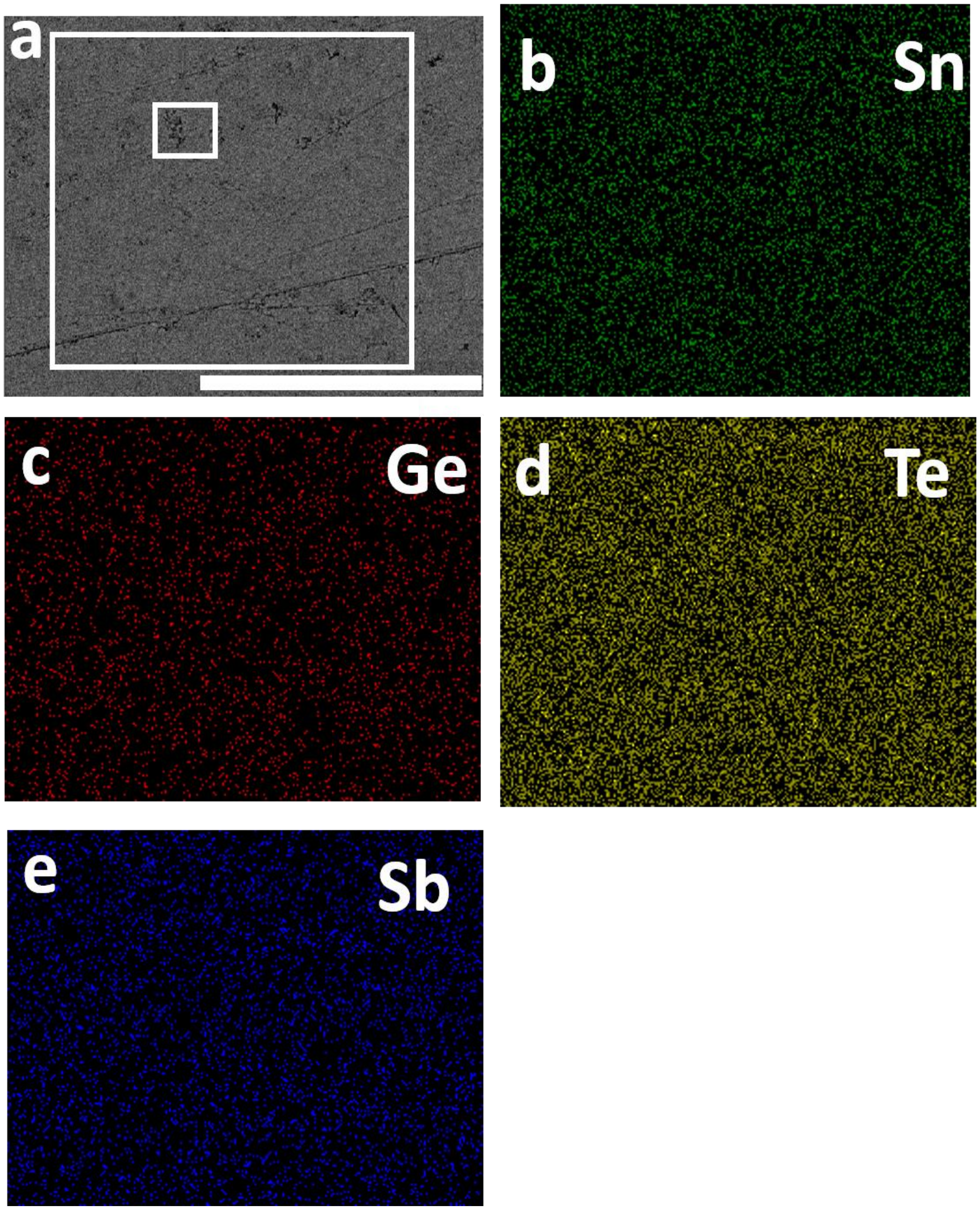

Fig 3.S11:(a) Back-scattered electron image; and (b-e) elemental mappings of Sn, Ge, Te and Sb of $(Sn_{0.5}Ge_{0.5})_{0.85}Sb_{0.1}Te$. EDS analysis of the selected areas in (a) yielded Sn, Ge, Te and Sb with 23.3(1), 21.0(1), 50.1(1) and 5.6(1) at. %, respectively.

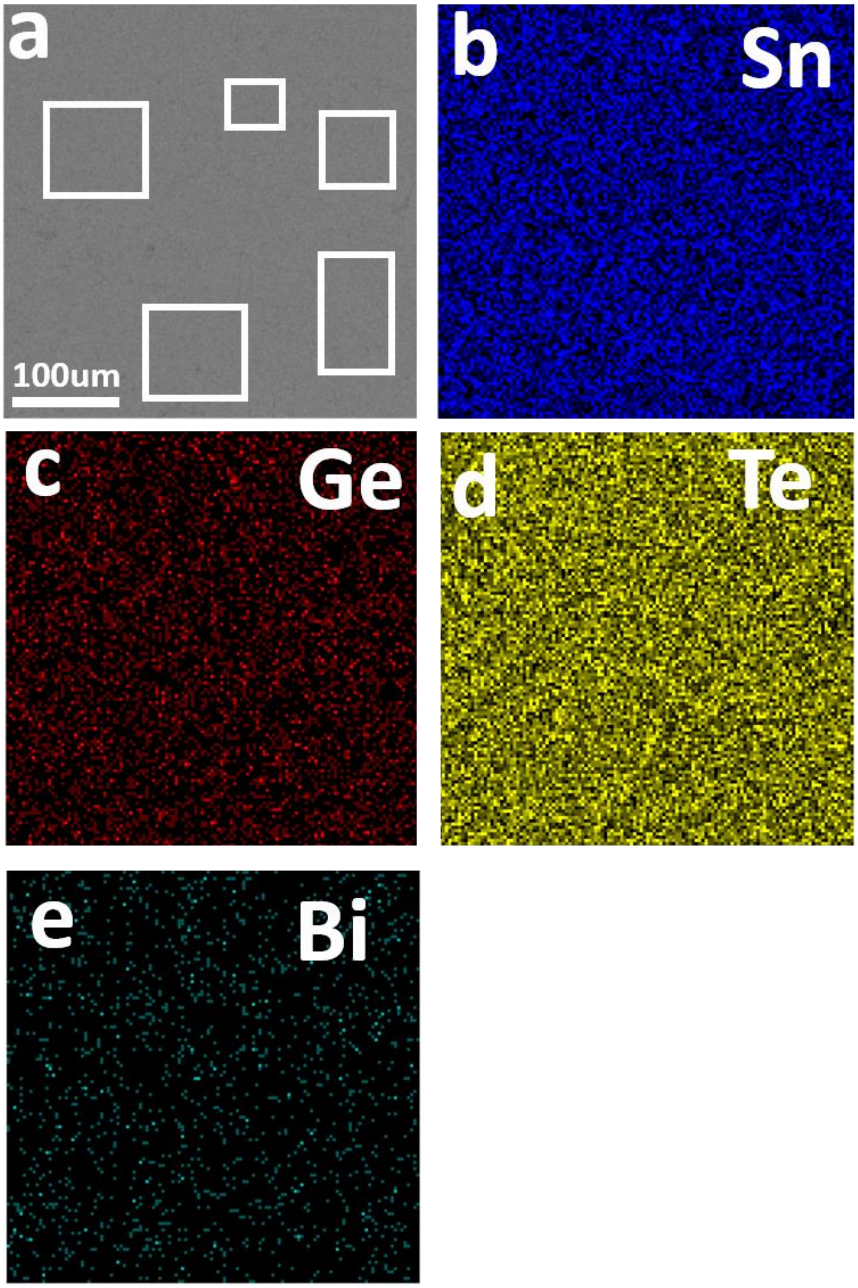

Fig 3.S12:(a) Back-scattered electron image; and (b-e) elemental mappings of Sn, Ge, Te and Bi of $(Sn_{0.5}Ge_{0.5})_{0.97}Bi_{0.02}Te$. EDS analysis of the selected areas in (a) yielded Sn, Ge, Te and Bi with 25.2(1), 24.6(4), 49.1(3) and 1.1(2) at. %, respectively.

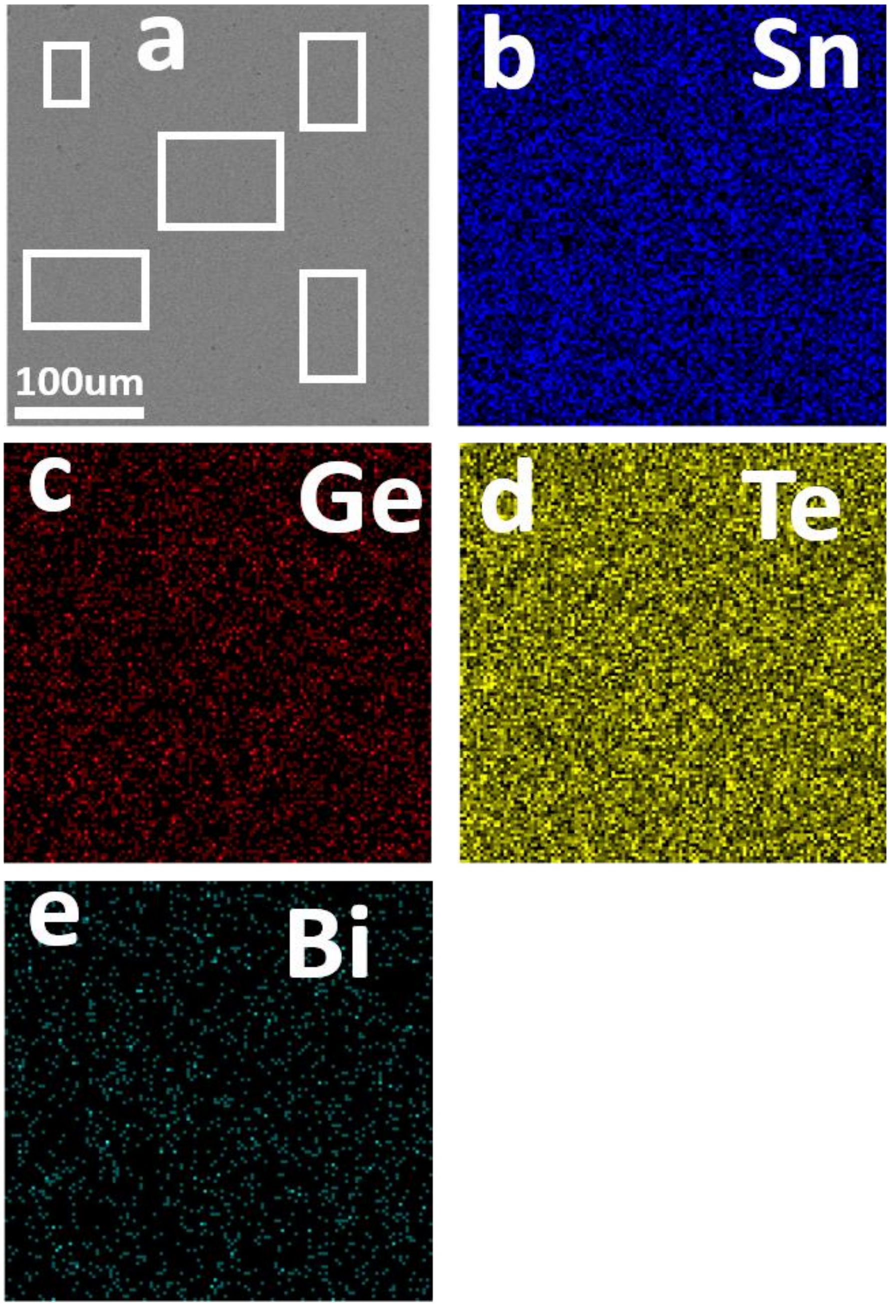

Fig 3.S13:(a) Back-scattered electron image; and (b-e) elemental mappings of Sn, Ge, Te and Bi of $(Sn_{0.5}Ge_{0.5})_{0.91}Bi_{0.06}Te$. EDS analysis of the selected areas in (a) yielded Sn, Ge, Te and Bi with 24.3(3), 23.3(3), 49.3(4) and 3.1(2) at. %, respectively.

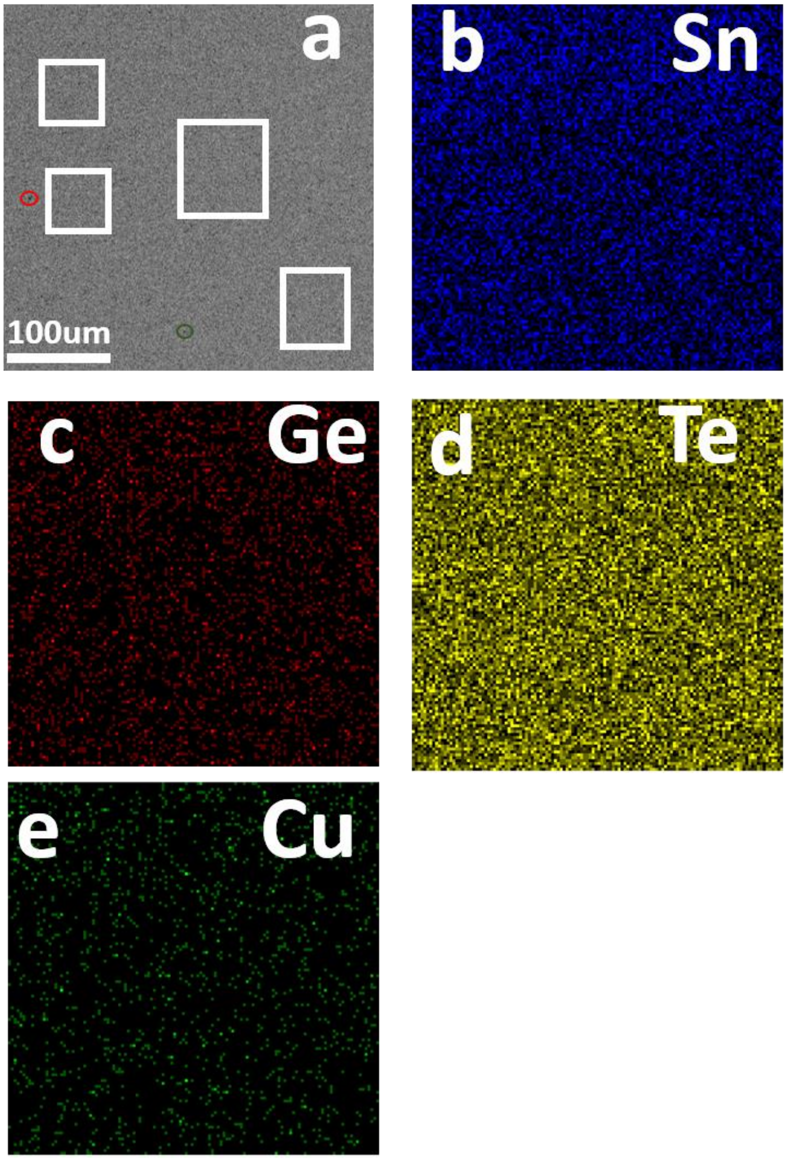

Fig 3.S14:(a) Back-scattered electron image, $Cu_{1.8}Te$ as a secondary phase that gray spots in green circle, Ge as a tertiary phase that black spots in red circle; and (b-e) elemental mappings of Sn, Ge, Te and Cu of $Sn_{0.5}Ge_{0.5}Te(Cu_2Te)_{0.03}$. EDS analysis of the selected areas in (a) yielded Sn, Ge, Te and Cu with 24.9(6), 23.9(3), 48.3(4) and 2.9(3) at. %, respectively.

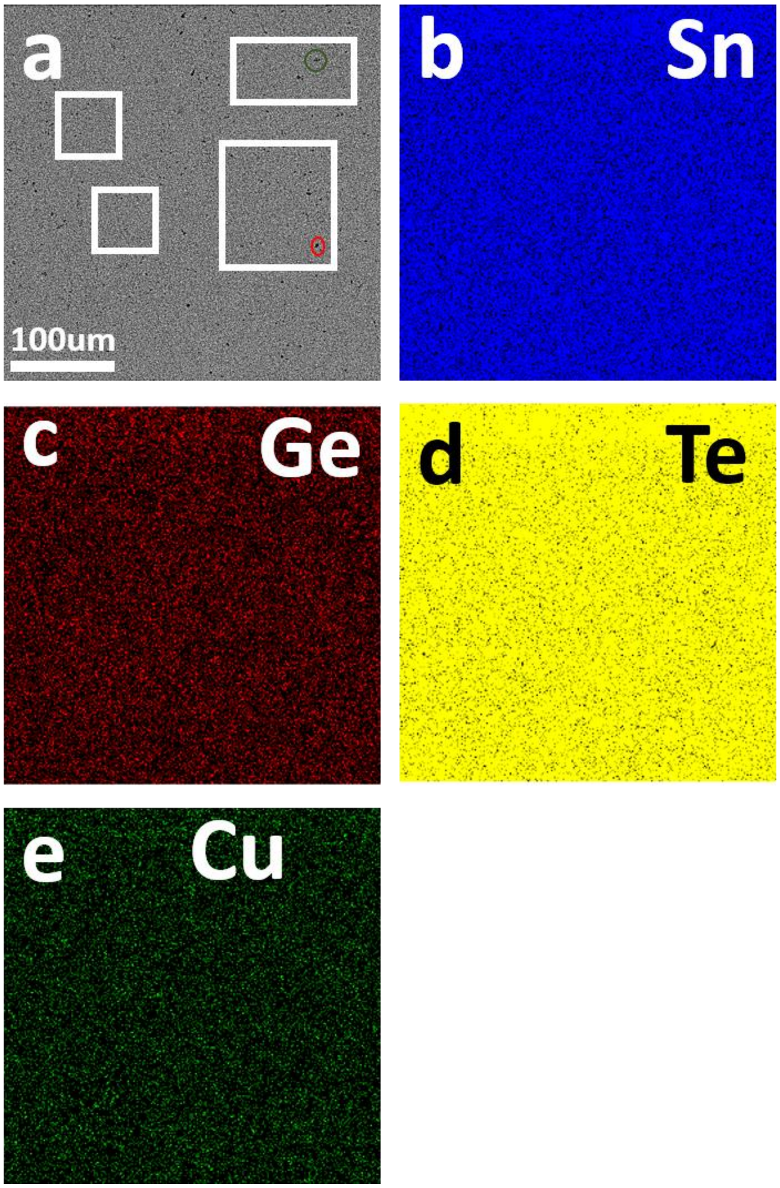

Fig 3.S15:(a) Back-scattered electron image, $Cu_{1.8}Te$ as a secondary phase that gray spots in green circle, Ge as a tertiary phase that black spots in red circle; and (b-e) elemental mappings of Sn, Ge, Te and Cu of $Sn_{0.5}Ge_{0.5}Te(Cu_2Te)_{0.05}$. EDS analysis of the selected areas in (a) yielded Sn, Ge, Te and Cu with 24.2(3), 23.4(4), 47.6(2) and 4.8(1) at. %, respectively.

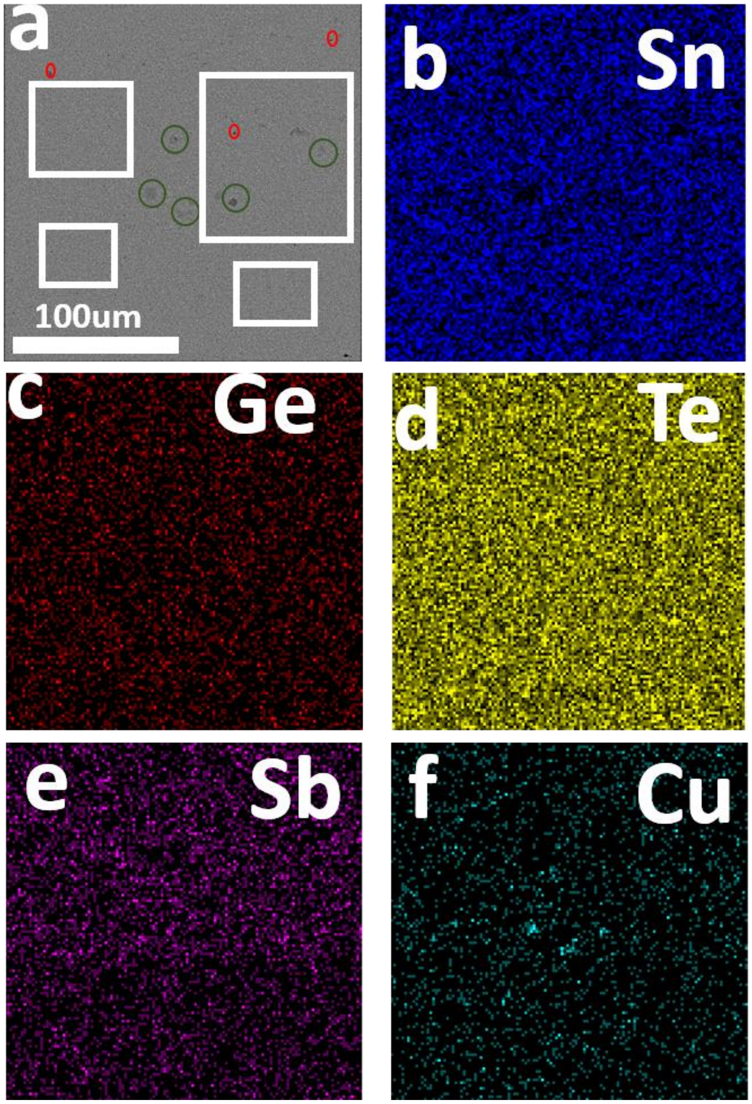

Fig 3.S16: (a) Back-scattered electron image, $Cu_{1.8}Te$ as a secondary phase that gray spots in green circle, Ge as a tertiary phase that black spots in red circle; (b-f) elemental mappings of Sn, Ge, Te, Sb and Cu of $(Sn_{0.5}Ge_{0.5})_{0.91}Sb_{0.06}Te(Cu_2Te)_{0.05}$. EDS analysis of the selected area in (a) yielded Sn, Ge, Te, Sb and Cu with 22.1(5), 21.4(5), 49.3(5), 2.8(4) and 4.4(8) at. %, respectively.

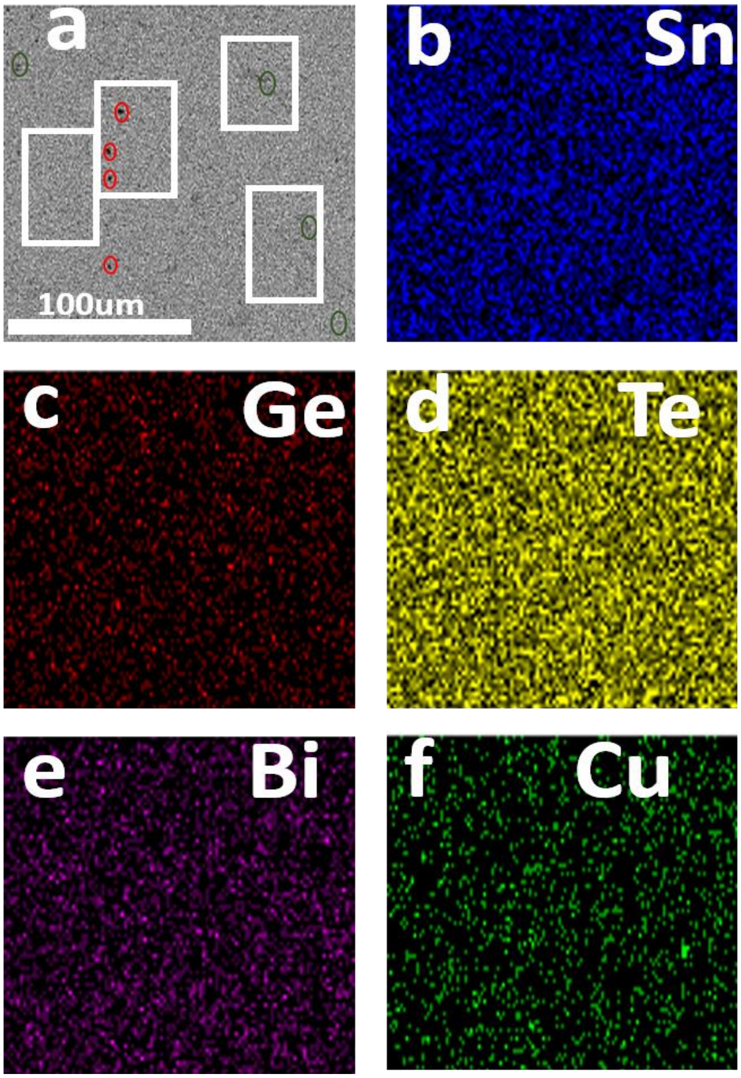

Fig 3.S17: (a) Back-scattered electron image, $Cu_{1.8}Te$ as a secondary phase that gray spots in green circle, Ge as a tertiary phase that black spots in red circle; (b-f) elemental mappings of Sn, Ge, Te, Bi and Cu of $(Sn_{0.5}Ge_{0.5})_{0.91}Bi_{0.06}Te(Cu_2Te)_{0.05}$. EDS analysis of the selected area in (a) yielded Sn, Ge, Te, Bi and Cu with 22.6(6), 21.2(2), 49.0(3), 2.9(3) and 4.3(6) at. %, respectively.

Chapter 4. Enhancing Thermoelectric Performance of $Sn_{0.5}Ge_{0.5}Te$ via Doping with In/Zn, In/Sb and In/Bi.

This chapter encompasses the manuscript "Enhancing Thermoelectric Performance of $Sn_{0.5}Ge_{0.5}Te$ via Doping with In/Zn, In/Sb and In/Bi", which was published in *Journal of Solid State Chemistry* (*Journal of Solid State Chemistry* **2021**, *302*, 122444). Mr. Zan Yang collected electronic structure calculations, and partial sample preparations were performed by Mr. Yuyang Huang at the laboratory of Dr. Yurij Mozharivskyj, Department of Chemistry and Chemical Biology, McMaster University, Hamilton, ON. Mr. Suneesh Meledath Valiyaveettil collected the thermal diffusivities, specific heat capacity, and density of materials at the Department of Physics, National Central University, Taoyuan City 32001, Taiwan. The candidate completed the experimental procedures, sample characterization, electrical properties measurements, data interpretation, and manuscript preparation.

Reproduced with permission from **Song, S**.; Yang, Z.; Huang, Y.; Tseng, Y.-C.; Valiyaveettil, S. M.; Chen, K.-H.; Mozharivskyj, *Journal of Solid State Chemistry.* **2021**, *302*, 122444. Copyright by 2021 Elsevier

This work provides a comparative study of the thermoelectric properties for the $Sn_{0.5}Ge_{0.5}Te$ phases doped with In, and subsequently with Zn, Sb and Bi. The In doping on the Sn/Ge site induces resonant levels around the Fermi level, and thus, enhances the thermopower. Further doping with Sb and Bi in $(Sn_{0.5}Ge_{0.5})_{0.98}In_{0.2}Te$ leads to the valence band convergence (thus increasing the thermopower) and optimizes the thermal conductivity. Comparison of the results for $(Sn_{0.5}Ge_{0.5})_{0.89}In_{0.02}Bi_{0.06}Te$ and pristine SnTe reveal significant improvements in the average and highest ZT values by 446% (0.71 vs. 0.13) and 125% (0.80 vs. 0.36), respectively, within 100-500 ˚C.

4.1 Introduction

Today, fossil fuels still play a dominant role as an energy source in numerous industries, which expel massive amounts of waste heat into the environment. Thermoelectric technology can convert this waste heat into useful electricity, thus reducing the environmental impact of burning fossil fuels and increasing the efficiency of various processes. Efficiency of thermoelectric materials, which are at the heart of thermoelectric technology, is represented by the figure of merit, ZT: $ZT = \frac{\alpha^2\sigma}{\kappa_C+\kappa_l}T$, where α, σ, κ_C, κ_l and T are Seebeck coefficient, electrical conductivity, carrier thermal conductivity, lattice conductivity, and absolute temperature respectively.[219] The ideal thermoelectric material is expected to have a high metal-like electrical conductivity, a low, glass-like thermal conductivity, and a large Seebeck coefficient.[39] However, it is challenging to find a single, simple material that satisfies all the above-mentioned properties since parameters α, σ, κ_C are interrelated. For example, α is inversely proportional to n, but σ is directly proportional to n. Also, κ_C and σ are linearly related via the Wiedemann-Franz law: $\kappa_C = L\sigma T$.[39]

In the last decade, thermoelectric research focused on decoupling these interdependent parameters and improving the figure of merit. Efforts have been made to improve the power factor ($\alpha^2\sigma$)[177,201,220,221] and optimize the lattice thermal conductivity.[36,84,141,209,222,223] Lead tellurides have been developed as high-performance thermoelectric materials at mid temperatures (400-900K). However, their industrial applications are becoming restricted due to the Pb toxicity. Instead, other tellurides, such as SnTe and GeTe, with similar crystal structures are explored as potential replacements for lead telluride (PbTe). However, pristine SnTe has a much higher lattice thermal conductivity and a much lower Seebeck coefficient.[80,141,201]To optimize the SnTe properties, band structure engineering[75,76,184,224–227] and nano-structuring[183,228–230] are employed. Still, the TE performance of the SnTe-based materials falls below that of the PbTe-based materials.[83,230–232]

Germanium telluride (GeTe) is another potential candidate. But similarly to SnTe, the TE performance of GeTe is limited by its very high p-type carrier density (~10^{21}cm^{-3}) and lattice thermal conductivity.[37,84] Doping with In,[179] Sb,[199] and Bi[199,233] has been shown to suppress the hole concentration in GeTe. Also, the lattice thermal conductivity of GeTe could be effectively optimized by nano-structuring.[234–238] Since the high cost of germanium cannot be ignored in real industry applications, many research groups are exploring $Sn_{(1-x)}Ge_xTe$ alloys.[201,209,223,239–241] In our previous work, we observed that $Sn_{0.5}Ge_{0.5}Te$ shows the largest power factor, *PF*, and lowest thermal conductivity among the $Sn_{1-x}Ge_xTe$

($x \leq 0.5$) phases from 100°C to 500°C.[223] In this work, we explore the $Sn_{0.5}Ge_{0.5}Te$-based thermoelectric materials further; we employ In doping to introduce resonant levels at the valence band edge, and the In/Sb and In/Bi co-doping to optimize the thermopower and thermal conductivity.

4.2 Experimental

4.2.1. Synthesis

Polycrystalline samples of $(Sn_{0.5}Ge_{0.5})_{1-1.5x}In_xTe$ (x = 0.02, 0.04), $(Sn_{0.5}Ge_{0.5})_{0.96}In_{0.02}Zn_{0.02}Te$, $(Sn_{0.5}Ge_{0.5})_{0.89}In_{0.02}Sb_{0.06}Te$, $(Sn_{0.5}Ge_{0.5})_{0.935}In_{0.02}Bi_{0.03}Te$ and $(Sn_{0.5}Ge_{0.5})_{0.89}In_{0.02}Bi_{0.06}Te$ were made by solid state synthesis of the elemental tin, germanium, tellurium, antimony, bismuth and indium (purity of all elements was 99.99 wt.% or better). The elements with the desired ratios were loaded into silica tubes, that were evacuated below 0.002 torr and flame sealed. The samples were heated to 1000 °C and kept at 1000 °C for 12 hours to achieve compositional homogeneity. The samples were quenched in the water-ice bath.

4.2.2. Spark Plasma Sintering (SPS)

For the SPS, finely grinded samples were loaded into a graphite die 15 mm in diameter. To avoid a direct contact between the sample and graphite plungers, a layer of graphite paper was placed in between. The samples were heated up to 600 °C at 100 °C/min under the 45 MPa pressure and kept at this temperature for 5 minutes. After that, the samples were cooled to room temperature.

4.2.3. X-ray Powder Diffraction

All samples were analyzed by X-ray powder diffraction (PXRD) on a PANalytical X'Pert Pro diffractometer with the CuKα_1 radiation and an X'Celerator detector. The samples were finely grinded using an agate mortar and pestle and deposited on zero-background silicon discs. The diffraction data were collected in the 2θ range of 20° to 140°. Rietveld refinement (Rietica program[154]) was used to determine the sample purity and lattice parameters. We have refined the profile parameters (background, peak shape), sample displacement, lattice parameters, and atomic displacement parameters.

4.2.4. Thermoelectric Measurements

Samples were cut into 3mm × 3mm × 10mm rectangular bars for the Seebeck coefficient and electrical conductivity measurements. Cutting was done with a low-speed diamond saw, and kerosene was used as a lubricant to prevent sample oxidation during cutting. Electrical conductivity and Seebeck coefficient were measured on a ULVAC-RIKO ZEM-3 instrument. The 10 mm × 10 mm × 1 mm plates were prepared for measurements of thermal conductivity, carrier concentration and Hall carrier mobility. Thermal diffusivity, D, was measured using the laser flash diffusivity method on a Netzsch LFA 457 instrument, and the total thermal conductivity was calculated by $\kappa_{total} = D \times C_p \times \rho$. For the temperature dependent specific heat capacity C_p measurements, the standard sample (pyrocrearm) was used as a reference. The density ρ of the samples was measured by the Archimedes method. The hole concentration was calculated based on the equation of $n_\mathrm{p} = \frac{1}{eR_H}$, where e is an electron charge and R_H is the Hall coefficient. The Hall coefficient was calculated from

$R_H = \frac{t \times V_H}{I \times B}$, where t is the thickness of the sample, I is the AC current fixed at 5 mA, B is the magnetic field swapped from -1.3 T to 1.3 T, V_H is the Hall voltage measured at room temperature. To eliminate measurement errors, a scatter graph was plotted based on the V_H as the y axis and B as the x axis, and the Hall coefficient was derived from with the linear fit. The Hall carrier mobility μ_H was calculated by $\mu_H = {R_H}/{\rho}$, where ρ is the sheet resistance measured by the Van der Pauw method.

4.2.5. Density Functional Theory (DFT) calculation

Band structure and density of state (DOS) calculations were performed with the density functional theory via the Quantum Espresso software.[171,172] Projector-augmented wave (PAW) technique was chosen to model the electron-ion interaction for the Ge, In, Sb, Bi and Te atoms.[173] The exchange-correlation energy was chosen in the form of the Perdew-Burke-Ernzerhof (PBE) approximation and the cutoff energy for the wave functions was set to 50 Ry.[174] Calculations were performed on the 3 × 3 ×3 rhombohedral supercells containing 27 Ge and 27 Te sites and the 2 × 2 ×2 cubic phase supercell containing 16 Ge, 16 Sn and 32 Te sites. Since the dominant defects in the phases studied are Ge vacancies, only the Ge substitution was considered. 2 Ge sites were randomly chosen to be replaced by Bi, In or Sb. Both cell parameters and atomic positions were fully relaxed until the force on each atom was less than 0.001 eV/Å.

4.2.6. Scanning Electron Microscopy-Energy Dispersive X-ray Spectroscopy (SEM-EDS)

The samples were polished with 800 and 1200 grit sand papers and attached to the SEM sample holders using a double-sided carbon tape. The SEM images and EDS data were collected on a TESCAN VEGA II LSU scanning electron microscope (20 kV accelerating voltage) equipped with an X-MAX (80 mm^2) X-ray EDS spectrometer (Oxford Instruments). Pure nickel metal was used as a calibration standard during the EDS analysis.

4.3 Results and Discussion

4.3.1 In-doped $Sn_{0.5}Ge_{0.5}Te$

Resonant levels around the Fermi level can increase the DOS effective mass, and thus improve the thermopower and performance of thermoelectric materials.[177,179,242–244] In-doping has been shown to introduce resonant levels at the top of the valence band in SnTe[177] and GeTe,[179] and the same phenomenon can be expected in the $Sn_{0.5}Ge_{0.5}Te$ system. The In doping of $Sn_{0.5}Ge_{0.5}Te$ was done according to the $(Sn_{0.5}Ge_{0.5})_{1-x}In_xTe$ formula, i.e. an equimolar substitution was pursued. This substitution does not follow the charge balance expected from the 3+ oxidation state of indium. However, previous experimental studies on the In-containing SnTe system indicate that In acts as an electron donor at low levels but becomes an electron acceptor at higher concentrations.[177] It has been suggested that first In fills in the Sn vacancies and provides extra electrons to the valence band (the resulting hole concentration is lower), but upon further doping, it substitutes for Sn and reduces the Fermi level in the valence band (the hole concentration becomes larger).[245,246] Such reduction is possible if the *s* electrons of In act as core ones and only one *p* electron (instead of 2 from Sn) is donated to the valence band. In the light of this uncertainty, we have decided to pursue equimolar substitution with In.

SEM-EDS images (Figures 4.S10-4.S12) show a homogenous distribution of elements in the $Sn_{0.5}Ge_{0.5}Te$, $(Sn_{0.5}Ge_{0.5})_{0.98}In_{0.02}Te$ and $(Sn_{0.5}Ge_{0.5})_{0.96}In_{0.04}Te$ samples. Based on the room temperature X-ray powder diffraction patterns (Figure 4.1 (a)), $(Sn_{0.5}Ge_{0.5})_{0.98}In_{0.02}Te$ adopts a rhombohedral symmetry as indicated by peak splitting ($R3m$), while a cubic symmetry ($Fm\bar{3}m$) is observed for $(Sn_{0.5}Ge_{0.5})_{0.96}In_{0.04}Te$. More crystallographic data are provided in the Supporting Information. It must be stated that while the macroscopic symmetry in $(Sn_{0.5}Ge_{0.5})_{0.96}In_{0.04}Te$ is cubic, the local atomic environment may be still distorted as in the rhombohedral structure. The indication for this comes from the lattice thermal conductivity that has an uptake above 450 ^{o}C, which is associated with the rhombohedral to cubic transition (see below).[247]

Electrical conductivity, Seebeck coefficient and power factor of the In-doped samples in comparison to $Sn_{0.5}Ge_{0.5}Te$ are shown in Figure 4.1 (b-d). From 100 to 500 ˚C, the electrical conductivity of all samples decreases with temperature, indicating a typical degenerate semiconductor behavior. Upon In doping, the electrical conductivity is reduced pronouncedly, while the Seebeck coefficient is improved throughout the whole temperature range. The power factor of the In-doped samples is higher at lower temperatures but drops below that of $Sn_{0.5}Ge_{0.5}Te$ at higher temperatures (Figure 4.1 (d)). To understand how the charge transport properties are affected by the In doping, we measured the Hall effect at room temperature. Using the Hall carrier concertation and Seebeck coefficient, the Density of States (DOS) effective mass was derived by assuming the single parabolic band (SPB) model.[67] Using the relationship $m_d^* = N_v^{2/3} m_b^*$ between the DOS (m_d^*) and conductivity (m_b^*) effective masses and the expression for the carrier mobility $\mu = e\tau/m_b^*$,[25,248] we can draw some conclusions. As judged from the data in Table 4.1, an increase in the effective mass does not scale up with a drop in the mobility between $(Sn_{0.5}Ge_{0.5})_{0.98}In_{0.02}Te$ and $Sn_{0.5}Ge_{0.5}Te$, both of which adopt the rhombohedral structure. Thus, there must be a decrease in the relaxation time, τ, due to the increased point defect scattering in $(Sn_{0.5}Ge_{0.5})_{0.98}In_{0.02}$. A further decrease in the carrier mobility of $(Sn_{0.5}Ge_{0.5})_{0.96}In_{0.04}Te$ is more challenging to rationalize, as $(Sn_{0.5}Ge_{0.5})_{0.96}In_{0.04}Te$ adopts a cubic structure, and a direct comparison of its DOS effective mass to those of $(Sn_{0.5}Ge_{0.5})_{0.98}In_{0.02}$ and $Sn_{0.5}Ge_{0.5}Te$ is not suitable. Additionally, the lower carrier mobility of $(Sn_{0.5}Ge_{0.5})_{0.96}In_{0.04}Te$ can be in part related to the more pronounced impurity scattering[249] due to the larger In substitution. Also, a larger amount of Ge precipitates in $(Sn_{0.5}Ge_{0.5})_{0.96}In_{0.04}Te$ (2.3(1) mol. % vs 0.94(9) mol. % in $Sn_{0.5}Ge_{0.5}Te$) may play some role, although their impact on the carrier scattering is likely to be smaller in comparison to other effects.

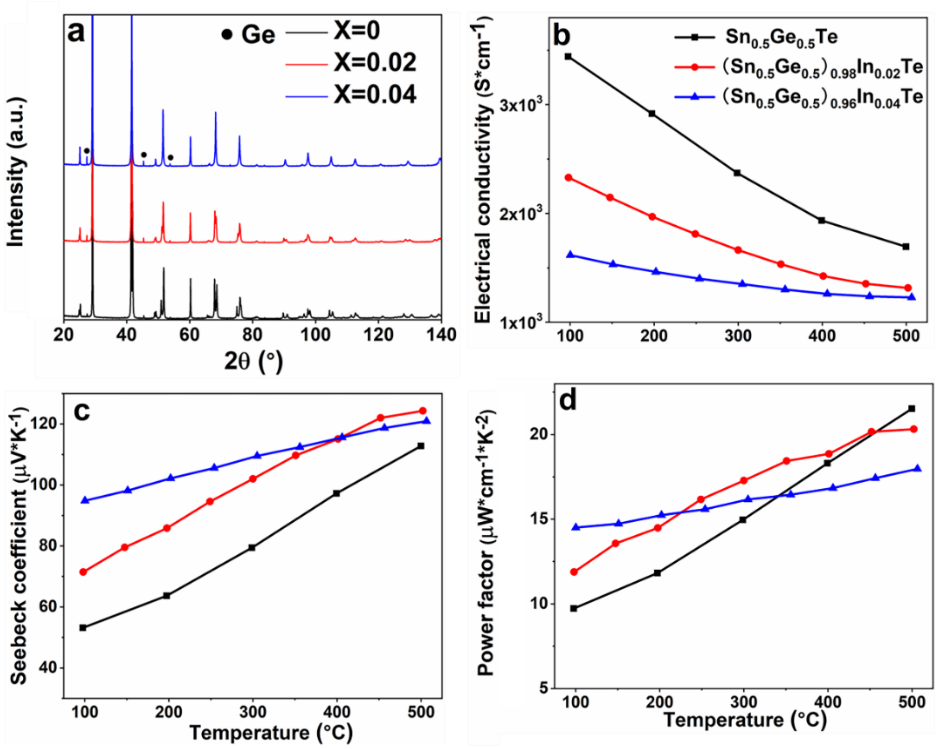

Figure 4.1 (a) Powder X-ray diffraction patterns of $(Sn_{0.5}Ge_{0.5})_{1-x}In_xTe$ at room temperature. (b) Electrical conductivity, (c) Seebeck coefficient and (d) power factor of $((Sn_{0.5}Ge_{0.5})_{1-x}In_xTe$.

Table 4.1 Hall concentration, Hall mobility, carrier concentration, carrier mobility and DOS effective mass of $Sn_{0.5}Ge_{0.5}Te$, $(Sn_{0.5}Ge_{0.5})_{0.98}In_{0.02}Te$ and $(Sn_{0.5}Ge_{0.5})_{0.96}In_{0.04}Te$ at room temperature.

Composition	Carrier concentration (10^{21} cm^{-3})	Carrier mobility ($cm^2V^{-1}s^{-1}$)	m^*/m_0
$Sn_{0.5}Ge_{0.5}Te$	1.75(4)	11.2(3)	3.00
$(Sn_{0.5}Ge_{0.5})_{0.98}In_{0.02}Te$	1.57(5)	6.0(2)	4.21
$(Sn_{0.5}Ge_{0.5})_{0.96}In_{0.04}Te$	1.80(9)	4.2(2)	6.26

An increase in the DOS effective mass is relatively large and this is discussed in more details. DOS m^* is 3.00 m_0 for $Sn_{0.5}Ge_{0.5}Te$, 4.21 m_0 for $(Sn_{0.5}Ge_{0.5})_{0.98}In_{0.02}Te$ and 6.26 m_0 for $(Sn_{0.5}Ge_{0.5})_{0.96}In_{0.04}Te$. Such heavier holes can be attributed to the In resonant levels around the Fermi level as revealed by the calculations provided below. Such conclusions would be in line with other published data.[177,179] It also has to be noted that $(Sn_{0.5}Ge_{0.5})_{0.96}In_{0.04}Te$ is cubic (the other two phases are rhombohedral) and its larger DOS m^* maybe also in part due to the increased band degeneracy and band convergence,[199,248] i.e. multiple bands, some with heavier carriers, may contribute to the charge transport properties. But this assumption will have to be verified through detailed electronic structure calculations.

In order to understand the effects of the In doping on the transport properties, electronic structure of the rhombohedral $Sn_{14}Ge_{13}Te_{27}$ and $Sn_{13}Ge_{13}InTe_{27}$ were calculated by the density-functional theory (DFT). The band structure with and without spin-orbit coupling

(SOC) for $Sn_{14}Ge_{13}Te_{27}$ are shown in Figure 4.2 (a). The SOC, produced by the coupling between the orbital and spin angular momenta,[250] is significant in the $Sn_{14}Ge_{13}Te_{27}$ phase. Due to the strong SOC effects, we will analyze only the results obtained with the SOC calculations. Figure 4.2 (b) shows the projected DOS of $Sn_{14}Ge_{13}Te_{27}$; the Te 5*p* orbitals have the dominant contribution to the valence band and the Sn 5*p* and Ge 4*p* are dominant in the conduction band.

The band structure and projected DOS of $Sn_{13}Ge_{13}InTe_{27}$ for Ge, Sn, In and Te are shown in Figures 4.2 (c) and (d), respectively. The calculations yielded the Fermi level ca. 0.2eV deep into the valence band. For comparison purposes and to remove effects of the In concentration on the Fermi energy, we placed the Fermi level at the top of valence band. The principal valence band maximum (VBM) occurs at L+ δ along the L→P direction. The changes in the electronic structure of $Sn_{13}Ge_{13}InTe_{27}$ in comparison to that of $Sn_{14}Ge_{13}Te_{27}$ can be attributed to the In-related levels around the Fermi level.[177] This is further explored by analyzing the Ge 3*d*, 4*s*, 4*p*, In, Sn, Te 4*d*, 5*s* and 5*p* orbital contributions to the DOS in Figure 4.3. It is interesting to note that In orbitals contribute significantly to the states around the Fermi level, despite that fact that In is only 1 out of 27 cations in the structure (ca. 3.7 at. %). Additionally, most of the In states originate from the *s* orbitals and they are located below the Fermi level. This supports the statement made earlier that In acts as a *p*-dopant (due to its +1 oxidation state) when introduced on the Sn/Ge site. The Ge 4*p*, Sn and Te *5p* orbitals contribute significantly to the new DOS features around the Fermi level. Therefore, the resonant states, while triggered by the In presence, really stem from the *s-p* and *p-p* orbital mixing involving all the atoms.

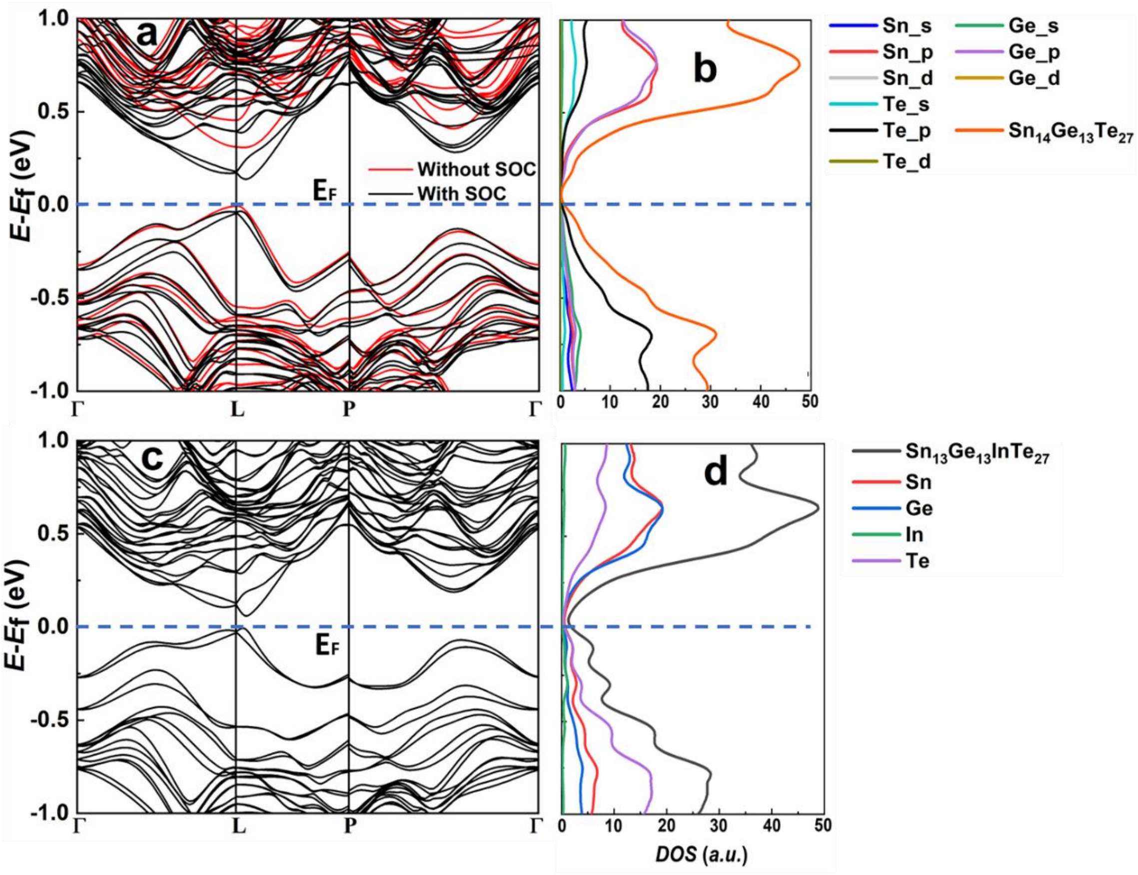

Figure 4.2 (a) Band structure of the rhombohedral $Sn_{14}Ge_{13}Te_{27}$ calculated without and with SOC; (b) The density of state (DOS) calculated with SOC for the rhombohedral $Sn_{14}Ge_{13}Te_{27}$ phase. The projected DOS is for *3d*, *4s* and *4p* of Ge; *4d*, *5s* and *5p* of Sn; and *4d*, *5s* and *5p* of Te. (c) Band structure and (d) projected DOS for the rhombohedral $Sn_{13}Ge_{13}InTe_{27}$ phase.

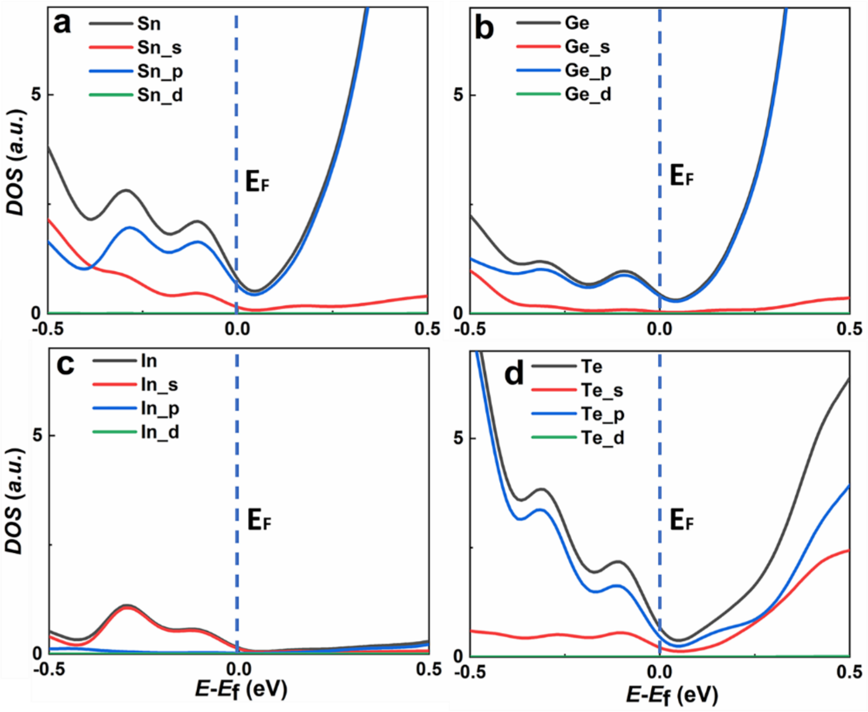

Figure 4.3 The calculated DOS with SOC for (a) 4*d*, 5*s* and 5*p* of Sn; (b) 3*d*, 4*s* and 4*p* of Ge and (c) 4*d*, 5*s* and 5*p* of In; (d) 4*d*, 5*s* and 5*p* of Te in $Sn_{13}Ge_{13}InTe_{27}$.

The temperature dependence of the lattice (k_L), charge carrier (k_c) and total (k_{total}) conductivity is presented in Figure 4.4. The carrier thermal conductivity is estimated from the Wiedemann-Franz law ($k_c=L\sigma T$), where L is the Lorentz factor defined from: $L= 1.5 + \exp(-{|S|}/{116})$.[293] Both In-doping samples have a lower k_c compared with $Sn_{0.5}Ge_{0.5}Te$ within 100 ˚C to 500 ˚C (Figure 4.4 (a)). The carrier conductivity of $(Sn_{0.5}Ge_{0.5})_{0.98}In_{0.02}Te$ is almost temperature independent, while that of $(Sn_{0.5}Ge_{0.5})_{0.96}In_{0.04}Te$ increases from 100 ˚C to 500 ˚C. Such behavior in $(Sn_{0.5}Ge_{0.5})_{0.96}In_{0.04}Te$ can be related to the thermal excitation of carriers from the valence band into the conduction band.

The lattice contribution, k_{L}, is estimated by $k_{\mathrm{L}} = k_{\mathrm{total}} - k_{\mathrm{c}}$. As indicated by Figure 4.4 (b), both In-doping samples have a lower k_{L} than $Sn_{0.5}Ge_{0.5}Te$ within 100 ˚C to 450 ˚C, which could be attributed to the additional point defect scattering. The lattice thermal conductivity of $(Sn_{0.5}Ge_{0.5})_{0.98}In_{0.02}Te$ and $(Sn_{0.5}Ge_{0.5})_{0.96}In_{0.04}Te$ increase rapidly above 450 ˚C; for $(Sn_{0.5}Ge_{0.5})_{0.98}In_{0.02}Te$ such increase can be related to a macroscopic, long-range $R3m$ to $Fm\overline{3}m$ structural transformation, while for $(Sn_{0.5}Ge_{0.5})_{0.96}In_{0.04}Te$ it is likely related to the local $R3m$ to $Fm\overline{3}m$ transition.[247] These hypotheses will need to be confirmed via HT diffraction studies. $(Sn_{0.5}Ge_{0.5})_{0.96}In_{0.04}Te$ has the lowest total thermal conductivity within 100 ˚C to 450 ˚C due to its lowest lattice and carrier contribution (Figure 4.4 (c)).

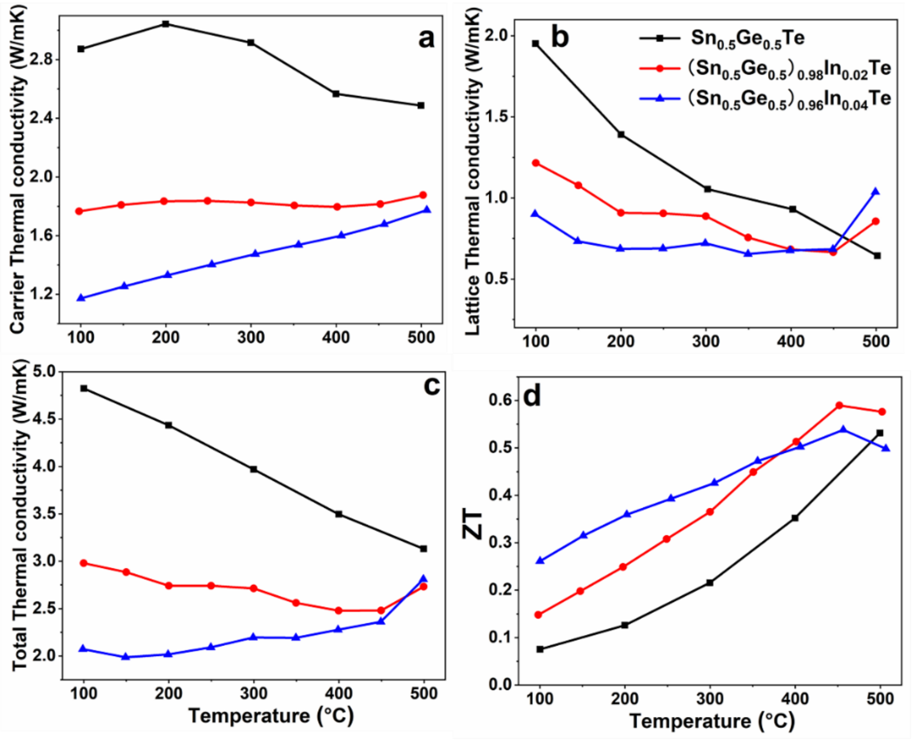

Figure 4.4 Temperature dependent (a) lattice thermal conductivity; (b) carrier thermal conductivity; (c) total thermal conductivity and (d) ZT values for $(Sn_{0.5}Ge_{0.5})_{0.98}In_{0.2}Te$, $(Sn_{0.5}Ge_{0.5})_{0.96}In_{0.4}Te$ and $Sn_{0.5}Ge_{0.5}Te$.

The *ZT* values are shown in Figure 4.4 (d). Based on these results, we may conclude that the thermoelectric performance of $Sn_{0.5}Ge_{0.5}Te$ could be effectively improved by doping In on the Sn/Ge site. $(Sn_{0.5}Ge_{0.5})_{0.98}In_{0.02}Te$ has a better thermoelectric performance than $(Sn_{0.5}Ge_{0.5})_{0.96}In_{0.04}Te$ below 400 ˚C. Therefore, $(Sn_{0.5}Ge_{0.5})_{0.98}In_{0.02}Te$ has been selected for further optimization of its thermoelectric properties via Zn, Sb, and Bi doping.

4.3.2. Zn-, Sb- and Bi-doped $(Sn_{0.5}Ge_{0.5})_{0.98}In_{0.02}Te$

Sb- and Bi- doping in GeTe induces valence band convergence and enhances valence band degeneracy, both of which significantly enhance the Seebeck coefficient in GeTe.[138,199,233] Zn-doping in GeTe suppresses a bipolar effect by increasing the band gap and promotes a heavy hole valence band to participate in the charge carrier transport, thereby improving the Seebeck coefficient. Therefore, Zn, Sb and Bi were selected as dopants to optimize the electronic structure of $(Sn_{0.5}Ge_{0.5})_{0.98}In_{0.02}Te$. The SEM results (Figure 4.S13-4.S14) show a homogenous elemental distribution in $(Sn_{0.5}Ge_{0.5})_{0.89}In_{0.02}Sb_{0.06}Te$ and $(Sn_{0.5}Ge_{0.5})_{0.89}In_{0.02}Bi_{0.06}Te$.

Room temperature X-ray powder diffraction patterns of the Zn-, Sb- and Bi-doped $(Sn_{0.5}Ge_{0.5})_{0.98}In_{0.02}Te$ samples are shown in Figure 4.5 (a). $(Sn_{0.5}Ge_{0.5})_{0.96}In_{0.02}Zn_{0.02}Te$ exhibits a clear peak splitting associated with the rhombohedral symmetry ($R3m$), while $(Sn_{0.5}Ge_{0.5})_{0.935}In_{0.02}Bi_{0.03}Te$, $(Sn_{0.5}Ge_{0.5})_{0.89}In_{0.02}Bi_{0.06}Te$, and $(Sn_{0.5}Ge_{0.5})_{0.89}In_{0.02}Sb_{0.06}Te$ adopt a cubic ($Fm\bar{3}m$) structure. Ge precipitates are detected in the $(Sn_{0.5}Ge_{0.5})_{0.96}In_{0.02}Zn_{0.02}Te$, $(Sn_{0.5}Ge_{0.5})_{0.935}In_{0.02}Bi_{0.03}Te$ and $(Sn_{0.5}Ge_{0.5})_{0.89}In_{0.02}Bi_{0.06}Te$ samples but not in $(Sn_{0.5}Ge_{0.5})_{0.89}In_{0.02}Sb_{0.06}Te$. The lattice parameters derived from the Rietveld refinement are presented in Table 4.S1.

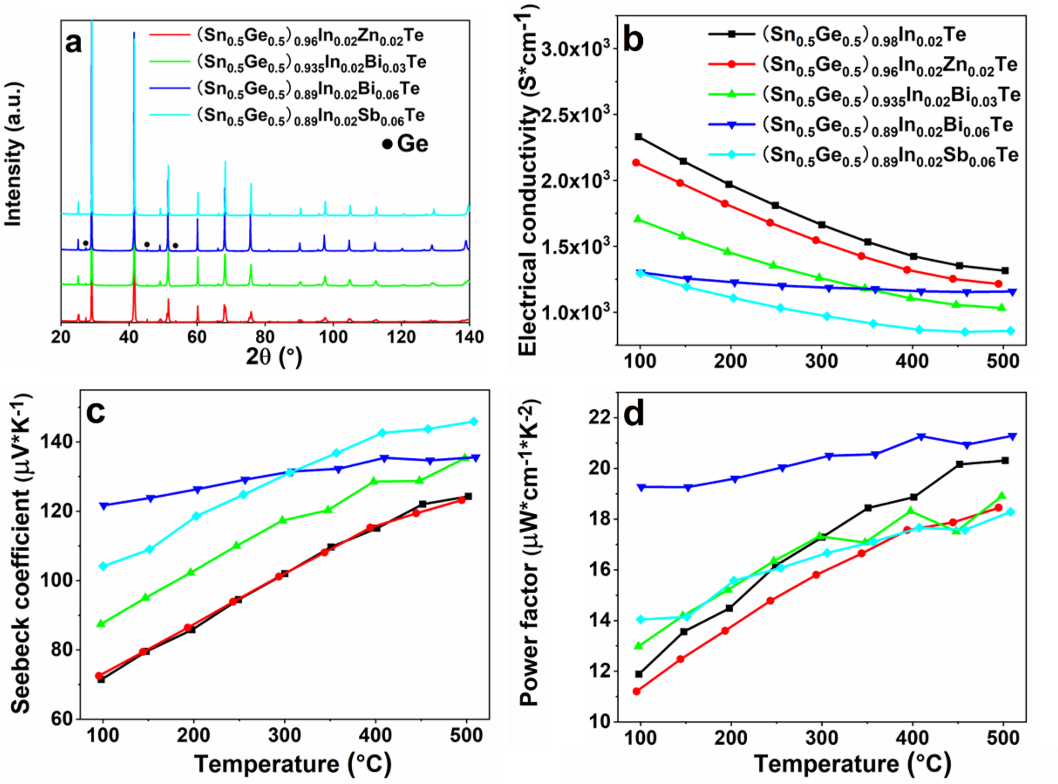

Figure 4.5 (a) Powder X-ray diffraction patterns of $(Sn_{0.5}Ge_{0.5})_{1-x}In_{0.02}M_xTe$ (M = Zn, Bi or Sb) at room temperature. (b) Electrical conductivity, (c) Seebeck coefficient and (d) power factor of $(Sn_{0.5}Ge_{0.5})_{1-x}In_{0.02}M_xTe$ (M = Zn, Bi or Sb).

The electrical conductivities of the Zn-, Sb- and Bi-doped samples (Figure 4.5 (b)) are lower than that of $(Sn_{0.5}Ge_{0.5})_{0.98}In_{0.2}Te$, with those of the Sb- and Bi-doped ones being noticeably lower than that of the Zn- doped one. Seebeck coefficients (Figure 4.5 (c)) suggest a *p*-type behavior for all the samples. The 2 mol. % Zn doping has almost no influence on the Seebeck coefficient, however larger Seebeck coefficients are observed for the Sb- and Bi-doped samples. This can be related with the rhombohedral-to-cubic transition induced by the Sb and Bi doping. This will increase the valence band degeneracy,[199] which could lead to a larger DOS effective mass and larger Seebeck coefficient (provided the conductivity effective mass stays the same). Figure 4.5 (d) displays the power factors, *PF*. The highest *PF* is observed for $(Sn_{0.5}Ge_{0.5})_{0.89}In_{0.02}Bi_{0.06}Te$, and it stems primarily from the optimized Seebeck coefficient. The power factors of the other samples are close to each other.

The larger *PF* of the $(Sn_{0.5}Ge_{0.5})_{0.89}In_{0.02}Bi_{0.06}Te$ sample prompted us to investigate its transport properties further. For comparison, the $(Sn_{0.5}Ge_{0.5})_{0.89}In_{0.02}Sb_{0.06}Te$ sample was investigated as well. As shown in Table 4.2, both $(Sn_{0.5}Ge_{0.5})_{0.89}In_{0.02}Sb_{0.06}Te$ and $(Sn_{0.5}Ge_{0.5})_{0.89}In_{0.02}Bi_{0.06}Te$ have lower carrier concentrations, larger carrier mobilities and heavier DOS effective masses than $(Sn_{0.5}Ge_{0.5})_{0.98}In_{0.02}Te$. The carrier mobility depends linearly on the carrier relaxation time and inversely on the conductivity effective mass, which in turn depends on the electronic (and crystal) structure. The effective mass reported in Table 4.2 is the DOS effective mass, which is proportional to the band degeneracy.[248] As the structure changes from the rhombohedral to cubic one upon the Sb- and Bi-doping, the degeneracy parameter increases,[137] and the DOS effective mass will follow provided the conductivity effective mass stays the same. The complication stems from the fact that symmetry changes are rather subtle and the local environment in the cubic structures can be similar to those in the rhombohedral one; also, different bands with different degeneracies can be occupied in different structures. All of these make a direct comparison of the effective masses in Table 4.2 not very straightforward. If we use those values in Table 4.2 as guides, we find it difficult to explain the lower mobility of $(Sn_{0.5}Ge_{0.5})_{0.98}In_{0.02}Te$, considering that additional Sb and Bi on the Sn/Ge site should contribute to an increased charge scattering and thus lead to lower mobilities in those phases. We propose that the increased charger carrier scattering in $(Sn_{0.5}Ge_{0.5})_{0.98}In_{0.02}Te$ must be attributed to the rhombohedral distortion in this phase (e.g., formation of microscopic twins in the rhombohedral $(Sn_{0.5}Ge_{0.5})_{0.98}In_{0.02}Te$ may disrupt carrier movement).

Table 4.2 Hall concentration, Hall mobility, carrier concentration, carrier mobility and DOS effective mass of $(Sn_{0.5}Ge_{0.5})_{0.98}In_{0.02}Te$, $(Sn_{0.5}Ge_{0.5})_{0.89}In_{0.02}Sb_{0.06}Te$ and $(Sn_{0.5}Ge_{0.5})_{0.89}In_{0.02}Bi_{0.06}Te$ at room temperature.

Composition	Carrier concentration (10^{21} cm^{-3})	Carrier mobility (cm^{2}V^{-1}s^{-1})	m^*/m_0
$(Sn_{0.5}Ge_{0.5})_{0.98}In_{0.02}Te$	1.57(5)	6.0(2)	4.21
$(Sn_{0.5}Ge_{0.5})_{0.89}In_{0.02}Sb_{0.06}Te$	1.26(6)	7.5(4)	5.24
$(Sn_{0.5}Ge_{0.5})_{0.89}In_{0.02}Bi_{0.06}Te$	1.29(2)	6.5(1)	6.47

We have performed electronic structure calculations on the cubic $Sn_{16}Ge_{14}InSbTe_{32}$ and $Sn_{16}Ge_{14}InBiTe_{32}$ (Figure 4.6). It has to be mentioned that while the lattice constants of the cubic $(Sn_{0.5}Ge_{0.5})_{0.89}In_{0.02}Sb_{0.06}Te$ and $(Sn_{0.5}Ge_{0.5})_{0.89}In_{0.02}Bi_{0.06}Te$ samples were used, the symmetry is decreased when the In, Sb and Bi atoms are introduced into the structure. Such symmetry lowering lifts the band degeneracy, i.e. bands, that should be overlapped, are now separated in energy. This is manifested by having many bands close to each other. Such band behavior was also observed for $Sn_{13}Ge_{13}InTe_{27}$ in Figure 4.2 (c). However, there is also a significant difference; while there are only two valence band maxima, VBM, around the L point in $Sn_{13}Ge_{13}InTe_{27}$, there are three and four VBM around the Γ point in

$Sn_{16}Ge_{14}InSbTe_{32}$ and $Sn_{16}Ge_{14}InBiTe_{32}$, respectively (Figure 4.6 (a) and (c)). Also, the bands are flatter around the Fermi level in $Sn_{16}Ge_{14}InSbTe_{32}$ and $Sn_{16}Ge_{14}InBiTe_{32}$; additionally, there are multiple bands just below the Fermi level in $Sn_{16}Ge_{14}InBiTe_{32}$. Such band features would suggest a larger carrier effective mass and higher Seebeck coefficient for $Sn_{16}Ge_{14}InSbTe_{32}$ and $Sn_{16}Ge_{14}InBiTe_{32}$, as experimentally observed. The origin of such band changes in $Sn_{16}Ge_{14}InSbTe_{32}$ and $Sn_{16}Ge_{14}InBiTe_{32}$ can be attributed to the smaller energy separation between the valence and conduction bands, especially in $Sn_{16}Ge_{14}InBiTe_{32}$. This leads to “band inversion” between the multiple bands and formation of numerous valence band maxima. This feature is known as a “band inversion” and it has been reported previously for the SnTe-based materials.[226,251] Figure 4.6 (c) also shows that the valence band maximum (VBM) is pushed up above the Fermi level, and consequently there is no band gap in the $Sn_{16}Ge_{14}InBiTe_{32}$.

The electronic structure analysis was further expanded through the DOS calculations. The DOS of $Sn_{16}Ge_{14}InSbTe_{32}$ (Figure 4.6 (b)) contains two peaks around the Fermi level. According to the partial DOS, the one at -0.17 eV is induced by In and the other at 0.15 eV by Sb. In $Sn_{16}Ge_{14}InBiTe_{32}$, the states associated the with Bi doping moved closer to those induced by In, as a result a pronounced DOS dip, present in the Sb-doped phase around the Fermi level, is absent in $Sn_{16}Ge_{14}InBiTe_{32}$. The DOS plots also indicate that incorporation of the electron-richer Sb and Bi into $(Sn_{0.5}Ge_{0.5})_{0.98}In_{0.02}Te$ shifts the Fermi level from the valence band into the energy range where a band gap used to be present. Thus, the Sb- and Bi-doping should potentially offset increases (if any) in the hole concentration due to the In doping.

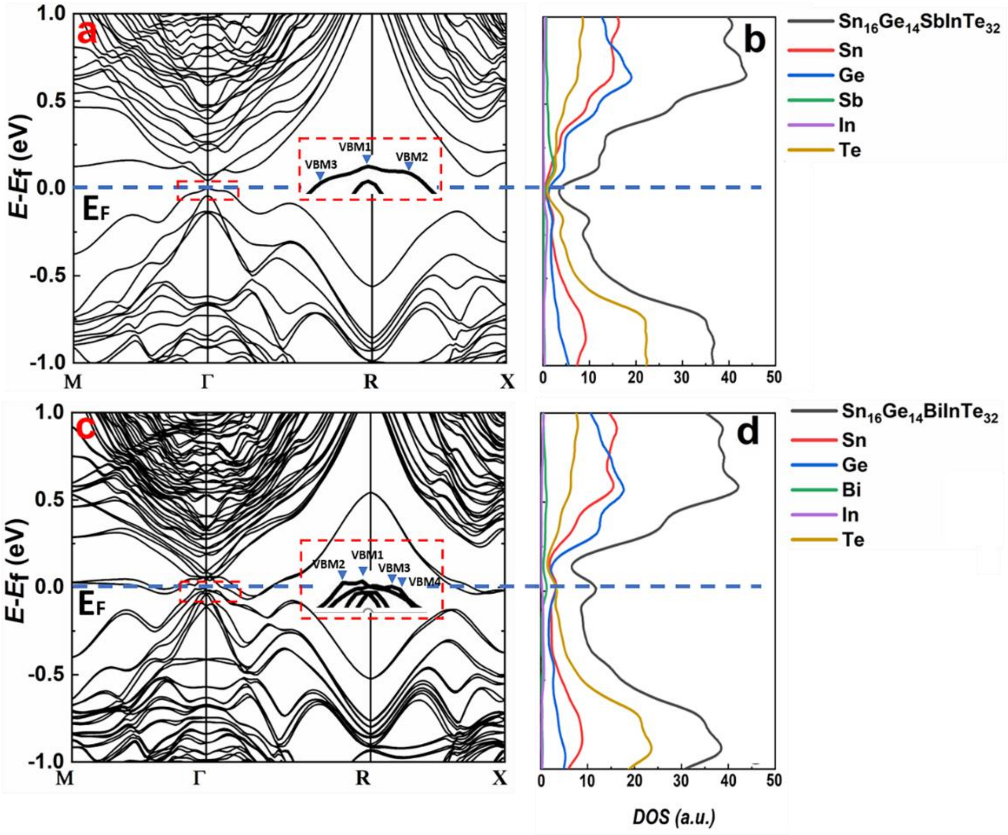

Figure 4.6. Calculated band structures with the SOC of (a) cubic $Sn_{16}Ge_{14}SbInTe_{32}$; (c) cubic $Sn_{16}Ge_{14}BiInTe_{32}$. Projected densities of state (DOS) with the SOC for (b) cubic $Sn_{16}Ge_{14}SbInTe_{32}$ and (d) $Sn_{16}Ge_{14}BiInTe_{32}$.

Figure 4.7 shows the temperature dependent thermal conductivities and ZT values of $(Sn_{0.5}Ge_{0.5})_{0.98}In_{0.02}Te$, $(Sn_{0.5}Ge_{0.5})_{0.89}In_{0.02}Sb_{0.06}Te$ and $(Sn_{0.5}Ge_{0.5})_{0.89}In_{0.02}Bi_{0.06}Te$. The total thermal conductivity of $(Sn_{0.5}Ge_{0.5})_{0.89}In_{0.02}Sb_{0.06}Te$ and $(Sn_{0.5}Ge_{0.5})_{0.89}In_{0.02}Bi_{0.06}Te$ are much lower than that of $(Sn_{0.5}Ge_{0.5})_{0.98}In_{0.02}Te$ (Figure 7(a)). The carrier thermal conductivity in Figure 4.7 (b) was calculated using the Wiedemann-Franz law ($k_e = L\sigma T$). While the carrier thermal conductivity is lower for $(Sn_{0.5}Ge_{0.5})_{0.89}In_{0.02}Sb_{0.06}Te$ and $(Sn_{0.5}Ge_{0.5})_{0.89}In_{0.02}Bi_{0.06}Te$, it increases with temperature, which can be attributed to easier thermal excitation of the charge carriers as their band gaps are reduced. The lattice thermal conductivity of $(Sn_{0.5}Ge_{0.5})_{0.89}In_{0.02}Sb_{0.06}Te$ decreases with temperature, which is characteristic of the Umklapp scattering.[60] On the other hand, the lattice conductivity of $(Sn_{0.5}Ge_{0.5})_{0.89}In_{0.02}Bi_{0.06}Te$ is almost temperature independent at 100 °C to 350 °C, which suggest that point defect scattering of phonons is likely a dominant scattering mechanism at this temperature range. Both the average and highest *ZT* of $(Sn_{0.5}Ge_{0.5})_{0.98}In_{0.02}Te$ are improved upon the Sb- and Bi-doping (Figure 4.7 (d)). The $(Sn_{0.5}Ge_{0.5})_{0.89}In_{0.02}Bi_{0.06}Te$ sample achieves the *ZT* of 0.8 at 400 ^{o}C and the average *ZT* of 0.71.

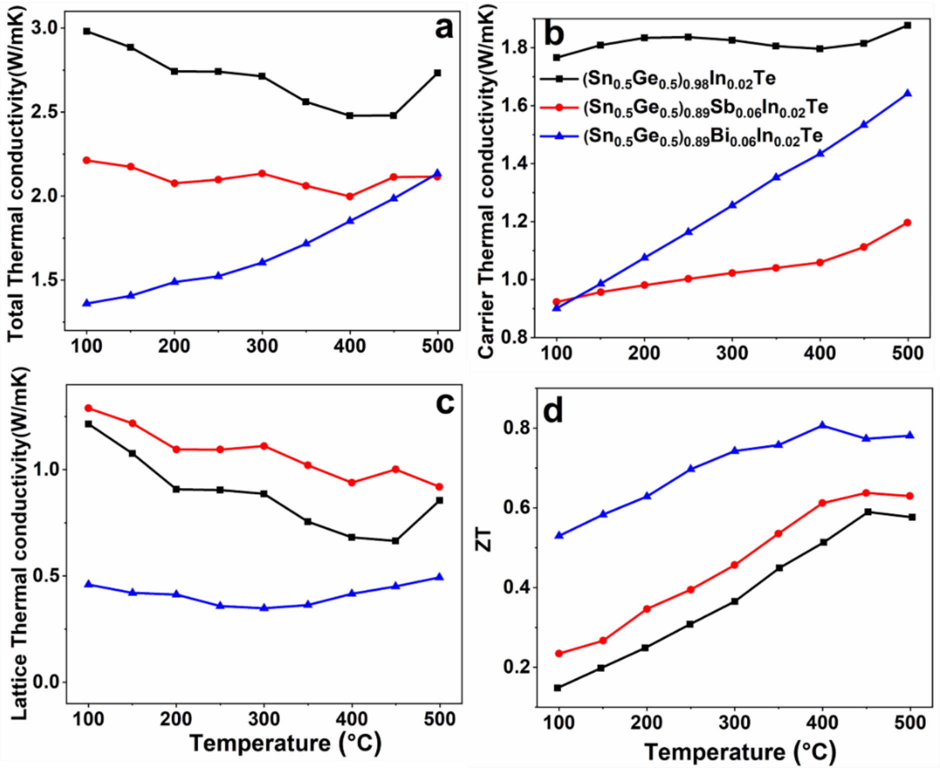

Figure 4.7 (a) Total, (b) carrier, and (c) lattice thermal conductivity and (d) ZT values of $(Sn_{0.5}Ge_{0.5})_{0.98}In_{0.02}Te$, $(Sn_{0.5}Ge_{0.5})_{0.89}In_{0.02}Sb_{0.06}Te$ and $(Sn_{0.5}Ge_{0.5})_{0.89}In_{0.02}Bi_{0.06}Te$.

4.4 Conclusion

Table 4.3 summarizes some of the published maximum, ZT_{max}, and average, ZT_{ave}, figure-of-merit values for the SnTe- and GeTe-based materials. According to the data, the elemental substitution can significantly improve the performance of the pristine SnTe and GeTe. In particular, incorporation of Pb yields very high *ZT* values.[137,224,226,252] Because of the Pb toxicity, we focused on other elements for property optimization. Our current work proves that thermoelectric performance of SnTe can be enhanced via Ge substitution, and In/Bi co-doping. However, the performance of our best sample, $(Sn_{0.5}Ge_{0.5})_{0.89}In_{0.02}Bi_{0.06}Te$, only approaches that of the pristine GeTe.

Still, the strategies employed for $(Sn_{0.5}Ge_{0.5})_{0.89}In_{0.02}Bi_{0.06}Te$ can be transferred to other materials. In particular, we found that In doping induces resonant levels around the Fermi level in $Sn_{0.5}Ge_{0.5}Te$, as a result the thermopower is improved. Subsequent Sb and Bi doping leads to band inversion, which creates multiple electronic valleys, thereby improving the Seebeck coefficient further. The Sb and Bi doping also induce extra atomic disorder that optimizes the lattice thermal conductivity.

Table 4.3 The ZT_{max} values and Average ZT of SnTe and GeTe based materials.

Sample	Maximum ZT_{max}		Average ZT_{av}		Ref.
	Value (~)	T (K)	Value (~)	T (K)	
SnTe	0.36	773	0.13	373-773	[223]
$Sn_{0.5}Ge_{0.5}Te$	0.53	773	0.25	373-773	[223]
$(Sn_{0.5}Ge_{0.5})_{0.89}In_{0.02}Bi_{0.06}Te$	0.8	673	0.71	373-773	**This work**
SnTe-20%$AgSbSe_2$	0.92	820	-	-	[253]
$Sn_{0.98}Cd_{0.02}Te_{0.9}Se_{0.1}$	0.78	773	-	-	[254]
$Sn_{0.98}Bi_{0.02}Te$-$HgInTe_2$	0.9	850	-	-	[227]
$Sn_{0.915}Mn_{0.11}In_{0.005}Te$	1.15	823	0.62	300-823	[76]
$Sn_{0.48}Cd_{0.02}Ge_{0.25}Pb_{0.25}Te$	1.42	873	-	-	[226]
$Sn_{1.04/3}Pb_{1/3}Ge_{1/3}Te$-18%MnTe	1.75	873	0.98	300-873	[224]
GeTe	0.86	773	0.46	373-773	[223]
$Ge_{0.85}Mg_{0.05}Sb_{0.1}Te$	1.84	800	1.2	300-800	[255]
$Ge_{0.87}Mn_{0.05}Sb_{0.08}Te$	1.67	773	0.9	300-773	[256]
$(GeTe)_{85}(AgSbTe_2)_{15}$	1.3	773	0.9	300-773	[257]
$Ge_{0.74}Ag_{0.13}Sb_{0.11}Nd_{0.02}Te$	1.65	727	-	-	[258]
$Ge_{0.86}Pb_{0.1}Bi_{0.04}Te$	2.4	600	1.6	300-600	[137]
GeTe-1.5%Cu_2Te-2%BiTe-8%PbTe	2.4	650	1.2	300-773	[252]

4.5 Supporting Information

Expanded view of the X-ray powder diffraction patterns.

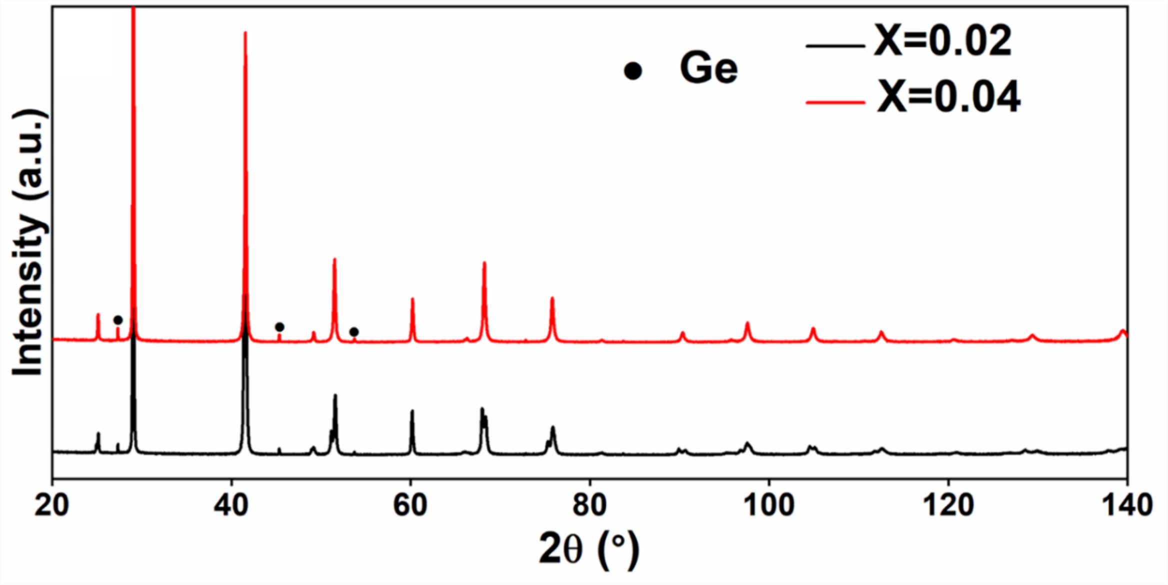

Fig 4.S1: Powder X-ray diffraction patterns of $(Sn_{0.5}Ge_{0.5})_{1-x}In_xTe$ in the (a) 20-140° 2θ range at room temperature. The peak splitting is representative of the rhombohedral symmetry.

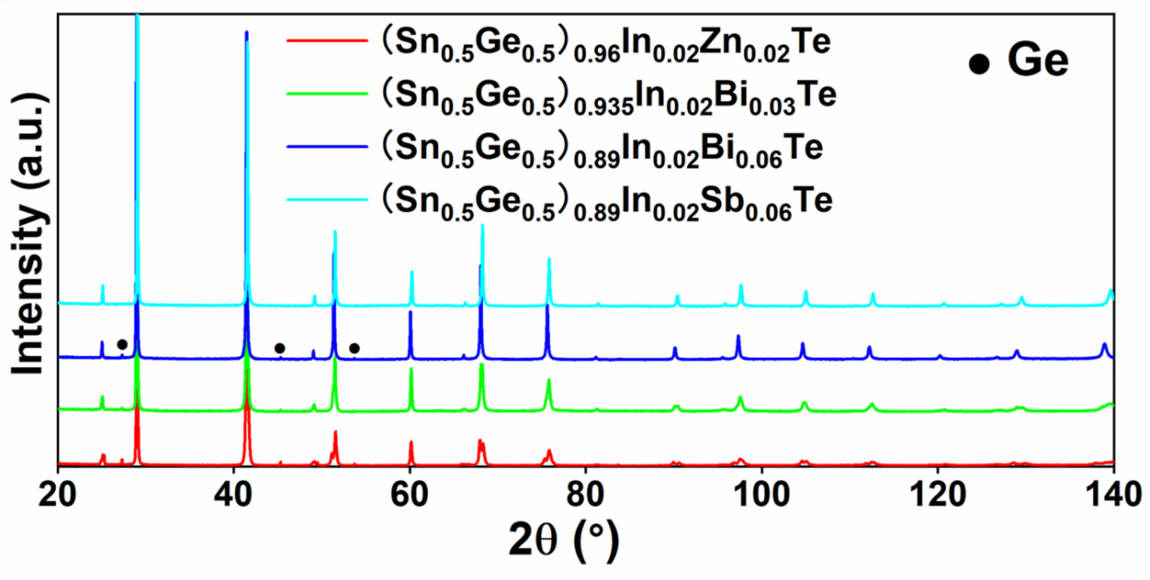

Fig 4.S2: Powder X-ray diffraction patterns of $(Sn_{0.5}Ge_{0.5})_{1-x}In_{0.02}M_xTe$ (M= Zn, Bi or Sb) in the (a) 20-140˚ 2*θ* range at room temperature. The peak splitting is representative of the rhombohedral symmetry.

Symmetry and lattice parameters.

The lattice parameters were derived by the Rietveld refinement of the PXRD data.

Table 4.S1: Symmetry, lattice parameters and R profile values.

	Space Group	a (Å^3)	c (Å^3)	Cell volume (Å^3)	Primitive cell volume (Å^3)	R_p (%)
$(Sn_{0.5}Ge_{0.5})Te$	*R*3*m*	4.324(1)	10.766(2)	174.33(4)	58.11(1)	9.86
$(Sn_{0.5}Ge_{0.5})_{0.98}In_{0.02}Te$	*R*3*m*	4.336(1)	10.714(3)	174.44(7)	58.15(2)	10.80
$(Sn_{0.5}Ge_{0.5})_{0.96}In_{0.04}Te$	*Fm*-3*m*	6.142(1)	6.142(1)	231.67(1)	57.92(1)	9.69
$(Sn_{0.5}Ge_{0.5})_{0.96}In_{0.02}Zn_{0.02}Te$	*R*3*m*	4.335(1)	10.713(3)	174.38(8)	58.13(3)	10.86
$(Sn_{0.5}Ge_{0.5})_{0.89}In_{0.02}Sb_{0.06}Te$	*Fm*-3*m*	6.142(1)	6.142(1)	231.73(3)	57.93(1)	7.32
$(Sn_{0.5}Ge_{0.5})_{0.935}In_{0.02}Bi_{0.03}Te$	*Fm*-3*m*	6.145(1)	6.145(1)	232.09(9)	58.02(2)	10.90
$(Sn_{0.5}Ge_{0.5})_{0.89}In_{0.02}Bi_{0.06}Te$	*Fm*-3*m*	6.156(1)	6.156(1)	233.29(3)	58.32(1)	8.70

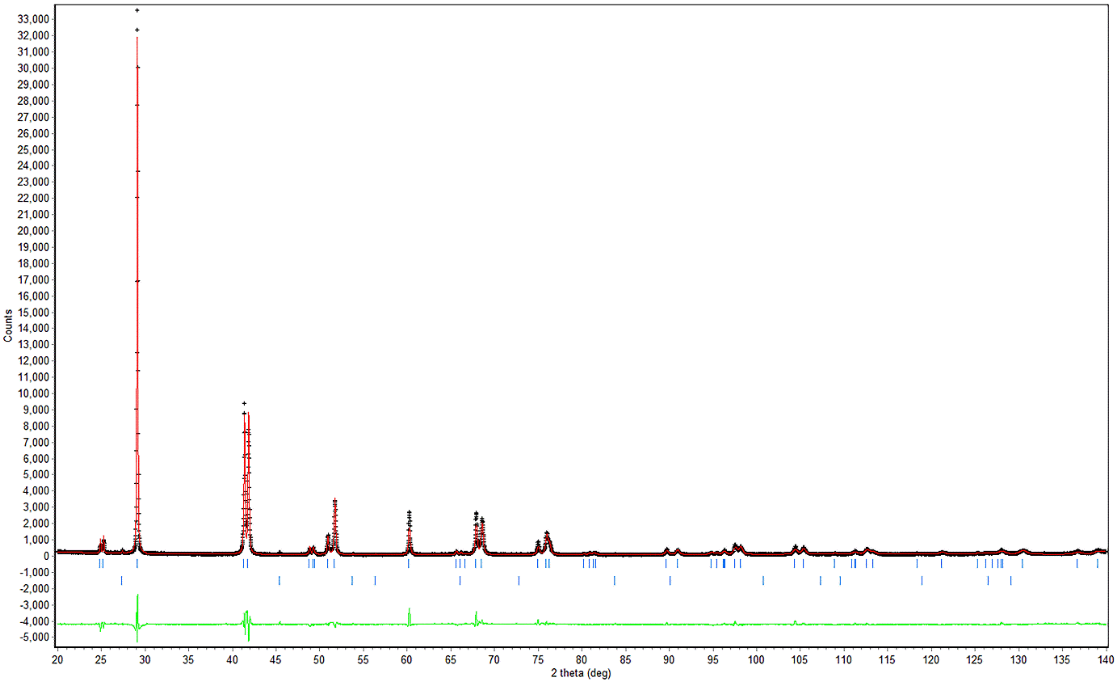

Fig 4.S3: Rietveld refinement of the powder diffraction data of $(Sn_{0.5}Ge_{0.5})Te$. Only the 2θ = 20-140° range is shown. Black crosses and the red line represent observed and calculated intensities; the green line is the difference between the intensities. The vertical bars show the position of Bragg peaks.

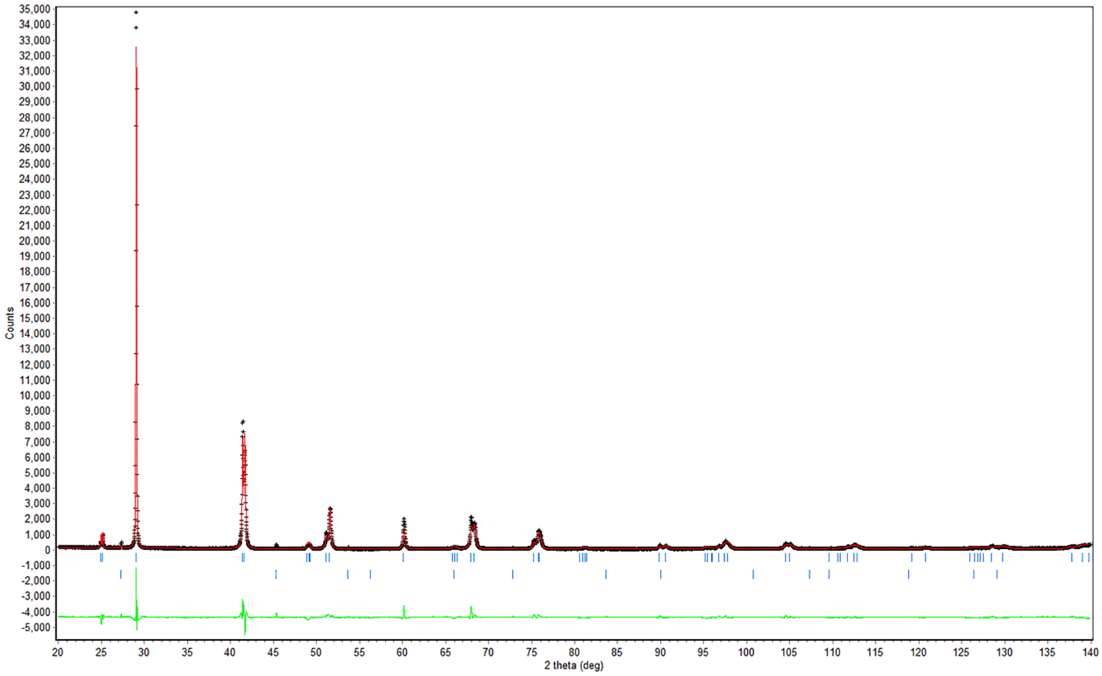

Fig 4.S4: Rietveld refinement of the powder diffraction data of $(Sn_{0.5}Ge_{0.5})_{0.98}In_{0.02}Te$. Only the 2θ = 20-140° range is shown. Black crosses and the red line represent observed and calculated intensities; the green line is the difference between the intensities. The vertical bars show the position of Bragg peaks.

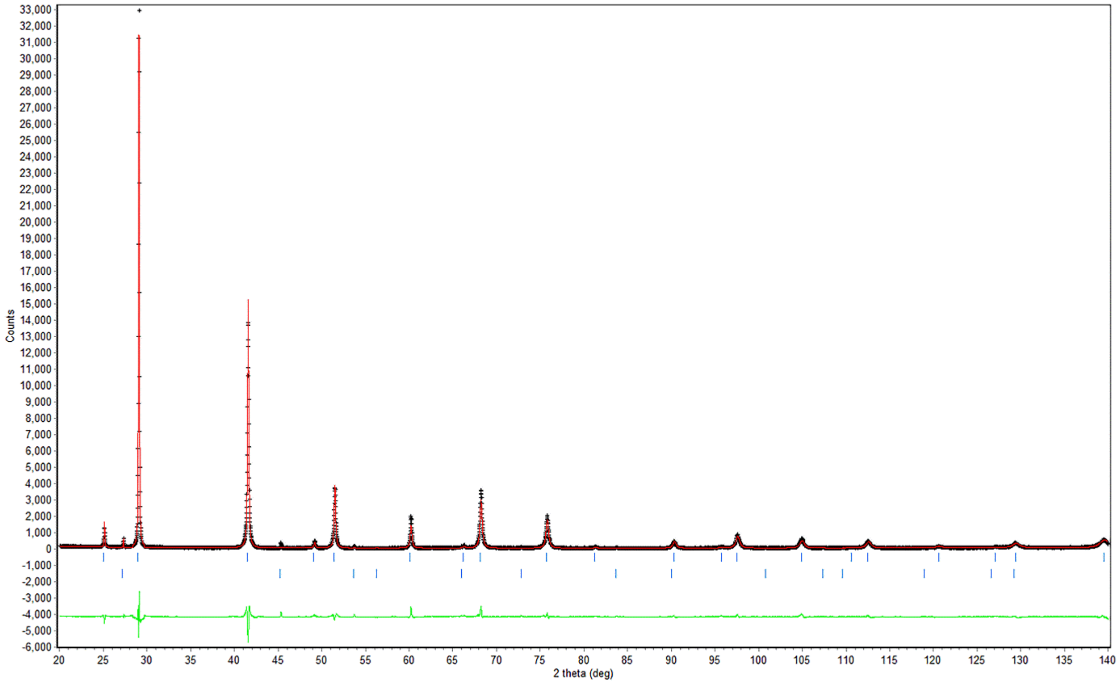

Fig 4.S5: Rietveld refinement of the powder diffraction data of $(Sn_{0.5}Ge_{0.5})_{0.96}In_{0.04}Te$. Only the 2θ = 20-140˚ range is shown. Black crosses and the red line represent observed and calculated intensities; the green line is the difference between the intensities. The vertical bars show the position of Bragg peaks.

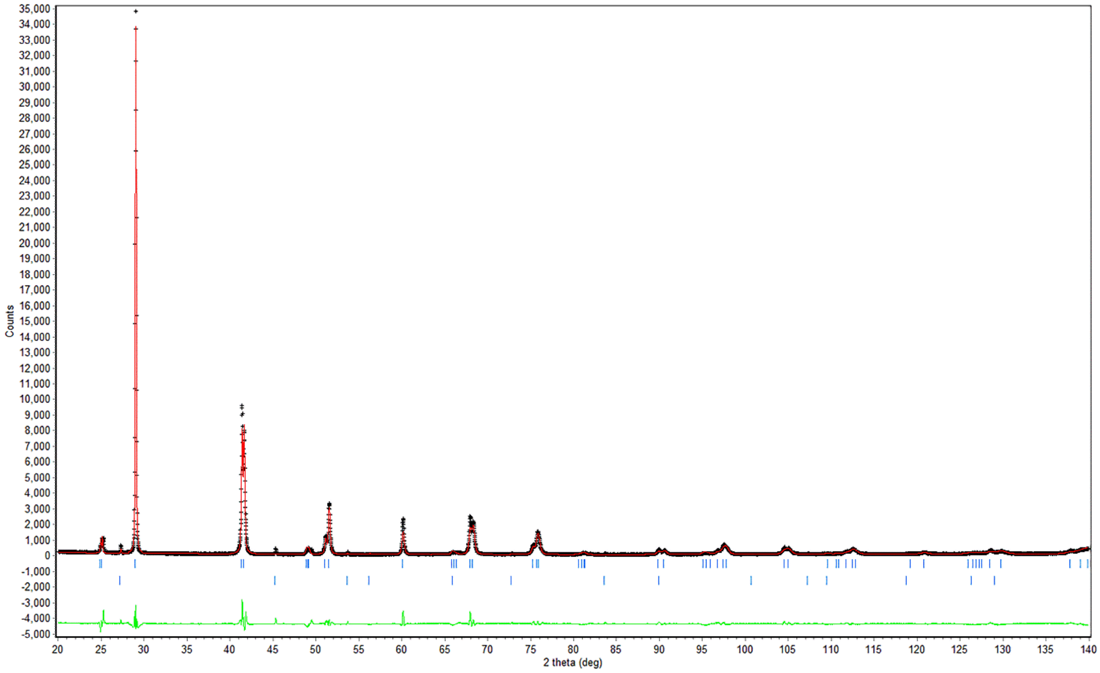

Fig 4.S6: Rietveld refinement of the powder diffraction data of $(Sn_{0.5}Ge_{0.5})_{0.96}In_{0.02}Zn_{0.02}Te$. Only the 2θ = 20-140° range is shown. Black crosses and the red line represent observed and calculated intensities; the green line is the difference between the intensities. The vertical bars show the position of Bragg peaks.

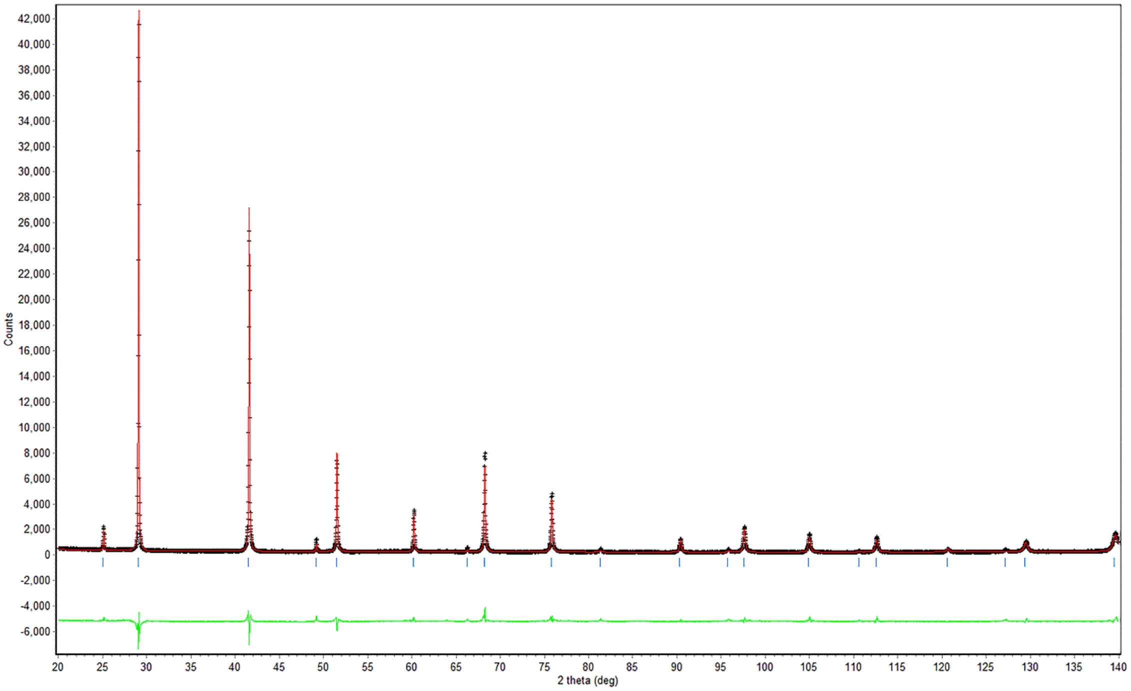

Fig 4.S7: Rietveld refinement of the powder diffraction data of $(Sn_{0.5}Ge_{0.5})_{0.89}In_{0.02}Sb_{0.06}Te$. Only the 2θ = 20-140˚ range is shown. Black crosses and the red line represent observed and calculated intensities; the green line is the difference between the intensities. The vertical bars show the position of Bragg peaks.

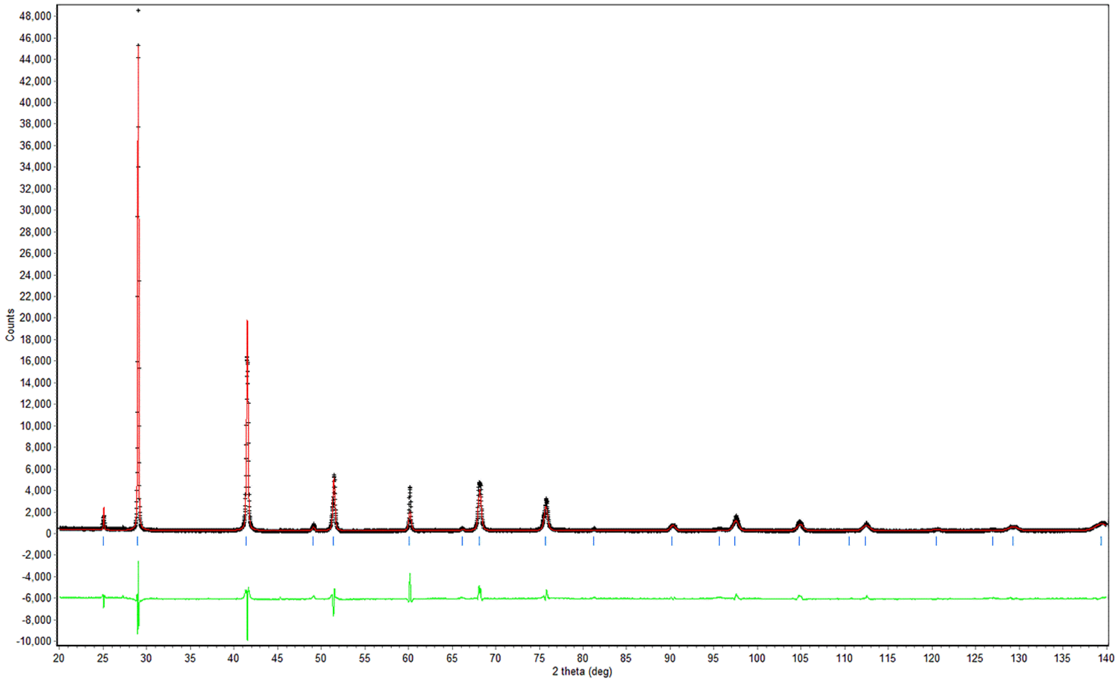

Fig 4.S8: Rietveld refinement of the powder diffraction data of $(Sn_{0.5}Ge_{0.5})_{0.935}In_{0.02}Bi_{0.03}Te$. Only the 2θ = 20-140˚ range is shown. Black crosses and the red line represent observed and calculated intensities; the green line is the difference between the intensities. The vertical bars show the position of Bragg peaks.

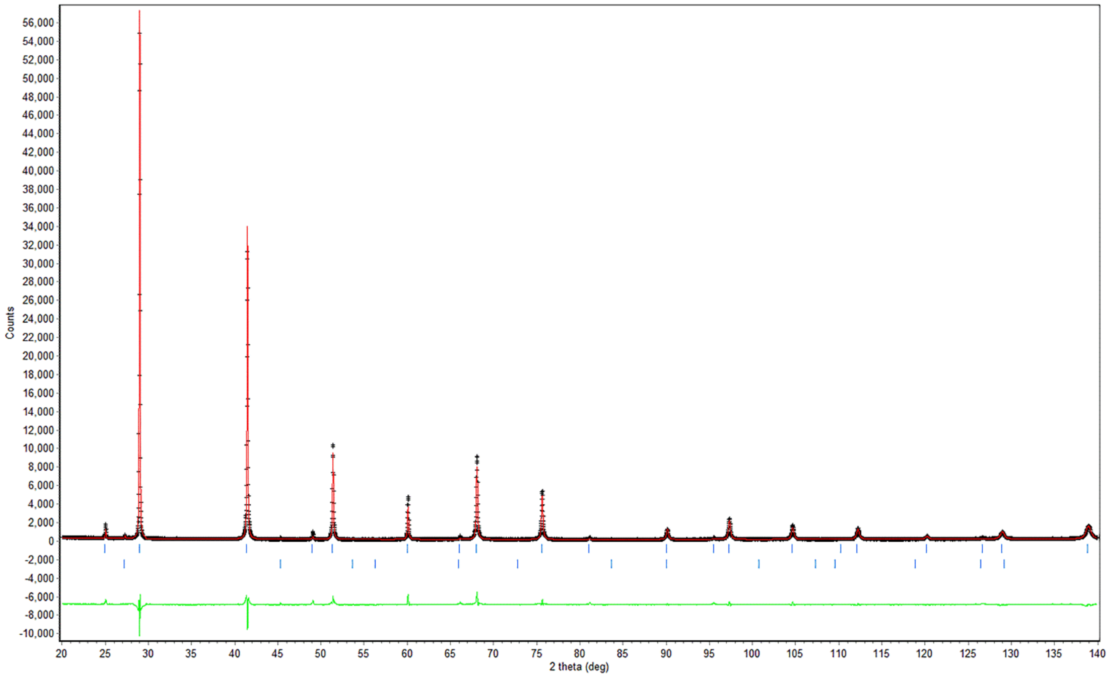

Fig 4.S9: Rietveld refinement of the powder diffraction data of $(Sn_{0.5}Ge_{0.5})_{0.89}In_{0.02}Bi_{0.06}Te$. Only the 2θ = 20-140° range is shown. Black crosses and the red line represent observed and calculated intensities; the green line is the difference between the intensities. The vertical bars show position of Bragg peaks.

Table 4.S2: Geometrical and Archimedes, densities and compactness of the samples

	Rietveld Refinement Density (g/cm^3)	Geometrical Density (g/cm^3)	Archimedean Density (g/cm^3)	Compactness (%)
$(Sn_{0.5}Ge_{0.5})_{0.98}In_{0.02}Te$	6.39	6.13	6.25	98.1
$(Sn_{0.5}Ge_{0.5})_{0.96}In_{0.04}Te$	6.28	6.16	6.27	98.2
$(Sn_{0.5}Ge_{0.5})_{0.96}In_{0.02}Zn_{0.02}Te$	6.42	6.22	6.34	98.1
$(Sn_{0.5}Ge_{0.5})_{0.935}In_{0.02}Bi_{0.03}Te$	6.35	6.17	6.28	98.2
$(Sn_{0.5}Ge_{0.5})_{0.89}In_{0.02}Bi_{0.06}Te$	6.58	6.43	6.50	98.9
$(Sn_{0.5}Ge_{0.5})_{0.89}In_{0.02}Sb_{0.06}Te$	6.34	6.20	6.29	98.6

Scanning Electron Microscopy-Energy Dispersive X-ray Spectroscopy (SEM-EDS).

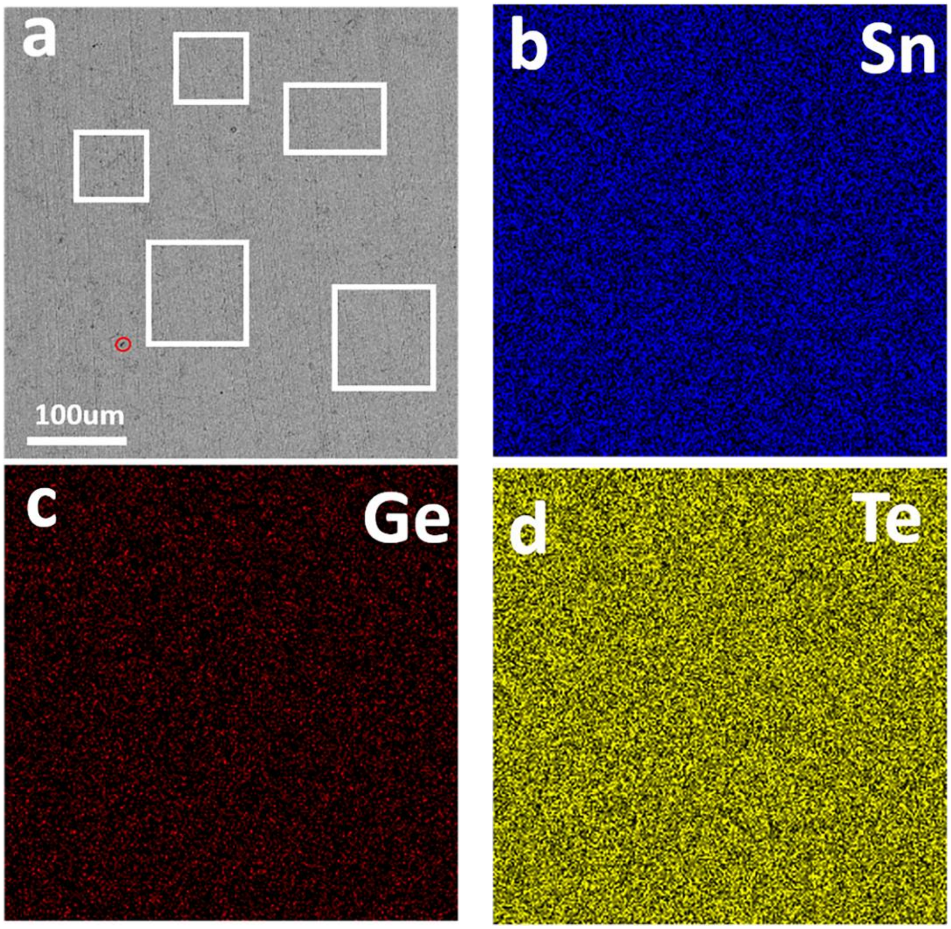

Fig 4.S10: (a) Back-scattered electron image. Black spots (one shown in the red circle) are Ge precipitates. and (b-d) elemental mappings of Te, Sn and Ge of $Sn_{0.5}Ge_{0.5}Te$. Composition of the selected areas in (a) 25.9(1) of Sn, 25.1(2) of Ge, and 49.0(2) at.% of Te.

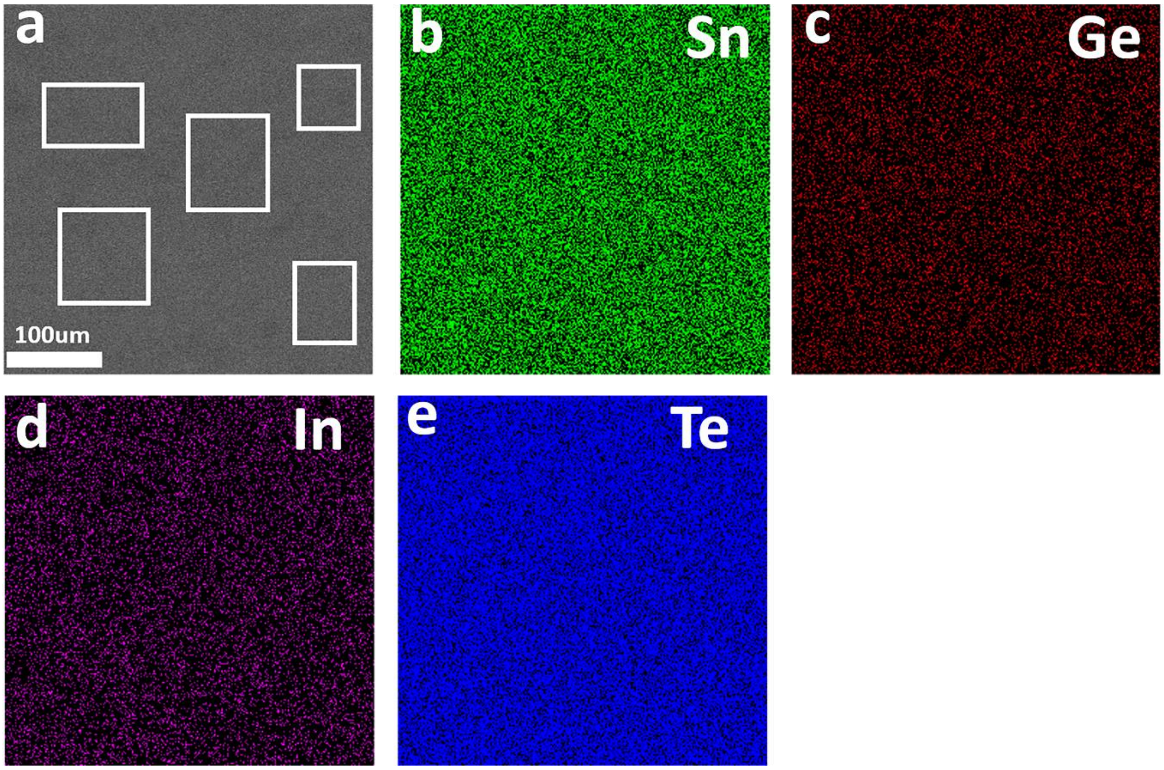

Fig 4.S11: (a) Back-scattered electron image; and (b-f) elemental mappings of Sn, Ge, In and Te of $(Sn_{0.5}Ge_{0.5})_{0.98}In_{0.02}Te$. The average composition of the selected areas in (a) is 25.0(7) of Sn, 24.5(9) of Ge, 1.2(2) of In and 49.3(4) at.% of Te.

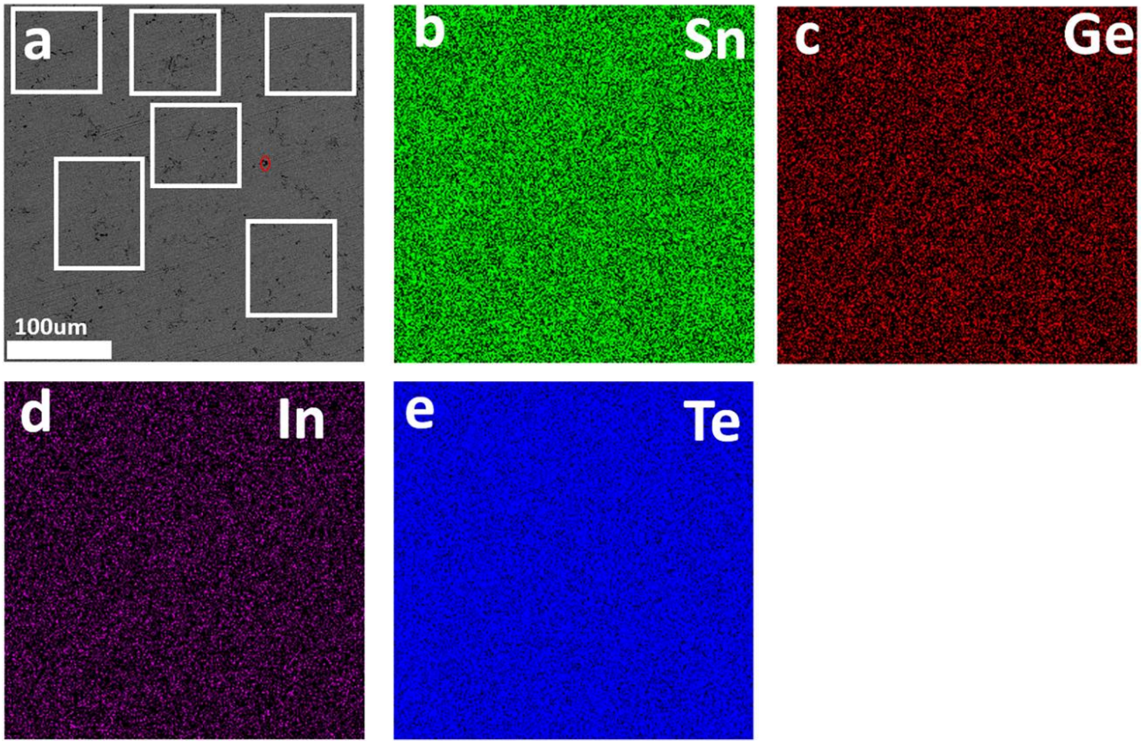

Fig 4.S12: (a) Back-scattered electron image of $(Sn_{0.5}Ge_{0.5})_{0.96}In_{0.04}Te$. Black spots (one shown in the red circle) are Ge precipitates. (b-f) Elemental mappings of Sn, Ge, In and Te. The average composition of the selected areas in (a) is 24.7(9) of Sn, 24.2(9) of Ge, 2.1(3) of In and 49.0(3) at.% of Te.

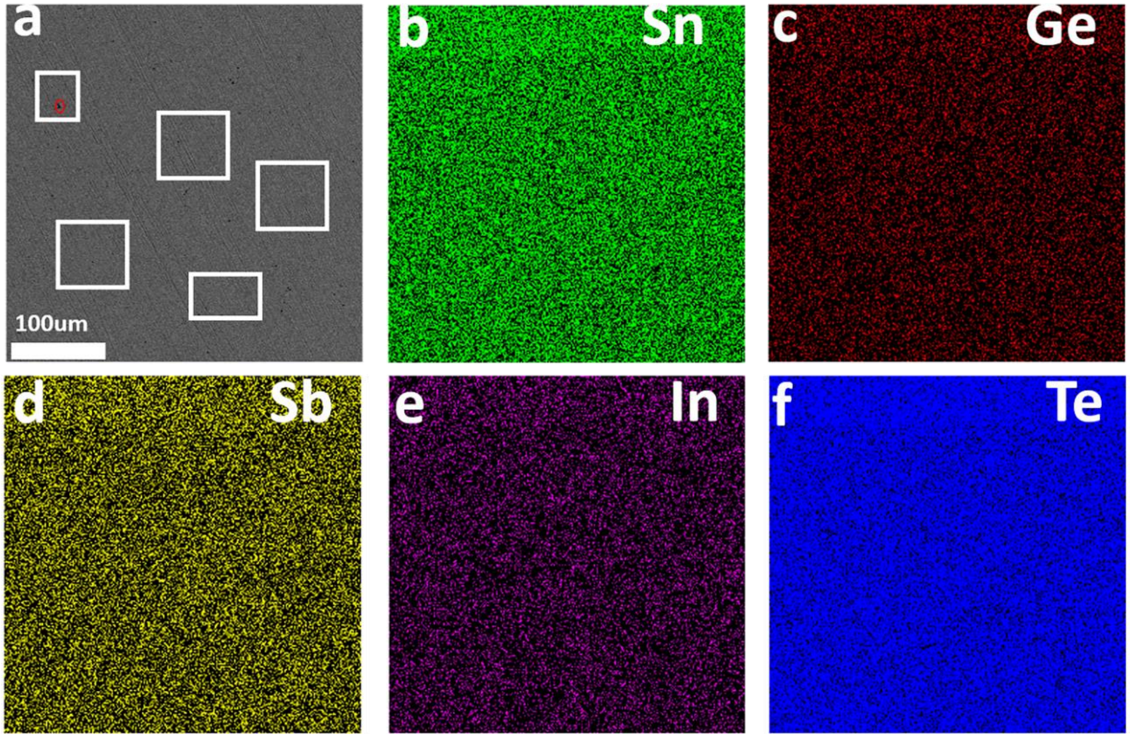

Fig 4.S13: (a) Back-scattered electron image of $(Sn_{0.5}Ge_{0.5})_{0.89}Sb_{0.06}In_{0.02}Te$. Black spots (one shown in the red circle) are Ge precipitates. (b-f) Elemental mappings of Sn, Ge, Sb, In and Te . The average composition of the selected areas in (a) is 23.5(2) of Sn, 23.2(3) of Ge, 2.6(2) of Sb, 0.9(2) of In and 49.8(4) at.% of Te.

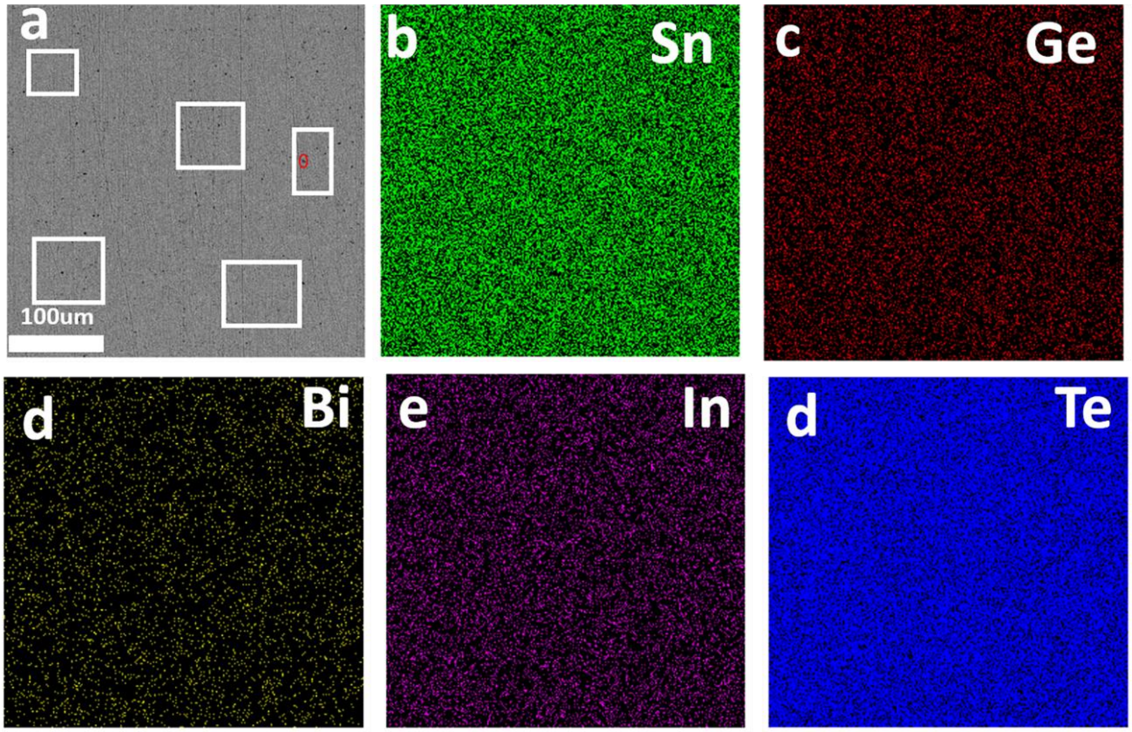

Fig 4.S14: (a) Back-scattered electron image of $(Sn_{0.5}Ge_{0.5})_{0.89}Bi_{0.06}In_{0.02}Te$. Black spots (one shown in the red circle) are Ge precipitates. (b-f) Elemental mappings of Sn, Ge, Bi, In and Te. The average composition of the selected areas in (a) is 23.4(9) of Sn, 22.7(9) of Ge, 3.2(2) of Bi, 1.0(2) of In and 49.7(7) at.% of Te.

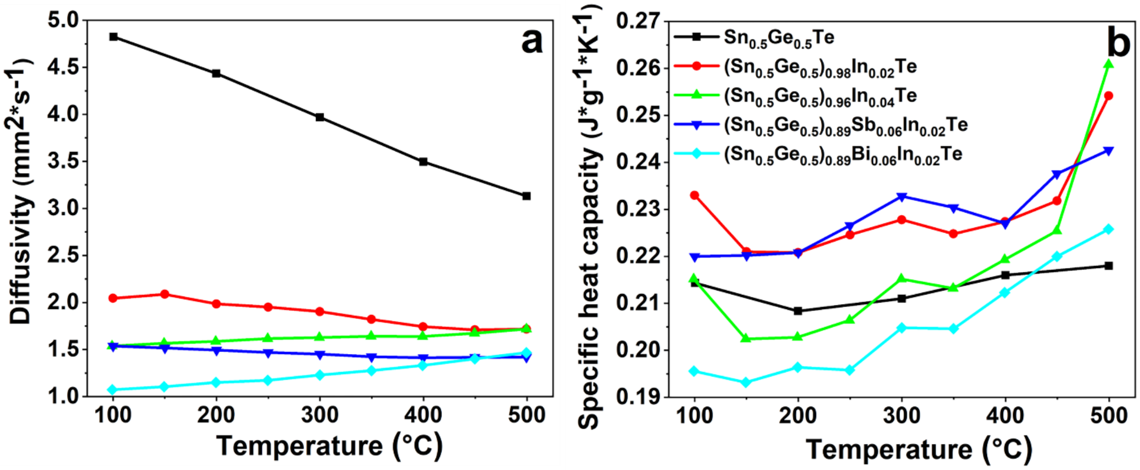

Fig 4.S15: Temperature dependent (a) Diffusivity, (b) Specific heat capacity of $Sn_{0.5}Ge_{0.5}Te$, $(Sn_{0.5}Ge_{0.5})_{0.98}In_{0.2}Te$, $(Sn_{0.5}Ge_{0.5})_{0.96}In_{0.4}Te$, $(Sn_{0.5}Ge_{0.5})_{0.89}In_{0.02}Sb_{0.06}Te$ and $(Sn_{0.5}Ge_{0.5})_{0.89}In_{0.02}Bi_{0.06}Te$.

Chapter 5. Optimizing thermoelectric performance of SnTe via alloying with $AgSnSe_2$ and PbTe

This chapter encompasses the manuscript "Optimizing thermoelectric performance of SnTe via alloying with $AgSnSe_2$ and PbTe", which was published in *Journal of Alloys and Compounds* **2023**, *947*, 169415. Some of the electrical properties were measured by Dr. Yu-Chih Tseng at CanmetMATERIALS, Natural Resources of Canada, Hamilton, ON. The candidate performed the experimental procedures, sample characterization, charge transport and thermal property measurements, data interpretation, and manuscript preparation.

Reproduced with permission from Song, S.; Tseng, Y.-C.; Mozharivskyj. *Journal of Alloys and Compounds* **2023**, *947*, 169415. Copyright by 2021 Elsevier

This work provides a comparative study of the thermoelectric properties $AgSnSe_2$-alloyed SnTe. We attempted to simultaneously optimize the electrical conductivity and thermal conductivity of SnTe. A strong atomic disorder was introduced via alloying with $AgSnSe_2$, which decreased thermal conductivity significantly. Also, $AgSnSe_2$ showed a donor behavior in the $AgSnSe_2$-alloyed SnTe; the increased carrier concentration compensated for the decrease in the carrier mobility and rendered a good electrical conductivity in the alloyed samples. Based on the experimental data, $(SnTe)_{0.95}(AgSnSe_2)_{0.05}$ shows the best thermoelectric performance. To further improve the performance, lead (Pb) was substituted for Sn in $(SnTe)_{0.95}(AgSnSe_2)_{0.05}$.

5.1 Introduction

To slow down climate change, it is urgent to reduce use of the fossil fuels and improve the efficiency of energy-intense processes based on fossil fuels. Thermoelectricity is one of the environmentally friendly energy conversion technologies since it can directly convert waste heat into electricity.[10] The energy conversion efficiency of thermoelectric materials is described by the dimensionless figure of merit *ZT*: $ZT = \frac{\alpha^2\sigma}{\kappa_{tot}}T$, where α, σ, κ_{tot} and T are Seebeck coefficient, electrical conductivity, totally thermal conductivity, and absolute temperature, respectively.[219] The total thermal conductivity (κ_{tot}) consists of the charge carrier and lattice contributions: $\kappa_{tot} = \kappa_C + \kappa_l$.[3] An ideal thermoelectric materials should have a high power factor ($\alpha^2\sigma$) and low κ_{tot}. However, achieving good thermoelectric performance is not straightforward, as the σ and α have an inverse dependence on the carrier concentration, and a high σ results in a high κ_C. Over the past few decades, extensive research have been conducted to circumvent this limitations and the following strategies have been employed: band engineering,[36,75,251,259,260] tuning of carrier concentration,[86,125,195,201,223,261,262], nano-structuring[177,228,236,253] and defect engineering.[38,263–266]

PbTe-based alloys are one of the best thermoelectric materials at mid temperatures (400-900 K). However, the widespread use of the PbTe-based alloys is limited by the high toxicity of Pb. Among the potential Pb-free replacements, SnTe is of the greatest interest as it has a similar crystal and electronic structures.[90,267] However, unlike pristine PbTe, pristine SnTe shows inferior thermoelectric performance because of the following: (i) a larger energy separation ($\Delta E_{L-\Sigma}$ ~0.35 eV) between the light hole and heavy hole valence bands at the *L* point,[143] which limits the heavy hole participation in the transport properties and leads to a low Seebeck coefficient. (ii) Significant intrinsic Sn deficiency results in a high hole concentration of 10^{20} to 10^{21}cm^{-3},[140] subsequently, in a lower thermoelectric performance in undoped SnTe.[141] (iii) The lattice thermal conductivity of SnTe is larger than that of PbTe (SnTe ~ 3.0 W/(mK)[268] vs. PbTe ~ 2.2 W/(mK)[269] at 300K, as estimated by the Debye-Callaway model[54,270]). Hence, extensive research has been undertaken recently to improve the thermoelectric performance of SnTe by optimizing its carrier concentration,[183,185,195,271] modifying its band structure,[142,185,226,259,268] and reducing its lattice thermal conductivity.[36,228,253]

The lattice thermal conductivity of SnTe can be effectively improved by alloying with the Ag-V-VI$_2$ compounds (V = Sb, Bi; VI= Te, Se),[36,272–274] which causes strong atomic disorder and phonon scattering. Following this approach, we attempted to alloy SnTe with

$AgSnSe_2$, that adopts a similar rock-salt crystal structure. Additionally, Liu et all.[275] observed that the lattice thermal conductivity of $SnSe_2$ can be reduced by alloying with $AgSnSe_2$, and Liang et all.[276] indicated that a strong atomic disorder could be introduced into the GeTe matrix through $AgSnSe_2$. Additionally, the low Seebeck coefficient of the pristine SnTe also needs to be addressed. It has been shown that 25% substitution of Sn by Pb improves the Seebeck coefficient through the band inversion between the valence band maximum and conduction band minimum.[226,277] Compared with the pristine PbTe, the Pb atomic amount decreased from 100% to 25%, which makes this material more suitable for applications. Motivated by these results, we pursued limited Pb substitution on the Sn site in $(SnTe)_{0.95}(AgSnSe_2)_{0.05}$ prepared during this study.

5.2 Experimental

5.2.1 Synthesis

The $(SnTe)_{1-x}(AgSnSe_2)_x$ (x = 0.01, 0.05 and 0.1), $(Sn_{0.875}Pb_{0.125}Te)_{0.95}(AgSnSe_2)_{0.05}$, and $(Sn_{0.75}Pb_{0.25}Te)_{0.95}(AgSnSe_2)_{0.05}$ samples were prepared via a solid-state melting method by using stoichiometric mixtures of the elemental tin, tellurium, selenium, silver, lead and manganese (purity of all elements was 99.99 wt.% or better). The stoichiometric mixtures were weighted and loaded into silica tubes with an inner diameter of 10mm, and this step was carried out in an Ar-filled glovebox (O_2 and H_2O amounts were below 0.1 ppm). The tubes were closed with a valve, transferred to a vacuum line, evacuated below 0.002 Torr, and flamed sealed. The samples were heated to 1000 °C at 100 °C/h, annealed for 24 hours, and then quenched in ice water.

5.2.2 Spark Plasma Sintering (SPS)

The samples were finely ground into powders using a mortar and pestle and then densified by SPS. Sample powders were loaded into a 15 mm diameter graphite die, placed into the SPS chamber, and evacuated. A layer of graphite paper was placed between the sample powder and graphite plungers to avoid direct contact. The samples were pressed under the uniaxial pressure of 45 MPa, heated to 550 °C at 100 °C/min, and annealed for 5 minutes, then cooling to room temperature, with all the steps being under dynamic vacuum.

5.2.3 X-ray Powder Diffraction

The powder X-ray diffraction (PXRD) analysis was performed on a PANalytical X'Pert Pro diffractometer with the $CuK\alpha_1$ radiation and an X'Celerator detector, and the diffraction data were collected in the 2θ range between 20° and 80° at room temperature. The Rietveld refinement (Rietica program[154]) was used to determine the lattice parameters and sample purity. Profile parameters (background, peak shape), lattice parameters, and sample displacement were refined. The atomic parameters and occupancies were taken from the work by Bauer et al. (for SnTe),[90] Schneider et al. and (for Ag_2Te),[278] and were not refined.

5.2.4 Thermoelectric Property Measurements

The electrical conductivity and Seebeck coefficient of all samples were performed on a bar shape specimen (3 mm × 3 mm × 10 mm) using a ULVAC-RIKO ZEM-3 instrument. A round shape specimen (Diameter = 12.75 mm) was used for the thermal diffusivity (D) measurement on a Netzsch LFA 467 instrument. The total thermal conductivity was calculated by $\kappa_{total} = D \times C_p \times \rho$. The heat capacity C_p was obtained from the Neumann-Kopp rule[161], which states that a compound's molar heat capacity equals the sum of its constituent molar heat capacities. The sample density ρ was determined by the Archimedes method.

Table 5.1. Specific heat capacity calculated by Neumann-Kopp rule.

Compound	C_p (J/(g·K))
$(SnTe)_{0.99}(AgSnSe_2)_{0.01}$	0.213
$(SnTe)_{0.95}(AgSnSe_2)_{0.05}$	0.217
$(Sn_{0.875}Pb_{0.125}Te)_{0.95}(AgSnSe_2)_{0.05}$	0.208
$(Sn_{0.75}Pb_{0.25}Te)_{0.95}(AgSnSe_2)_{0.05}$	0.200

5.2.5 Hall effect measurements

A square shape specimen *(*1 mm × 10 mm × 10 mm) was used for the Hall coefficients R_H measurement by the Van der Pauw method in an MMR Variable Temperature Hall System

(VTHS). The instrument was equipped with an AC excitation and a Stanford Research SR830 lock-in amplifier. The magnetic field (B) swapped from -1.3 T to 1.3 T and a fixed AC current (I) of 5 mA was applied.

The Hall coefficient was determined from $R_H = \frac{t \times V_H}{I \times B}$, where t is the thickness of the sample and V_H is the Hall voltage measured at room temperature. To eliminate the experimental errors, a linear fit was applied to a scatter graph with the V_H as the y axis and B as the x axis, and the slope gave the Hall coefficient. The hole concentration was determined from the equation $n_p = \frac{1}{eR_H}$, where e is an electron charge; the Hall carrier mobility μ_H was determined from $\mu_H = {R_H}/{\rho}$.

5.2.6 Scanning Electron Microscopy-Energy Dispersive X-ray Spectroscopy (SEM-EDS)

For the SEM-EDS analysis, the sample was polished with 800 and 1200-grit sandpapers, then secured with double sided carbon tape to the SEM sample holders. A pure nickel metal was used for signal calibration. The sample analysis was performed on a TESCAN VEGA II LSU scanning electron microscope (20 kV accelerating voltage) equipped with an X-MAX (80 mm^2) X-ray EDS spectrometer (Oxford Instruments). SEM results are provided in the Supporting Information.

3. Results and Discussion

5.3.1 $AgSnSe_2$ alloying of SnTe

The room temperature X-ray powder diffraction patterns of SnTe,[90] $(SnTe)_{1-x}(AgSnSe_2)_x$ (x = 0.01, 0.05 and 0.1), $AgSnSe_2$,[279] and Ag_2Te[278] are shown in Fig. 5.2 (a). The Rietveld refinement (Rietica program)[154] was used to establish the lattice parameter and sample impurity, and the refinement results are shown in the Supporting Information, Table 5.S1. The Bragg diffraction peaks of $(SnTe)_{1-x}(AgSnSe_2)_x$ (x = 0.01, 0.05 and 0.1) could be indexed to the rock salt structure ($Fm\bar{3}m$). No secondary phases were detected in $(SnTe)_{0.99}(AgSnSe_2)_{0.01}$ and $(SnTe)_{0.95}(AgSnSe_2)_{0.05}$, however, an Ag_2Te impurity was observed in $(SnTe)_{0.9}(AgSnSe_2)_{0.1}$. Presence of Ag_2Te in $(SnTe)_{0.99}(AgSnSe_2)_{0.01}$ suggests that the solubility limit for $(SnTe)_{1-x}(AgSnSe_2)_x$ has been reached, and that the final amount of $AgSnSe_2$ is different from the loading one. As the amount of $AgSnSe_2$ increases, the cell parameter a of $(SnTe)_{1-x}(AgSnSe_2)_x$ (x = 0.01, 0.05 and 0.1) decreases, which can be attributed to the smaller unit cell of $AgSnSe_2$ (a(SnTe) = 6.318(3) Å)[90] vs. a($AgSnSe_2$) = 5.677(3) Å)[279].

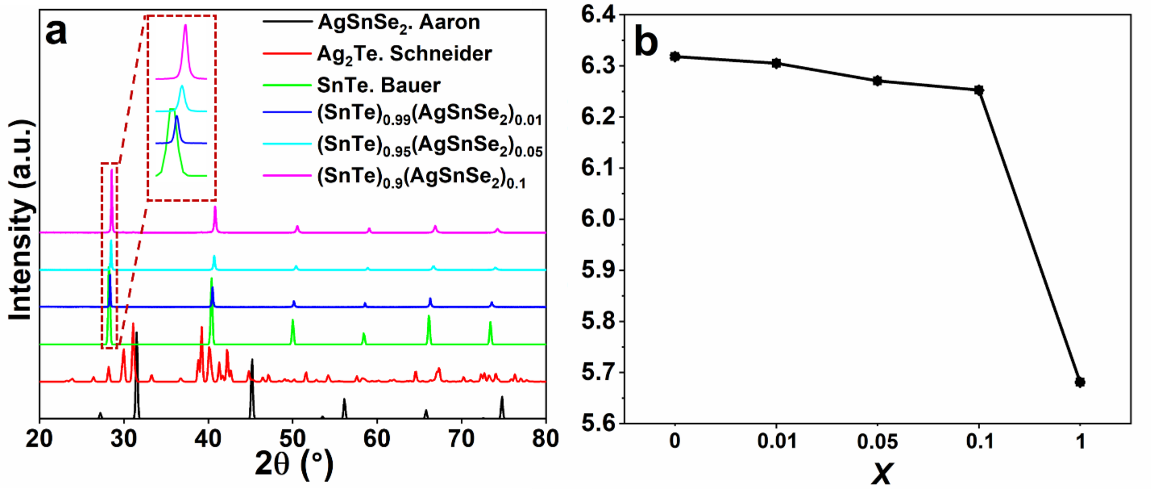

Figure 5.1. (a) PXRD patterns of SnTe,[90] $(SnTe)_{1-x}(AgSnSe_2)_x$ (x = 0.01, 0.05 and 0.1), $AgSnSe_2$,[279] and Ag_2Te[278] at room temperature. (b) The cell parameter a of $(SnTe)_{1-x}(AgSnSe_2)_x$ (x =0, 0.01, 0.05, 0.1 and 1).

Fig. 5.2 (a-c) show the electrical conductivity, Seebeck coefficient, and power factor of the SnTe, $(SnTe)_{1-x}(AgSnSe_2)_x$ ($x = 0.01$, 0.05 and 0.1) in the 25 – 600 ˚C temperature range. The electrical conductivity of the pristine SnTe decreases more rapidly with temperature and drops below that of the $(SnTe)_{1-x}(AgSnSe_2)_x$ samples above 200 ˚C, which can be related to different carrier scattering mechanisms. In pristine SnTe, the carrier scattering is dominated by phonon-electron interactions, which are temperature dependent.[29] In contrast, the carrier scattering in $(SnTe)_{1-x}(AgSnSe_2)_x$ is mainly associated with the atomic disorder, which is temperature independent.[188] Fig. 5.2 (b) shows a positive Seebeck coefficient for all samples, suggesting a *p*-type semiconductor behavior. The $(SnTe)_{0.9}(AgSnSe_2)_{0.1}$ shows the lowest Seebeck coefficient in $(SnTe)_{1-x}(AgSnSe_2)_x$; this can be related to the *n*-type Ag_2Te impurity. In comparison to pristine SnTe, the $(SnTe)_{1-x}(AgSnSe_2)_x$ samples show a higher Seebeck coefficient below 200 ˚C but a lower one at 250 – 600 ˚C. Since the Seebeck coefficient is inversely proportional to the carrier concentration;[280] the hole concentration is likely to be higher upon the $AgSnSe_2$ alloying if we consider the high temperature data. This conclusion is supported by the Hall carrier concentration data (Table 5.1). Benefiting from the higher Seebeck coefficient in 25 - 200 ˚C and higher electrical conductivity at 150 - 600 ˚C, $(SnTe)_{0.95}(AgSnSe_2)_{0.05}$ shows a higher power factor than the pristine SnTe in the 25 – 600 ˚C temperature range.

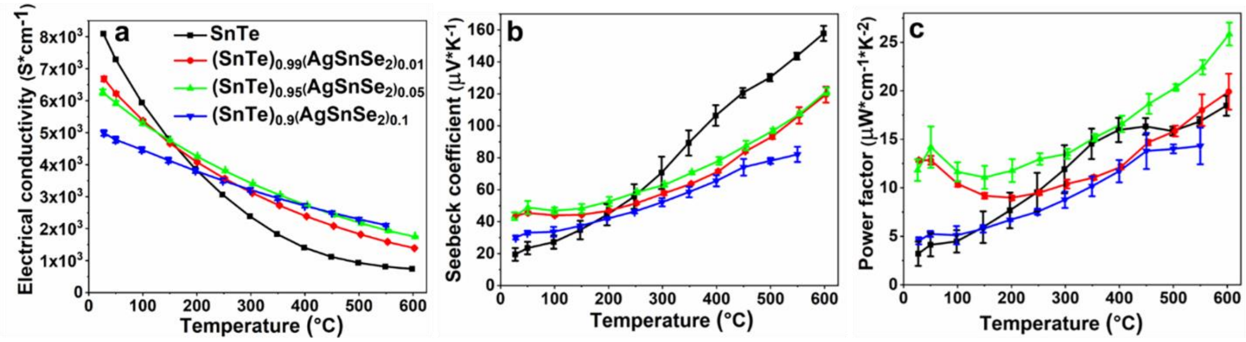

Figure 5.2. (a) Electrical conductivity, (c) Seebeck coefficient and (d) power factor of SnTe, $(SnTe)_{1-x}(AgSnSe_2)_x$ (x = 0.01, 0.05 and 0.1).

Increase in the carrier concentration in $(SnTe)_{1-x}(AgSnSe_2)_x$ is intriguing and most likely related to the Sn oxidation state. As was shown for $AgSnSe_2$, the +3 formal oxidation state for Sn in $AgSnSe_2$ results from the valence skipping between the +2 and +4 oxidation states.[281] One can argue, that upon the $AgSnSe_2$ alloying, the Sn from $AgSnSe_2$ tend to adopt predominantly the +2 state, identical to that of Sn in pristine SnTe. This leads to a higher hole concentration. A similar behavior was observed in GeTe-$AgSnSe_2$.[276] While $AgSnSe_2$ alloying increases the carrier concertation, it reduces the carrier mobility (Table 5.2). The carrier mobility decreases from 107 $cm^2V^{-1}s^{-1}$ in the pristine SnTe to 35 $cm^2V^{-1}s^{-1}$ in $(SnTe)_{0.95}(AgSnSe_2)_{0.05}$, primarily due to a more disordered structure, which intensifies carrier scattering. The carrier mean free path l_c of $(SnTe)_{1-x}(AgSnSe_2)_x$ was estimated according to $l_c = (\frac{\hbar\mu_H}{e})(3\pi^2 n_H)^{\frac{1}{3}}$,[220,276] where $\hbar$ is the reduced Planck constant and e is the elementary charge. As seen from the data in Table 5.2, the l_c decreases significantly upon the $AgSnSe_2$ alloying.

Table 5.2. Hall concentration, Hall mobility, carrier concentration, carrier mobility and Carrier mean free path l_c of SnTe, $(SnTe)_{0.99}(AgSnSe_2)_{0.01}$ and $(SnTe)_{0.95}(AgSnSe_2)_{0.05}$ at room temperature.

Composition	Carrier concentration n_H (10^{20} cm^{-3})	Carrier mobility μ_H (cm^{2}V^{-1}s^{-1})	Carrier mean free path l_c (nm)
SnTe	3.7(1)	107(2)	16.2
$(SnTe)_{0.99}(AgSnSe_2)_{0.01}$	4.7(3)	69(4)	9.4
$(SnTe)_{0.95}(AgSnSe_2)_{0.05}$	9.1(4)	35(2)	7.5

The thermal properties were measured for $(SnTe)_{1-x}(AgSnSe_2)_x$ (x = 0.01, 0.05 and 0.1). As shown in Fig. 5.3 (a), the pristine SnTe has a high total thermal conductivity (k_{total}) of ~9.1 Wm^{-1}K^{-1} at 25 ˚C, and it drops steadily with temperature. Below 350˚C, $(SnTe)_{0.99}(AgSnSe_2)_{0.01}$ shows a lower total thermal conductivity than the pristine SnTe, but a higher valuer after 350 ˚C. On the other hand, SnTe alloyed with 5 mol% $AgSnSe_2$ displays a lower thermal conductivity in the entire temperature range.

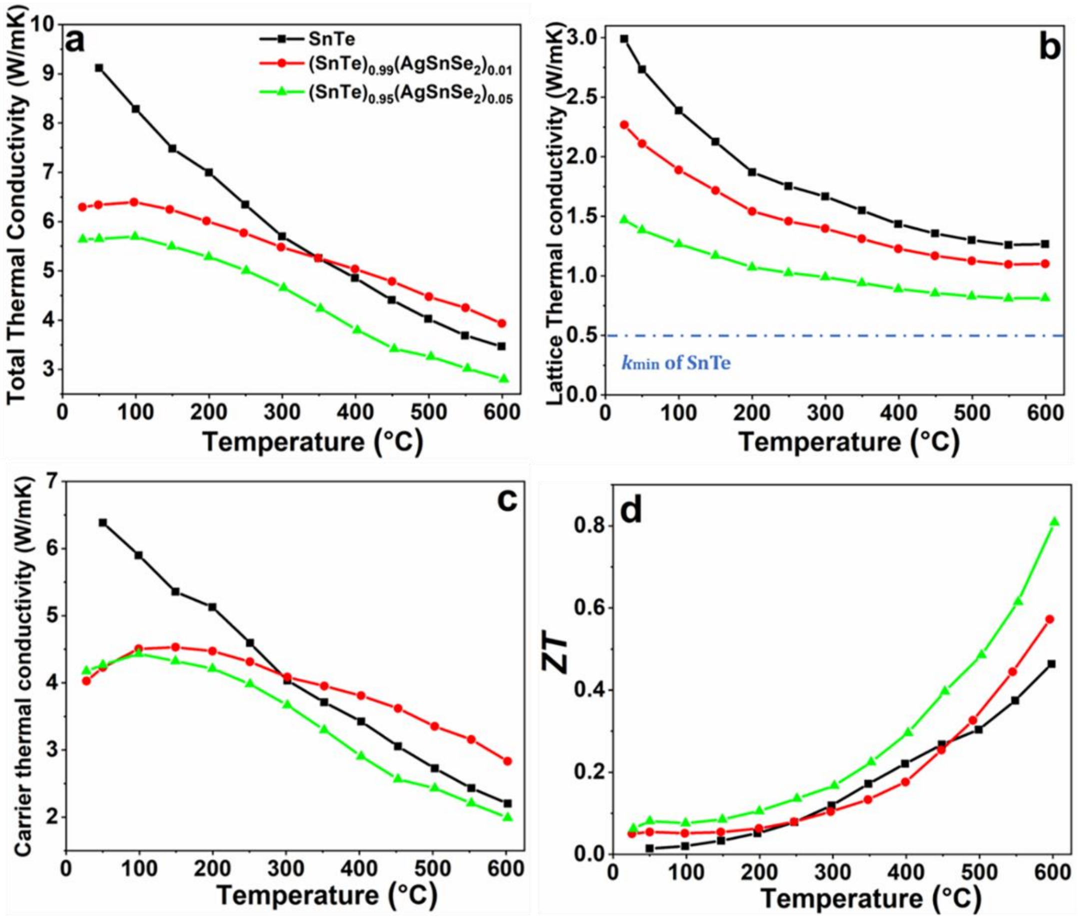

Figure 5.3. Temperature-dependent (a) total thermal conductivity; (b) lattice thermal conductivity; (c) carrier thermal conductivity, and (d) *ZT* values for $(SnTe)_{1-x}(AgSnSe_2)_x$ (x = 0, 0.01 and 0.05).

To better understand effect of $AgSnSe_2$ on the thermal conductivity of SnTe, the carrier thermal conductivity was calculated by the Wiedemann-Franz law ($k_e = L\sigma T$),[30] where L is the Lorentz factor defined from L= 1.5 + exp (-$^{|S|}/_{116}$).[42] The lattice thermal conductivity (k_l) was obtained by subtracting k_e from k_{total}. As shown in Fig. S1, k_l of $(SnTe)_{0.95}(AgSnSe_2)_{0.05}$ is lower than k_{min} of SnTe based materials (~0.5 $Wm^{-1}K^{-1}$) estimated from the model proposed by Chaill et al.[344] above 300 ˚C. This can be related to overestimation of the Lorentz factor, which leads to higher k_e and lower k_l. Since the Wiedemann-Franz law cannot be applied to $(SnTe)_{1-x}(AgSnSe_2)_x$, the Klemens-Drabble model[345] was used to predict lattice thermal conductivity.

$$\kappa_l^a = \frac{tan^{-1}u}{u}\kappa_l^p \text{ (5-1)}$$

$$u^2 = \left(\frac{\pi^2\theta_D\Omega}{hv^2}\right)\kappa_l^p\Gamma \text{ (5-2)}$$

$$\Gamma = x(1-x)[\left(\frac{\Delta M}{M}\right)^2 + \varepsilon\left(\frac{\Delta a}{a}\right)^2] \text{ (5-3)}$$

Where κ_l^a, κ_l^p, u, θ_D, Ω, h, v, Γ, x, and ε are the lattice thermal conductivity of the alloy and pure material, respectively, the disorder scaling parameter, the Debye temperature (θ_D= 140 K for SnTe)[282], the average volume per atom, the Plank constant, the sound velocity (υ = 1800 m s^{-1}, for SnTe)[282], the scattering parameter, alloying fractions, and a phenomenological parameter (163 for SnTe[209]). Moreover, M and a are the molar mass and lattice constant of the alloy, ΔM and Δa are the difference in molar mass and lattice constant between the two constituents. The κ_l^p of SnTe[268] was calculated by the Debye-Callaway model.[54,270]

Fig. 5.3 (b) shows the k_l of SnTe[268] calculated by the Debye-Callaway model, and k_l of $(SnTe)_{0.99}(AgSnSe_2)_{0.01}$ and $(SnTe)_{0.95}(AgSnSe_2)_{0.05}$ calculated by the Klemens-Drabble model. The lattice thermal conductivity is effectively optimized by alloying with $AgSnSe_2$, which could be attributed to the additional phonon scattering induced by point defects and mass fluctuation.[283] The k_l of SnTe and $(SnTe)_{0.99}(AgSnSe_2)_{0.01}$ decrease with temperature following T^{-1} law in the 25 – 600 ˚C temperature range, suggesting that the Umklapp process dominates the phonon scattering.[60] Such behavior is also observed for

$(SnTe)_{0.95}(AgSnSe_2)_{0.05}$ at 25 – 450 ˚C. As shown in Fig. 5.3 (a), the k_e of pristine SnTe decrease more rapidly with temperature and drop below that of the $AgSnSe_2$-alloyed samples above 150 ˚C, which can be related to the increase phonon-electron scattering.

The ZT values of the samples are presented in Fig. 5.3 (d). $(SnTe)_{0.95}(AgSnSe_2)_{0.05}$ displays the highest performance in the 25 – 600 ˚C temperature range (Fig. 5.3 (d)), with the largest *ZT* value being 0.81 at 600 ^{o}C. Next, we try to optimize the thermoelectric performance even further through Pb substitution.

5.3.2 Pb-substituted $(SnTe)_{0.95}(AgSnSe_2)_{0.05}$

Based on the room temperature PXRD data (Fig. 5.4 (a)), $(SnTe)_{0.95}(AgSnSe_2)_{0.05}$, $(Sn_{0.875}Pb_{0.125}Te)_{0.95}(AgSnSe_2)_{0.05}$ and $(Sn_{0.75}Pb_{0.25}Te)_{0.95}(AgSnSe_2)_{0.05}$ adopt a rock salt structure ($Fm\overline{3}m$), and no secondary phases could be detected. The cell parameter *a* increase with the Pb amount, which can be attributed to the larger effective cationic radius of Pb^{2+} (1.19Å vs. 1Å for Sn^{2+}).[284] Fig. 5.4 (b-d) shows the electrical conductivity, Seebeck coefficient, and power factor of $(SnTe)_{0.95}(AgSnSe_2)_{0.05}$, $(Sn_{0.875}Pb_{0.125}Te)_{0.95}(AgSnSe_2)_{0.05}$ and $(Sn_{0.75}Pb_{0.25}Te)_{0.95}(AgSnSe_2)_{0.05}$ in the 25 - 600 ˚C range. The electrical conductivity decreases with the Pb amount in the whole temperature range, and this stems primarily from a lower carrier concentration (Table 5.3). The Seebeck coefficient is slightly improved upon the Pb substitution, and $(Sn_{0.75}Pb_{0.25}Te)_{0.95}(AgSnSe_2)_{0.05}$ shows a higher Seebeck coefficient than $(SnTe)_{0.95}(AgSnSe_2)_{0.05}$ in the 100 - 600 ˚C range. However, the power factor for $(Sn_{0.75}Pb_{0.25}Te)_{0.95}(AgSnSe_2)_{0.05}$ is lower than for $(SnTe)_{0.95}(AgSnSe_2)_{0.05}$

in the whole temperature range, and this is primarily due to the decreased electrical conductivity.

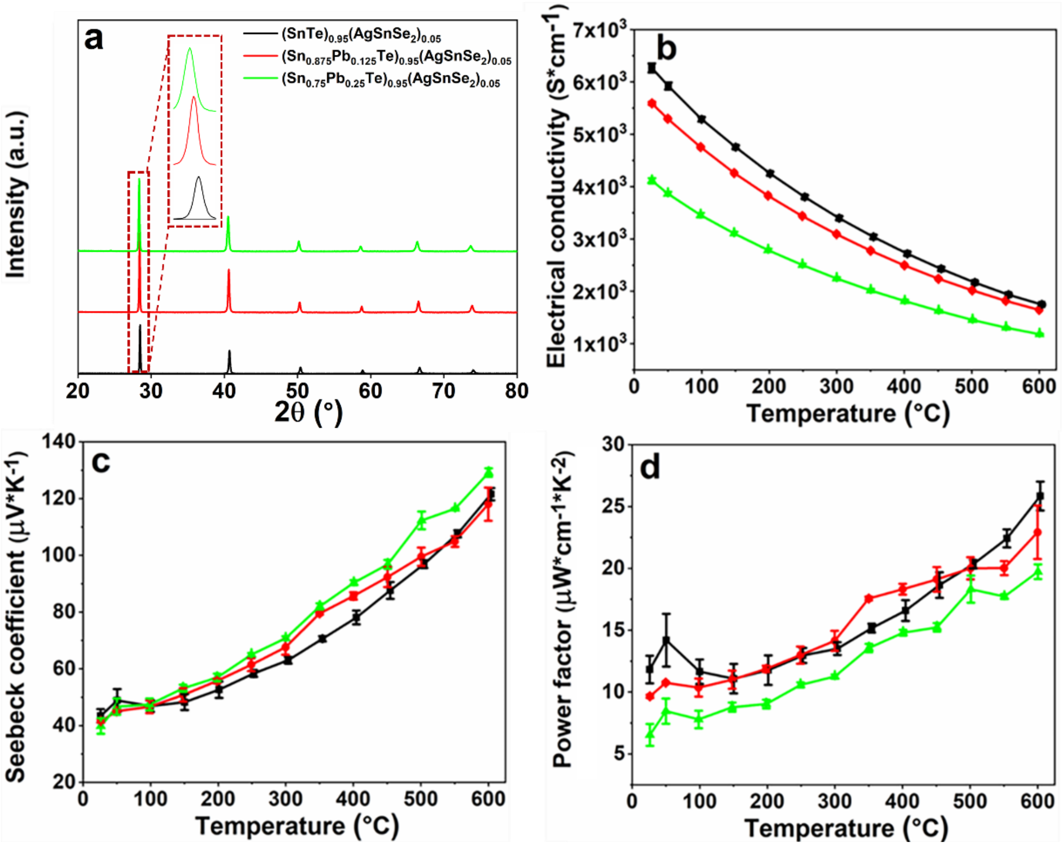

Figure 5.4. (a) PXRD patterns at room temperature. (b) Electrical conductivity, (c) Seebeck coefficient and (d) power factor.

As shown in Table 5.3, the carrier concentration decreases upon the Pb substitution; this can be attributed to the suppression of the Sn cation vacancies.[89,277] The carrier mobility does not change noticeably between $(SnTe)_{0.95}(AgSnSe_2)_{0.05}$ and the Pb-substituted samples. The carrier-carrier scattering is assumed to be suppressed by the Pb substitution due to the lower carrier concentration. However, the carrier scattering induced by point defects probably increases due to the extra atomic disorder. Thus, a decrease in l_c is most likely related to the extra atomic disorder.

Table 5.3. Hall concentration, Hall mobility, carrier concentration, carrier mobility and Carrier mean free path l_c of $(SnTe)_{0.95}(AgSnSe_2)_{0.05}$, $(Sn_{0.875}Pb_{0.125}Te)_{0.95}(AgSnSe_2)_{0.05}$ and $(Sn_{0.75}Pb_{0.25}Te)_{0.95}(AgSnSe_2)_{0.05}$ at room temperature.

Composition	Carrier concentration n_H (10^{20} cm^{-3})	Carrier mobility μ_H (cm^{2}V^{-1}s^{-1})	Carrier mean free path l_c (nm)
$(SnTe)_{0.95}(AgSnSe_2)_{0.05}$	9.1(4)	35(2)	7.5
$(Sn_{0.875}Pb_{0.125}Te)_{0.95}(AgSnSe_2)_{0.05}$	7.8(7)	32(3)	6.6
$(Sn_{0.75}Pb_{0.25}Te)_{0.95}(AgSnSe_2)_{0.05}$	6.7(3)	31(1)	6.2

Fig. 5.5 shows the room-temperature Seebeck coefficient vs. the Hall carrier concentration for the $AgSnSe_2$-alloyed SnTe samples. These data are compared to the theoretical Pisarenko plot for the pristine SnTe, computed by using the single parabolic band (SPB) model.[67,285] Also are shown the previously reported experimental data for the best-performing SnTe-based samples, with Ag,[286] $AgBiSe_2$,[274] $AgSbSe_2$[92] and $AgSbTe_2$[287]. All of the data points are above the theoretical Pisarenko curve, which suggests a heavier density of state (DOS) effective mass than in the pristine SnTe.[30,32]The increase in the DOS effective mass is probably due to the valence band convergence as reported for other SnTe-based phases.[25,248] It should be noted that the Seebeck coefficient and Hall concentration of $(SnTe)_{0.95}(AgSnSe_2)_{0.05}$ slightly decrease after the Pb substitution.

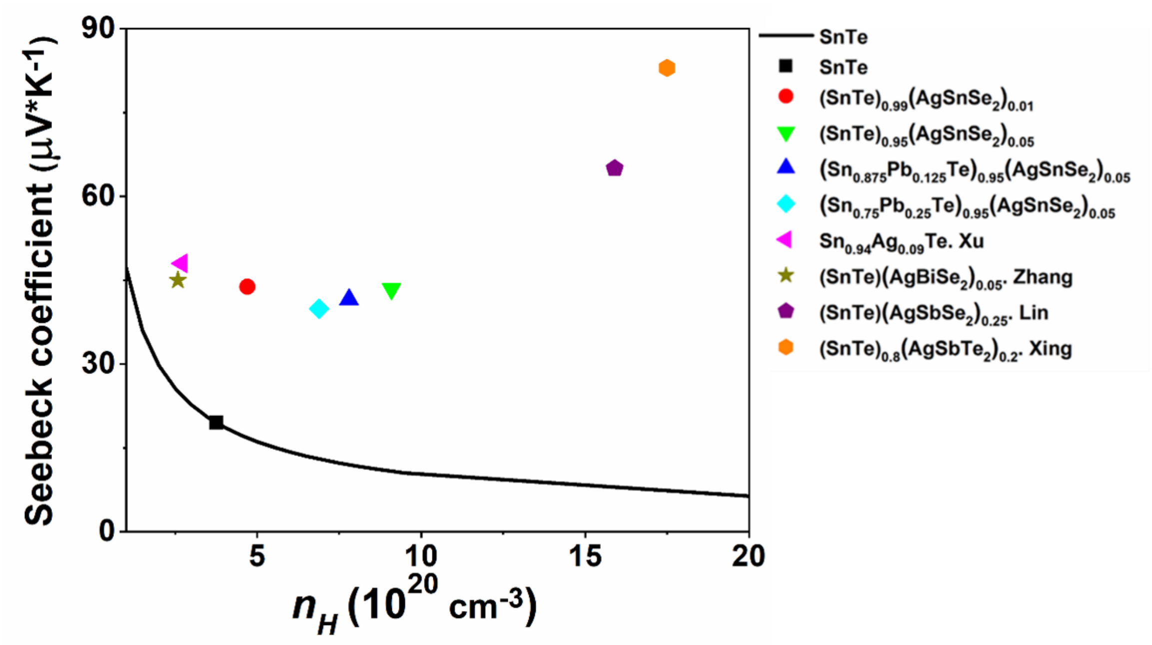

Figure 5.5. Pisarenko plot for pristine SnTe[285] and experimental data points for $(SnTe)_{0.99}(AgSnSe_2)_{0.01}$, $(SnTe)_{0.95}(AgSnSe_2)_{0.05}$, $(Sn_{0.875}Pb_{0.125}Te)_{0.95}(AgSnSe_2)_{0.05}$, $(Sn_{0.75}Pb_{0.25}Te)_{0.95}(AgSnSe_2)_{0.05}$, $Sn_{0.94}Ag_{0.09}Te$,[286] $(SnTe)(AgBiSe_2)_{0.05}$,[274] $(SnTe)(AgSbSe_2)_{0.25}$[92] and $(SnTe)_{0.8}(AgSbTe_2)_{0.2}$.[287]

Fig. 5.6 (a) shows thermal conductivity of the Pb-substituted samples. As can be seen, presence of Pb lowers thermal conductivity which can be attributed to the increased phonon scattering induced by extra atomic disorder and mass fluctuation. $(Sn_{0.875}Pb_{0.125}Te)_{0.95}(AgSnSe_2)_{0.05}$ achieves the *ZT* of 0.86 at 600 ˚C. Fig. 5.6 (c) compares our results within 25 - 600 ˚C with the literature ones.[92,274,286,287] According to the data, the thermoelectrical performance of pristine SnTe can be significantly improved via the AgXY_2 (X = Sn, Sb and Bi, Y = Te and Se) alloying. The experiment data suggests that $AgSnSe_2$-alloyed SnTe has a slightly better performance than the Ag-doped and $AgSbTe_2$-alloyed SnTe.

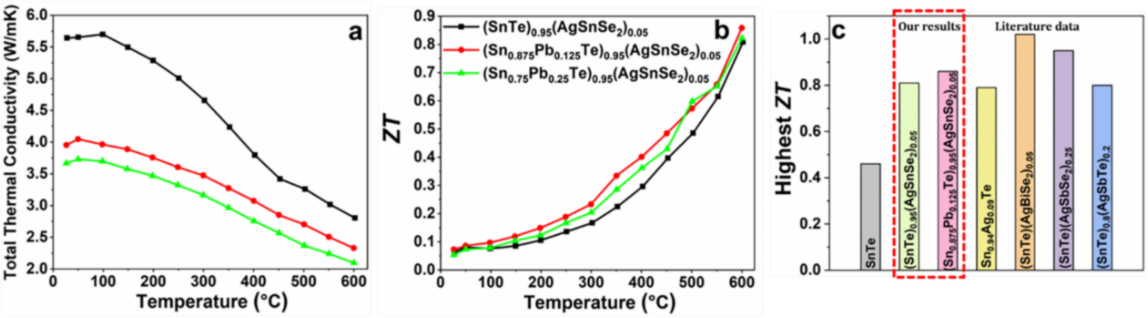

Figure 5.6. Temperature dependent (a) total thermal conductivity and (b) ZT values for $(SnTe)_{0.95}(AgSnSe_2)_{0.05}$, $(Sn_{0.875}Pb_{0.125}Te)_{0.95}(AgSnSe_2)_{0.05}$ and $(Sn_{0.75}Pb_{0.25}Te)_{0.95}(AgSnSe_2)_{0.05}$. (c) Comparisons of the Highest *ZT* within 25 - 600 ˚C of pristine SnTe, $(SnTe)_{0.95}(AgSnSe_2)_{0.05}$, $(Sn_{0.875}Pb_{0.125}Te)_{0.95}(AgSnSe_2)_{0.05}$, $Sn_{0.94}Ag_{0.09}Te$,[286] $(SnTe)(AgBiSe_2)_{0.05}$,[274] $(SnTe)(AgSbSe_2)_{0.25}$[92] and $(SnTe)_{0.8}(AgSbTe_2)_{0.2}$.[287]

5.4 Conclusions

The thermoelectrical performance of the pristine SnTe is significantly increased through the $AgSnSe_2$ alloying, which leads to the improved power factor and thermal conductivity. The thermal conductivity of $(SnTe)_{0.95}(AgSnSe_2)_{0.05}$ is further optimized by the Pb substitution, and $(Sn_{0.875}Pb_{0.125}Te)_{0.95}(AgSnSe_2)_{0.05}$ achieves the *ZT* of 0.86 at 600 ˚C. Unfortunately, the Pisarenko curve (Fig. 5.5) indicates that the Pb substitution lowers the DOS effective mass, which explains why the Seebeck coefficient of $(Sn_{0.875}Pb_{0.125}Te)_{0.95}(AgSnSe_2)_{0.05}$ is not improved significantly despite a lower carrier concentration. Still, the strategies employed for SnTe can be transferred to other materials. In particular, strong phonon scattering induced by the $AgSnSe_2$ alloying can be used to optimize the lattice thermal conductivity.

5.5 Supporting Information

Table 5.S1. *R* profile values, cell parameter *a* and impurity phases in $(SnTe)_{1-x}(AgSnSe_2)_x$ (x = 0.01, 0.05 and 0.1).

Composition	***Rp* (%)**	**Cell parameter *a* (Å)**	**Impurity phases (molar %)**	**X-ray density (g/cm^3)**	**Archimedes density (g/cm^3)**
$(SnTe)_{0.99}(AgSnSe_2)_{0.01}$	13.7	6.3067 (2)	-	6.49	6.384
$(SnTe)_{0.95}(AgSnSe_2)_{0.05}$	10.8	6.2695 (2)	-	6.494	6.422
$(SnTe)_{0.9}(AgSnSe_2)_{0.1}$	9.9	6.2524 (2)	Ag_2Te ~ 2.4(1)	6.423	6.387
$(Sn_{0.875}Pb_{0.125}Te)_{0.95}(AgSnSe_2)_{0.05}$	9.5	6.2829(1)	-	6.723	6.618
$(Sn_{0.75}Pb_{0.25}Te)_{0.95}(AgSnSe_2)_{0.05}$	8.7	6.2988(2)	-	6.937	6.827
$(Sn_{0.93}Mn_{0.07}Te)_{0.95}(AgSnSe_2)_{0.05}$	12.4	6.2691(2)	MnSe ~ 9.6(4) $MnSe_2$ ~ 1.1(2)	6.388	6.269

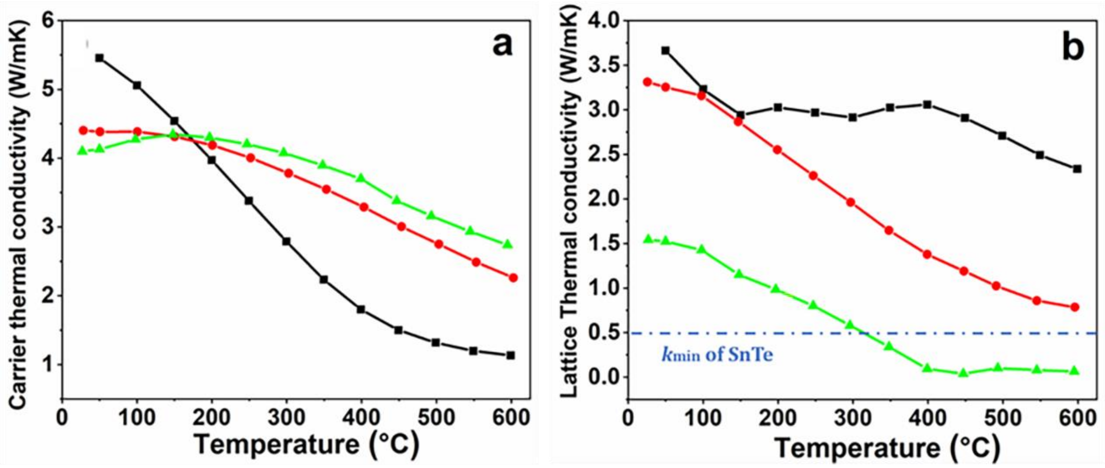

Fig. 5.S1**:** Temperature dependent (a) carrier thermal conductivity calculated by the Wiedemann-Franz law; (c) lattice thermal conductivity calculated by subtracting k_e from k_{total}.

Scanning Electron Microscopy-Energy Dispersive X-ray Spectroscopy (SEM-EDS)

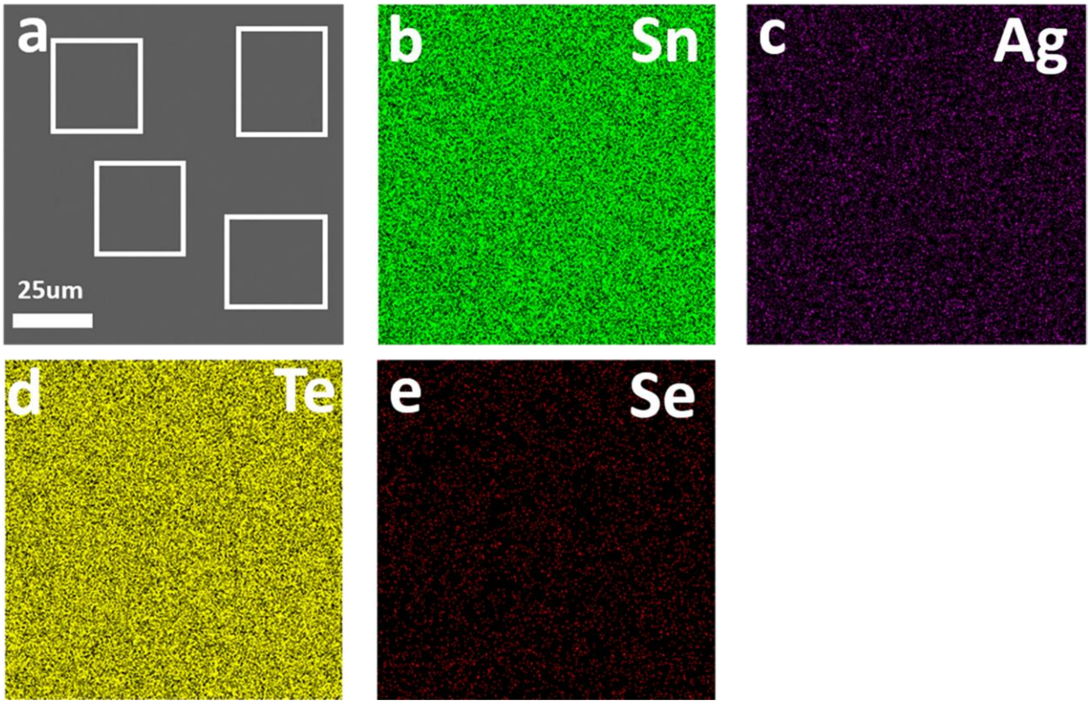

Fig. 5.S2: (a) Back-scattered electron image and (b-d) elemental mappings of Sn, Ag, Te and Se of $(SnTe)_{0.99}(AgSnSe_2)_{0.01}$. The average composition of the selected areas in (a) is 49.6(5) of Sn, 0.5(1) of Ag, 48.9(6) of Te and 1.0(1) at.% of Se.

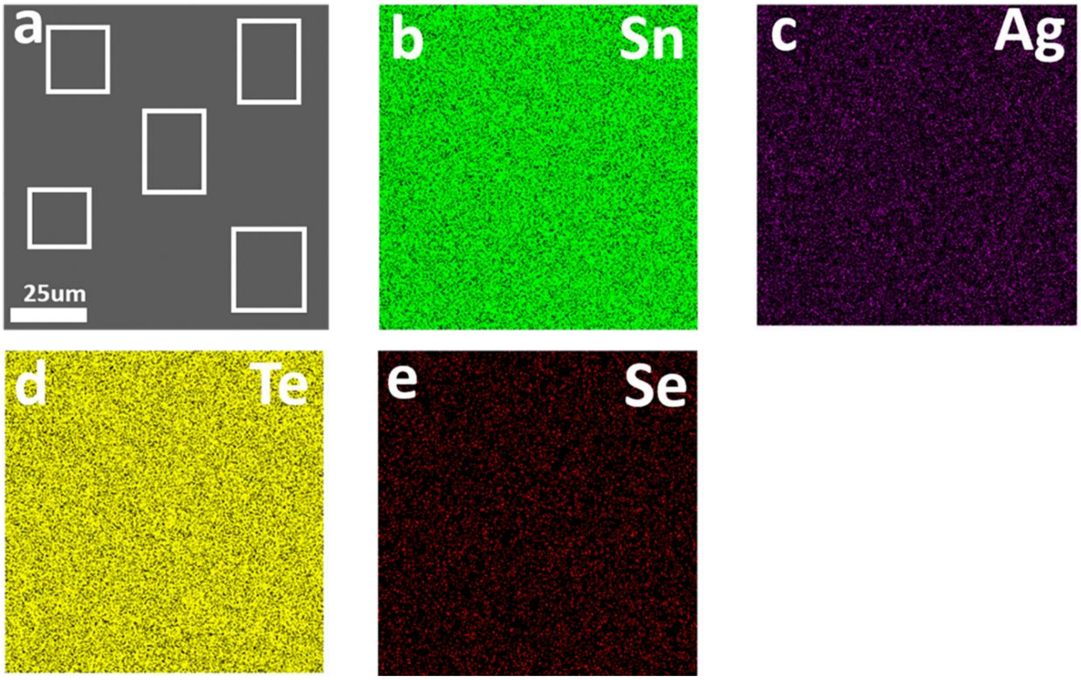

Fig. 5.S3: (a) Back-scattered electron image and (b-d) elemental mappings of Sn, Ag, Te and Se of $(SnTe)_{0.95}(AgSnSe_2)_{0.05}$. The average composition of the selected areas in (a) is 47.6(5) of Sn, 2.4(6) of Ag, 45.7(1) of Te and 4.3(4) at.% of Se.

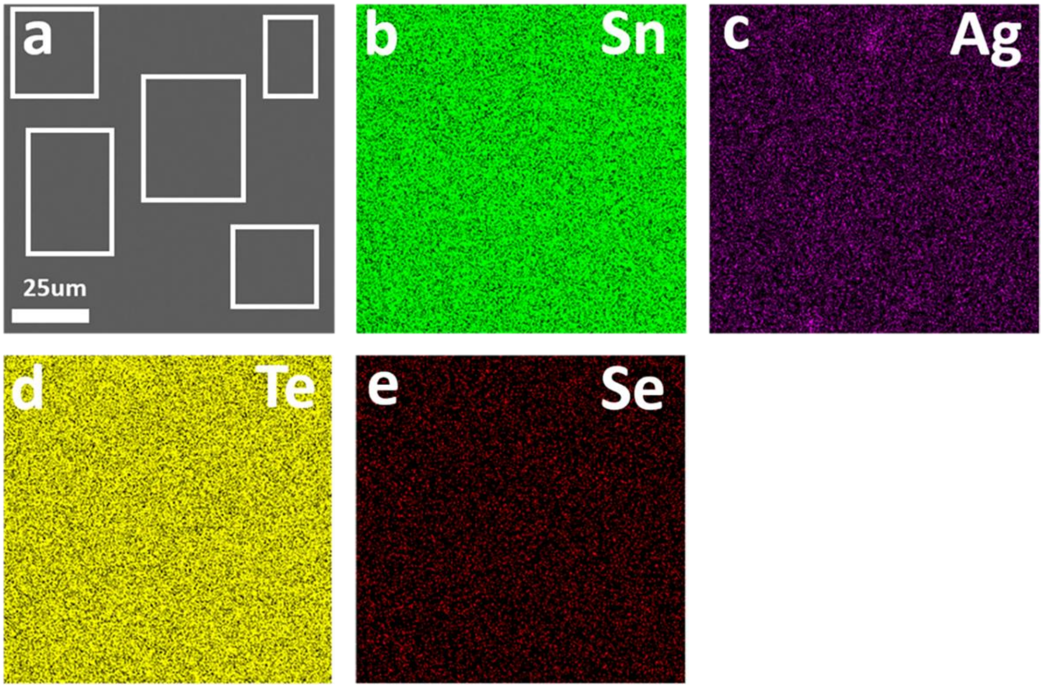

Fig. 5.S4: (a) Back-scattered electron image and (b-d) elemental mappings of Sn, Ag, Te and Se of $(SnTe)_{0.9}(AgSnSe_2)_{0.1}$. The average composition of the selected areas in is (a) 47.3(1) of Sn, 4.5(2) of Ag, 39.4(5) of Te and 8.8(5) at.% of Se.

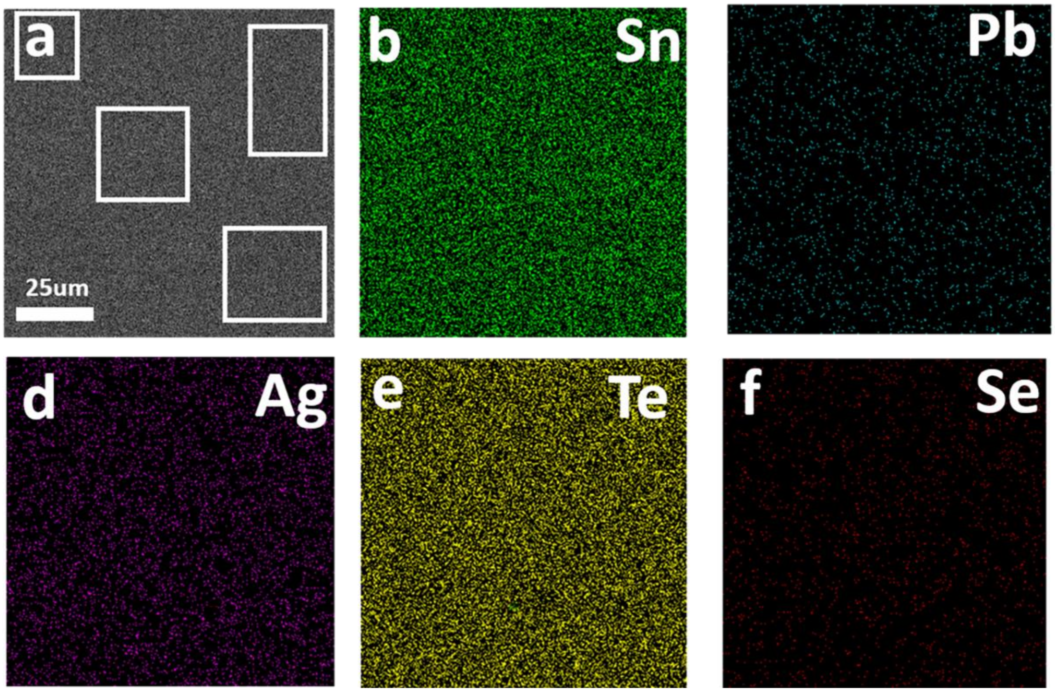

Fig. 5.S5: (a) Back-scattered electron image and (b-d) elemental mappings of Sn, Pb, Ag, Te and Se of $(Sn_{0.875}Pb_{0.125}Te)_{0.95}(AgSnSe_2)_{0.05}$. The average composition of the selected areas in (a) is 41.9(3) of Sn, 5.6(4) of Pb, 2.3(4) of Ag, 45.8(3) of Te and 4.4(3) at.% of Se.

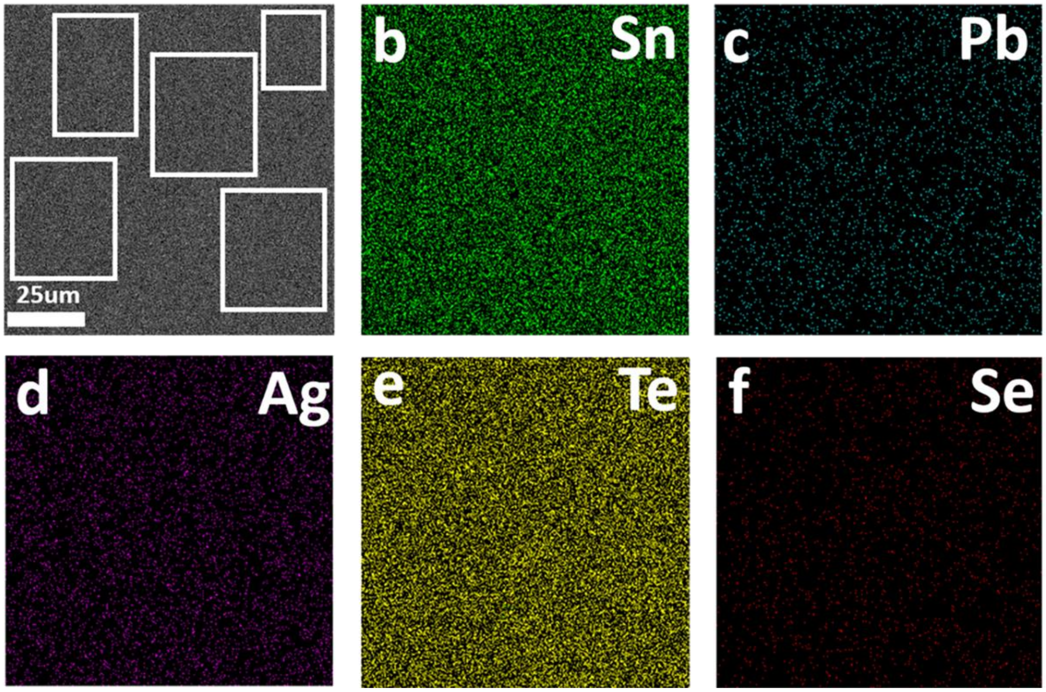

Fig. 5.S6: (a) Back-scattered electron image and (b-d) elemental mappings of Sn, Pb, Ag, Te and Se of $(Sn_{0.75}Pb_{0.25}Te)_{0.95}(AgSnSe_2)_{0.05}$. The average composition of the selected areas in (a) is 36.8(8) of Sn, 11.0(1) of Pb, 2.2(2) of Ag, 45.5(7) of Te and 4.5(3) at.% of Se.

Chapter 6. Converting n-Type $Co_4Ge_6Te_6$ Skutterudite into p-Type and Enhancing its Thermoelectric Properties through Fe Substitution

This chapter encompasses the manuscript "Converting *n*-Type $Co_4Ge_6Te_6$ Skutterudite into *p*-Type and Enhancing its Thermoelectric Properties through Fe Substitution", which was published in *Journal of Alloys and Compounds* (Journal of Alloys and Compounds 2022, 913, 165314). Partial sample preparations and characterization were performed by Mr. Yuyang Huang at the laboratory of Dr. Yurij Mozharivskyj, Department of Chemistry and Chemical Biology, McMaster University, Hamilton, ON. Mr. Suneesh Meledath Valiyaveettil collected the thermal diffusivities, specific heat capacity, and density of materials at the Department of Physics, National Central University, Taoyuan City 32001, Taiwan. The candidate completed the experimental procedures, sample characterization, electrical properties measurements, band structure calculation, data interpretation, and manuscript preparation.

Reproduced with permission from Song, S.; Huang, Y.; Tseng, Y.-C.; Valiyaveettil, S. M.; Chen, K.-H.; Mozharivskyj, *Journal of Alloys and Compounds* **2022**, 913, 165314.

This study is devoted to converting an *n*-type mixed anion $Co_4Ge_6Te_6$ skutterudite into a *p*-type material through partial substitution of Fe for Co. $Co_{4-x}Fe_xGe_6Te_6$ (x = 0, 0.04 and 0.12) samples were prepared by solid-state methods and characterized by scanning electron microscopy and powder X-ray diffraction. Thermoelectric properties of the spark plasma sintering samples were investigated in the temperature range of 50 to 500 °C. The positive Seebeck and Hall coefficients of $Co_{4-x}Fe_xGe_6Te_6$ (x = 0.04 and 0.12) suggest that the *n*-type $Co_4Ge_6Te_6$ was successfully converted into a *p*-type semiconductor via the Fe substitution. Also, an increased carrier concentration in $Co_{4-x}Fe_xGe_6Te_6$ (x = 0.04 and 0.12) leads to a significant increase in the electrical conductivity, which improves the thermoelectric performance of the mixed anion $Co_{4-x}Fe_xGe_6Te_6$ skutterudite.

6.1 Introduction

In recent years, environmental issues prompted a growing interest in thermoelectric materials due to their ability to directly convert waste heat into electricity without any negative environmental impacts.[288] Usually, the efficiency of thermoelectric material is determined by the dimensionless figure of merit , ZT: $ZT = \frac{\alpha^2\sigma}{\kappa_C+\kappa_l}T$, where α, σ, κ_C, κ_l and T are Seebeck coefficient, electrical conductivity, carrier thermal conductivity, lattice conductivity, and absolute temperature, respectively.[219] The ideal thermoelectric material is expected to behave as a phonon-glass electron-crystal (PGEC), which has a high, metal-like electrical conductivity and a low, glass-like thermal conductivity.[39] However, since α, σ, κ_C are interconnected via the charge carrier concentration and only κ_l could be modified independently,[39] it is challenging to find a simple material to work as a PGEC. In order to improve the ZT to the fullest extent, the current major strategies target not only improvements in the power factor ($\alpha^2\sigma$) by band structure engineering[76,184,224,225,229] and carrier concertation optimization,[195,261,266,271] but also reduction of κ_l by alloying[223,246,264,266] and introducing nanostructures.[228,236,237]

Binary skutterudites have the general formula MX_3 and adopt the space group $Im\overline{3}$ (M = Co, Rh or Ir; X = P, As, or Sb). The MX_3 structures contain X_4 rectangular anion rings formed by tilted MX_6 octahedra.[109–111] Large voids present in the MX_3 structures can be filled by electropositive atoms, and the composition of these filled skutterudites can be represented by the general formula $A_yM_4X_{12}$.[112] The binary $CoSb_3$ skutterudite attracted a lot of interest as it possesses excellent charge transport properties.[35,113] However, it also displays high thermal conductivity that limits its thermoelectric performance. The thermal conductivity of $CoSb_3$ and other binary skutterudites can be optimized by introducing guest atoms into voids (as in filled $A_yM_4X_{12}$), which leads to a significant phonon scattering.[116–120] These guest atoms also work as electronic dopants, and as a result they improve thermoelectric performance of the $CoSb_3$-based materials.

Ternary anion-mixed skutterudites with the $AX_{1.5}Y_{1.5}$ formula result from the isoelectronic substitution of the anion site in the binary skutterudites by two aliovalent p elements. $CoGe_{1.5}Y_{1.5}$ (Y = S, Se) is one member of such family,[121] and its structure was refined by Vaqueiro et al. using powder neutron diffraction.[122] Figure 6.1 shows the crystal structures of $CoSb_3$ and $CoGe_{1.5}Te_{1.5}$. Compared with the binary $CoSb_3$, which has only one crystallographically distinct four-membered ring ($[Sb_4]^{4-}$) with a rectangular shape (Figure 6.1 (c)),[126] the ternary $CoGe_{1.5}Te_{1.5}$ has two crystallographically distinct four-membered rings ($[Ge_2Te_2]^{4-}$, Figure 6.1 (c)), in which the Ge and Te atoms are trans to the same atoms.[122] Also, the $[Ge_2Te_2]^{4-}$ rings of $CoGe_{1.5}Te_{1.5}$ are diamond-like rather than rectangular.[122] According to the powder neutron diffraction study, the anions are ordered in the layers perpendicular to the [111] direction in the $CoGe_{1.5}Te_{1.5}$ unit cell. This arrangement along with the distortion of the anion ring leads to the symmetry reduction from the cubic $Im\bar{3}$ to the rhombohedral $R\bar{3}$ one.[122] At 610 °C, $CoGe_{1.5}Te_{1.5}$ undergoes a phase transition from the rhombohedral $R\bar{3}$ to the cubic $Im\bar{3}$.[123]

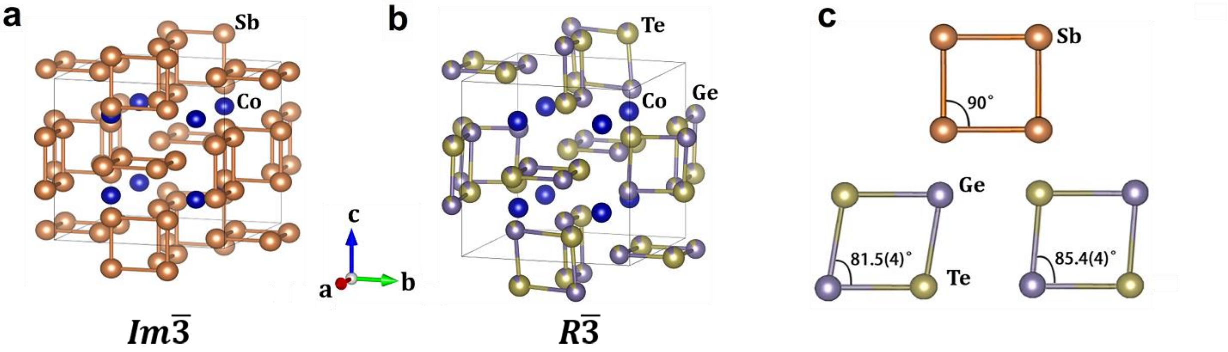

Figure 6.1 Crystal structure of (a) $CoSb_3$[126] (space group $Im\bar{3}$) and (b) $CoGe_{1.5}Te_{1.5}$[128] (space group $R\bar{3}$). In $CoGe_{1.5}Te_{1.5}$, the Ge sites have some Te atoms and vice versa. (c) A four-membered rectangular ring ($[Sb_4]^{4-}$) in $CoSb_3$ and two crystallographically distinct diamond-like rings ($[Ge_2Te_2]^{4-}$) in $CoGe_{1.5}Te_{1.5}$.

Unlike binary skutterudites, ternary skutterudites display low electrical conductivity, high Seebeck coefficient, and low lattice thermal conductivity.[123,289–292] Volja et all.[293] applied first principles calculations to study the electronic band structure of both binary and ternary skutterudites. In comparison with the binary $CoSb_3$ skutterudite, $Co_4Ge_6Te_6$ and $Co_4Sn_6Te_6$ each have a larger Seebeck coefficient and a lower electrical conductivity, which were attributed to their multivalley band structure with heavy charge carriers. Also, a much lower lattice conductivity was observed in both $Co_4Ge_6Te_6$ and $Co_4Sn_6Te_6$, which can be attributed to the extra phonon scattering induced by the larger complexity of and significant anionic disorder in the unit cell.[293] In the past decade, numerous studies explored the *n*-type $Co_4Ge_6Te_6$,[122,123,289,293] however, the *p*-type $Co_4Ge_6Te_6$ was not investigated to a similar extend. In this work, Fe substitution on the Co site is employed to convert an *n*-type $Co_4Ge_6Te_6$ into a *p*-type material, and the thermoelectric properties of the *p*-type $Co_{4-x}Fe_xGe_6Te_6$ (x = 0.04 and 0.12) is reported.

6.2 Experimental

6.2.1 Synthesis

Polycrystalline $Fe_xCo_{4-x}Ge_6Te_6$ samples (x = 0, 0.04, 0.12 and 0.2) were prepared from stoichiometric mixtures of cobalt (99.9 wt.%), germanium (99.99 wt.%), tellurium (99.999 wt.%) and iron (99.5 wt.%). Germanium and tellurium were ground into fine powders and mixed with the cobalt and iron powders inside an Ar-filled glovebox (O_2 and H_2O amounts were below 0.1 ppm). The mixtures were cold pressed into pellets and then loaded into carbon-coated silica tubes in the Ar-filled glovebox. The tubes were closed, transferred to a vacuum line, evacuated below 0.002 Torr and flamed sealed. The samples were heated at 100 °C/h to 400 °C and annealed at this temperature for 12 hours. This was followed by heating at 100 °C/h to 1150 °C, where the samples were annealed for 6 hours and then quenched in ice water. The solid products were hand-ground and cold-pressed in air. Subsequently it was annealed in evacuated silica tubes at 610 °C for 96 hours and quenched in ice water. The last annealing process was repeated one more time to eliminate the impurity phases.

6.2.2 Spark Plasma Sintering (SPS)

The annealed samples were finely ground into powders and loaded into a 15 mm diameter graphite die. A layer of mica paper was placed between the sample and graphite plungers to avoid direct contact between them. The samples were heated at 100 °C/min to 550 °C and annealed for 25 minutes under the uniaxial pressure of 45 MPa, followed by cooling to room temperature.

6.2.3 X-ray Powder Diffraction

The powder X-ray diffraction (PXRD) analysis was carried out in a PANalytical X'Pert Pro diffractometer with the $\mathrm{CuK}\alpha_1$ radiation and an X'Celerator detector. The samples were ground into fine powder and loaded on a zero-background silicon disc. The diffraction data were collected in the 2θ range of 20° to 80° at room temperature. The sample purity and lattice parameters were determined by the Rietveld refinement (Rietica program[154]). The profile parameters (background, peak shape), lattice parameters and sample displacement were refined. The atomic parameters and occupancies were taken from the work by Vaqueiro et al. (for $Co_4Ge_6Te_6$),[128] Betzembroeck et al. (for CoTe),[294] Muhler et al. (for $CoTe_2$),[295] and Samanta et al. (for GeTe),[296] and were not refined.

6.2.4 Thermoelectric Measurements

SPS pellets were cut into rectangular bars (3 mm × 3 mm × 10 mm) for the Seebeck coefficient and electrical conductivity measurements, or into squares (10 mm × 10 mm × 1 mm) for thermal conductivity, Hall carrier concentration and mobility measurements. The sample was cut on a low-speed diamond saw, and kerosene was used as a lubricant to prevent sample oxidation during cutting.

Electrical conductivity and Seebeck coefficient measurements were carried out on a ULVAC-RIKO ZEM-3 instrument. A Netzsch LFA 457 instrument was used to collect the thermal diffusivity (D) of samples, and the total thermal conductivity was calculated by $\kappa_{total} = D \times C_p \times \rho$. The standard sample (pyroceram) was used as a reference for the temperature dependent specific heat capacity C_p measurements. The density ρ of the $Co_{3.88}Fe_{0.12}Ge_6Te_6$ sample was measured by the Archimedes method and it was 96.8% of the theoretical density.

6.2.5 Hall Effect Measurements

The Hall coefficients R_H were measured by the Van der Pauw method in an MMR Variable Temperature Hall System (VTHS) modified with AC excitation and detection from a Stanford Research SR830 lock-in amplifier. The magnetic field (B) swapped from -1.3 T to 1.3 T and the AC current (I) was fixed at 5 mA. The Hall coefficient was calculated from $R_H = \frac{t \times V_H}{I \times B}$, where t is the thickness of the sample and V_H is the Hall voltage measured at room temperature. A scatter graph plotted with the V_H as the y axis and B as the x axis was used to obtain a linear fit, the slope of which allowed the Hall coefficient to be derived.

The Hall carrier mobility μ_H was calculated by $\mu_H = {}^{R_H}/_{\rho}$, where ρ is the sheet resistance, and the hole concentration was calculated based on the equation of $n_\mathrm{p} = \frac{1}{eR_H}$, where e is an electron charge.

6.2.6 Scanning Electron Microscopy-Energy Dispersive X-ray Spectroscopy (SEM-EDS)

For the SEM-EDS analysis, the samples were polished with 800 and 1200 grit sandpapers and then secured with double-sided carbon tape on the SEM sample holders. The SEM-EDS analysis was carried out on a TESCAN VEGA II LSU scanning electron microscope (20 kV accelerating voltage) equipped with an X-MAX (80 mm^2) X-ray EDS spectrometer (Oxford Instruments). The standard sample (pure nickel metal) was used for the signal calibration.

6.2.7 Computational Details

The room-temperature structure of $Co_8Ge_{12}Te_{12}$[128] was used for the tight-binding linear-muffin-tin-orbital calculations using the atomic sphere approximation (TB-LMTO-ASA)[168]. Space-filling empty spheres were included into the unit cell by the automatic sphere generation to satisfy the overlap criteria. The 3*d*, 4*s* orbitals of Co, 3*d*, 4*s*, and 4*p* ones of Ge and 4*d*, 5*s*, 5*p* ones of Te were employed during the TB-LMTO-ASA calculations.

6.3 Results and Discussion

Among the binary skutterudites, the *p*-type $CoSb_3$-based materials have been extensively studied[115,115,297–299] due to their excellent electrical properties and their relatively simple solid state synthesis. Among the ternary mixed anion skutterudites, the *n*-type $Co_4Ge_6Te_6$ received a lot of attention as it has a larger Seebeck coefficient[123] and a lower thermal conductivity than the binary $CoSb_3$.[300] However, the development of *p*-type $Co_4Ge_6Te_6$ was lagging, possibly because of the difficulties in preparing the $Co_4Ge_6Te_6$-based materials. This work describes our efforts to convert *n*-type $Co_4Ge_6Te_6$ into a *p*-type material via partial Fe substitution. Our approach relies on the idea that Fe will adopt a 3+ oxidation state like Co, but because of its lower electron count (d^5 in Fe^{3+} vs. d^6 in Co^{3+}), the Fermi level in the Fe-substituted $Co_4Ge_6Te_6$ will shift into the valence band, leading to the *p*-type conductivity.

Based on the room temperature X-ray powder diffraction patterns (Figure 6.2), $Co_{4-x}Fe_xGe_6Te_6$ (x = 0, 0.04, 0.12 and 0.2) adopts a rhombohedral symmetry ($R\overline{3}$). Three impurity phases, CoTe (*Pnnm*), $CoTe_2$($P6_3/mmc$), and GeTe ($R3m$), could be detected in small quantities. The sample purity and lattice parameter were determined by the Rietveld refinement (Rietica program)[154], and the refinement results are shown in Table 6.1 With an increasing Fe amount, the cell volume of $Co_{4-x}Fe_xGe_6Te_6$ (x = 0, 0.04, and 0.12) goes up, which can be attributed to a slightly larger effective cationic radius of Fe^{3+} (0.55Å vs. 0.545Å for Co^{3+}).[284] The smaller cell volume for $x = 0.2$ in comparison to $x = 0.12$ suggests that the solubility limit for $Co_{4-x}Fe_xGe_6Te_6$ has already been reached and some non-equilibrium processes occur in the sample. While the Fe impurities could be suspected in the $Co_{3.80}Fe_{0.20}Ge_6Te_6$ sample, the concentration of elemental Fe could not be reliably refined due to the overlap of the most intensive (110) peak of Fe with the peaks from $Co_{4-x}Fe_xGe_6Te_6$ and CoTe. To verify the conclusions from the PXRD analysis, the Co_{4-}

$_x$Fe$_x$Ge$_6$Te$_6$ (x = 0, 0.04, 0.12 and 0.2) sample were analyzed by the SEM-EDS technique. As seen in the SEM-EDS images (Figures 6.S.1-6.S.3), the $Co_4Ge_6Te_6$, $Co_{3.96}Fe_{0.04}Ge_6Te_6$, and $Co_{3.88}Fe_{0.12}Ge_6Te_6$ samples feature a homogenous elemental distribution with small amounts of GeTe, CoTe and $CoTe_2$. The $Co_{3.80}Fe_{0.20}Ge_6Te_6$ sample contains Fe precipitates (Figure 6.S4) in addition to the CoTe and $CoTe_2$ impurities that have already been identified through the PXRD.

Table 6.1 *R* profile values, unit cell volume and impurity phases of $Co_{4-x}Fe_xGe_6Te_6$ (x = 0, 0.04, 0.12 and 0.2)

Composition	***Rp*, %**	**Cell volume, Å³**	**Impurity phases (molar %)**
$Co_4Ge_6Te_6$	4.63	1988.15(7)	CoTe~ 0.02 (1) $CoTe_2$~ 0.07 (2) GeTe~0.2(1)
$Co_{3.96}Fe_{0.04}Ge_6Te_6$	4.80	1988.55(9)	CoTe~ 0.03 (2) $CoTe_2$~ 0.2 (1) GeTe~0.2(1)
$Co_{3.88}Fe_{0.12}Ge_6Te_6$	7.06	1989.49(9)	CoTe~ 0.15 (2) $CoTe_2$~ 0.3(1) GeTe~0.3(1)
$Co_{3.80}Fe_{0.20}Ge_6Te_6$	6.46	1989.08(6)	CoTe~ 0.28 (3) $CoTe_2$~ 0.9 (1)

Electrical conductivity, Seebeck coefficient, and power factor of the Fe-substituted samples in comparison to pristine $Co_4Ge_6Te_6$ are shown in Fig. 6.2 (b-d). Fe substitution leads to an increase in electrical conductivity. The electrical conductivity of $Co_{3.8}Fe_{0.2}Ge_6Te_6$ almost equals to that of $Co_{3.88}Fe_{0.12}Ge_6Te_6$, which supports that the maximum solubility of Fe has already been reached before $x = 0.2$. For all Fe-doped samples, the electrical conductivity decreases with an increasing temperature from 150 to 400 or 450 °C, which is likely due to the phonon-electron scattering[52,283]. Above 400 or 450 °C, the electrical conductivity increases whereas the Seebeck coefficient decreases, and both of these changes can be attributed to the bipolar effect.[301] The negative thermopower of the pristine $Co_4Ge_6Te_6$ (Fig 6.2 (c)) implies that electrons are the dominant charge carriers, and the positive values of the Fe-substituted samples indicates that holes are the dominant ones. These data suggest that the *n*-type $Co_4Ge_6Te_6$ has been successfully converted into a *p*-type material via Fe substitution. Besides, the power factor of the Fe-substituted samples is higher than that of the pristine $Co_4Ge_6Te_6$ (Fig 6. 2 (d)), and this is primarily due to the improved electrical conductivity.

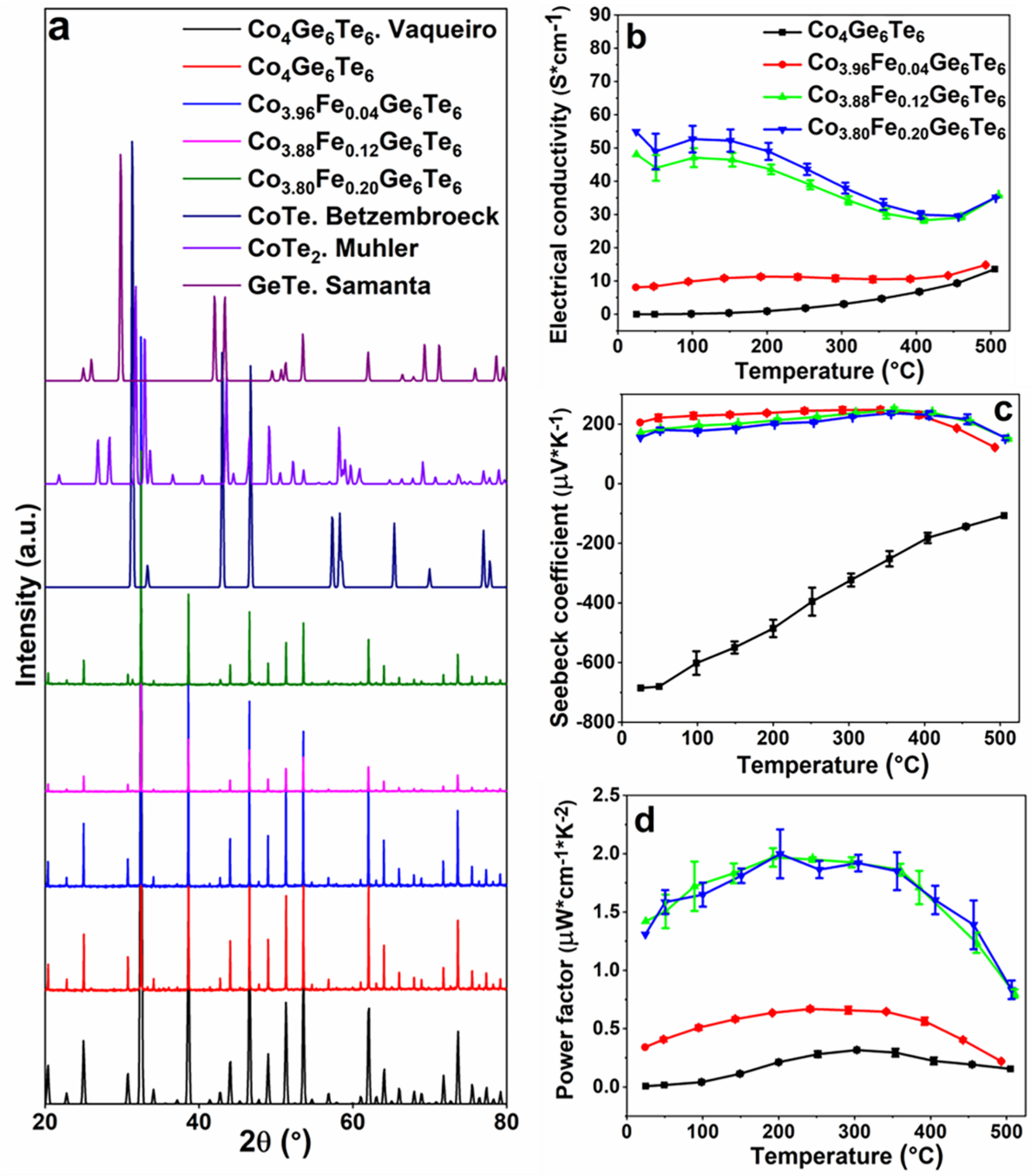

Figure 6.2 PXRD patterns of $Co_4Ge_6Te_6$,[128] $Co_{4-x}Fe_xGe_6Te_6$ (x = 0, 0.04, 0.12 and 0.2), CoTe,[294] $CoTe_2$[295] and GeTe[296] at room temperature. (b) Electrical conductivity, (c) Seebeck coefficient and (d) power factor of $Co_{4-x}Fe_xGe_6Te_6$.

To gain further insights into the charge transport properties, we measured the Hall effect. The positive Hall coefficient of $Co_{4-x}Fe_xGe_6Te_6$ (x = 0.04, and 0.12, Table 6.2) indicates that holes are the dominant carriers upon the Fe substitution, thus confirming the successful conversion of the *n*-type $Co_4Ge_6Te_6$ into a *p*-type material. The carrier concentration of $Co_{4-x}Fe_xGe_6Te_6$ (x = 0, 0.04, and 0.12) increases with the Fe amount. Using the Hall carrier concentration, Seebeck coefficient and employing the single parabolic band (SPB) model[67], we derived a DOS effective mass at room temperature. The Fe-substituted samples have significantly lighter charge carriers, which translates into a higher carrier mobility despite the fact that an additional atomic disorder on the Co site should lead to a larger carrier scattering and shorter relaxation time.

Table 6.2 Hall coefficient, Hall concentration, Hall mobility, carrier concentration, carrier mobility and DOS effective mass of $Co_4Ge_6Te_6$, $Co_{3.96}Fe_{0.04}Ge_6Te_6$ and $Co_{3.88}Fe_{0.12}Ge_6Te_6$ at room temperature.

Composition	Hall coefficient (10^{-6} mm^3/C)	Carrier concentration (10^{18} cm^{-3})	Carrier mobility (cm^{2}V^{-1}s^{-1})	m^*/m_0
$Co_4Ge_6Te_6$	-9.08(1)	0.68(5)	3.2(2)	5.46
$Co_{3.96}Fe_{0.04}Ge_6Te_6$	1.19(1)	5.2(1)	5.0(1)	0.47
$Co_{3.88}Fe_{0.12}Ge_6Te_6$	0.18(1)	33.0(5)	4.3(6)	1.19

Figure 6.3 (a) demonstrates the band structure of $Co_4Ge_6Te_6$; the Fermi level was placed at the bottom of conduction band since the pristine $Co_4Ge_6Te_6$ is an n-type conductor. The conduction band minimum (CBM) is flatter than the valence band maximum (VBM), and both are found at the Γ point. Multiple flat bands are also observed slightly above the Fermi level in $Co_4Ge_6Te_6$, and their occupancy would increase the carrier effective mass. These

band features suggest that the *n*-type $Co_4Ge_6Te_6$ should have a higher Seebeck coefficient than the *p*-type $Co_4Ge_6Te_6$, which is consistent with the experimental results. For the Fe-substituted $Co_4Ge_6Te_6$, the Fermi level shifts into the valence band, and as the Fe concentration increases, the hole concentration increases, and the Fermi level moves deeper into the valence band. This also leads to heavier carriers,[74,302,303] as now the flatter bands just below the VBM can contribute to the transport properties. Figure 6.3 (b) shows the density of states (DOS) of $Co_4Ge_6Te_6$ and projected DOS of Co, Ge and Te. The valence band is dominated by the Co states, except for the VBM where the contribution from Te is similar. In the light of the Co contribution to the valence band, Fe substitution in the *p*-type $Co_{4-x}Fe_xGe_6Te_6$ is expected to disrupt hole transport, leading to the shorter relaxation time, τ. This explains why the carrier mobility ($\mu = e\tau/m^*$) did not increase commensurately with a drop in the carrier effective mass (Table 6.2).

The calculated band gap (E_g) of $Co_4Ge_6Te_6$ is 0.46 eV, which is similar to E_g = 0.51 eV obtained by D. Volja et al.[398] The band gap can be also estimated from the experimental data by using the $|S_{max}| = E_g /(2eT_{max})$ equation,[32] where S_{max} is the maximum value of Seebeck coefficient, e the electron charge and T_{max} is the absolute temperature at which the maximum occurs. For the pristine $Co_4Ge_6Te_6$, the highest $|S_{max}|$ of 685 μV/K is observed at T_{max} = 298 K, which yield E_g = 0.41 eV, the value close to the calculated E_g. For the Fe-substituted samples, the peak in the thermopower shifts to higher temperatures, and the calculated E_g values are 0.30 and 0.31 eV for $Co_{3.96}Fe_{0.04}Ge_6Te_6$ and $Co_{3.88}Fe_{0.12}Ge_6Te_6$, respectively. Based on these results, one can speculate that the band structure and band gap are modified upon the Fe substitution, but additional electronic structure analysis will have to be performed to gain better understanding.

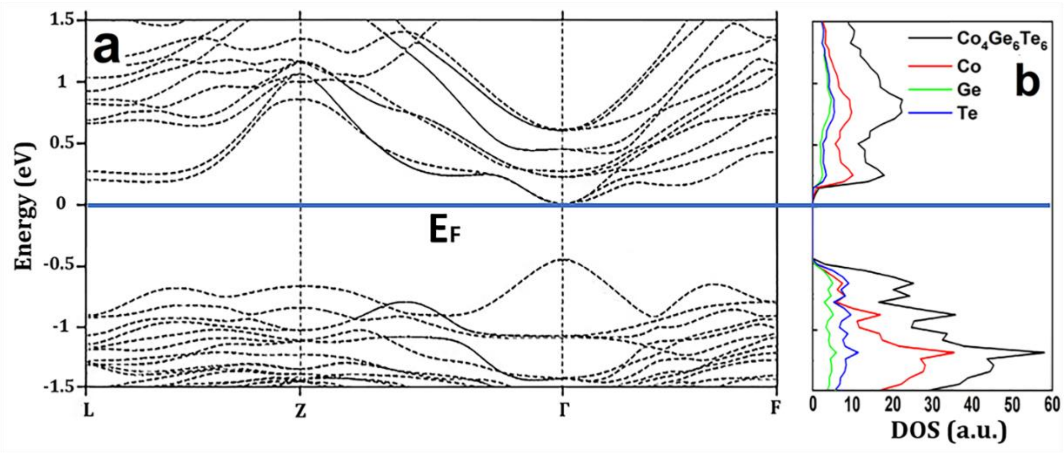

Figure 6.3 (a) The calculated band structure of $Co_8Ge_{12}Te_{12}$; (b) The total and projected density of states (DOS) for $Co_8Ge_{12}Te_{12}$.

$Co_{3.88}Fe_{0.12}Ge_6Te_6$ was intentionally selected for thermal properties investigation as it has the highest power factor from 50 to 500 °C (Figure 6.2 d) and smaller amount of impurities than $Co_{3.80}Fe_{0.20}Ge_6Te_6$. Figure 6.4 illustrates the temperature-dependent thermal conductivities and *ZT* values of $Co_{3.88}Fe_{0.12}Ge_6Te_6$. As shown in Figure 6.4 (a), its carrier thermal conductivity, which is calculated using the Wiedemann-Franz law ($k_e = L\sigma T$),[30] where L is the Lorentz factor defined from: L= 1.5 + exp (-$^{|S|}/_{116}$)[42], can be almost neglected from 50 to 500 °C.Thus the lattice thermal conductivity ($k_l = k_{total} - k_e$) makes the major contribution to its total thermal conductivity. Also, a decrease in its lattice thermal conductivity with the increasing temperature is representative of the Umklapp scattering.[60] In the 50–500 °C temperature range, the highest *ZT* of pristine $Co_4Ge_6Te_6$ is

0.05 at 400 °C,[123] and the highest *ZT* of $Co_{3.88}Fe_{0.12}Ge_6Te_6$ is 0.12 at 400 °C (Figure 6.4 (b)). The low electrical conductivity is the major reason that limits the thermoelectrical performance of $Co_{3.88}Fe_{0.12}Ge_6Te_6$.

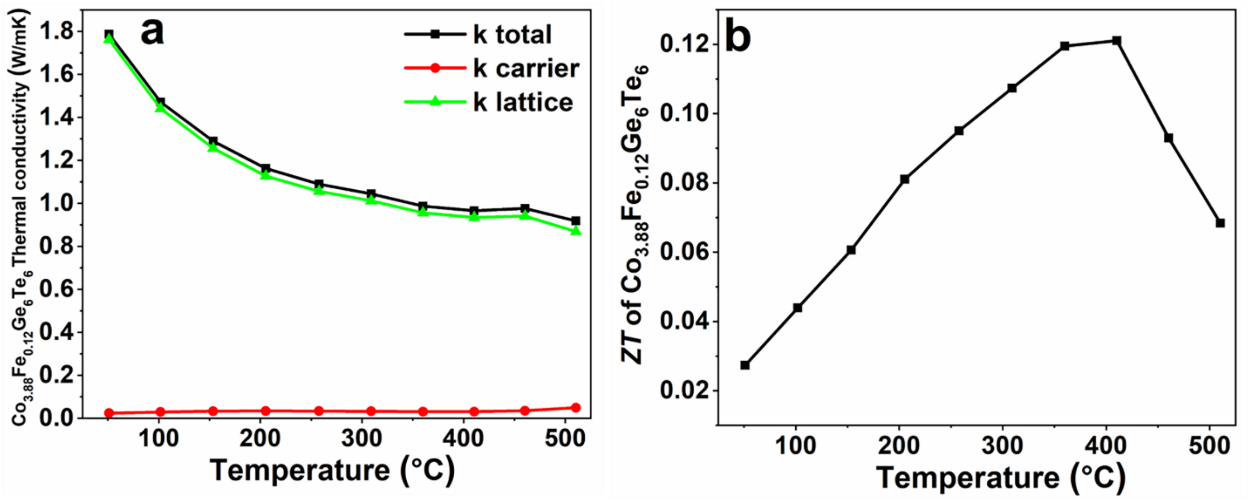

Figure 6.4 (a) Total, carrier, and lattice thermal conductivity; (b) *ZT* values of $Co_{3.88}Fe_{0.12}Ge_6Te_6$.

6.4 Conclusion

In this study, the mixed anion skutterudites $Co_{4-x}Fe_xGe_6Te_6$ (x = 0.04 and 0.12) were synthesized, and their structural and electrical properties were investigated. The positive Seebeck and Hall coefficients observed in the Fe-substituted $Co_4Ge_6Te_6$ samples indicate that holes are the dominant charge carriers in $Co_{4-x}Fe_xGe_6Te_6$ (x = 0.04 and 0.12). This also proves that substitution by electron deficient atoms in $Co_4Ge_6Te_6$ results in the conversion of the *n*-type $Co_4Ge_6Te_6$ into a *p*-type material. Among all the prepared samples, $Co_{3.88}Fe_{0.12}Ge_6Te_6$ was favored for thermal conductivity studies, and the results point at the dominance of its lattice thermal conductivity from 50 to 500 °C. The highest *ZT* value of

0.12 was achieved for $Co_{3.88}Fe_{0.12}Ge_6Te_6$ at 400 °C. However, the 140% improvement in *ZT* over the pristine $Co_4Ge_6Te_6$ does not meet the performance requirements for wide-scale thermoelectrical applications. Low electrical conductivity of $Co_{3.88}Fe_{0.12}Ge_6Te_6$ is a significant drawback which needs to be addressed.

6.5 Supporting Information

Table 6.S1. X-ray and Archimedes densities of the $Co_{3.88}Fe_{0.12}Ge_6Te_6$ sample.

	X-ray density	Archimedes density	Relative density, %
$Co_{3.88}Fe_{0.12}Ge_6Te_6$	7.19 (g/cm^3)	6.96 (g/cm^3)	96.8

Scanning Electron Microscopy-Energy Dispersive X-ray Spectroscopy (SEM-EDS).

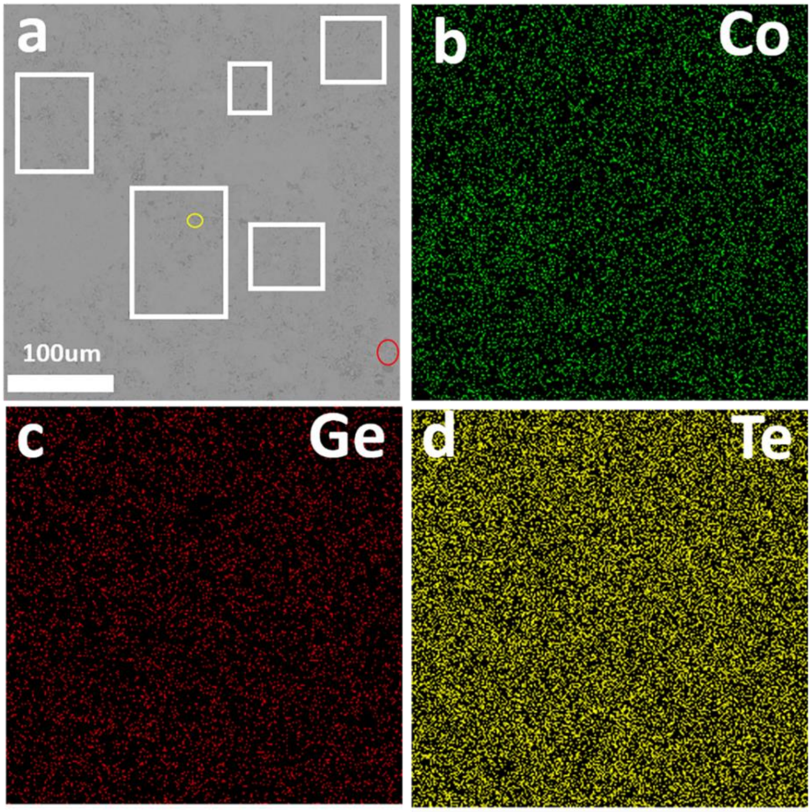

Fig 6.S1: (a) Back-scattered electron image; GeTe impurity is dark grey spots in the red circle, CoTe and $CoTe_2$ are grey spots in the yellow circle. (b-d) Elemental mappings of Co, Ge and Te in $Co_4Ge_6Te_6$. Composition of the selected areas in (a) is 24.4(7) at. % of Co, 37.8(5) at. % of Ge and 37.8(4) at. % of Te.

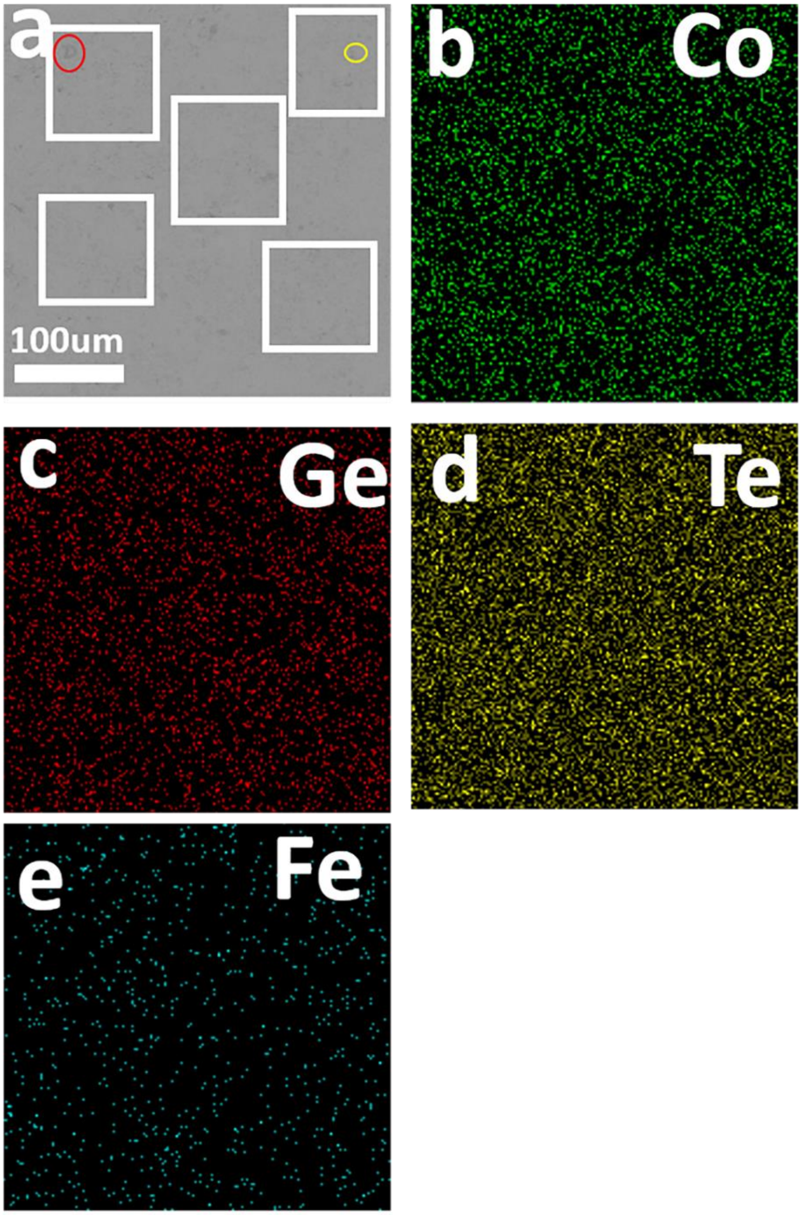

Fig 6.S2: (a) Back-scattered electron image; GeTe impurity is represented by dark grey spots in the red circle, CoTe and $CoTe_2$ by grey spots in the yellow circle. (b-e) Elemental mappings of Co, Ge, Te and Fe in $Co_{3.96}Fe_{0.04}Ge_6Te_6$. Composition of the selected areas in (a) is 23.4(8) at. % of Co, 37.7(5) at. % of Ge, 38.7(9) at. % of Te and 0.2(1) at.% of Fe.

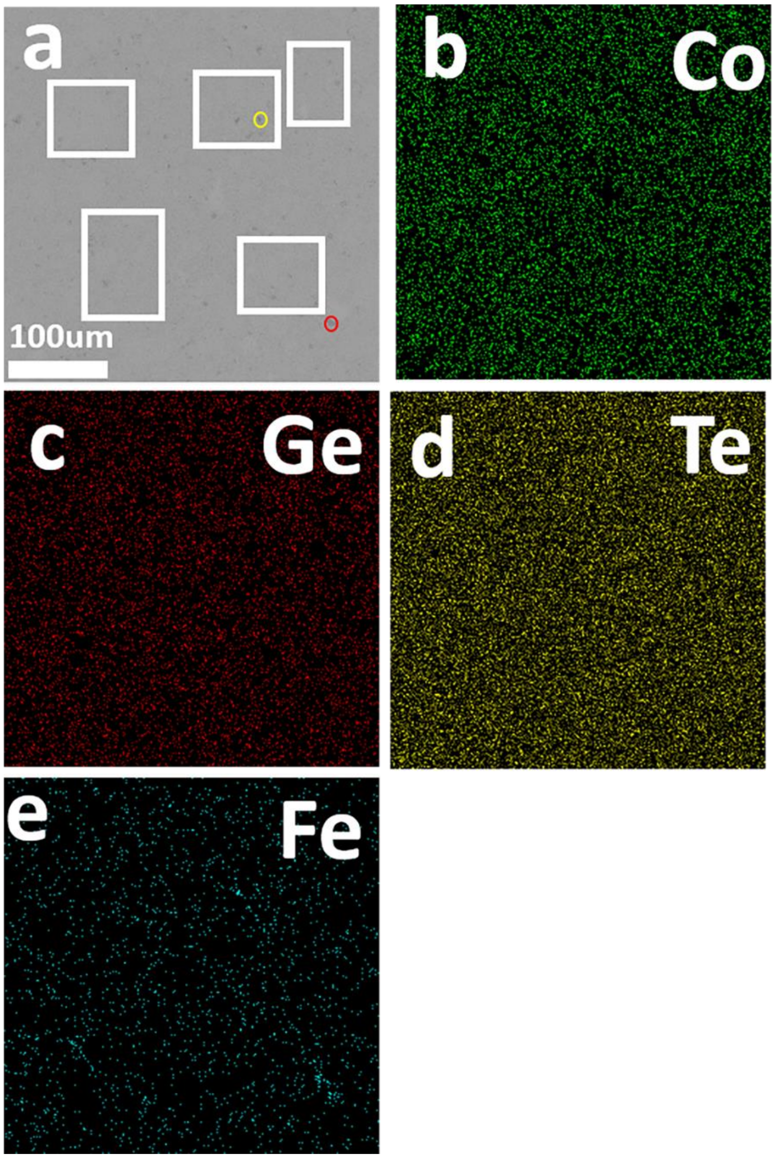

Fig 6.S3: (a) Back-scattered electron image: GeTe impurity is represented by dark grey spots in the red circle, CoTe and $CoTe_2$ by grey spots in the yellow circle. (b-e) Elemental mappings of Co, Ge, Te and Fe in $Co_{3.88}Fe_{0.12}Ge_6Te_6$. Composition of the selected areas in (a) is 22.9(7) at. % of Co, 37.6(3) at. % of Ge, 38.7(9) at. % of Te, and 0.8(2) at. % of Fe.

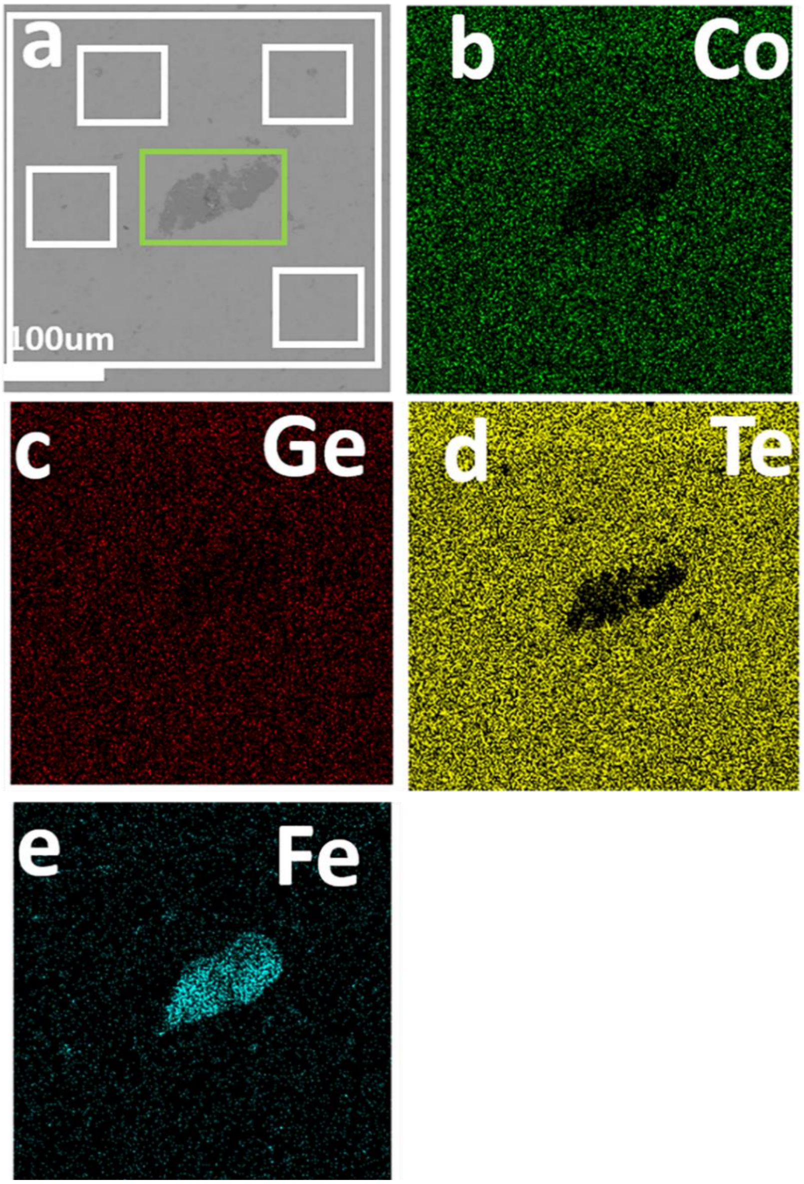

Fig 6.S4: (a) Back-scattered electron image; Fe impurity is a dark gray spot in the green rectangle. (b-e) Elemental mappings of Co, Ge, Te and Fe in $Co_{3.8}Fe_{0.2}Ge_6Te_6$. Composition of the selected areas in (a) is 23.2(4) at. % of Co, 37.5(9) at. % of Ge, 38.0(8) at. % of Te and 1.3(3) at. % of Fe.

Chapter 7. Conclusions and Further Work

In this dissertation, the synthesis, physical properties, crystal and electronic structures of several SnTe-based phases have been studied. Unlike benchmark chalcogenide thermoelectric materials, the SnTe is considered an inferior thermoelectric material because of its low Seebeck coefficient and high thermal conductivity. Nonetheless, its relatively high electrical conductivity, crystal and electronic structures, that are similar with PbTe, make SnTe a potential candidate to replace PbTe for thermoelectric applications.

The goal of my research was to improve the thermoelectric performance of SnTe and $Sn_{0.5}Ge_{0.5}Te$ and make them suitable for industrial applications. This objective was achieved by first understanding and then optimizing the SnTe and $Sn_{0.5}Ge_{0.5}Te$ electronic structure and charge transport properties. Additionally, extra atomic disorder was introduced to minimize the thermal conductivity.

7.1 SnTe: Ge Substitution

The first step undertaken was to substitute Ge for Sn in SnTe. Our results (Chapter 3) showed that the thermoelectrical performance can be substantially improved when 50% Ge is introduced on the Sn site in SnTe. However, a higher-than-expected thermal conductivity and lower-than-expected Seebeck coefficient in $Sn_{0.5}Ge_{0.5}Te$ suggested that further optimization was still required for this material to be competitive. To mitigate those challenges, further doping and alloying of $Sn_{0.5}Ge_{0.5}Te$ were pursued.

7.2 $Sn_{0.5}Ge_{0.5}Te$: Doping with Sb/Bi and Alloying with Cu_2Te

Sb- and Bi-doping of $(Sn_{0.5}Ge_{0.5})Te$ lead to the convergence of the light and heavy hole valence bands and, as a result, to an increased carrier effective mass (Chapter 3). To further optimize thermal conductivity, the samples were alloyed with Cu_2Te. The lattice thermal conductivity of the Cu_2Te-alloyed $(Sn_{0.5}Ge_{0.5})_{0.91}Sb_{0.06}Te$ and $(Sn_{0.5}Ge_{0.5})_{0.91}Bi_{0.06}Te$ was sharply reduced. The $(Sn_{0.5}Ge_{0.5})_{0.91}Bi_{0.06}Te(Cu_2Te)_{0.05}$ sample achieved the maximum figure of merit, *ZT*, of 0.99 at 500 ˚C and displayed an increase in the average and highest *ZT* values by 384% (0.63 vs. 0.13) and 175% (0.99 vs. 0.36), respectively, over SnTe within the 100 to 500 ˚C range.

7.3 $Sn_{0.5}Ge_{0.5}Te$: Electronic Band Structure Optimization via Doping with In, In/Sb, and In/Bi

Effects of In, In/Sb, and In/Bi doping on the electronic structure $Sn_{(1-x)}Ge_xTe$ were explored through the density-function theory (DFT). The results (Chapter 4) indicated that In-doping on the Sn/Ge site introduces resonant levels around the Fermi level in $Sn_{0.5}Ge_{0.5}Te$, which increases the carrier effective mass and improves the Seebeck coefficient. As the result, $(Sn_{0.5}Ge_{0.5})_{0.98}In_{0.02}Te$ shows the high thermoelectric performance and was selected for further optimization via the Sb and Bi doping.

The DFT calculations (Chapter 4) revealed that the Sb and Bi doping in $(Sn_{0.5}Ge_{0.5})_{0.98}In_{0.02}Te$ leads to band inversion, creating multiple electronic valleys. It was also observed that the charge carrier transport in the Sb- and Bi-doped samples is dominated by heavy holes. These results suggested that the Seebeck coefficient of

$(Sn_{0.5}Ge_{0.5})_{0.98}In_{0.02}Te$ can be effectively improved through the Sb and Bi doping. Moreover, the lattice thermal conductivity of $(Sn_{0.5}Ge_{0.5})_{0.89}In_{0.02}Bi_{0.06}Te$ was effectively optimized by additional phonon scattering at the point defects. Comparison of the results for $(Sn_{0.5}Ge_{0.5})_{0.89}In_{0.02}Bi_{0.06}Te$ and pristine SnTe reveal significant improvements in the average and highest *ZT* values by 446% (0.71 vs. 0.13) and 122% (0.80 vs. 0.36), respectively, within 100-500 ˚C.

7.4 SnTe: alloying with $AgSnSe_2$ and PbTe

The relatively high thermal conductivity of SnTe is a major drawback of its thermoelectric performance. Introducing extra atomic disorder can suppress the thermal conductivity, however, the electrical conductivity will be impaired as well. An approach to suppress the thermal conductivity without damaging the electrical conductivity of SnTe was explored.

Our experimental results (Chapter 5) show that the thermal conductivity of SnTe is effectively suppressed via alloying with $AgSnSe_2$ within 25-600˚C. Simultaneously, $AgSnSe_2$ exhibits an electron acceptor behavior in the alloyed samples. Thus, the electrical conductivity is maintained as the reduction in the carrier mobility is compensated by larger a carrier concentration. The *ZT* of 0.81 is achieved for $(SnTe)_{0.95}(AgSnSe_2)_{0.05}$ at 600 ˚C. To further improve the performance, $(SnTe)_{0.95}(AgSnSe_2)_{0.05}$ was alloyed with PbTe. The Pb substitution on the Sn sites was expected to positively affect the band structure and, therefore, improve the Seebeck coefficient. However, the experimental results showed only a slight improvement in thermopower for $(SnTe)_{0.95}(AgSnSe_2)_{0.05}$. Nevertheless, the Pb substitution further suppressed the thermal conductivity of $(SnTe)_{0.95}(AgSnSe_2)_{0.05}$. As a result, the maximum *ZT* increases from 0.81 to 0.86 for the Pb substitution of 12.5 at. %.

7.5 $Co_4Ge_6Te_6$: converting n-type skutterudite into p-type via substitution with Fe

Effect of substituting Fe for Co in $Co_4Ge_6Te_6$ was investigated. The positive Seebeck and Hall coefficients (Chapter 6) of the $Co_{4-x}Fe_xGe_6Te_6$ samples (x = 0.04 and 0.12) indicate that holes became the dominant charge carriers and that the *n*-type $Co_4Ge_6Te_6$ was successfully converted into a *p*-type material through the Fe substitution. Also, the experimental results showed that the electrical conductivity significantly increased in $Co_{3.88}Fe_{0.12}Ge_6Te_6$ due to a higher carrier concentration when compared to $Co_4Ge_6Te_6$. Analysis of the thermal conductivity of $Co_{3.88}Fe_{0.12}Ge_6Te_6$ suggests that its lattice thermal conductivity ($k_l = k_{total} - k_e$, $k_e = L\sigma T$, L= 1.5 + exp (-$|S|/116$))[42] makes a significant contribution to its total thermal conductivity. The highest *zT* value increased from 0.05 in $Co_4Ge_6Te_6$ to 0.12 in $Co_{3.88}Fe_{0.12}Ge_6Te_6$ at 400 °C.

7.6 Further work

The pristine SnTe is considered an inferior thermoelectric material; one of the primary reasons is intrinsic Sn vacancies that induce a high hole concentration of 10^{20} to 10^{21} cm^{-3},[140] while the optimal concentration is 10^{19} to 10^{20} cm^{-3}.[39] If the high hole concentration could be suppressed, SnTe may possess an outstanding thermoelectric performance. Like SnTe, GeTe also has a high hole concentration of ~10^{21} cm^{-3} induced by the Ge vacancies.[261] According to Dong *et al.*,[304] the formation of Ge vacancies can be diminished by adding an excessive amount of Ge into the sample matrix, effectively reducing the hole concentration. Dong *et al*. also indicated that carrier mobility increases in the Ge-richer samples as the carrier scattering due to the Ge vacancies is suppressed.[304] Ideally, the strategies employed for GeTe can be transferred to SnTe, allowing to optimize the hole concentration and carrier mobility. Hence, the $Sn_{1+x}Te$ phases may be of interest and can also be used as springboard for further doping/substituting/alloying studies.

Since elemental tin is easily oxidized, tin oxide may be present in the final products. Zhou *et al*.[108] showed that tin oxides adversely affect the lattice thermal conductivity, electrical conductivity, and Seebeck coefficient of SnSe, and thereby impede the thermoelectric performance. In this light, the Sn purification process as proposed by Zhou *et al*.[108] may be of benefit to the SnTe samples, as it minimizes the presence of tin oxides.

Also, melt-spinning synthesis can be applied to the SnTe samples to optimize their thermal conductivity. Compared to the traditional solid-state synthesis, the melt spinning considerably increases formation of the hierarchical microstructure due to the ultrafast quenching. As a result, the lattice thermal conductivity can be suppressed by extra phonon scattering, thereby enhancing the thermoelectric performance of consolidated bulk samples. In the past decades, the melt-spinning approach has been successfully applied for the synthesis of different thermoelectric materials.[97,305–309] Thus, the knowledge gained can be employed for the development of high-performance SnTe-based alloys. The atmosphere (Ar/He/N), nozzle diameter, wheel speed, and ejection pressure are the key control parameters affecting melt-spinning ribbons' composition and microstructure, and they will have to be tuned for each phase.

In recent decades, low-dimensional metal-semiconductor interfaces (MSI) has been applied in thermoelectric materials to improve their *ZT*.[100,310–313] Generally, the Seebeck coefficient can be enhanced with a MSI as the low-energy carriers are filtered out by the potential barriers at the MSI.[312] Moreover, metal nanoparticles effectively scatter phonons with mid to long wavelengths and, thus, suppresses the lattice thermal conductivity.[314] Considering the relatively low Seebeck coefficient and high lattice thermal conductivity of SnTe, introducing MSI into the sample matrix is worth exploring. Ag nanoparticles can be incorporated into SnTe. Ag has a work function of ~ 4.73 eV,[315] and SnTe has a work function of ~ 4.88 eV,[316] which forms an energy barrier of ~ 0.15 eV at the MSI.[312] Therefore, low-energy holes may be filtered during the charge transport between Ag and SnTe, and thus the Seebeck coefficient would be improved.

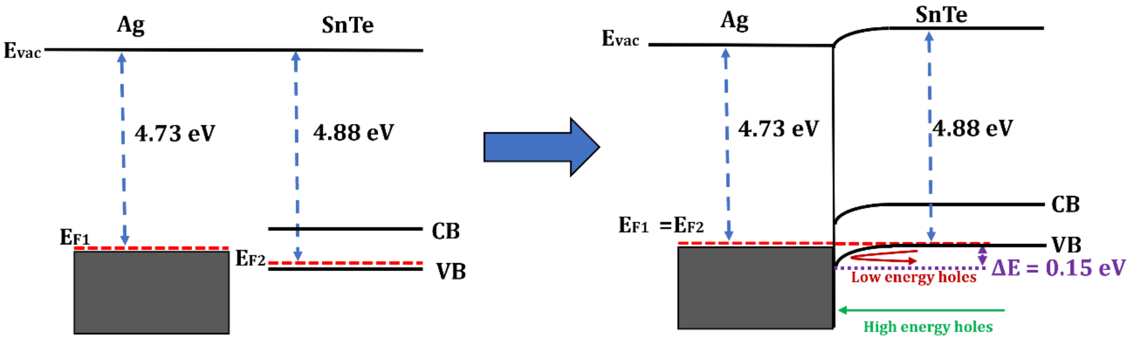

Figure 7.1. Schematics of the band diagram of Ag nanoparticles and SnTe, and carrier transfer from the Ag nanoparticles to the SnTe matrix.

Furthermore, the thermal conductivity of the material can be reduced by utilizing SnTe-nano-crystallites, synthesized by the method developed by Xu *et al*.[317] (size of ~ 43 nm in diameter). To prepare the composite of Ag nanoparticles and SnTe nano-crystallites, the degassed silver nitrate solution can be applied; this decorating method was developed by (Dun *et al*,).[318] Synthetic procedures will be performed under an argon gas on a Schlenk line.

Bibliography:

(1) Yang, J.; Caillat, T. Thermoelectric Materials for Space and Automotive Power Generation. *MRS Bulletin* **2006**, *31* (3), 224–229. https://doi.org/10.1557/mrs2006.49.

(2) Wood, C. Materials for Thermoelectric Energy Conversion. *Rep. Prog. Phys.* **1988**, *51* (4), 459–539. https://doi.org/10.1088/0034-4885/51/4/001.

(3) Beretta, D.; Neophytou, N.; Hodges, J. M.; Kanatzidis, M. G.; Narducci, D.; Martin-Gonzalez, M.; Beekman, M.; Balke, B.; Cerretti, G.; Tremel, W.; Zevalkink, A.; Hofmann, A. I.; Müller, C.; Dörling, B.; Campoy-Quiles, M.; Caironi, M. Thermoelectrics: From History, a Window to the Future. *Materials Science and Engineering: R: Reports* **2019**, *138*, 100501. https://doi.org/10.1016/j.mser.2018.09.001.

(4) Seebeck, T. J. Ueber die magnetische Polarisation der Metalle und Erze durch Temperaturdifferenz. *Ann. Phys.* **1826**, *82* (3), 253–286. https://doi.org/10.1002/andp.18260820302.

(5) Oersted. Notiz von neuen electrisch - magnetischen Versuchen des Herrn Seebeck in Berlin. *Ann. Phys. phys. Chem.* **1823**, *73* (4), 430–432. https://doi.org/10.1002/andp.18230730410.

(6) Goldsmid, H. J. The Physics of Thermoelectric Energy Conversion; IOP concise physics; San Rafael, CA : Morgan & Claypool Publishers ; Bristol, UK : IOP Publishing, 2017.

(7) Rowe, D. M. *CRC Handbook of Thermoelectrics*, 1st ed.; CRC Press, 1995.

(8) Goupil, C.; Ouerdane, H.; Zabrocki, K.; Seifert, W.; Hinsche, N. F.; Müller, E. Thermodynamics and Thermoelectricity. In *Continuum Theory and Modeling of Thermoelectric Elements*; Goupil, C., Ed.; Wiley, 2016; pp 1–74. https://doi.org/10.1002/9783527338405.ch1.

(9) Thomson, W. Account of Researches in Thermo-Electricity. *Royal Society* **1854**, *7*, 49–58. https://doi.org/10.1098/rspl.1854.0016.

(10) Lee, H. The Thomson Effect and the Ideal Equation on Thermoelectric Coolers. *Energy* **2013**, *56*, 61–69. https://doi.org/10.1016/j.energy.2013.04.049.

(11) Bell, L. E. Cooling, Heating, Generating Power, and Recovering Waste Heat with Thermoelectric Systems. *Science* **2008**, *321* (5895), 1457–1461. https://doi.org/10.1126/science.1158899.

(12) Ioffe, A. F.; Stil'bans, L. S.; Iordanishvili, E. K.; Stavitskaya, T. S.; Gelbtuch, A.; Vineyard, G. *Semiconductor Thermoelements and Thermoelectric Cooling*. *Physics Today* **1959**, *12* (5), 42–42. https://doi.org/10.1063/1.3060810.

(13) Nolas, G. S.; Sharp, J.; Goldsmid, H. J. *Thermoelectrics: Basic Principles and New Materials Developments*; Hull, R., Osgood, R. M., Sakaki, H., Zunger, A., Series Eds.; Springer Series in MATERIALS SCIENCE; Springer Berlin Heidelberg: Berlin, Heidelberg, 2001; Vol. 45. https://doi.org/10.1007/978-3-662-04569-5.

(14) Nemir, D.; Beck, J. On the Significance of the Thermoelectric Figure of Merit Z. *Journal of Elec Materi* **2010**, *39* (9), 1897–1901. https://doi.org/10.1007/s11664-009-1060-4.

(15) Goldsmid, H. J. *Introduction to Thermoelectricity*; Springer Berlin, Heidelberg, 2009.

(16) Ibach, H. The Free-Electron Gas in an Infinite Square-Well Potential. In *Solid State Physics: An Introduction to Principles of Materials Science.*; Springer: Berlin, 2009; pp 135–140.

(17) Kittel, C. Free Electron Fermi Gas. In *Introduction to Solid State Physics, 8th Edition*; John Wiley & Sons: New York, 2004; pp 131–156.

(18) Ibach, H. The Nearly Free-Electron Approximation. In *Solid State Physics: An Introduction to Principles of Materials Science.*; Springer: Berlin, 2009.

(19) Kittel, C. Nearly Free Electron Model. In *Introduction to Solid State Physics, 8th Edition*; John Wiley & Sons: New York, 2004; pp 161–167.

(20) Ibach, H. Diffraction from Periodic Structure. In *Solid State Physics: An Introduction to Principles of Materials Science.*; Springer: Berlin, 2009.

(21) Roald, H. *Solids And Surfaces: A Chemist's View Of Bonding In Extended Structures*; VCH Publishers: New York, 1988.

(22) Wang, H.; Pei, Y.; LaLonde, A. D.; Jeffery Snyder, G. Material Design Considerations Based on Thermoelectric Quality Factor. In *Thermoelectric Nanomaterials*; Koumoto, K., Mori, T., Eds.; Springer Series in Materials Science; Springer Berlin Heidelberg: Berlin, Heidelberg, 2013; Vol. 182, pp 3–32. https://doi.org/10.1007/978-3-642-37537-8_1.

(23) Robinson, J. E. Thermoelectric Power in the Nearly-Free-Electron Model. *Phys. Rev.* **1967**, *161* (3), 533–539. https://doi.org/10.1103/PhysRev.161.533.

(24) He, J.; Tan, X.; Xu, J.; Liu, G.-Q.; Shao, H.; Fu, Y.; Wang, X.; Liu, Z.; Xu, J.; Jiang, H.; Jiang, J. Valence Band Engineering and Thermoelectric Performance Optimization in SnTe by Mn-Alloying via a Zone-Melting Method. *J. Mater. Chem. A* **2015**, *3* (39), 19974–19979. https://doi.org/10.1039/C5TA05535K.

(25) Setyawan, W.; Curtarolo, S. High-Throughput Electronic Band Structure Calculations: Challenges and Tools. *Computational Materials Science* **2010**, *49* (2), 299–312. https://doi.org/10.1016/j.commatsci.2010.05.010.

(26) Lau, A.; Ortix, C. Novel Topological Insulators from Crystalline Symmetries. *Eur. Phys. J. Spec. Top.* **2018**, *227* (12), 1309–1321. https://doi.org/10.1140/epjst/e2018-800098-y.

(27) Mary, A. W. *Physical Properties of Materials*, 3rd ed.; CRC: Boca Raton, 2018.

(28) Dugdale, J. S. Electrical Conductivity. In *The Electrical Properties of Metals and Alloys*; Dover Publications: London, 2016; pp 82–91.

(29) Overy, A. R.; Simonov, A.; Chater, P. A.; Tucker, M. G.; Goodwin, A. L. Phonon Broadening from Supercell Lattice Dynamics: Random and Correlated Disorder: Phonon Broadening from Supercell Lattice Dynamics. *Phys. Status Solidi B* **2017**, *254* (4), 1600586. https://doi.org/10.1002/pssb.201600586.

(30) Jonson, M.; Mahan, G. D. Mott's Formula for the Thermopower and the Wiedemann-Franz Law. *Phys. Rev. B* **1980**, *21* (10), 4223–4229. https://doi.org/10.1103/PhysRevB.21.4223.

(31) Cutler, M.; Leavy, J. F.; Fitzpatrick, R. L. Electronic Transport in Semimetallic Cerium Sulfide. *Phys. Rev.* **1964**, *133* (4A), A1143–A1152. https://doi.org/10.1103/PhysRev.133.A1143.

(32) Goldsmid, H. J.; Sharp, J. W. Estimation of the Thermal Band Gap of a Semiconductor from Seebeck Measurements. *Journal of Elec Materi* **1999**, *28* (7), 869–872. https://doi.org/10.1007/s11664-999-0211-y.

(33) Kresse, G.; Joubert, D. From Ultrasoft Pseudopotentials to the Projector Augmented-Wave Method. *Phys. Rev. B* **1999**, *59* (3), 1758–1775. https://doi.org/10.1103/PhysRevB.59.1758.

(34) Wang, S.; Yang, J.; Toll, T.; Yang, J.; Zhang, W.; Tang, X. Conductivity-Limiting Bipolar Thermal Conductivity in Semiconductors. *Sci Rep* **2015**, *5* (1), 10136. https://doi.org/10.1038/srep10136.

(35) Hamid Elsheikh, M.; Shnawah, D. A.; Sabri, M. F. M.; Said, S. B. M.; Haji Hassan, M.; Ali Bashir, M. B.; Mohamad, M. A Review on Thermoelectric Renewable

Energy: Principle Parameters That Affect Their Performance. *Renewable and Sustainable Energy Reviews* **2014**, *30*, 337–355. https://doi.org/10.1016/j.rser.2013.10.027.

(36) Li, W.; Zheng, L.; Ge, B.; Lin, S.; Zhang, X.; Chen, Z.; Chang, Y.; Pei, Y. Promoting SnTe as an Eco-Friendly Solution for p-PbTe Thermoelectric via Band Convergence and Interstitial Defects. *Adv. Mater.* **2017**, *29* (17), 1605887. https://doi.org/10.1002/adma.201605887.

(37) Liu, W.; Wang, D.; Liu, Q.; Zhou, W.; Shao, Z.; Chen, Z. High-Performance GeTe-Based Thermoelectrics: From Materials to Devices. *Adv. Energy Mater.* **2020**, *10* (19), 2000367. https://doi.org/10.1002/aenm.202000367.

(38) Wu, Y.; Chen, Z.; Nan, P.; Xiong, F.; Lin, S.; Zhang, X.; Chen, Y.; Chen, L.; Ge, B.; Pei, Y. Lattice Strain Advances Thermoelectrics. *Joule* **2019**, *3* (5), 1276–1288. https://doi.org/10.1016/j.joule.2019.02.008.

(39) Snyder, G. J.; Toberer, E. S. Complex Thermoelectric Materials. *Nature Materials* **2008**, *7* (2), 105–114. https://doi.org/10.1038/nmat2090.

(40) Kittel, C. Ratio of Thermal to Electrical Conductivity. In *Introduction to Solid State Physics, 8th Edition*; John Wiley & Sons: New York, 2004; pp 156–157.

(41) Yadav, A.; Deshmukh, P.; Roberts, K.; Jisrawi, N.; Valluri, S. An Analytic Study of the Wiedemann–Franz Law and the Thermoelectric Figure of Merit. *J. Phys. Commun.* **2019**, *3* (10), 105001. https://doi.org/10.1088/2399-6528/ab444a.

(42) Kim, H.-S.; Gibbs, Z. M.; Tang, Y.; Wang, H.; Snyder, G. J. Characterization of Lorenz Number with Seebeck Coefficient Measurement. *APL Materials* **2015**, *3* (4), 041506. https://doi.org/10.1063/1.4908244.

(43) Mary, A. W. Thermal Conductivity. In *Properties of Materials*; CRC Press: New York, 1999; pp 187–192.

(44) Kittel, C. Phonon Heat Capacity. In *Introduction to Solid State Physics, 8th Edition*; John Wiley & Sons: New York, 2004; pp 107–117.

(45) Mary, A. W. Debye Model. In *Physical Properties of Materials*; CRC Press: New York, 1999; pp 137–139.

(46) Mary, A. W. Dulong–Petit Law. In *Physical Properties of Materials*; CRC Press: New York, 1999; pp 135–136.

(47) Kittel, C. Experimental Heat Capacity of Metals. In *Introduction to Solid State Physics, 8th Edition*; John Wiley & Sons: New York, 2004; p 145.

(48) Mary, A. W. Heat Capacity of Metals. In *Physical Properties of Materials*; CRC Press: New York, 1999.

(49) Fultz, B. Vibrational Thermodynamics of Materials. *Progress in Materials Science* **2010**, *55* (4), 247–352. https://doi.org/10.1016/j.pmatsci.2009.05.002.

(50) Kittel, C. Two Atoms per Primitive Basis. In *Introduction to Solid State Physics, 8th Edition*; John Wiley & Sons: New York, 2004; pp 97–98.

(51) Wu, Y. Experimental Investigation of Size Effects on Surface Phonon Polaritons and Phonon Transport. 129.

(52) Sharp, J. W.; Goldsmid, H. J. Boundary Scattering of Charge Carriers and Phonons. In *Eighteenth International Conference on Thermoelectrics. Proceedings, ICT'99 (Cat. No.99TH8407)*; IEEE: Baltimore, MD, USA, 1999; pp 709–712. https://doi.org/10.1109/ICT.1999.843484.

(53) Toberer, E. S.; Zevalkink, A.; Snyder, G. J. Phonon Engineering through Crystal Chemistry. *J. Mater. Chem.* **2011**, *21* (40), 15843. https://doi.org/10.1039/c1jm11754h.

(54) Callaway, J. Model for Lattice Thermal Conductivity at Low Temperatures. *Phys. Rev.* **1959**, *113* (4), 1046–1051. https://doi.org/10.1103/PhysRev.113.1046.

(55) Holland, M. G. Analysis of Lattice Thermal Conductivity. *Phys. Rev.* **1963**, *132* (6), 2461–2471. https://doi.org/10.1103/PhysRev.132.2461.

(56) Kittel, C. Anharmonic Crystal Interactions. In *Introduction to Solid State Physics, 8th Edition*; John Wiley & Sons: New York, 2004.

(57) Shafique, A.; Shin, Y.-H. Thermoelectric and Phonon Transport Properties of Two-Dimensional IV–VI Compounds. *Sci Rep* **2017**, *7* (1), 506. https://doi.org/10.1038/s41598-017-00598-7.

(58) Ibach, H. Heat Conduction by Phonons. In *Solid State Physics: An Introduction to Principles of Materials Science.*; Springer: Berlin, 2009; pp 124–129.

(59) Kittel, C. Umklapp Processes. In *Introduction to Solid State Physics, 8th Edition*; John Wiley & Sons: New York, 2004; pp 125–126.

(60) Maznev, A. A.; Wright, O. B. Demystifying Umklapp vs Normal Scattering in Lattice Thermal Conductivity. *American Journal of Physics* **2014**, *82* (11), 1062–1066. https://doi.org/10.1119/1.4892612.

(61) Kruglyak, Y. Landauer-Datta-Lundstrom Generalized Transport Model for Nanoelectronics. *Journal of Nanoscience* **2014**, *2014*, 1–15. https://doi.org/10.1155/2014/725420.

(62) Jeong, C.; Kim, R.; Lundstrom, M. S. On the Best Bandstructure for Thermoelectric Performance: A Landauer Perspective. *Journal of Applied Physics* **2012**, *111* (11), 113707. https://doi.org/10.1063/1.4727855.

(63) Maassen, J.; Lundstrom, M. (Invited) The Landauer Approach to Electron and Phonon Transport. *ECS Trans.* **2015**, *69* (9), 23–36. https://doi.org/10.1149/06909.0023ecst.

(64) The Landauer Approach to Transport. In *Fundamentals of Nanotransistors*; Lessons from Nanoscience: A Lecture Notes Series; WORLD SCIENTIFIC, 2017; Vol. 06, pp 197–216. https://doi.org/10.1142/9018.

(65) Jeong, C.; Kim, R.; Luisier, M.; Datta, S.; Lundstrom, M. On Landauer versus Boltzmann and Full Band versus Effective Mass Evaluation of Thermoelectric Transport Coefficients. *Journal of Applied Physics* **2010**, *107* (2), 023707. https://doi.org/10.1063/1.3291120.

(66) Lundstrom, M. *Fundamentals of Nanotransistors*; Lessons from Nanoscience: A Lecture Notes Series; WORLD SCIENTIFIC, 2017; Vol. 06. https://doi.org/10.1142/9018.

(67) Rowe, D. M. General Principles and Theoretical Considerations. In *Materials, Preparation, and Characterization in Thermoelectrics*; CRC Press, 2012; pp 1-1-15–1.

(68) de Boor, J. On the Applicability of the Single Parabolic Band Model to Advanced Thermoelectric Materials with Complex Band Structures. *Journal of Materiomics* **2021**, *7* (3), 603–611. https://doi.org/10.1016/j.jmat.2020.10.013.

(69) Jaworski, C. M.; Nielsen, M. D.; Wang, H.; Girard, S. N.; Cai, W.; Porter, W. D.; Kanatzidis, M. G.; Heremans, J. P. Valence-Band Structure of Highly Efficient p - Type Thermoelectric PbTe-PbS Alloys. *Phys. Rev. B* **2013**, *87* (4), 045203. https://doi.org/10.1103/PhysRevB.87.045203.

(70) Liu, W.; Tan, X.; Yin, K.; Liu, H.; Tang, X.; Shi, J.; Zhang, Q.; Uher, C. Convergence of Conduction Bands as a Means of Enhancing Thermoelectric Performance of n -Type Mg</sub> 2 $_{\mathrm{Si}}$ 1-x $_{\mathrm{Sn}}$ x <sub> Solid Solutions. *Phys. Rev. Lett.* **2012**, *108* (16), 166601. https://doi.org/10.1103/PhysRevLett.108.166601.

(71) Naithani, H.; Dasgupta, T. Critical Analysis of Single Band Modeling of Thermoelectric Materials. *ACS Appl. Energy Mater.* **2020**, *3* (3), 2200–2213. https://doi.org/10.1021/acsaem.9b02015.

(72) May, A. F.; Toberer, E. S.; Saramat, A.; Snyder, G. J. Characterization and Analysis of Thermoelectric Transport in n -Type Ba 8 Ga 16 − x Ge 30 + x. *Phys. Rev. B* **2009**, *80* (12), 125205. https://doi.org/10.1103/PhysRevB.80.125205.

(73) Pei, Y.; May, A. F.; Snyder, G. J. Self-Tuning the Carrier Concentration of PbTe/Ag_2Te Composites with Excess Ag for High Thermoelectric Performance. *Adv. Energy Mater.* **2011**, *1* (2), 291–296. https://doi.org/10.1002/aenm.201000072.

(74) Chakraborty, P. K.; Biswas, S. K.; Ghatak, K. P. On the Modification of the Fermi–Dirac Distribution Function in Degenerate Semiconductors. *Physica B: Condensed Matter* **2004**, *352* (1–4), 111–117. https://doi.org/10.1016/j.physb.2004.06.062.

(75) Banik, A.; Shenoy, U. S.; Anand, S.; Waghmare, U. V.; Biswas, K. Mg Alloying in SnTe Facilitates Valence Band Convergence and Optimizes Thermoelectric Properties. *Chem. Mater.* **2015**, *27* (2), 581–587. https://doi.org/10.1021/cm504112m.

(76) Wang, L.; Tan, X.; Liu, G.; Xu, J.; Shao, H.; Yu, B.; Jiang, H.; Yue, S.; Jiang, J. Manipulating Band Convergence and Resonant State in Thermoelectric Material SnTe by Mn–In Codoping. *ACS Energy Lett.* **2017**, *2* (5), 1203–1207. https://doi.org/10.1021/acsenergylett.7b00285.

(77) Yang, J.; Yan, Y.; Wang, Y. X.; Yang, G. Improved Thermoelectric Performance of $CuGaTe_2$ with Convergence of Band Valleys: A First-Principles Study. *RSC Adv.* **2014**, *4* (54), 28714. https://doi.org/10.1039/c4ra02595d.

(78) Zhang, Q.; Wang, R.; Song, K.; Tan, X.; Hu, H.; Guo, Z.; Wu, G.; Sun, P.; Liu, G.-Q.; Jiang, J. Raised Solubility in SnTe by $GeMnTe_2$ Alloying Enables Converged Valence Bands, Low Thermal Conductivity, and High Thermoelectric Performance. *Nano Energy* **2022**, *94*, 106940. https://doi.org/10.1016/j.nanoen.2022.106940.

(79) Wang, S.; Sun, Y.; Yang, J.; Duan, B.; Wu, L.; Zhang, W.; Yang, J. High Thermoelectric Performance in Te-Free $(Bi,Sb)_2Se_3$ via Structural Transition Induced Band Convergence and Chemical Bond Softening. *Energy Environ. Sci.* **2016**, *9* (11), 3436–3447. https://doi.org/10.1039/C6EE02674E.

(80) Zhang, Y.; Sun, J.; Shuai, J.; Tang, X.; Tan, G. Lead-Free SnTe-Based Compounds as Advanced Thermoelectrics. *Materials Today Physics* **2021**, *19*, 100405. https://doi.org/10.1016/j.mtphys.2021.100405.

(81) Xiao, Y.; Zhao, L.-D. Charge and Phonon Transport in PbTe-Based Thermoelectric Materials. *npj Quant Mater* **2018**, *3* (1), 55. https://doi.org/10.1038/s41535-018-0127-y.

(82) Shi, X.-L.; Zou, J.; Chen, Z.-G. Advanced Thermoelectric Design: From Materials and Structures to Devices. *Chem. Rev.* **2020**, *120* (15), 7399–7515. https://doi.org/10.1021/acs.chemrev.0c00026.

(83) Chen, Z.; Guo, X.; Zhang, F.; Shi, Q.; Tang, M.; Ang, R. Routes for Advancing SnTe Thermoelectrics. *J. Mater. Chem. A* **2020**, *8* (33), 16790–16813. https://doi.org/10.1039/D0TA05458E.

(84) Roychowdhury, S.; Samanta, M.; Perumal, S.; Biswas, K. Germanium Chalcogenide Thermoelectrics: Electronic Structure Modulation and Low Lattice Thermal Conductivity. *Chem. Mater.* **2018**, *30* (17), 5799–5813. https://doi.org/10.1021/acs.chemmater.8b02676.

(85) Pan, Y.; Li, J.-F. Thermoelectric Performance Enhancement in N-Type Bi2(TeSe)3 Alloys Owing to Nanoscale Inhomogeneity Combined with a Spark Plasma-Textured Microstructure. *NPG Asia Mater* **2016**, *8* (6), e275–e275. https://doi.org/10.1038/am.2016.67.

(86) Xiao, Y.; Wu, H.; Cui, J.; Wang, D.; Fu, L.; Zhang, Y.; Chen, Y.; He, J.; Pennycook, S. J.; Zhao, L.-D. Realizing High Performance N-Type PbTe by Synergistically Optimizing Effective Mass and Carrier Mobility and Suppressing Bipolar Thermal Conductivity. *Energy Environ. Sci.* **2018**, *11* (9), 2486–2495. https://doi.org/10.1039/C8EE01151F.

(87) Lee, M. H.; Park, J. H.; Park, S.-D.; Rhyee, J.-S.; Oh, M.-W. Grain Growth Mechanism and Thermoelectric Properties of Hot Press and Spark Plasma Sintered Na-Doped PbTe. *Journal of Alloys and Compounds* **2019**, *786*, 515–522. https://doi.org/10.1016/j.jallcom.2019.01.387.

(88) Li, S.; Wang, Y.; Chen, C.; Li, X.; Xue, W.; Wang, X.; Zhang, Z.; Cao, F.; Sui, J.; Liu, X.; Zhang, Q. Heavy Doping by Bromine to Improve the Thermoelectric Properties of N-Type Polycrystalline SnSe. *Adv. Sci.* **2018**, *5* (9), 1800598. https://doi.org/10.1002/advs.201800598.

(89) Pang, H.; Qiu, Y.; Wang, D.; Qin, Y.; Huang, R.; Yang, Z.; Zhang, X.; Zhao, L.-D. Realizing N-Type SnTe Thermoelectrics with Competitive Performance through Suppressing Sn Vacancies. *J. Am. Chem. Soc.* **2021**, *143* (23), 8538–8542. https://doi.org/10.1021/jacs.1c02346.

(90) Bauer Pereira, P.; Sergueev, I.; Gorsse, S.; Dadda, J.; Müller, E.; Hermann, R. P. Lattice Dynamics and Structure of GeTe, SnTe and PbTe: Lattice Dynamics and

Structure of GeTe, SnTe and PbTe. *Phys. Status Solidi B* **2013**, *250* (7), 1300–1307. https://doi.org/10.1002/pssb.201248412.

(91) Kihoi, S. K.; Shenoy, U. S.; Kahiu, J. N.; Kim, H.; Bhat, D. K.; Lee, H. S. Ultralow Lattice Thermal Conductivity and Enhanced Mechanical Properties of Cu and Sb Co-Doped SnTe Thermoelectric Material with a Complex Microstructure Evolution. *ACS Sustainable Chem. Eng.* **2022**, *10* (4), 1367–1372. https://doi.org/10.1021/acssuschemeng.1c07817.

(92) Lin, S.-X.; Tan, X.; Shao, H.; Xu, J.; Wu, Q.; Liu, G.-Q.; Zhang, W.-H.; Jiang, J. Ultralow Lattice Thermal Conductivity in SnTe by Manipulating the Electron–Phonon Coupling. *J. Phys. Chem. C* **2019**, *123* (26), 15996–16002. https://doi.org/10.1021/acs.jpcc.9b03329.

(93) Subrati, A.; Kim, Y.; Al Wahedi, Y.; Tzitzios, V.; Alhassan, S.; Kim, H. J.; Lee, S.; Sakellis, E.; Boukos, N.; Stephen, S.; Lee, S. M.; Lee, J. B.; Fardis, M.; Papavassiliou, G. Monitoring the Multiphasic Evolution of Bismuth Telluride Nanoplatelets. *CrystEngComm* **2020**, *22* (45), 7918–7928. https://doi.org/10.1039/D0CE00719F.

(94) Witting, I. T.; Chasapis, T. C.; Ricci, F.; Peters, M.; Heinz, N. A.; Hautier, G.; Snyder, G. J. The Thermoelectric Properties of Bismuth Telluride. *Adv. Electron. Mater.* **2019**, *5* (6), 1800904. https://doi.org/10.1002/aelm.201800904.

(95) Goldsmid, H. Bismuth Telluride and Its Alloys as Materials for Thermoelectric Generation. *Materials* **2014**, *7* (4), 2577–2592. https://doi.org/10.3390/ma7042577.

(96) Goldsmid, H. J. Recent Studies of Bismuth Telluride and Its Alloys. *Journal of Applied Physics* **1961**, *32* (10), 2198–2202. https://doi.org/10.1063/1.1777042.

(97) Xie, W.; Tang, X.; Yan, Y.; Zhang, Q.; Tritt, T. M. Unique Nanostructures and Enhanced Thermoelectric Performance of Melt-Spun BiSbTe Alloys. *Appl. Phys. Lett.* **2009**, *94* (10), 102111. https://doi.org/10.1063/1.3097026.

(98) Chen, Z.-G.; Han, G.; Yang, L.; Cheng, L.; Zou, J. Nanostructured Thermoelectric Materials: Current Research and Future Challenge. *Progress in Natural Science: Materials International* **2012**, *22* (6), 535–549. https://doi.org/10.1016/j.pnsc.2012.11.011.

(99) Hong, M.; Chen, Z.-G.; Zou, J. Fundamental and Progress of Bi_2Te_3-Based Thermoelectric Materials. *Chinese Phys. B* **2018**, *27* (4), 048403. https://doi.org/10.1088/1674-1056/27/4/048403.

(100) Nandihalli, N. Imprints of Interfaces in Thermoelectric Materials. *Critical Reviews in Solid State and Materials Sciences* **2022**, 1–50. https://doi.org/10.1080/10408436.2022.2053499.

(101) Wu, P.; Ishikawa, Y.; Hagihala, M.; Lee, S.; Peng, K.; Wang, G.; Torii, S.; Kamiyama, T. Crystal Structure of High-Performance Thermoelectric Materials by High Resolution Neutron Powder Diffraction. *Physica B: Condensed Matter* **2018**, *551*, 64–68. https://doi.org/10.1016/j.physb.2017.11.076.

(102) Chattopadhyay, T.; Pannetier, J.; Von Schnering, H. G. Neutron Diffraction Study of the Structural Phase Transition in SnS and SnSe. *Journal of Physics and Chemistry of Solids* **1986**, *47* (9), 879–885. https://doi.org/10.1016/0022-3697(86)90059-4.

(103) Kim, S.; Duong, A.-T.; Cho, S.; Rhim, S. H.; Kim, J. A Microscopic Study Investigating the Structure of SnSe Surfaces. *Surface Science* **2016**, *651*, 5–9. https://doi.org/10.1016/j.susc.2016.03.013.

(104) Zhao, L.-D.; Lo, S.-H.; Zhang, Y.; Sun, H.; Tan, G.; Uher, C.; Wolverton, C.; Dravid, V. P.; Kanatzidis, M. G. Ultralow Thermal Conductivity and High Thermoelectric Figure of Merit in SnSe Crystals. *Nature* **2014**, *508* (7496), 373–377. https://doi.org/10.1038/nature13184.

(105) Zhao, L.-D.; Chang, C.; Tan, G.; Kanatzidis, M. G. SnSe: A Remarkable New Thermoelectric Material. *Energy Environ. Sci.* **2016**, *9* (10), 3044–3060. https://doi.org/10.1039/C6EE01755J.

(106) Chen, C.-L.; Wang, H.; Chen, Y.-Y.; Day, T.; Snyder, G. J. Thermoelectric Properties of P-Type Polycrystalline SnSe Doped with Ag. *J. Mater. Chem. A* **2014**, *2* (29), 11171–11176. https://doi.org/10.1039/C4TA01643B.

(107) Sassi, S.; Candolfi, C.; Vaney, J.-B.; Ohorodniichuk, V.; Masschelein, P.; Dauscher, A.; Lenoir, B. Assessment of the Thermoelectric Performance of Polycrystalline *p* -Type SnSe. *Appl. Phys. Lett.* **2014**, *104* (21), 212105. https://doi.org/10.1063/1.4880817.

(108) Zhou, C.; Lee, Y. K.; Yu, Y.; Byun, S.; Luo, Z.-Z.; Lee, H.; Ge, B.; Lee, Y.-L.; Chen, X.; Lee, J. Y.; Cojocaru-Mirédin, O.; Chang, H.; Im, J.; Cho, S.-P.; Wuttig, M.; Dravid, V. P.; Kanatzidis, M. G.; Chung, I. Polycrystalline SnSe with a Thermoelectric Figure of Merit Greater than the Single Crystal. *Nat. Mater.* **2021**. https://doi.org/10.1038/s41563-021-01064-6.

(109) Fleurial, J.-P.; Caillat, T.; Borshchevsky, A. Skutterudites: A New Class of Promising Thermoelectric Materials. In *AIP Conference Proceedings*; AIP: Kansas City, Missouri (USA), 1994; Vol. 316, pp 40–44. https://doi.org/10.1063/1.46831.

(110) Fleurial, J.-P.; Caillat, T.; Borshchevsky, A. Skutterudites: An Update. In *XVI ICT '97. Proceedings ICT'97. 16th International Conference on Thermoelectrics (Cat. No.97TH8291)*; IEEE: Dresden, Germany, 1997; pp 1–11. https://doi.org/10.1109/ICT.1997.666968.

(111) Artini, C.; Carlini, R.; Spotorno, R.; Failamani, F.; Mori, T.; Mele, P. Structural Properties and Thermoelectric Performance of the Double-Filled Skutterudite (Sm,Gd)y(FexNi1-x)4Sb12. *Materials* **2019**, *12* (15), 2451. https://doi.org/10.3390/ma12152451.

(112) Luo, H. A Large Family of Filled Skutterudites Stabilized by Electron Count. *NATURE COMMUNICATIONS* **2015**, 10.

(113) Liu, Z.-Y.; Zhu, J.-L.; Tong, X.; Niu, S.; Zhao, W.-Y. A Review of $CoSb_3$-Based Skutterudite Thermoelectric Materials. *J Adv Ceram* **2020**, *9* (6), 647–673. https://doi.org/10.1007/s40145-020-0407-4.

(114) Kim, I.-H.; Ur, S.-C. Electronic Transport Properties of Ni-Doped $CoSb_3$ Prepared by Encapsulated Induction Melting. 6.

(115) Liu, R.; Yang, J.; Chen, X.; Shi, X.; Chen, L.; Uher, C. P-Type Skutterudites RxMyFe3CoSb12 (R, M = Ba, Ce, Nd, and Yb): Effectiveness of Double-Filling for the Lattice Thermal Conductivity Reduction. *Intermetallics* **2011**, *19* (11), 1747–1751. https://doi.org/10.1016/j.intermet.2011.06.010.

(116) Matsubara, M.; Asahi, R. Optimization of Filler Elements in $CoSb_3$-Based Skutterudites for High-Performance n-Type Thermoelectric Materials. *Journal of Elec Materi* **2016**, *45* (3), 1669–1678. https://doi.org/10.1007/s11664-015-4155-0.

(117) Chen, L. D.; Kawahara, T.; Tang, X. F.; Goto, T.; Hirai, T.; Dyck, J. S.; Chen, W.; Uher, C. Anomalous Barium Filling Fraction and *n* -Type Thermoelectric Performance of BayCo4Sb12. *Journal of Applied Physics* **2001**, *90* (4), 1864–1868. https://doi.org/10.1063/1.1388162.

(118) Kuznetsov, V. L.; Kuznetsova, L. A.; Rowe, D. M. Effect of Partial Void Filling on the Transport Properties of $Nd_{x}Co_{4}Sb_{12}$ Skutterudites. *J. Phys.: Condens. Matter* **2003**, *15* (29), 5035–5048. https://doi.org/10.1088/0953-8984/15/29/315.

(119) Shi, X.; Yang, J.; Salvador, J. R.; Chi, M.; Cho, J. Y.; Wang, H.; Bai, S.; Yang, J.; Zhang, W.; Chen, L. Multiple-Filled Skutterudites: High Thermoelectric Figure of Merit through Separately Optimizing Electrical and Thermal Transports. *J. Am. Chem. Soc.* **2011**, *133* (20), 7837–7846. https://doi.org/10.1021/ja111199y.

(120) Nolas, G. S.; Kaeser, M.; Littleton, R. T.; Tritt, T. M. High Figure of Merit in Partially Filled Ytterbium Skutterudite Materials. *Appl. Phys. Lett.* **2000**, *77* (12), 1855. https://doi.org/10.1063/1.1311597.

(121) Korenstein, R.; Soled, S.; Wold, A.; Collin, G. Preparation and Characterization of the Skutterudite-Related Phases $_{1.5}$ and $_{1.5}$. *Inorg. Chem.* **1977**, *16* (9), 2344–2346. https://doi.org/10.1021/ic50175a038.

(122) Vaqueiro, P.; Sobany, G. G.; Powell, A. V.; Knight, K. S. Structure and Thermoelectric Properties of the Ordered Skutterudite $_{1.5}$. *Journal of Solid State Chemistry* **2006**, *179* (7), 2047–2053. https://doi.org/10.1016/j.jssc.2006.04.004.

(123) Kaltzoglou, A.; Powell, A. V.; Knight, K. S.; Vaqueiro, P. High-Temperature Order–Disorder Transitions in the Skutterudites $CoGe_{1.5}Q_{1.5}$ (Q=S, Te). *Journal of Solid State Chemistry* **2013**, *198*, 525–531. https://doi.org/10.1016/j.jssc.2012.11.025.

(124) Navrátil, J.; Plechá, T. Transport Properties of Partially Filled $Yb_xCo_4Ge_6Te_6$-Based Skutterudites. 4.

(125) Song, S.; Huang, Y.; Tseng, Y.-C.; Valiyaveettil, S. M.; Chen, K.-H.; Mozharivskyj, Y. Converting N-Type $Co_4Ge_6Te_6$ Skutterudite into p-Type and Enhancing Its Thermoelectric Properties through Fe Substitution. *Journal of Alloys and Compounds* **2022**, *913*, 165314. https://doi.org/10.1016/j.jallcom.2022.165314.

(126) Schmidt, Th.; Kliche, G.; Lutz, H. D. Structure Refinement of Skutterudite-Type Cobalt Triantimonide, $CoSb_3$. *Acta Crystallogr C Cryst Struct Commun* **1987**, *43* (9), 1678–1679. https://doi.org/10.1107/S0108270187090590.

(127) Meledath Valiyaveettil, S.; Nguyen, D.-L.; Wong, D. P.; Hsing, C.-R.; Paradis-Fortin, L.; Qorbani, M.; Sabbah, A.; Chou, T.-L.; Wu, K.-K.; Rathinam, V.; Wei, C.-M.; Chen, L.-C.; Chen, K.-H. Enhanced Thermoelectric Performance in Ternary Skutterudite $Co(Ge_{0.5}Te_{0.5})_3$ via Band Engineering. *Inorg. Chem.* **2022**, *61* (10), 4442–4452. https://doi.org/10.1021/acs.inorgchem.1c03947.

(128) Vaqueiro, P.; Sobany, G. G.; Powell, A. V. A Synchrotronpowder X-Ray Diffraction Study of the Skutterudite-Related Phases $AB_{1.5}Te_{1.5}$ (A = Co, Rh, Ir; B = Ge, Sn). *Dalton Trans.* **2010**, *39* (4), 1020–1026. https://doi.org/10.1039/B913578B.

(129) Noda, Y.; Ohba, S.; Sato, S.; Saito, Y. Charge Distribution and Atomic Thermal Vibration in Lead Chalcogenide Crystals. *Acta Crystallogr B Struct Sci* **1983**, *39* (3), 312–317. https://doi.org/10.1107/S0108768183002463.

(130) Allgaier, R. S. Valence Bands in Lead Telluride. *Journal of Applied Physics* **1961**, *32* (10), 2185–2189. https://doi.org/10.1063/1.1777039.

(131) Delaire, O.; Ma, J.; Marty, K.; May, A. F.; McGuire, M. A.; Du, M.-H.; Singh, D. J.; Podlesnyak, A.; Ehlers, G.; Lumsden, M. D.; Sales, B. C. Giant Anharmonic Phonon Scattering in PbTe. *Nature Mater* **2011**, *10* (8), 614–619. https://doi.org/10.1038/nmat3035.

(132) Hsu, K. F.; Loo, S.; Guo, F.; Chen, W.; Dyck, J. S.; Uher, C.; Hogan, T.; Polychroniadis, E. K.; Kanatzidis, M. G. Cubic $AgPb_m SbTe_{2+m}$: Bulk Thermoelectric Materials with High Figure of Merit. *Science* **2004**, *303* (5659), 818–821. https://doi.org/10.1126/science.1092963.

(133) Quarez, E.; Hsu, K.-F.; Pcionek, R.; Frangis, N.; Polychroniadis, E. K.; Kanatzidis, M. G. Nanostructuring, Compositional Fluctuations, and Atomic Ordering in the Thermoelectric Materials $AgPb_m SbTe_{2+m}$. The Myth of Solid Solutions. *J. Am. Chem. Soc.* **2005**, *127* (25), 9177–9190. https://doi.org/10.1021/ja051653o.

(134) Tan, G.; Shi, F.; Hao, S.; Zhao, L.-D.; Chi, H.; Zhang, X.; Uher, C.; Wolverton, C.; Dravid, V. P.; Kanatzidis, M. G. Non-Equilibrium Processing Leads to Record High Thermoelectric Figure of Merit in PbTe–SrTe. *Nat Commun* **2016**, *7* (1), 12167. https://doi.org/10.1038/ncomms12167.

(135) Lee, M. H.; Yun, J. H.; Kim, G.; Lee, J. E.; Park, S.-D.; Reith, H.; Schierning, G.; Nielsch, K.; Ko, W.; Li, A.-P.; Rhyee, J.-S. Synergetic Enhancement of Thermoelectric Performance by Selective Charge Anderson Localization–Delocalization Transition in n-Type Bi-Doped PbTe/Ag_2Te Nanocomposite. *ACS Nano* **2019**, *13* (4), 3806–3815. https://doi.org/10.1021/acsnano.8b08579.

(136) Chattopadhyay, T.; Boucherle, J. X.; vonSchnering, H. G. Neutron Diffraction Study on the Structural Phase Transition in GeTe. *J. Phys. C: Solid State Phys.* **1987**, *20* (10), 1431–1440. https://doi.org/10.1088/0022-3719/20/10/012.

(137) Li, J.; Zhang, X.; Chen, Z.; Lin, S.; Li, W.; Shen, J.; Witting, I. T.; Faghaninia, A.; Chen, Y.; Jain, A.; Chen, L.; Snyder, G. J.; Pei, Y. Low-Symmetry Rhombohedral GeTe Thermoelectrics. *Joule* **2018**, *2* (5), 976–987. https://doi.org/10.1016/j.joule.2018.02.016.

(138) Samanta, M.; Biswas, K. Low Thermal Conductivity and High Thermoelectric Performance in $(GeTe)_{1-2x}(GeSe)_x(GeS)_x$: Competition between Solid Solution and Phase Separation. *J. Am. Chem. Soc.* **2017**, *139* (27), 9382–9391. https://doi.org/10.1021/jacs.7b05143.

(139) Yang, S. H.; Zhu, T. J.; Sun, T.; He, J.; Zhang, S. N.; Zhao, X. B. Nanostructures in High-Performance $(GeTe)_x(AgSbTe_2)_{100-x}$ Thermoelectric Materials. *Nanotechnology* **2008**, *19* (24), 245707. https://doi.org/10.1088/0957-4484/19/24/245707.

(140) Mašek, J.; Nuzhnyj, D. N. Changes of Electronic Structure of SnTe Due to High Concentration of Sn Vacancies. *Acta Phys. Pol. A* **1997**, *92* (5), 915–918. https://doi.org/10.12693/APhysPolA.92.915.

(141) Moshwan, R.; Yang, L.; Zou, J.; Chen, Z.-G. Eco-Friendly SnTe Thermoelectric Materials: Progress and Future Challenges. *Adv. Funct. Mater.* **2017**, *27* (43), 1703278. https://doi.org/10.1002/adfm.201703278.

(142) Moshwan, R.; Liu, W.-D.; Shi, X.-L.; Wang, Y.-P.; Zou, J.; Chen, Z.-G. Realizing High Thermoelectric Properties of SnTe via Synergistic Band Engineering and Structure Engineering. *Nano Energy* **2019**, *65*, 104056. https://doi.org/10.1016/j.nanoen.2019.104056.

(143) Rogers, L. M. Valence Band Structure of SnTe. *J. Phys. D: Appl. Phys.* **1968**, *1* (7), 845–852. https://doi.org/10.1088/0022-3727/1/7/304.

(144) Rogacheva, E. Nonstoichiometry and Properties of SnTe Semiconductor Phase of Variable Composition. In *Stoichiometry and Materials Science - When Numbers Matter*; Innocenti, A., Ed.; InTech, 2012. https://doi.org/10.5772/34579.

(145) Anselmi-Tamburini, U. Spark Plasma Sintering. In *Encyclopedia of Materials: Technical Ceramics and Glasses*; Elsevier, 2021; pp 294–310. https://doi.org/10.1016/B978-0-12-803581-8.11730-8.

(146) Guillon, O.; Gonzalez-Julian, J.; Dargatz, B.; Kessel, T.; Schierning, G.; Räthel, J.; Herrmann, M. Field-Assisted Sintering Technology/Spark Plasma Sintering: Mechanisms, Materials, and Technology Developments. *Adv. Eng. Mater.* **2014**, *16* (7), 830–849. https://doi.org/10.1002/adem.201300409.

(147) Ibach, H. The Bragg Interpretation of the Laue Condition. In *Solid State Physics: An Introduction to Principles of Materials Science.*; Springer: Berlin, 2009.

(148) Pecharsky, V. K.; Zavalij, P. Y. Geometry of Diffraction by Lattices. In *Fundamentals of powder diffraction and structural characterization of materials*; Springer: New York, 2005; pp 147–152.

(149) Ewald, P. P. *P.P. Ewald and His Dynamical Theory of X-Ray Diffraction : A Memorial Volume for Paul P. Ewald, 23 January 1888-August 1985*; Oxford Oxfordshire, 1992.

(150) Kittel, C. Wave Diffraction and the Reciprocal Lattice. In *Introduction to Solid State Physics, 8th Edition*; John Wiley & Sons: New York, 2004.

(151) Pecharsky, V. K.; Zavalij, P. Y. Structure Factor. In *Fundamentals of powder diffraction and structural characterization of materials*; Springer: New York, 2005.

(152) Pecharsky, V. K.; Zavalij, P. Y. Phase Problem. In *Fundamentals of powder diffraction and structural characterization of materials*; Springer: New York, 2005.

(153) Pecharsky, V. K.; Zavalij, P. Y. Properties and Sources of Radiation. In *Fundamentals of powder diffraction and structural characterization of materials*; Springer: New York, 2005; pp 102–113.

(154) Hunter, B. A. A Visual Rietveld Program; 1998; Vol. 20.

(155) Lee, J. D.; Goodacre, G. W. Weighting Schemes in Least Squares Structure Refinement: Choice of Suitable Constants by Graphical and Computer Methods. *International Journal of Mathematical Education in Science and Technology* **1970**, *1* (2), 175–183. https://doi.org/10.1080/0020739700010207.

(156) Ludwig, R. Emission of Electrons and XRay Quanta. In *Scanning Electron Microscopy: Physics of Image Formation and Microanalysis*; Springer, 2013.

(157) *Microprobe Techniques in the Earth Sciences*, 1st ed.; Potts, P. J., Mineralogical Society (Great Britain), Eds.; Mineralogical Society series; Chapman & Hall: London ; New York, 1995.

(158) Martin, J.; Tritt, T.; Uher, C. High Temperature Seebeck Coefficient Metrology. *Journal of Applied Physics* **2010**, *108* (12), 121101. https://doi.org/10.1063/1.3503505.

(159) Zevalkink, A.; Smiadak, D. M.; Blackburn, J. L.; Ferguson, A. J.; Chabinyc, M. L.; Delaire, O.; Wang, J.; Kovnir, K.; Martin, J.; Schelhas, L. T.; Sparks, T. D.; Kang, S. D.; Dylla, M. T.; Snyder, G. J.; Ortiz, B. R.; Toberer, E. S. A Practical Field Guide to Thermoelectrics: Fundamentals, Synthesis, and Characterization. *Applied Physics Reviews* **2018**, *5* (2), 021303. https://doi.org/10.1063/1.5021094.

(160) *Seebeck Coefficient / Electric Resistance Measurement System ZEM-3 series*. ADVANCE RIKO,Inc. https://advance-riko.com/en/products/zem-3/ (accessed 2023-02-23).

(161) Hermann, K. Investigations of the Specific Heat of Solid Bodies. *Royal Society* **1865**. https://doi.org/10.1098/rstl.1865.0003.

(162) Parker, W. J.; Jenkins, R. J.; Butler, C. P.; Abbott, G. L. Flash Method of Determining Thermal Diffusivity, Heat Capacity, and Thermal Conductivity. *Journal of Applied Physics* **1961**, *32* (9), 1679–1684. https://doi.org/10.1063/1.1728417.

(163) von Klitzing, K. The Quantized Hall Effect. *Rev. Mod. Phys.* **1986**, *58* (3), 519–531. https://doi.org/10.1103/RevModPhys.58.519.

(164) Kittel, C. The Tight-Binding Model. In *Introduction to Solid State Physics, 8th Edition*; John Wiley & Sons: New York, 2004.

(165) Ibach, H. The Tight-Binding Approximation. In *Solid State Physics: An Introduction to Principles of Materials Science.*; Springer: Berlin, 2009; pp 167–173.

(166) Linear Muffin-Tin Orbital Method in the Atomic Sphere Approximation. In *Full-Potential Electronic Structure Method: Energy and Force Calculations with Density Functional and Dynamical Mean Field Theory*; Springer Series in Solid-State Sciences; Springer Berlin Heidelberg: Berlin, Heidelberg, 2010; Vol. 167. https://doi.org/10.1007/978-3-642-15144-6.

(167) Andersen, O. K. Linear Methods in Band Theory. *Phys. Rev. B* **1975**, *12* (8), 3060–3083. https://doi.org/10.1103/PhysRevB.12.3060.

(168) Andersen, O. K.; Pawlowska, Z.; Jepsen, O. Illustration of the Linear-Muffin-Tin-Orbital Tight-Binding Representation: Compact Orbitals and Charge Density in Si. *Phys. Rev. B* **1986**, *34* (8), 5253–5269. https://doi.org/10.1103/PhysRevB.34.5253.

(169) Bylaska, E. J. Plane-Wave DFT Methods for Chemistry. In *Annual Reports in Computational Chemistry*; Elsevier, 2017; Vol. 13, pp 185–228. https://doi.org/10.1016/bs.arcc.2017.06.006.

(170) Density Functional Theory and the Kohn-Sham Equation. In *Full-Potential Electronic Structure Method: Energy and Force Calculations with Density Functional and Dynamical Mean Field Theory*; Springer Series in Solid-State Sciences; Springer Berlin Heidelberg: Berlin, Heidelberg, 2010; Vol. 167. https://doi.org/10.1007/978-3-642-15144-6.

(171) Giannozzi, P.; Baroni, S.; Bonini, N.; Calandra, M.; Car, R.; Cavazzoni, C.; Ceresoli, D.; Chiarotti, G. L.; Cococcioni, M.; Dabo, I.; Dal Corso, A.; de Gironcoli, S.; Fabris, S.; Fratesi, G.; Gebauer, R.; Gerstmann, U.; Gougoussis, C.; Kokalj, A.; Lazzeri, M.; Martin-Samos, L.; Marzari, N.; Mauri, F.; Mazzarello, R.; Paolini, S.; Pasquarello, A.; Paulatto, L.; Sbraccia, C.; Scandolo, S.; Sclauzero, G.; Seitsonen, A. P.; Smogunov, A.; Umari, P.; Wentzcovitch, R. M. QUANTUM ESPRESSO: A Modular and Open-Source Software Project for Quantum Simulations of Materials.

J. Phys.: Condens. Matter **2009**, *21* (39), 395502. https://doi.org/10.1088/0953-8984/21/39/395502.

(172) Giannozzi, P.; Andreussi, O.; Brumme, T.; Bunau, O.; Buongiorno Nardelli, M.; Calandra, M.; Car, R.; Cavazzoni, C.; Ceresoli, D.; Cococcioni, M.; Colonna, N.; Carnimeo, I.; Dal Corso, A.; de Gironcoli, S.; Delugas, P.; DiStasio, R. A.; Ferretti, A.; Floris, A.; Fratesi, G.; Fugallo, G.; Gebauer, R.; Gerstmann, U.; Giustino, F.; Gorni, T.; Jia, J.; Kawamura, M.; Ko, H.-Y.; Kokalj, A.; Küçükbenli, E.; Lazzeri, M.; Marsili, M.; Marzari, N.; Mauri, F.; Nguyen, N. L.; Nguyen, H.-V.; Otero-de-la-Roza, A.; Paulatto, L.; Poncé, S.; Rocca, D.; Sabatini, R.; Santra, B.; Schlipf, M.; Seitsonen, A. P.; Smogunov, A.; Timrov, I.; Thonhauser, T.; Umari, P.; Vast, N.; Wu, X.; Baroni, S. Advanced Capabilities for Materials Modelling with Quantum ESPRESSO. *J. Phys.: Condens. Matter* **2017**, *29* (46), 465901. https://doi.org/10.1088/1361-648X/aa8f79.

(173) Torrent, M.; Holzwarth, N. A. W.; Jollet, F.; Harris, D.; Lepley, N.; Xu, X. Electronic Structure Packages: Two Implementations of the Projector Augmented Wave (PAW) Formalism. *Computer Physics Communications* **2010**, *181* (11), 1862–1867. https://doi.org/10.1016/j.cpc.2010.07.036.

(174) Perdew, J. P.; Burke, K.; Ernzerhof, M. Generalized Gradient Approximation Made Simple. *Phys. Rev. Lett.* **1996**, *77* (18), 3865–3868. https://doi.org/10.1103/PhysRevLett.77.3865.

(175) Stabler, F. R. Commercialization of Thermoelectric Technology. *MRS Online Proceedings Library Archive* **2005**, *886*. https://doi.org/10.1557/PROC-0886-F01-04.

(176) Zhang, X.; Zhao, L.-D. Thermoelectric Materials: Energy Conversion between Heat and Electricity. *Journal of Materiomics* **2015**, *1* (2), 92–105. https://doi.org/10.1016/j.jmat.2015.01.001.

(177) Zhang, Q.; Liao, B.; Lan, Y.; Lukas, K.; Liu, W.; Esfarjani, K.; Opeil, C.; Broido, D.; Chen, G.; Ren, Z. High Thermoelectric Performance by Resonant Dopant Indium in Nanostructured SnTe. *Proceedings of the National Academy of Sciences* **2013**, *110* (33), 13261–13266. https://doi.org/10.1073/pnas.1305735110.

(178) Heremans, J. P.; Jovovic, V.; Toberer, E. S.; Saramat, A.; Kurosaki, K.; Charoenphakdee, A.; Yamanaka, S.; Snyder, G. J. Enhancement of Thermoelectric Efficiency in PbTe by Distortion of the Electronic Density of States. *Science* **2008**, *321* (5888), 554–557. https://doi.org/10.1126/science.1159725.

(179) Wu, L.; Li, X.; Wang, S.; Zhang, T.; Yang, J.; Zhang, W.; Chen, L.; Yang, J. Resonant Level-Induced High Thermoelectric Response in Indium-Doped GeTe. *NPG Asia Mater* **2017**, *9* (1), e343–e343. https://doi.org/10.1038/am.2016.203.

(180) Pei, Y.; Shi, X.; LaLonde, A.; Wang, H.; Chen, L.; Snyder, G. J. Convergence of Electronic Bands for High Performance Bulk Thermoelectrics. *Nature* **2011**, *473* (7345), 66–69. https://doi.org/10.1038/nature09996.

(181) Zhao, L. D.; Wu, H. J.; Hao, S. Q.; Wu, C. I.; Zhou, X. Y.; Biswas, K.; He, J. Q.; Hogan, T. P.; Uher, C.; Wolverton, C.; Dravid, V. P.; Kanatzidis, M. G. All-Scale Hierarchical Thermoelectrics: MgTe in PbTe Facilitates Valence Band Convergence and Suppresses Bipolar Thermal Transport for High Performance. *Energy Environ. Sci.* **2013**, *6* (11), 3346. https://doi.org/10.1039/c3ee42187b.

(182) Hong, M.; Chen, Z.-G.; Pei, Y.; Yang, L.; Zou, J. Limit of z T Enhancement in Rocksalt Structured Chalcogenides by Band Convergence. *Phys. Rev. B* **2016**, *94* (16), 161201. https://doi.org/10.1103/PhysRevB.94.161201.

(183) Zhao, L.-D.; Zhang, X.; Wu, H.; Tan, G.; Pei, Y.; Xiao, Y.; Chang, C.; Wu, D.; Chi, H.; Zheng, L.; Gong, S.; Uher, C.; He, J.; Kanatzidis, M. G. Enhanced Thermoelectric Properties in the Counter-Doped SnTe System with Strained Endotaxial SrTe. *J. Am. Chem. Soc.* **2016**, *138* (7), 2366–2373. https://doi.org/10.1021/jacs.5b13276.

(184) Tan, G.; Shi, F.; Hao, S.; Chi, H.; Bailey, T. P.; Zhao, L.-D.; Uher, C.; Wolverton, C.; Dravid, V. P.; Kanatzidis, M. G. Valence Band Modification and High Thermoelectric Performance in SnTe Heavily Alloyed with MnTe. *J. Am. Chem. Soc.* **2015**, *137* (35), 11507–11516. https://doi.org/10.1021/jacs.5b07284.

(185) Guo, F.; Cui, B.; Liu, Y.; Meng, X.; Cao, J.; Zhang, Y.; He, R.; Liu, W.; Wu, H.; Pennycook, S. J.; Cai, W.; Sui, J. Thermoelectric SnTe with Band Convergence, Dense Dislocations, and Interstitials through Sn Self-Compensation and Mn Alloying. *Small* **2018**, *14* (37), 1802615. https://doi.org/10.1002/smll.201802615.

(186) Biswas, K.; He, J.; Zhang, Q.; Wang, G.; Uher, C.; Dravid, V. P.; Kanatzidis, M. G. Strained Endotaxial Nanostructures with High Thermoelectric Figure of Merit. *Nature Chem* **2011**, *3* (2), 160–166. https://doi.org/10.1038/nchem.955.

(187) Biswas, K.; He, J.; Blum, I. D.; Wu, C.-I.; Hogan, T. P.; Seidman, D. N.; Dravid, V. P.; Kanatzidis, M. G. High-Performance Bulk Thermoelectrics with All-Scale Hierarchical Architectures. *Nature* **2012**, *489* (7416), 414–418. https://doi.org/10.1038/nature11439.

(188) Banik, A.; Biswas, K. Lead-Free Thermoelectrics: Promising Thermoelectric Performance in p-Type SnTe1−xSex System. *J. Mater. Chem. A* **2014**, *2* (25), 9620. https://doi.org/10.1039/c4ta01333f.

(189) Zhao, L.-D.; Dravid, V. P.; Kanatzidis, M. G. The Panoscopic Approach to High Performance Thermoelectrics. *Energy Environ. Sci.* **2014**, *7* (1), 251–268. https://doi.org/10.1039/C3EE43099E.

(190) Poudel, B.; Hao, Q.; Ma, Y.; Lan, Y.; Minnich, A.; Yu, B.; Yan, X.; Wang, D.; Muto, A.; Vashaee, D.; Chen, X.; Liu, J.; Dresselhaus, M. S.; Chen, G.; Ren, Z. High-Thermoelectric Performance of Nanostructured Bismuth Antimony Telluride Bulk Alloys. *Science* **2008**, *320* (5876), 634–638. https://doi.org/10.1126/science.1156446.

(191) Zhang, Q.; Wang, H.; Liu, W.; Wang, H.; Yu, B.; Zhang, Q.; Tian, Z.; Ni, G.; Lee, S.; Esfarjani, K.; Chen, G.; Ren, Z. Enhancement of Thermoelectric Figure-of-Merit by Resonant States of Aluminium Doping in Lead Selenide. *Energy Environ. Sci.* **2012**, *5* (1), 5246–5251. https://doi.org/10.1039/C1EE02465E.

(192) Biswas, K.; He, J.; Wang, G.; Lo, S.-H.; Uher, C.; Dravid, V. P.; Kanatzidis, M. G. High Thermoelectric Figure of Merit in Nanostructured P-Type PbTe–MTe (M = Ca, Ba). *Energy Environ. Sci.* **2011**, *4* (11), 4675. https://doi.org/10.1039/c1ee02297k.

(193) Santhanam, S.; Chaudhuri, A. K. Transport Properties of SnTe Interpreted by Means of a Two Valence Band Model. *Materials Research Bulletin* **1981**, *16* (8), 911–917. https://doi.org/10.1016/0025-5408(81)90131-8.

(194) Littlewood, P. B. The Crystal Structure of IV-VI Compounds. I. Classification and Description. *J. Phys. C: Solid State Phys.* **1980**, *13* (26), 4855–4873. https://doi.org/10.1088/0022-3719/13/26/009.

(195) Banik, A.; Biswas, K. AgI Alloying in SnTe Boosts the Thermoelectric Performance via Simultaneous Valence Band Convergence and Carrier Concentration Optimization. *Journal of Solid State Chemistry* **2016**, *242*, 43–49. https://doi.org/10.1016/j.jssc.2016.02.012.

(196) Singh, D. J. THERMOPOWER OF SnTe FROM BOLTZMANN TRANSPORT CALCULATIONS. *Funct. Mater. Lett.* **2010**, *03* (04), 223–226. https://doi.org/10.1142/S1793604710001299.

(197) Han, G.; Zhang, R.; Popuri, S.; Greer, H.; Reece, M.; Bos, J.-W.; Zhou, W.; Knox, A.; Gregory, D. Large-Scale Surfactant-Free Synthesis of p-Type SnTe Nanoparticles for Thermoelectric Applications. *Materials* **2017**, *10* (3), 233. https://doi.org/10.3390/ma10030233.

(198) Pei, Y.; LaLonde, A.; Iwanaga, S.; Snyder, G. J. High Thermoelectric Figure of Merit in Heavy Hole Dominated PbTe. *Energy Environ. Sci.* **2011**, *4* (6), 2085. https://doi.org/10.1039/c0ee00456a.

(199) Perumal, S.; Roychowdhury, S.; Negi, D. S.; Datta, R.; Biswas, K. High Thermoelectric Performance and Enhanced Mechanical Stability of P-Type Ge_{1-x} Sb_{x} Te. *Chem. Mater.* **2015**, *27* (20), 7171–7178. https://doi.org/10.1021/acs.chemmater.5b03434.

(200) Perumal, S.; Roychowdhury, S.; Biswas, K. High Performance Thermoelectric Materials and Devices Based on GeTe. *J. Mater. Chem. C* **2016**, *4* (32), 7520–7536. https://doi.org/10.1039/C6TC02501C.

(201) Aminzare, M.; Tseng, Y.-C.; Ramakrishnan, A.; Chen, K.-H.; Mozharivskyj, Y. Effect of Single Metal Doping on the Thermoelectric Properties of SnTe. *Sustainable Energy Fuels* **2019**, *3* (1), 251–263. https://doi.org/10.1039/C8SE00385H.

(202) Lewis, J. E. The Defect Structure of Non-Stoichiometric Germanium Telluride from Magnetic Susceptibility Measurements. *phys. stat. sol. (b)* **1970**, *38* (1), 131–140. https://doi.org/10.1002/pssb.19700380110.

(203) Pauling, L. Atomic Radii and Interatomic Distances in Metals. *J. Am. Chem. Soc.* **1947**, *69* (3), 542–553. https://doi.org/10.1021/ja01195a024.

(204) Polking, M. J.; Urban, J. J.; Milliron, D. J.; Zheng, H.; Chan, E.; Caldwell, M. A.; Raoux, S.; Kisielowski, C. F.; Ager, J. W.; Ramesh, R.; Alivisatos, A. P. Size-Dependent Polar Ordering in Colloidal GeTe Nanocrystals. *Nano Lett.* **2011**, *11* (3), 1147–1152. https://doi.org/10.1021/nl104075v.

(205) May, A. F.; Snyder, G. J. Introduction to Modeling Thermoelectric Transport at High Temperatures. In *Materials, Preparation, and Characterization in Thermoelectrics*; 2012.

(206) Morelli, D. T.; Jovovic, V.; Heremans, J. P. Intrinsically Minimal Thermal Conductivity in Cubic I − V − VI 2 Semiconductors. *Phys. Rev. Lett.* **2008**, *101* (3), 035901. https://doi.org/10.1103/PhysRevLett.101.035901.

(207) Zhang, Q.; Cao, F.; Liu, W.; Lukas, K.; Yu, B.; Chen, S.; Opeil, C.; Broido, D.; Chen, G.; Ren, Z. Heavy Doping and Band Engineering by Potassium to Improve the Thermoelectric Figure of Merit in P-Type PbTe, PbSe, and PbTe $_{1-y}$ Se $_{y}$. *J. Am. Chem. Soc.* **2012**, *134* (24), 10031–10038. https://doi.org/10.1021/ja301245b.

(208) Pei, Y.; Wang, H.; Gibbs, Z. M.; LaLonde, A. D.; Snyder, G. J. Thermopower Enhancement in $Pb_{1-x}Mn_{x}Te$ Alloys and Its Effect on Thermoelectric Efficiency. *NPG Asia Mater* **2012**, *4* (9), e28–e28. https://doi.org/10.1038/am.2012.52.

(209) Banik, A.; Ghosh, T.; Arora, R.; Dutta, M.; Pandey, J.; Acharya, S.; Soni, A.; Waghmare, U. V.; Biswas, K. Engineering Ferroelectric Instability to Achieve

Ultralow Thermal Conductivity and High Thermoelectric Performance in Sn $_{1-x}$ Ge $_{x}$ Te. *Energy Environ. Sci.* **2019**, *12* (2), 589–595. https://doi.org/10.1039/C8EE03162B.

(210) Jiang, M. P.; Trigo, M.; Savić, I.; Fahy, S.; Murray, É. D.; Bray, C.; Clark, J.; Henighan, T.; Kozina, M.; Chollet, M.; Glownia, J. M.; Hoffmann, M. C.; Zhu, D.; Delaire, O.; May, A. F.; Sales, B. C.; Lindenberg, A. M.; Zalden, P.; Sato, T.; Merlin, R.; Reis, D. A. The Origin of Incipient Ferroelectricity in Lead Telluride. *Nat Commun* **2016**, *7* (1), 12291. https://doi.org/10.1038/ncomms12291.

(211) Xie, H.; Wang, H.; Pei, Y.; Fu, C.; Liu, X.; Snyder, G. J.; Zhao, X.; Zhu, T. Beneficial Contribution of Alloy Disorder to Electron and Phonon Transport in Half-Heusler Thermoelectric Materials. *Adv. Funct. Mater.* **2013**, *23* (41), 5123–5130. https://doi.org/10.1002/adfm.201300663.

(212) Zheng, Z.; Su, X.; Deng, R.; Stoumpos, C.; Xie, H.; Liu, W.; Yan, Y.; Hao, S.; Uher, C.; Wolverton, C.; Kanatzidis, M. G.; Tang, X. Rhombohedral to Cubic Conversion of GeTe via MnTe Alloying Leads to Ultralow Thermal Conductivity, Electronic Band Convergence, and High Thermoelectric Performance. *J. Am. Chem. Soc.* **2018**, *140* (7), 2673–2686. https://doi.org/10.1021/jacs.7b13611.

(213) Zhang, Y.; Skoug, E.; Cain, J.; Ozoliņš, V.; Morelli, D.; Wolverton, C. First-Principles Description of Anomalously Low Lattice Thermal Conductivity in Thermoelectric Cu-Sb-Se Ternary Semiconductors. *Phys. Rev. B* **2012**, *85* (5), 054306. https://doi.org/10.1103/PhysRevB.85.054306.

(214) Xiao, Y.; Wu, H.; Li, W.; Yin, M.; Pei, Y.; Zhang, Y.; Fu, L.; Chen, Y.; Pennycook, S. J.; Huang, L.; He, J.; Zhao, L.-D. Remarkable Roles of Cu To Synergistically Optimize Phonon and Carrier Transport in N-Type PbTe-Cu $_{2}$ Te. *J. Am. Chem. Soc.* **2017**, *139* (51), 18732–18738. https://doi.org/10.1021/jacs.7b11662.

(215) Pei, Y.; Zheng, L.; Li, W.; Lin, S.; Chen, Z.; Wang, Y.; Xu, X.; Yu, H.; Chen, Y.; Ge, B. Interstitial Point Defect Scattering Contributing to High Thermoelectric Performance in SnTe. *Adv. Electron. Mater.* **2016**, *2* (6), 1600019. https://doi.org/10.1002/aelm.201600019.

(216) Tang, J.; Gao, B.; Lin, S.; Wang, X.; Zhang, X.; Xiong, F.; Li, W.; Chen, Y.; Pei, Y. Manipulation of Solubility and Interstitial Defects for Improving Thermoelectric SnTe Alloys. *ACS Energy Lett.* **2018**, *3* (8), 1969–1974. https://doi.org/10.1021/acsenergylett.8b01098.

(217) Cook, B. A.; Kramer, M. J.; Wei, X.; Harringa, J. L.; Levin, E. M. Nature of the Cubic to Rhombohedral Structural Transformation in (AgSbTe2)15(GeTe)85

Thermoelectric Material. *Journal of Applied Physics* **2007**, *101* (5), 053715. https://doi.org/10.1063/1.2645675.

(218) Gelbstein, Y.; Ben-Yehuda, O.; Pinhas, E.; Edrei, T.; Sadia, Y.; Dashevsky, Z.; Dariel, M. P. Thermoelectric Properties of (Pb,Sn,Ge)Te-Based Alloys. *Journal of Elec Materi* **2009**, *38* (7), 1478–1482. https://doi.org/10.1007/s11664-008-0652-8.

(219) Tan, G.; Zhao, L.-D.; Kanatzidis, M. G. Rationally Designing High-Performance Bulk Thermoelectric Materials. *Chem. Rev.* **2016**, *116* (19), 12123–12149. https://doi.org/10.1021/acs.chemrev.6b00255.

(220) Banik, A.; Shenoy, U. S.; Saha, S.; Waghmare, U. V.; Biswas, K. High Power Factor and Enhanced Thermoelectric Performance of SnTe-$AgInTe_2$: Synergistic Effect of Resonance Level and Valence Band Convergence. *J. Am. Chem. Soc.* **2016**, *138* (39), 13068–13075. https://doi.org/10.1021/jacs.6b08382.

(221) He, J.; Tritt, T. M. Advances in Thermoelectric Materials Research: Looking Back and Moving Forward. *Science* **2017**, *357* (6358), eaak9997. https://doi.org/10.1126/science.aak9997.

(222) Sootsman, J. R.; Chung, D. Y.; Kanatzidis, M. G. New and Old Concepts in Thermoelectric Materials. *Angew. Chem. Int. Ed.* **2009**, *48* (46), 8616–8639. https://doi.org/10.1002/anie.200900598.

(223) Song, S.; Lo, C.-W. T.; Aminzare, M.; Tseng, Y.-C.; Valiyaveettil, S. M.; Mozharivskyj, Y. Enhancing the Thermoelectric Performance of $Sn_{0.5}Ge_{0.5}Te$ *via* Doping with Sb/Bi and Alloying with Cu_2Te: Optimization of Transport Properties and Thermal Conductivities. *Dalton Trans.* **2020**, *49* (18), 6135–6144. https://doi.org/10.1039/D0DT00544D.

(224) Tang, J.; Yao, Z.; Wu, Y.; Lin, S.; Xiong, F.; Li, W.; Chen, Y.; Zhu, T.; Pei, Y. Atomic Disordering Advances Thermoelectric Group IV Telluride Alloys with a Multiband Transport. *Materials Today Physics* **2020**, *15*, 100247. https://doi.org/10.1016/j.mtphys.2020.100247.

(225) Tang, J.; Yao, Z.; Chen, Z.; Lin, S.; Zhang, X.; Xiong, F.; Li, W.; Chen, Y.; Pei, Y. Maximization of Transporting Bands for High-Performance SnTe Alloy Thermoelectrics. *Materials Today Physics* **2019**, *9*, 100091. https://doi.org/10.1016/j.mtphys.2019.03.005.

(226) Xie, G. Band Inversion Induced Multiple Electronic Valleys for High Thermoelectric Performance of SnTe with Strong Lattice Softening. *Nano Energy* **2020**, 9.

(227) Tan, X.; Liu, G.; Xu, J.; Tan, X.; Shao, H.; Hu, H.; Jiang, H.; Lu, Y.; Jiang, J. Thermoelectric Properties of In-Hg Co-Doping in SnTe: Energy Band Engineering. *Journal of Materiomics* **2018**, *4* (1), 62–67. https://doi.org/10.1016/j.jmat.2017.12.001.

(228) Zhang, X.; Zhou, Y.; Pei, Y.; Chen, Y.; Yuan, B.; Zhang, S.; Deng, Y.; Gong, S.; He, J.; Zhao, L.-D. Enhancing Thermoelectric Performance of SnTe via Nanostructuring Particle Size. *Journal of Alloys and Compounds* **2017**, *709*, 575–580. https://doi.org/10.1016/j.jallcom.2017.02.283.

(229) Zhou, Y. M.; Wu, H. J.; Pei, Y. L.; Chang, C.; Xiao, Y.; Zhang, X.; Gong, S. K.; He, J. Q.; Zhao, L.-D. Strategy to Optimize the Overall Thermoelectric Properties of SnTe via Compositing with Its Property-Counter CuInTe2. *Acta Materialia* **2017**, *125*, 542–549. https://doi.org/10.1016/j.actamat.2016.11.049.

(230) Zhang, L.; Wang, J.; Cheng, Z.; Sun, Q.; Li, Z.; Dou, S. Lead-Free SnTe-Based Thermoelectrics: Enhancement of Thermoelectric Performance by Doping with Gd/Ag. *J. Mater. Chem. A* **2016**, *4* (20), 7936–7942. https://doi.org/10.1039/C6TA01994C.

(231) Su, C.-H. Design, Growth and Characterization of PbTe-Based Thermoelectric Materials. *Progress in Crystal Growth and Characterization of Materials* **2019**, *65* (2), 47–94. https://doi.org/10.1016/j.pcrysgrow.2019.04.001.

(232) Dughaish, Z. H. Lead Telluride as a Thermoelectric Material for Thermoelectric Power Generation. *Physica B: Condensed Matter* **2002**, *322* (1–2), 205–223. https://doi.org/10.1016/S0921-4526(02)01187-0.

(233) Liu, Z.; Sun, J.; Mao, J.; Zhu, H.; Ren, W.; Zhou, J.; Wang, Z.; Singh, D. J.; Sui, J.; Chu, C.-W.; Ren, Z. Phase-Transition Temperature Suppression to Achieve Cubic GeTe and High Thermoelectric Performance by Bi and Mn Codoping. *Proc Natl Acad Sci USA* **2018**, *115* (21), 5332–5337. https://doi.org/10.1073/pnas.1802020115.

(234) Perumal, S.; Bellare, P.; Shenoy, U. S.; Waghmare, U. V.; Biswas, K. Low Thermal Conductivity and High Thermoelectric Performance in Sb and Bi Codoped GeTe: Complementary Effect of Band Convergence and Nanostructuring. *Chem. Mater.* **2017**, *29* (24), 10426–10435. https://doi.org/10.1021/acs.chemmater.7b04023.

(235) Jin, Y.; Zhang, X.; Xiao, Y.; He, W.; Wang, D.; Li, J.; Zheng, S.; Ren, D.; Qiu, Y.; Zhao, L.-D. Synergistically Improving Thermoelectric and Mechanical Properties of Ge0.94Bi0.06Te through Dispersing Nano-SiC. *Scripta Materialia* **2020**, *183*, 22–27. https://doi.org/10.1016/j.scriptamat.2020.03.018.

(236) Luo, Z.; Zhang, X.; Hua, X.; Tan, G.; Bailey, T. P.; Xu, J.; Uher, C.; Wolverton, C.; Dravid, V. P.; Yan, Q.; Kanatzidis, M. G. High Thermoelectric Performance in Supersaturated Solid Solutions and Nanostructured N-Type PbTe–GeTe. *Adv. Funct. Mater.* **2018**, *28* (31), 1801617. https://doi.org/10.1002/adfm.201801617.

(237) Samanta, M.; Roychowdhury, S.; Ghatak, J.; Perumal, S.; Biswas, K. Ultrahigh Average Thermoelectric Figure of Merit, Low Lattice Thermal Conductivity and Enhanced Microhardness in Nanostructured $(GeTe)_{x}(AgSbSe_{2})_{100-x}$. *Chem. Eur. J.* **2017**, *23* (31), 7438–7443. https://doi.org/10.1002/chem.201701480.

(238) Zybała, R. Preparation and Characterization of Nanostructured (GeTe)75(AgSbTe2)x(AgSbSe2)y Thermoelectric Materials. *Synthetic Metals* **2020**, *270*, 116606. https://doi.org/10.1016/j.synthmet.2020.116606.

(239) Zhao, S. Y.; Chen, R.; Li, J. Q.; Yang, L.; Zhang, C. H.; Li, Y.; Liu, F. S.; Ao, W. Q. Synergistic Effects on Thermoelectric Properties of $Sn_{0.5}Ge_{0.4875}Te$ with Pb Alloying. *Journal of Alloys and Compounds* **2019**, *777*, 1334–1339. https://doi.org/10.1016/j.jallcom.2018.11.051.

(240) Charles Robert, M.; Saravanan, R. Single Crystal X-Ray Analysis of the Electronic Structure of the Thermoelectric Material $Sn_{1-x}Ge_{x}Te$. *Indian J Phys* **2010**, *84* (9), 1203–1210. https://doi.org/10.1007/s12648-010-0115-y.

(241) Li, J. Q.; Huang, S.; Chen, Z. P.; Li, Y.; Song, S. H.; Liu, F. S.; Ao, W. Q. Phases and Thermoelectric Properties of SnTe with (Ge, Mn) Co-Doping. *Phys. Chem. Chem. Phys.* **2017**, *19* (42), 28749–28755. https://doi.org/10.1039/C7CP04931E.

(242) Heremans, J. P.; Wiendlocha, B.; Chamoire, A. M. Resonant Levels in Bulk Thermoelectric Semiconductors. *Energy Environ. Sci.* **2012**, *5* (2), 5510–5530. https://doi.org/10.1039/C1EE02612G.

(243) Jaworski, C. M.; Kulbachinskii, V.; Heremans, J. P. Resonant Level Formed by Tin in Bi 2 Te 3 and the Enhancement of Room-Temperature Thermoelectric Power. *Phys. Rev. B* **2009**, *80* (23), 233201. https://doi.org/10.1103/PhysRevB.80.233201.

(244) Bhat, D. K.; Shenoy, U. S. Resonance Levels in GeTe Thermoelectrics: Zinc as a New Multifaceted Dopant. *New J. Chem.* **2020**, 10.1039.D0NJ04273K. https://doi.org/10.1039/D0NJ04273K.

(245) Qiu, Y.; Jin, Y.; Wang, D.; Guan, M.; He, W.; Peng, S.; Liu, R.; Gao, X.; Zhao, L.-D. Realizing High Thermoelectric Performance in GeTe through Decreasing the Phase Transition Temperature *via* Entropy Engineering. *J. Mater. Chem. A* **2019**, *7* (46), 26393–26401. https://doi.org/10.1039/C9TA10963C.

(246) Guo, F.; Cui, B.; Geng, H.; Zhang, Y.; Wu, H.; Zhang, Q.; Yu, B.; Pennycook, S. J.; Cai, W.; Sui, J. Simultaneous Boost of Power Factor and Figure-of-Merit in In–Cu Codoped SnTe. **2019**, 10.

(247) Dangić, Đ.; Hellman, O.; Fahy, S.; Savić, I. The Origin of the Lattice Thermal Conductivity Enhancement at the Ferroelectric Phase Transition in GeTe. *npj Comput Mater* **2021**, *7* (1), 57. https://doi.org/10.1038/s41524-021-00523-7.

(248) Pei, Y.; Wang, H.; Snyder, G. J. Band Engineering of Thermoelectric Materials. *Adv. Mater.* **2012**, *24* (46), 6125–6135. https://doi.org/10.1002/adma.201202919.

(249) Conwell, E.; Weisskopf, V. F. Theory of Impurity Scattering in Semiconductors. *Phys. Rev.* **1950**, *77* (3), 388–390. https://doi.org/10.1103/PhysRev.77.388.

(250) Islam, Md. R.; Islam, Md. S.; Ferdous, N.; Anindya, K. N.; Hashimoto, A. Spin–Orbit Coupling Effects on the Electronic Structure of Two-Dimensional Silicon Carbide. *J Comput Electron* **2019**, *18* (2), 407–414. https://doi.org/10.1007/s10825-019-01326-2.

(251) Gao, X.; Daw, M. S. Investigation of Band Inversion in (Pb,Sn)Te Alloys Using *Ab Initio* Calculations. *Phys. Rev. B* **2008**, *77* (3), 033103. https://doi.org/10.1103/PhysRevB.77.033103.

(252) Bu, Z.; Li, W.; Li, J.; Zhang, X.; Mao, J.; Chen, Y.; Pei, Y. Dilute Cu_2Te-Alloying Enables Extraordinary Performance of r-GeTe Thermoelectrics. *Materials Today Physics* **2019**, *9*, 100096. https://doi.org/10.1016/j.mtphys.2019.100096.

(253) He, J.; Xu, J.; Tan, X.; Liu, G.-Q.; Shao, H.; Liu, Z.; Jiang, H.; Jiang, J. Synthesis of SnTe/AgSbSe 2 Nanocomposite as a Promising Lead-Free Thermoelectric Material. *Journal of Materiomics* **2016**, *2* (2), 165–171. https://doi.org/10.1016/j.jmat.2016.05.001.

(254) Wang, L.; Chang, S.; Zheng, S.; Fang, T.; Cui, W.; Bai, P.; Yue, L.; Chen, Z.-G. Thermoelectric Performance of Se/Cd Codoped SnTe via Microwave Solvothermal Method. *ACS Appl. Mater. Interfaces* **2017**, *9* (27), 22612–22619. https://doi.org/10.1021/acsami.7b06083.

(255) Xing, T.; Song, Q.; Qiu, P.; Zhang, Q.; Xia, X.; Liao, J.; Liu, R.; Huang, H.; Yang, J.; Bai, S.; Ren, D.; Shi, X.; Chen, L. Superior Performance and High Service Stability for GeTe-Based Thermoelectric Compounds. *National Science Review* **2019**, *6* (5), 944–954. https://doi.org/10.1093/nsr/nwz052.

(256) Kumar, A.; Bhumla, P.; Parashchuk, T.; Baran, S.; Bhattacharya, S.; Wojciechowski, K. T. Engineering Electronic Structure and Lattice Dynamics to

Achieve Enhanced Thermoelectric Performance of Mn–Sb Co-Doped GeTe. *Chem. Mater.* **2021**, *33* (10), 3611–3620. https://doi.org/10.1021/acs.chemmater.1c00331.

(257) Kumar, A.; Vermeulen, P. A.; Kooi, B. J.; Rao, J.; van Eijck, L.; Schwarzmüller, S.; Oeckler, O.; Blake, G. R. Phase Transitions of Thermoelectric TAGS-85. *Inorg. Chem.* **2017**, *56* (24), 15091–15100. https://doi.org/10.1021/acs.inorgchem.7b02433.

(258) Lyu, W. Y.; Hong, M.; Liu, W. D.; Li, M.; Sun, Q.; Xu, S. D.; Zou, J.; Chen, Z.-G. Rare-Earth Nd Inducing Record-High Thermoelectric Performance of $(GeTe)_{85}(AgSbTe_2)_{15}$. *Energy Material Advances* **2021**, *2021*, 1–8. https://doi.org/10.34133/2021/2414286.

(259) Song, S.; Yang, Z.; Huang, Y.; Tseng, Y.-C.; Valiyaveettil, S. M.; Chen, K.-H.; Mozharivskyj, Y. Enhancing Thermoelectric Performance of $Sn_{0.5}Ge_{0.5}Te$ via Doping with In/Zn, In/Sb and In/Bi. *Journal of Solid State Chemistry* **2021**, *302*, 122444. https://doi.org/10.1016/j.jssc.2021.122444.

(260) Zhang, Z.; Zheng, S.; Li, J.; Wang, B.; Yue, L.; Wu, Y.; Dong, X.; Chen, L.; Gao, L.; Lu, G. Realizing High Thermoelectric Performance in the ZnTe-Alloyed $CuGaTe_2$ through Band Engineering. *ACS Appl. Energy Mater.* **2020**, *3* (12), 12400–12406. https://doi.org/10.1021/acsaem.0c02386.

(261) Li, J.; Chen, Z.; Zhang, X.; Yu, H.; Wu, Z.; Xie, H.; Chen, Y.; Pei, Y. Simultaneous Optimization of Carrier Concentration and Alloy Scattering for Ultrahigh Performance GeTe Thermoelectrics. *Adv. Sci.* **2017**, *4* (12), 1700341. https://doi.org/10.1002/advs.201700341.

(262) Wei, J.; Liu, H. J.; Cheng, L.; Zhang, J.; Liang, J. H.; Jiang, P. H.; Fan, D. D.; Shi, J. Tuning the Carrier Concentration to Improve the Thermoelectric Performance of $CuInTe_2$ Compound. *AIP Advances* **2015**, *5* (10), 107230. https://doi.org/10.1063/1.4935051.

(263) Hanghofer, I.; Brinek, M.; Eisbacher, S. L.; Bitschnau, B.; Volck, M.; Hennige, V.; Hanzu, I.; Rettenwander, D.; Wilkening, H. M. R. Substitutional Disorder: Structure and Ion Dynamics of the Argyrodites Li_6PS_5Cl, Li_6PS_5Br and Li_6PS_5I. *Phys. Chem. Chem. Phys.* **2019**, *21* (16), 8489–8507. https://doi.org/10.1039/C9CP00664H.

(264) Tang, J.; Gao, B.; Lin, S.; Li, J.; Chen, Z.; Xiong, F.; Li, W.; Chen, Y.; Pei, Y. Manipulation of Band Structure and Interstitial Defects for Improving Thermoelectric SnTe. *Adv. Funct. Mater.* **2018**, *28* (34), 1803586. https://doi.org/10.1002/adfm.201803586.

(265) Zhang, J.; Li, S.; Wu, Z.; Zhang, J. Enhanced Thermoelectric Properties of Bismuth and Zinc Co-Doped SnTe by Band Engineering and All-Scale Structure Defects. *Journal of Alloys and Compounds* **2022**, *889*, 161651. https://doi.org/10.1016/j.jallcom.2021.161651.

(266) Yao, Z.; Li, W.; Tang, J.; Chen, Z.; Lin, S.; Biswas, K.; Burkov, A.; Pei, Y. Solute Manipulation Enabled Band and Defect Engineering for Thermoelectric Enhancements of SnTe. *InfoMat* **2019**, *1* (4), 571–581. https://doi.org/10.1002/inf2.12044.

(267) Ye, Z.-Y.; Deng, H.-X.; Wu, H.-Z.; Li, S.-S.; Wei, S.-H.; Luo, J.-W. The Origin of Electronic Band Structure Anomaly in Topological Crystalline Insulator Group-IV Tellurides. *npj Comput Mater* **2015**, *1* (1), 15001. https://doi.org/10.1038/npjcompumats.2015.1.

(268) Yan, X.; Zheng, S.; Zhou, Z.; Wu, H.; Zhang, B.; Huang, Y.; Lu, X.; Han, G.; Wang, G.; Zhou, X. Melt-Spun $Sn_{1-x-y}Sb_x$ Mn_y Te with Unique Multiscale Microstructures Approaching Exceptional Average Thermoelectric ZT. *Nano Energy* **2021**, *84*, 105879. https://doi.org/10.1016/j.nanoen.2021.105879.

(269) He, J.; Girard, S. N.; Kanatzidis, M. G.; Dravid, V. P. Microstructure-Lattice Thermal Conductivity Correlation in Nanostructured $PbTe_{0.7}$ $S_{0.3}$ Thermoelectric Materials. *Adv. Funct. Mater.* **2010**, *20* (5), 764–772. https://doi.org/10.1002/adfm.200901905.

(270) Ma, J.; Li, W.; Luo, X. Examining the Callaway Model for Lattice Thermal Conductivity. *Phys. Rev. B* **2014**, *90* (3), 035203. https://doi.org/10.1103/PhysRevB.90.035203.

(271) Guo, F. Enhanced Thermoelectric Performance of SnTe Alloy with Ce and Li Co-Doping. *Materials Today Physics* **2019**, 6.

(272) Tan, G.; Shi, F.; Sun, H.; Zhao, L.-D.; Uher, C.; Dravid, V. P.; Kanatzidis, M. G. SnTe–$AgBiTe_2$ as an Efficient Thermoelectric Material with Low Thermal Conductivity. *J. Mater. Chem. A* **2014**, *2* (48), 20849–20854. https://doi.org/10.1039/C4TA05530F.

(273) Chen, Y.; Nielsen, M. D.; Gao, Y.-B.; Zhu, T.-J.; Zhao, X.; Heremans, J. P. SnTe-AgSbTe2 Thermoelectric Alloys. *Adv. Energy Mater.* **2012**, *2* (1), 58–62. https://doi.org/10.1002/aenm.201100460.

(274) Zhang, Q.; Guo, Z.; Tan, X.; Mao, L.; Yin, Y.; Xiao, Y.; Hu, H.; Tan, C.; Wu, Q.; Liu, G.-Q.; Xu, J.; Jiang, J. Effects of AgBiSe2 on Thermoelectric Properties of SnTe. *Chemical Engineering Journal* **2020**, *390*, 124585. https://doi.org/10.1016/j.cej.2020.124585.

(275) Liu, C.; Huang, Z.; Wang, D.; Wang, X.; Miao, L.; Wang, X.; Wu, S.; Toyama, N.; Asaka, T.; Chen, J.; Nishibori, E.; Zhao, L.-D. Dynamic Ag^+ -Intercalation with $AgSnSe_2$ Nano-Precipitates in Cl-Doped Polycrystalline $SnSe_2$ toward Ultra-High Thermoelectric Performance. *J. Mater. Chem. A* **2019**, *7* (16), 9761–9772. https://doi.org/10.1039/C9TA01678C.

(276) Liang, G.; Lyu, T.; Hu, L.; Qu, W.; Zhi, S.; Li, J.; Zhang, Y.; He, J.; Li, J.; Liu, F.; Zhang, C.; Ao, W.; Xie, H.; Wu, H. $(GeTe)_{1-x}(AgSnSe_2)_x$: Strong Atomic Disorder-Induced High Thermoelectric Performance near the Ioffe–Regel Limit. *ACS Appl. Mater. Interfaces* **2021**, *13* (39), 47081–47089. https://doi.org/10.1021/acsami.1c14801.

(277) Wang, N.; West, D.; Liu, J.; Li, J.; Yan, Q.; Gu, B.-L.; Zhang, S. B.; Duan, W. Microscopic Origin of the p -Type Conductivity of the Topological Crystalline Insulator SnTe and the Effect of Pb Alloying. *Phys. Rev. B* **2014**, *89* (4), 045142. https://doi.org/10.1103/PhysRevB.89.045142.

(278) Schneider, J.; Schulz, H. X-Ray Powder Diffraction of $_2$ at Temperatures up to 1123K. 15.

(279) Wold, A. Structure NaCl des phases $Ag_xSn_{1-x}X$ (X = S, Se). No. 6, 5.

(280) Wei, T.-R.; Tan, G.; Zhang, X.; Wu, C.-F.; Li, J.-F.; Dravid, V. P.; Snyder, G. J.; Kanatzidis, M. G. Distinct Impact of Alkali-Ion Doping on Electrical Transport Properties of Thermoelectric *p* -Type Polycrystalline SnSe. *J. Am. Chem. Soc.* **2016**, *138* (28), 8875–8882. https://doi.org/10.1021/jacs.6b04181.

(281) Wakita, T.; Paris, E.; Kobayashi, K.; Terashima, K.; Hacisalihoğlu, M. Y.; Ueno, T.; Bondino, F.; Magnano, E.; Píš, I.; Olivi, L.; Akimitsu, J.; Muraoka, Y.; Yokoya, T.; Saini, N. L. The Electronic Structure of $Ag_{1-x}Sn_{1+x}Se_2$ (x = 0.0, 0.1, 0.2, 0.25 and 1.0). *Phys. Chem. Chem. Phys.* **2017**, *19* (39), 26672–26678. https://doi.org/10.1039/C7CP05369J.

(282) Banik, A.; Vishal, B.; Perumal, S.; Datta, R.; Biswas, K. The Origin of Low Thermal Conductivity in $Sn_{1-x}Sb_xTe$: Phonon Scattering via Layered Intergrowth Nanostructures. *Energy Environ. Sci.* **2016**, *9* (6), 2011–2019. https://doi.org/10.1039/C6EE00728G.

(283) Sergeev, A.; Mitin, V. Electron-Phonon Interaction in Disordered Conductors: Static and Vibrating Scattering Potentials. *Phys. Rev. B* **2000**, *61* (9), 6041–6047. https://doi.org/10.1103/PhysRevB.61.6041.

(284) Giacovazzo, C. *Fundamentals of Crystallography*, 3rd ed.; IUCr/Oxford University Press, 2011.

(285) Pöhls, J.-H.; Mozharivskyj, Y. TOSSPB: Thermoelectric Optimization Based on Scattering-Dependent Single-Parabolic Band Model. *Computational Materials Science* **2022**, *206*, 111152. https://doi.org/10.1016/j.commatsci.2021.111152.

(286) Xu, W.; Zhang, Z.; Liu, C.; Gao, J.; Ye, Z.; Chen, C.; Peng, Y.; Bai, X.; Miao, L. Substantial Thermoelectric Enhancement Achieved by Manipulating the Band Structure and Dislocations in Ag and La Co-Doped SnTe. *J Adv Ceram* **2021**, *10* (4), 860–870. https://doi.org/10.1007/s40145-021-0480-3.

(287) Xing, Z.-B.; Li, Z.-Y.; Tan, Q.; Wei, T.-R.; Wu, C.-F.; Li, J.-F. Composition Optimization of P-Type $AgSn_m$ $SbTe_{m+2}$Thermoelectric Materials Synthesized by Mechanical Alloying and Spark Plasma Sintering. *Journal of Alloys and Compounds* **2014**, *615*, 451–455. https://doi.org/10.1016/j.jallcom.2014.06.176.

(288) Tritt, T. M. Thermoelectric Phenomena, Materials, and Applications. *Annu. Rev. Mater. Res.* **2011**, *41* (1), 433–448. https://doi.org/10.1146/annurev-matsci-062910-100453.

(289) Aminzare, M.; Tseng, Y.-C.; Mozharivskyj, Y. Effect of Spark Plasma Sintering and Sb Doping on the Thermoelectric Properties of $Co_4Ge_6Te_6$ Skutterudite. *Journal of Solid State Chemistry* **2019**, *269*, 434–441. https://doi.org/10.1016/j.jssc.2018.10.020.

(290) Liang, Y.; Fang, B.; Zhu, X. M.; Liang, M. M. Superstructure and Physical Properties of Skutterudite-Related Phase $CoGe_{1.5}Se_{1.5}$. *IOP Conf. Ser.: Mater. Sci. Eng.* **2017**, *182*, 012012. https://doi.org/10.1088/1757-899X/182/1/012012.

(291) Dong, Y.; Wei, K.; Nolas, G. S. Transport Properties of Partially Filled Skutterudite Derivatives $Ce_{0.13}Co_4Ge_6Se_6$and $Yb_{0.14}Co_4Ge_6Se_6$. *Phys. Rev. B* **2013**, *87* (19), 195203. https://doi.org/10.1103/PhysRevB.87.195203.

(292) Zevalkink, A.; Star, K.; Aydemir, U.; Snyder, G. J.; Fleurial, J.-P.; Bux, S.; Vo, T.; von Allmen, P. Electronic Structure and Thermoelectric Properties of Pnictogen-Substituted $A\,Sn_{1.5}Te_{1.5}$ (A = Co, Rh, Ir) Skutterudites. *Journal of Applied Physics* **2015**, *118* (3), 035107. https://doi.org/10.1063/1.4926479.

(293) Volja, D.; Kozinsky, B.; Li, A.; Wee, D.; Marzari, N.; Fornari, M. Electronic, Vibrational, and Transport Properties of Pnictogen-Substituted Ternary Skutterudites. *Phys. Rev. B* **2012**, *85* (24), 245211. https://doi.org/10.1103/PhysRevB.85.245211.

(294) de Meester de Betzembroeck, P.; Naud, J. Étude par Diffraction-X de Quelques Composés du Système Ni-Co-Te Obtenus par Synthèse Thermique. *Bull. Soc. Chim. Belges* **2010**, *80* (1–2), 107–116. https://doi.org/10.1002/bscb.19710800112.

(295) Muhler, M.; Bensch, W.; Schur, M. Preparation, Crystal Structures, Experimental and Theoretical Electronic Band Structures of Cobalt Tellurides in the Composition Range. *J. Phys.: Condens. Matter* **1998**, *10* (13), 2947–2962. https://doi.org/10.1088/0953-8984/10/13/012.

(296) Samanta, M.; Ghosh, T.; Arora, R.; Waghmare, U. V.; Biswas, K. Realization of Both N- and p-Type GeTe Thermoelectrics: Electronic Structure Modulation by AgBiSe $_2$ Alloying. *J. Am. Chem. Soc.* **2019**, *141* (49), 19505–19512. https://doi.org/10.1021/jacs.9b11405.

(297) Zhou, L.; Qiu, P.; Uher, C.; Shi, X.; Chen, L. Thermoelectric Properties of P-Type YbxLayFe$_{2.7}$Co$_{1.3}$Sb$_{12}$ Double-Filled Skutterudites. *Intermetallics* **2013**, *32*, 209–213. https://doi.org/10.1016/j.intermet.2012.08.005.

(298) Dahal, T.; Gahlawat, S.; Jie, Q.; Dahal, K.; Lan, Y.; White, K.; Ren, Z. Thermoelectric and Mechanical Properties on Misch Metal Filled P-Type Skutterudites Mm$_{0.9}$Fe$_{4-x}$Co$_x$Sb$_{12}$. *J. Appl. Phys.* **2015**, *117* (5), 055101. https://doi.org/10.1063/1.4906954.

(299) Rogl, G.; Grytsiv, A.; Rogl, P.; Bauer, E.; Zehetbauer, M. A New Generation of P-Type Didymium Skutterudites with High ZT. *Intermetallics* **2011**, *19* (4), 546–555. https://doi.org/10.1016/j.intermet.2010.12.001.

(300) Kawaharada, Y.; Kurosaki, K.; Uno, M.; Yamanaka, S. Thermoelectric Properties of CoSb $_3$. *Journal of Alloys and Compounds* **2001**, *315* (1–2), 193–197. https://doi.org/10.1016/S0925-8388(00)01275-5.

(301) Foster, S.; Neophytou, N. Doping Optimization for the Power Factor of Bipolar Thermoelectric Materials. *Journal of Elec Materi* **2019**, *48* (4), 1889–1895. https://doi.org/10.1007/s11664-018-06857-1.

(302) The Computation of Fermi-Dirac Functions. 40.

(303) Nguyen, T. H.; O'Leary, S. K. The Dependence of the Fermi Level on Temperature, Doping Concentration, and Disorder in Disordered Semiconductors. *Journal of Applied Physics* **2000**, *88* (6), 3479–3483. https://doi.org/10.1063/1.1289078.

(304) Dong, J.; Sun, F.-H.; Tang, H.; Pei, J.; Zhuang, H.-L.; Hu, H.-H.; Zhang, B.-P.; Pan, Y.; Li, J.-F. Medium-Temperature Thermoelectric GeTe: Vacancy Suppression and Band Structure Engineering Leading to High Performance. *Energy Environ. Sci.* **2019**, *12* (4), 1396–1403. https://doi.org/10.1039/C9EE00317G.

(305) Ebling, D. G.; Jacquot, A.; Jägle, M.; Böttner, H.; Kühn, U.; Kirste, L. Structure and Thermoelectric Properties of Nanocomposite Bismuth Telluride Prepared by

Melt Spinning or by Partially Alloying with IV-VI Compounds: Structure and Thermoelectric Properties of Nanocomposite Bismuth Telluride. *phys. stat. sol. (RRL)* **2007**, *1* (6), 238–240. https://doi.org/10.1002/pssr.200701174.

(306) Tan, H.; Zhang, B.; Wang, G.; Chen, Y.; Shen, X.; Guo, L.; Han, X.; Lu, X.; Zhou, X. Rapid Preparation of Ge0.9Sb0.1Te1+ via Unique Melt Spinning: Hierarchical Microstructure and Improved Thermoelectric Performance. *Journal of Alloys and Compounds* **2019**, *774*, 129–136. https://doi.org/10.1016/j.jallcom.2018.09.144.

(307) Tan, G.; Liu, W.; Wang, S.; Yan, Y.; Li, H.; Tang, X.; Uher, C. Rapid Preparation of CeFe4Sb12 Skutterudite by Melt Spinning: Rich Nanostructures and High Thermoelectric Performance. *J. Mater. Chem. A* **2013**, *1* (40), 12657. https://doi.org/10.1039/c3ta13024j.

(308) Thomas, R.; Rao, A.; Chauhan, N. S.; Vishwakarma, A.; Singh, N. K.; Soni, A. Melt Spinning: A Rapid and Cost Effective Approach over Ball Milling for the Production of Nanostructured p-Type Si80Ge20 with Enhanced Thermoelectric Properties. *Journal of Alloys and Compounds* **2019**, *781*, 344–350. https://doi.org/10.1016/j.jallcom.2018.11.414.

(309) Zheng, Y.; Xie, H.; Zhang, Q.; Suwardi, A.; Cheng, X.; Zhang, Y.; Shu, W.; Wan, X.; Yang, Z.; Liu, Z.; Tang, X. Unraveling the Critical Role of Melt-Spinning Atmosphere in Enhancing the Thermoelectric Performance of p-Type $Bi_{0.52}Sb_{1.48}Te_3$ Alloys. *ACS Appl. Mater. Interfaces* **2020**, *12* (32), 36186–36195. https://doi.org/10.1021/acsami.0c09656.

(310) Liu, Y.; Zhang, Y.; Lim, K. H.; Ibáñez, M.; Ortega, S.; Li, M.; David, J.; Martí-Sánchez, S.; Ng, K. M.; Arbiol, J.; Kovalenko, M. V.; Cadavid, D.; Cabot, A. High Thermoelectric Performance in Crystallographically Textured N-Type $Bi_2Te_{3-x}Se_x$ Produced from Asymmetric Colloidal Nanocrystals. *ACS Nano* **2018**, *12* (7), 7174–7184. https://doi.org/10.1021/acsnano.8b03099.

(311) Zheng, W.; Luo, Y.; Liu, Y.; Shi, J.; Xiong, R.; Wang, Z. Synergistical Tuning Interface Barrier and Phonon Propagation in Au–Sb_2Te_3 Nanoplate for Boosting Thermoelectric Performance. *J. Phys. Chem. Lett.* **2019**, *10* (17), 4903–4909. https://doi.org/10.1021/acs.jpclett.9b02312.

(312) Gayner, C.; Amouyal, Y. Energy Filtering of Charge Carriers: Current Trends, Challenges, and Prospects for Thermoelectric Materials. *Adv. Funct. Mater.* **2020**, *30* (18), 1901789. https://doi.org/10.1002/adfm.201901789.

(313) Ko, D.-K.; Kang, Y.; Murray, C. B. Enhanced Thermopower via Carrier Energy Filtering in Solution-Processable Pt–Sb_2Te_3 Nanocomposites. *Nano Lett.* **2011**, *11* (7), 2841–2844. https://doi.org/10.1021/nl2012246.

(314) Yang, J.; Xi, L.; Qiu, W.; Wu, L.; Shi, X.; Chen, L.; Yang, J.; Zhang, W.; Uher, C.; Singh, D. J. On the Tuning of Electrical and Thermal Transport in Thermoelectrics: An Integrated Theory–Experiment Perspective. *npj Comput Mater* **2016**, *2* (1), 15015. https://doi.org/10.1038/npjcompumats.2015.15.

(315) Anjum, F.; Nasir, H.; Lee, J.; Kim, H. J. Fabrication and Characterization of Silver Polycrystalline Photocathode. *Optik* **2022**, *269*, 169906. https://doi.org/10.1016/j.ijleo.2022.169906.

(316) Yoon, H.-S.; Lee, J.; Park, J.; Oh, J.-W.; Kang, Y.-C. Physicochemical Properties of SnTe Thin Films Dependent on Compositional Ratios. *Physica Status Solidi (a)* **2022**, *219* (12), 2200059. https://doi.org/10.1002/pssa.202200059.

(317) Xu, Y.; Al-Salim, N.; Hodgkiss, J. M.; Tilley, R. D. Solution Synthesis and Optical Properties of SnTe Nanocrystals. *Crystal Growth & Design* **2011**, *11* (7), 2721–2723. https://doi.org/10.1021/cg200660y.

(318) Dun, C.; Hewitt, C. A.; Li, Q.; Xu, J.; Schall, D. C.; Lee, H.; Jiang, Q.; Carroll, David. L. 2D Chalcogenide Nanoplate Assemblies for Thermoelectric Applications. *Adv. Mater.* **2017**, *29* (21), 1700070. https://doi.org/10.1002/adma.201700070.